UNIVERSITY OF SOUTHAMPTON

FACULTY OF ENGINEERING AND THE ENVIRONMENT

Electrochemical Monitoring of Nickel–Aluminium Bronze Crevice Corrosion Solutions using Boron–Doped Diamond Electrode

by

Stefano Neodo

Thesis for the degree of Doctor of Philosophy

April 2013

UNIVERSITY OF SOUTHAMPTON

ABSTRACT

FACULTY OF ENGINEERING AND THE ENVIRONMENT

Electrochemistry and Material Science

Thesis for the degree of Doctor of Philosophy

ELECTROCHEMICAL MONITORING OF NICKEL–ALUMINIUM BRONZE CREVICE CORROSION SOLUTIONS USING BORON–DOPED DIAMOND ELECTRODE

Stefano Neodo

This study has demonstrated the capability of electrochemically assessing the metal–ion concentrations generated from the localised corrosion of nickel–aluminium bronzes (NAB). Prior to investigating NAB crevice corrosion, its electrochemical properties were studied at different pHs and chloride concentrations. At solution pHs higher than 4 NAB exhibited a corrosion behaviour similar to that of unalloyed copper and its oxidation was controlled by the dissolution of the copper–rich α–phase. However, as the pH was decreased below 4 the corrosion mechanism changed and the other κ–phases rich in aluminium, iron and nickel underwent preferential oxidation. The NAB corrosion performance was also investigated in the presence of benzotriazole (inhibitor) by using potentiodynamic polarisation. The excellent corrosion properties showed by NAB when exposed to neutral benzotriazole solution made the studied inhibitor a promising candidate for limiting crevice corrosion.

With knowledge of the NAB corrosion behaviour and the relatively high copper– and nickel–ion extents present within the crevice corrosion solutions, a study related to their electrochemical behaviour and detection was undertaken using a boron–doped diamond (BDD) electrode at different pHs and chloride levels in order to establish viable electrochemical protocols for effectively assess these concentrations. Before investigating the copper and nickel electrochemical behaviours on BDD electrode, the diamond substrate was studied using a number of different techniques such as potentiodynamic polarisation, cyclic voltammetry and electrochemical impedance spectroscopy. Results highlighted its excellent performance having a wide potential window (ca. 3 V) and a low capacitive current (20 μF cm^{-2} in 0.5 M H_2SO_4) available for electroanalysis purposes.

Finally, the NAB crevice corrosion was monitored using a BDD microelectrode array. The employed setup created an artificial crevice and accommodated the BDD microelectrode array

for *in situ* and a real–time monitoring. The electrochemical response showed the only presence of copper(I) during the investigated time, whose concentration increased within the first two hundred hours to a level of ca. 0.4 mM and then remained stable for the following hundred hours. No copper(II), or other metal–ions, were determined in the crevice solutions, thus suggesting that within the investigated time the copper–rich α–phase dominated the NAB corrosion behaviour. Furthermore, results also indicated (*ii*) the low dissolved oxygen concentration within the crevice (since it promotes the oxidation of copper(I) to copper(II)) and (*ii*) that the local pH did not decreased below 4, where the NAB corrosion is controlled by the selective dissolution of the aluminium–, iron– and nickel–rich κ–phases.

Contents

List of tables

List of figures

DECLARATION OF AUTHORSHIP

I, Stefano Neodo

declare that the thesis entitled

Electrochemical Monitoring of Nickel–Aluminium Bronze Crevice Corrosion Solutions using Boron–Doped Diamond Electrode

and the work presented in the thesis are both my own, and have been generated by me as the result of my own original research. I confirm that:

- this work was done wholly or mainly while in candidature for a research degree at this University;
- where any part of this thesis has previously been submitted for a degree or any other qualification at this University or any other institution, this has been clearly stated;
- where I have consulted the published work of others, this is always clearly attributed;
- where I have quoted from the work of others, the source is always given. With the exception of such quotations, this thesis is entirely my own work;
- I have acknowledged all main sources of help;
- where the thesis is based on work done by myself jointly with others, I have made clear exactly what was done by others and what I have contributed myself;
- none of this work has been published before submission,

Signed: ……..

Date:…….

Acknowledgements

I would like to express my gratitude to Prof. R.J. Wood and Dr. J.A. Wharton who supervised me during the PhD and gave the opportunity to undertake the responsibility of this project. I would like also to thank my girlfriend Anna, my family and all my friends; in particular: Richard (and his animal dolls), Faye, Robert, Martin, Chao, Fei–Fei, Kuan, Ben, Michele, Chiara, Dario, Lorenzo, Federico, Maria, Marco, Mohammad, Liping, Ying, Yikun, Mengyan, Terry, Liam, Cyborg, Bit, Marco, Davide and all those I have forgotten to mention.

Publications and Awards

- Shreir Prize, Electrochem 2011, Bath;
- S. Neodo, M. Nie, J.A. Wharton, K.R. Stokes, Nickel–Ion Detection on a Boron–Doped Diamond Electrode in Acidic Media, *Electrochim. Acta* 88 (2013) 718–725;
- S. Neodo, D. Carugo, J.A. Wharton, K.R. Stokes, Electrochemical Behaviour of Nickel–Aluminium Bronze in Chloride Media: Influenc of pH and Benzotriazole, *J. Electroanal. Chem.* 695 (2013) 38–46.
- S. Neodo, J.A. Wharton, K.R. Stokes, Investigation of the Electron Transfer Mechansim and Equilibrium Potentials of the copper(I) / copper(II) System in Chloride Media, *J. Phys. Chem C.* (submitted).

List of Symbols and Acronyms

Symbol	Name	Value / Unit
A	Electrode area	cm^2
α	NAB alpha–phase	–
α_a	Anodic transfer coefficient	–
α_c	Cathodic transfer coefficient	–
α	Activity	mol L^{-1}
AdSV	Adsorptive stripping voltammetry	–
AFM	Atomic force microscopy	–
Ag/AgCl	Silver / silver chloride reference electrode (3.5 M KCl)	0.205 V *vs*. SHE
b	Tafel slope	mV dec^{-1}
b_a^{app}	Apparent Tafel slope (for copper)	mV dec^{-1}
b_a^{ps}	Pseudo Tafel slope (for copper)	mV dec^{-1}
b_0	Linear regression intercept	–
b_1	Linear regression slope coefficient	–
β	Formation constant from aquo–complex metal–ion	–
β	NAB beta–phase	–
β^o	Formation constant from aquo–complex metal–ion at infinite dilution	–
B.E.	Binding energy	eV
BDD	Boron–doped diamond	–
BTA^-	Deprotonated benzotriazole	–

BTAH	Benzotriazole	–
$BTAH_2^+$	Protonated benzotriazole	–
C	Double layer capacitance	μF cm^{-2}
c	Concentration	mol L^{-1}
c^*	Surface concentration	mol L^{-1}
c_H	Proton concentration	mol L^{-1}
CA	Chronoamperometry	–
ChlER	Chlorine evolution reaction	–
CV	Cyclic voltammetry	–
CVD	Chemical vapour deposition	–
CE	Capillary electrophoresis	–
CSV	Cathodic stripping voltammetry	–
DLC	Diamond–like carbon	–
DPAV	Differential pulse anodic voltammetry	–
DPV	Differential pulse voltammetry	–
ΔG°_{ads}	Standard adsorption free energy	kJ mol^{-1}
D	Diffusion coefficient	–
D_H	Proton diffusion coefficient	–
E	Electrode potential	V *vs*. Ref. Electrode
E^o	Equilibrium potential	V *vs*. Ref. Electrode
EIS	Electrochemical impedance spectroscopy	–
EQCM	Electrochemical quartz crystal	–

	microbalance	
η	Overpotential	V *vs*. E^o
F	Faraday constant	96485 C mol^{-1}
f_c	Impedance frequency	Hz
FT–IR	Fourier–transform infrared spectroscopy	–
g	Interaction parameter term	–
$\gamma_{\pm}$	Coefficient activity	–
HER	Hydrogen evolution reaction	–
HPHTP	High pressure and high temperature process	–
I	Current	mA
I.E.	Inhibition efficiency	
I_p	Current peak	mA
I_L	Diffusion–limiting Current	mA
I_m	Molal ionic strength	mol kg^{-1}
I_M	Molar ionic strength	mol L^{-1}
j	Current density	mA cm^{-2} μA cm^{-2}
j_0	Exchange current density	μA cm^{-2}
j_{corr}	Corrosion current density	μA cm^{-2}
j_{app}	Apparent current density	μA cm^{-2}
j_{ads}	Adsorption current density	μA cm^{-2}
k_{app}^0	Apparent electron–transfer rate constant	cm s^{-1}

k_e	Oxidation rate constant (for $[Fe(CN)_6]^{3-/4-}$)	$cm\ s^{-1}$
k_{-e}	Cathodic rate constant (for $[Fe(CN)_6]^{3-/4-}$)	$cm\ s^{-1}$
k_1	Anodic rate constant (for copper dissolution)	$mol^{-1}\ cm^{-3}\ s^{-1}$
k_{-1}	Cathodic rate constant (for copper dissolution)	s^{-1}
k_2	Desorption rate constant (for copper dissolution)	$mol^{-1}\ cm^{-3}\ s^{-1}$
k_{-2}	Adsorption rate constant (for copper dissolution)	$mol^{-1}\ cm^{-3}\ s^{-1}$
κ_I–κ_{IV}	NAB kappa–phases	–
K	Equilibrium constant	–
K_{ads}	Adsorption equilibrium constant	–
K^o	Equilibrium constant at infinite dilution	–
Γ	CuCl coverage	$mol\ cm^{-2}$
χ	Displacement of solvent molecules	–
l	Layer thickness	cm
LOD	Limit of detection	$\mu mol\ L^{-1}$
m	molality	$mol\ kg^{-1}$
M	molarity	$mol\ kg^{-1}$
m	Number of experiment repetitions in linear regression	–
n	Number of values in linear regression	–
n	Constant phase element number	–
OCP	Open circuit potential	V

OER	Oxygen evolution reaction	–
ORR	Oxygen reduction reaction	–
PP	Potentiodynamic polarisation	–
p	Microelectrode diffusion parameter	
Q	Charge density	C cm^{-2}
R	Universal standard gas constant	8.314 kJ K^{-1} mol^{-1}
R_a	Surface Roughness	nm
R_{ct}	Charge transfer resistance	Ω cm^{-2}
RCE	Rotating cylinder electrode	–
R^2	Least square residual	–
RDE	Rotating disc electrode	–
r_d	Microelectrode radius	cm
s	Standard deviation	–
SCE	Saturated calomel reference electrode	0.244 V *vs*. SHE
SERS	Surface enhanced raman scattering	–
SHE	Standard hydrogen (reference) electrode	0.000 V
STM	Scanning tunnelling microscopy	–
T	Absolute temperature	K
t	Time	s
UV	Ultraviolet–visible spectroscopy	–
UPD	Under potential deposition	
WL	Weight loss	–

XPS	X–ray photoelectron spectroscopy	–
x	Independent variable	–
x_i	i^{th} value of the independent variable	–
$\bar{x}$	Average value of the independent variable	–
y	Dependent variable	–
y_i	i^{th} value of the dependent variable	–
$\hat{y}$	dependent variable value predicted by linear regression	–
υ	Scan rate	mV s^{-1}
θ	Adsorption	–
z	Number of electrons	–
Z'	Real (part) impedance	Ω cm^2
Z''	Imaginary (part) impedance	Ω cm^2

1. Introduction

1.1 Overview of the Project

Corrosion is the process that takes place as a result of chemical and / or physical interactions between a metal and the surrounding environment. Most metals are not thermodynamically stable when in contact with the atmosphere (or aqueous solutions) and thus they spontaneously undergo corrosion. However, for most applications the corrosion rate can be kept sufficiently low by either using adequate preventative measures (surface treatment and coating) or electrochemical protection.

Corrosion is generally enhanced by the presence of certain chemical species such as sulphur, carbon dioxide or chloride, which can lead to serious consequences in terms of structural integrity of the engineered components. Shutdowns, contamination, loss of material, costly maintenance, waste of valuable resources are the main problems associated with corrosion, which can jeopardize safety and inhibit technological progress. The direct implications of corrosion on the society, *i.e.*, cost and metal structural integrity, require an in–depth analysis of the underlying problems in order to reduce expenditure and improve safety. Specifically, the probability of risks implicated in structure failures must be peremptory reduced and the probability of risk must be decreased as much as possible.

A report issued in 2003, sponsored by CC Technologies, NACE International and U.S. Department of Transportation [1], showed that the costs of metallic corrosion is widespread in many fields and can significantly affect the economy of a developed country, such as the USA. The costs attributed to corrosion represent between 3 to 5% of the Gross National Product of an industrialised country [1]. For the United States of America, in the period time between 1999 and 2001, an average annual expense of $276 billion was estimated in 26 different industrial sectors [1]. In particular, the economic impact of corrosion was evaluated to be $47.9 billion in the utilities sector (gas distribution, drinking water and sewer system, electrical utilities and telecommunication), $29.7 billion in the transportation sector (motor vehicles, ships, aircraft, railroad cars and hazardous material transport), $22.6 billion in infrastructures (highway bridges, gas and liquid transmission pipelines, waterways and ports, hazardous materials storage, airports and railroads), $20.1 billion in the government management (defence and nuclear waste storage) and $17.6 billion in the production and manufacturing sector (oil and gas exploration and production, mining, petroleum refining, chemical petrochemical, and pharmaceutical, pulp and paper, agricultural production, food processing, electronics and home appliances).

With respect to the conditions and the characteristics under which corrosion takes place, it can be categorised in different forms, such as, uniform corrosion, erosion–corrosion, galvanic corrosion and localised corrosion (pitting and crevice corrosion). Crevice corrosion is a particular type of localised corrosion occurring in confined spaces to which the access of a fluid from the environment is limited. Examples of crevices are gaps and contact areas between parts, under gaskets or seals, inside cracks and seams or small spaces filled with deposits. Due to the geometrical and / or structural constraints crevice corrosion is difficult to detect, whilst potentially affecting the integrity of metals that are generally passive under normal in–service conditions [2]. Therefore, as a result, structural failure can occur in situations that may have otherwise been unexpected [3].

Nickel–aluminium bronze is a copper–based alloy which due to its inherent mechanical and physical properties, and its good corrosion performance, is widely used for marine applications, such as seawater pumps and propellers [4]. However, unlike other copper–based alloys it has been reported that they are susceptible to crevice corrosion when not cathodically protected [5]. Rowland [6] reported that when immersed in chloride containing solutions NAB experiences significant crevice corrosion attacks; the NAB crevice corrosion rate was determined to be significantly greater than that of stainless steel UNS S30400, having values ranging from 0.70 and 1.00 mm y^{-1} for NAB and 0.25 mm y^{-1} for stainless steel UNS S30400, respectively. The reason behind the enhanced crevice corrosion rate of NAB was explained by Wharton *et al.* [7] in terms of aggressive environment generated within the crevice, *i.e.*, high chloride levels and acidic pHs, which induce corrosion attacks of some NAB microstructural–phases [6].

1.2 Objectives of the Project

The main objective of this work is the development of an electrochemical sensor capable of detecting *in situ* and at real–time metal–ions generated from localised corrosion. In order to fulfil this achievement, different aims were required to be successfully attained, such as:

- deeply understand the NAB corrosion behaviour and the influence caused by experimental variables such as pH and chloride concentration, which are relevant to crevice corrosion;
- study the NAB electrochemical properties in the presence of corrosion inhibitor (benzotriazole) in order to decrease the crevice corrosion rate;

- consider and characterise a suitable and promising electrochemical tool for crevice corrosion electroanalysis (BDD electrodes);
- investigate the electrochemical response of metal–ions likely to be present within crevice corrosion solutions using the considered electrode, thus establishing detection protocols for the *in situ* corrosion monitoring;
- electrochemically assess the NAB crevice corrosion using a setup which artificially generates crevices in either the presence or absence of the corrosion inhibitor.

1.3 Thesis Structure

The thesis has been structured in order to guide the reader through the various aspects of crevice corrosion and electrochemical monitoring. Below is briefly described the content of the thesis Chapters.

- Chapter 2 establishes the available background knowledge which is relevant and fundamental for this project. Topics such as (*i*) NAB corrosion performance, (*ii*) crevice corrosion of NAB, (*iii*) inhibition properties of benzotriazole, (*iv*) electrochemical performance of BDD electrode and (*v*) electroanalysis achieved using BDD materials were reviewed to obtain better insights for the analysis and understanding of the experimental part;
- Chapter 3 details the materials and methods employed in this study;
- Chapter 4 describes the NAB corrosion performance in either the presence or absence of benzotriazole at different pH values and chloride concentrations;
- In Chapter 5 is reported an electrochemical, morphological and chemical study of the BDD electrode employed for electroanalysis of simulated crevice corrosion solutions;
- In Chapter 6 the electrochemical reactivity of copper(I) and copper(II) on a BDD electrode is investigated, in the presence of different anion electrolytes such as perchlorate, sulphate and chloride. Furthermore, a copper(I) / copper(II) detection protocol in the presence of chloride was established on the basis of its assessed reactivity.
- Chapter 7 highlights a new electrochemical protocol for the nickel(II) determination in aqueous chloride solution in slightly acidic pH;
- Chapter 8 reports the electrochemical performance of the BDD microelectrode array;
- Chapter 9 demonstrates the potential of electrochemically assessing the NAB metal–ion concentration within crevice environment on BDD microelectrode array;

- Chapters 10 provides a final conclusion and overview of the research achieved in this thesis;
- Chapter 11 outlines potential developments and further work.

2. Literature Review

2.1 Nickel–Aluminium Bronze Properties and Corrosion Behaviour

2.1.1 Nickel–Aluminium Bronze Properties: Microstructure and Phase Composition

Nickel–aluminium bronze alloys containing 9–12 wt.% aluminium, with additions of up to 6 wt.% each of iron and nickel, represent one of the most important groups of aluminium bronzes due to their excellent mechanical properties and corrosion resistance [8]. Consequently, these materials have been extensively used in a broad range of marine applications, including valves and fittings, ship propellers (see Figure 2.1.1), pump shafts, valve stems and heat exchanger waterboxes [9]. Regarding the influence of the alloying elements on the NAB properties, it has been reported that aluminium and iron are principally responsible for the alloy strength whereas nickel increases the corrosion resistance.

NAB alloys have replaced the binary 10 wt.% aluminium bronze in many demanding applications [4]. In fact, the additions of iron and nickel alloying elements led to a reduction of the γ–phase within the binary aluminium bronzes. This particular phase, which is aluminium rich, has been shown to be susceptible to corrosion and then responsible for the lower corrosion performance exhibited by aluminium bronzes [4].

Figure 2.1.1. Nickel–aluminium bronze propeller.

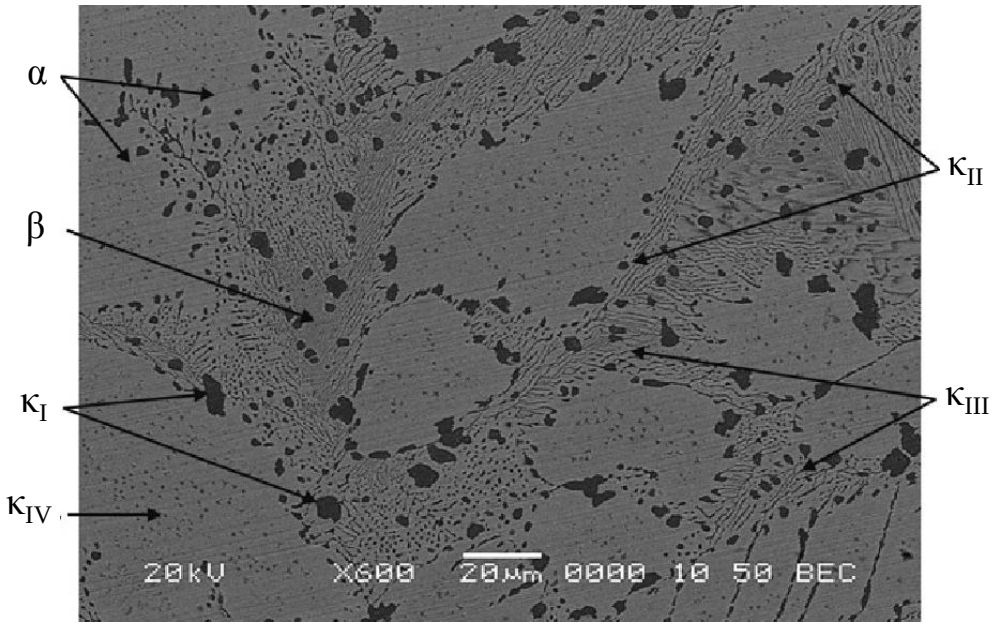

Figure 2.1.2. SEM backscattered of cast nickel–aluminium bronze and phase identification [5].

It has been reported that the alloying elements such as nickel and iron combine with aluminium forming a series of new κ–phases, thus effectively decreasing the content of the corrosion–susceptible γ–phase [4]. As can be seen from Figure 2.1.2, the NAB microstructure is predominantly comprised of a light etched α–phase, rich in copper, and a dark etched martensitic regions (β–phase), surrounded by a series of intermetallic κ–phases [10]. The κ–phases are identified as κ_I–, κ_{II}–, κ_{III}– and κ_{IV}, and characterised as follows [9]:

- κ_I–phase, globular or rosette forms which is rich in iron;
- κ_{II}–phase, globular form distributed at the α / β boundary, smaller than the κ_I–phase;
- κ_{III}–phase, lamellar form present at the α / β boundary and at the large κ_I–phase;
- κ_{IV}–phase, fine precipitate within the α–phase rich in iron.

When cast, NAB solidifies as "high temperature β" sometimes with large κ_I particles. On cooling, most of the "high temperature β" is transformed into α along with lamellar "eutectoid α plus κ_{III} ($\alpha + \kappa_{III}$)" and globular κ_{II} precipitate. At lower temperatures, fine κ_{IV}–phase precipitates also form. Any residual "high temperature β" transforms into "retained β" which has a martensitic form [11].

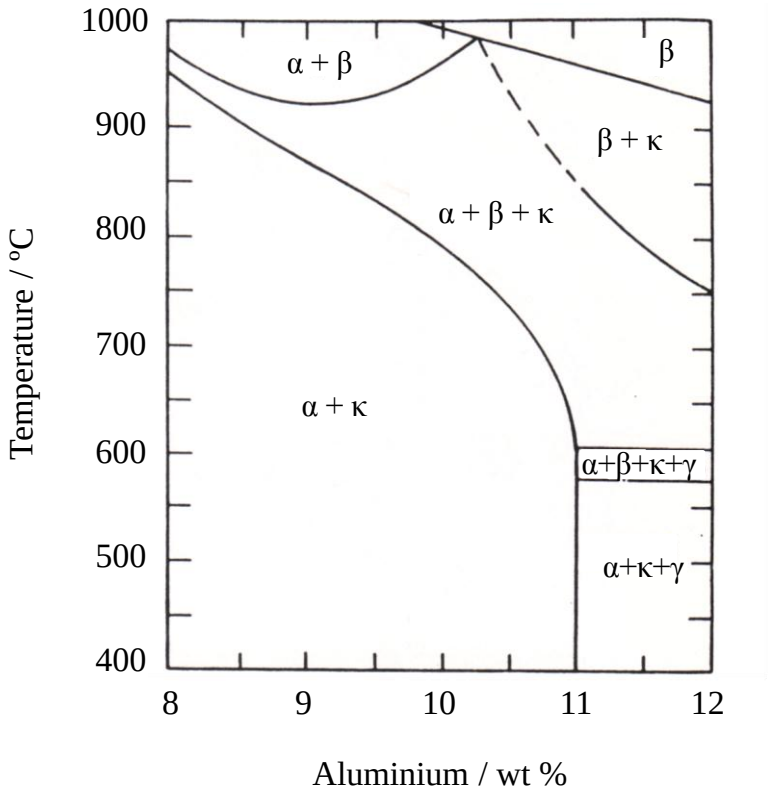

Figure 2.1.3. Phase equilibrium diagram of nickel–aluminium bronze (Cu–Al–5Ni–5Fe) at different Al contents [12].

The thermodynamic stability of the α–, β–, κ– and γ– phases, as a function of the temperature and the aluminium content, has been reported by Hasan *et al*. [12] for NAB with a nominal composition of Cu–Al–5Ni–5Fe, as shown in Figure 2.1.3. By inspecting the phase equilibrium diagram, it can be noted that at relatively low temperatures (less than 700 ºC) and low aluminium concentrations (less than 10 wt %) the α–phase, along with other κ–phases, predominate over the β–and the γ–phases. Conversely, the stability regions of the β– and the γ–phases can be found at either high temperature or high aluminium content, where the relative low concentrations of the alloying elements are not sufficient to avoid the formation of the γ–phase. Culpan and Rose [10] investigated the chemical composition of the different phases of NAB (Al 10 %, Ni 5% and Fe 5%) by using scanning electron microscope (SEM); the chemical compositions of the different phases are listed in Table 2.1.1.

Table 2.1.1. Chemical analysis of phases present in cast NAB [10].

	Elements / wt.%				
Phase	Al	Mn	Fe	Ni	Cu
α	8.3 ± 1.7	1.4 ± 0.1	2.7 ± 2.0	2.5 ± 1.4	85.4 ± 4.0
β	8.7	1.0	1.6	3.5	85.2
κ_I	13.5 ± 5.0	2.0 ± 0.4	55.0 ± 7.0	15.0 ± 3.0	15.0 ± 5.0
κ_{II}	19.0 ± 3.0	2.2 ± 0.6	32.0 ± 3.0	27.0 ± 4.0	21.0 ± 5.0
κ_{III}	18.0 ± 1.0	2.0 ± 0.3	22.0 ± 0.7	32.0 ± 2.0	26.4 ± 4.0
κ_{IV}	20.3 ± 3.0	1.5 ± 0.3	62.0 ± 4.0	4.0 ± 1.0	13.0 ± 1.0

2.1.2 Corrosion Behaviour of Nickel–Aluminium Bronze

Generally, NAB exposed to chloride–containing neutral solutions undergoes selective α–phase corrosion within the "α + κ_{III} phase". This has been related to the presence of a greater proportion of the cathodic phase (κ_{III}) in the eutectoid regions [4, 13]. The "retained β" phase is also susceptible to corrosion while the large κ_I particles are rarely attacked and usually remained within the corroded structure [13].

Wharton *et al*. [9] and Kear *et al*. [14] studied the electrochemical behaviour of NAB in chloride containing solutions by using rotating disc electrode (RDE) and rotating cylinder electrode (RCE). Figure 2.1.4 shows the NAB Tafel performance at different angular rotation velocities in filtered seawater reported by Kear *et al*. [14]. It is highlighted a series of distinct anodic Tafel slopes with increasing currents and similar anodic slopes, which ranged from +55 to +65 mV dec^{-1} [14].

$$Cu + 2Cl^- \rightarrow CuCl_2^- + e^- \qquad 2.1.1$$

Analogously with unalloyed copper, the oxidation mechanism was reported to be primarily driven by selective copper oxidation of the α–phase within the NAB microstructure, via the formation of $CuCl_2^-$, as shown in Equation 2.1.1 [9].

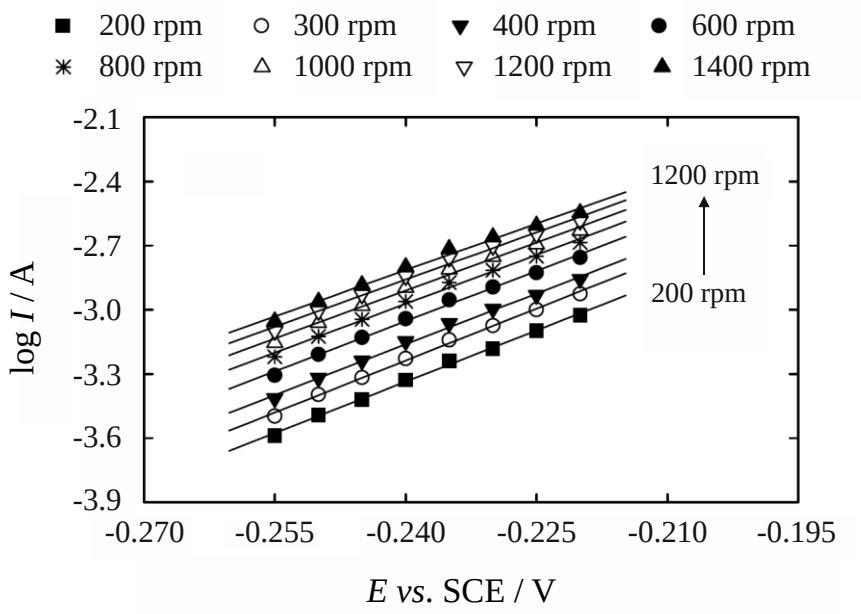

Figure 2.1.4. NAB apparent Tafel slopes of nickel–aluminium bronze as a function of rotating cylinder electrode angular velocity in aerated filtered seawater [14].

In the absence of cathodic protection, extensive crevice corrosion has been experienced on NAB when immersed in chloride containing solutions [6]. Differently from copper–based alloys, where generally the corrosion attack takes place at the exposed surfaces immediately adjacent the crevice, the crevice corrosion occurring at NAB has been reported to proceed through a selective phase attack and a microstructure dealloying [5]. Wharton *et al*. [5] studied the initiation of the crevice corrosion and its effects on the NAB microstructure in a 3.5 % NaCl solution using electrochemical measurements and SEM imaging. Regarding the mechanism, it was claimed an initial dissolution of the copper rich α–phase within the ($\alpha+\kappa_{III}$) eutectoid. This initial step induced the formation of a copper–ion concentration cell of primary importance for the further evolution of the crevice corrosion process. Indeed, it was reported that hydrolysis of the copper(I)–chloride complexes, accumulated within the crevice (see Equations 2.1.2–2.1.3), generally leads to a local solution acidification, which in turn triggers the κ_{III}–phase selective corrosion, vulnerable and susceptible to corrosion in acidic media [7].

The NAB crevice corrosion mechanism is highlighted in Figure 2.1.5. It can be noted that within the crevice, the metal–ion and proton concentrations are higher than those of the bulk solution, due to the NAB dissolution and the hydrolysis reaction of the corrosion metal–ions. Furthermore, also the crevice chloride concentration is greater than that present in the bulk solution, due to a diffusive process which attempts to maintain the crevice electroneutrality. On the contrary, the crevice oxygen concentration is reported to be significantly lower than that of the bulk of the solution [5], due to its rapid depletion attained by reduction reaction [7].

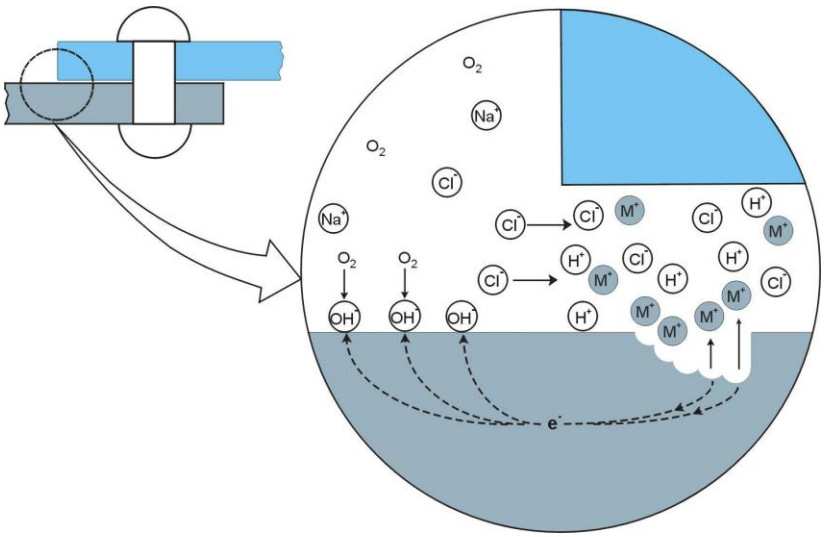

Figure 2.1.5. Schematic of the crevice corrosion mechanism.

Figure 2.1.6 [5] shows the cross–section SEM backscattered images of NAB underwent different corrosion mechanisms in a 3.5 % NaCl solution, *i.e.*, (a) uniform corrosion and (b) crevice corrosion. By inspecting Figure 2.1.6 a, it can be appreciated the selective corrosion of the copper rich α–phase within the ($\alpha+\kappa_{III}$) eutectoid after the NAB specimen underwent uniform corrosion. Generally, during NAB uniform corrosion no marked local acidifications are produced at the near metal surface (as contrary measured inside the NAB crevice) and the pH reflects that of the bulk solution [5].

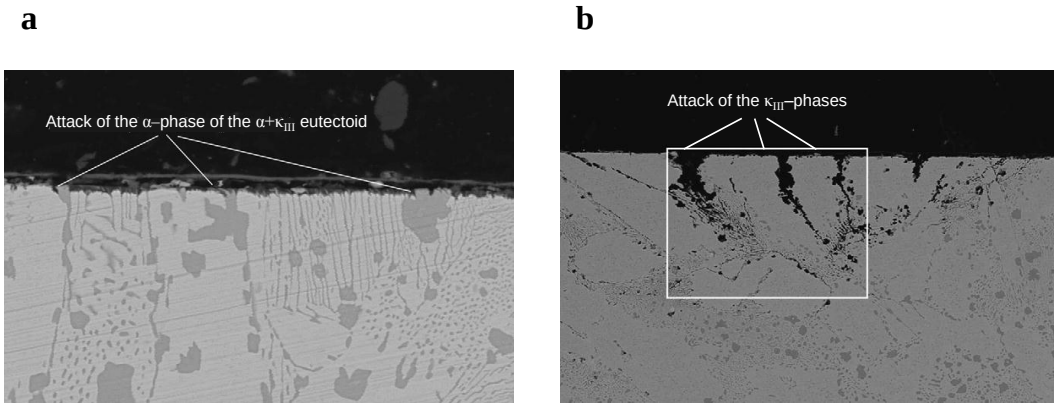

Figure 2.1.6. Cross–section SEM backscattered images of cast nickel–aluminium bronze after selective attack of (a) the α–phase within the ($\alpha+\kappa_{III}$) eutectoid and (b) the κ_{III}–phases in a 3.5 % NaCl solution [5].

Therefore, in these specific conditions, the mechanism was controlled by the copper–rich α–phase dissolution [5]. Conversely, Figure 2.1.6 b highlights the selective corrosion attacks of the κ_{III}–phases, associated with a NAB specimen underwent crevice corrosion. In this particular instance, the conditions generated and present inside the crevice, *i.e.*, high proton and chloride concentrations, led to the preferential dissolution of the κ_{III}–phases within the NAB microstructure [7].

It has been reported that the proton crevice concentration represents an insightful indicator of the corrosion development [15]. Generally pH values ranging between 3 and 4 have been reported after the hydrolysis of $CuCl^-_{2(aq)}$ and $CuCl^{2-}_{3(aq)}$ started inside the crevice, see Equations 2.1.2 and 2.1.3 [8]. The predominance of $CuCl^-_{2(aq)}$ over $CuCl^{2-}_{3(aq)}$ is dictated by the chloride concentration within the crevice, as highlighted in Section 2.4.1.

$$2CuCl_2^- + H_2O \rightarrow Cu_2O_{(s)} + 4Cl^- + 2H^+ \qquad 2.1.2$$

$$2CuCl_3^{2-} + H_2O \rightarrow Cu_2O_{(s)} + 6Cl^- + 2H^+ \qquad 2.1.3$$

Similar to the proton concentration, also the chloride concentration is an insightful indicator of the crevice corrosion evolution. This can be related to an increasingly cation concentration which lets the chloride ions to migrate from the bulk solution to the crevice, in order to maintain the solution electroneutrality. Kelly *et al*. [15] studied by means of capillary electrophoresis the effect of some aggressive anions on the crevice corrosion development of stainless steel. It was claimed that during the stabilisation of the crevice corrosion, the chloride concentration increased to approximately 3–4 M, from an initial concentration value of 0.9 M. Wharton *et al*. [7] also studied by means of capillary electrophoresis the evolving of the chloride and the metal–ion concentrations within NAB crevice corrosion solutions. Similarly to Kelly *et al*. [15], it was reported a chloride concentrations which increased from an initial value of 0.6 M to 2.7 M, within the first month of the NAB exposure.

To date, due to the strict dependence established between the proton and chloride concentrations and crevice corrosion, many studies have been addressed to the crevice corrosion monitoring using chloride– and proton–sensitive electrochemical sensors [16, 17]. In this work, a different approach has been used to monitor the crevice corrosion occurring at metals. As highlighted in Chapter 9, the method relied on the assessment of the metal–ions levels generated by crevice corrosion rather than the determination of indirect–corrosion related parameters, such as pH and chloride concentration.

2.2 Benzotriazole Inhibitor: Chemical Properties and Inhibition Mechanism on Copper and Copper Based Alloys

This section highlights the corrosion inhibition properties of benzotriazole for copper and copper–based alloys. The importance of the chemical characteristics of benzotriazole have been widely recognised to improve the corrosion performance of copper and copper–based substrates; accordingly an overview of the benzotriazole behaviour in aqueous media (pH–dependence) will be discussed in Section 2.2.1, which will allow for a better understanding of the adsorption mechanism and the high affinity of benzotriazole for copper surfaces. This is followed by a review of the most significant studies that have been conducted establishing (*i*) the chemical analysis of benzotriazole films (Section 2.2.2) and (*ii*) the inhibition mechanism and adsorption of benzotriazole on copper and copper–based alloys (Section 2.2.3), in order to allow an interpretation and analysis of the NAB electrochemical behaviour in the presence of benzotriazole.

2.2.1 Chemical Properties of Benzotriazole

Due to its good corrosion inhibition, 1,2,3–benzotriazole has been extensively investigated on copper to better understand the mechanism behind its corrosion performance as well as its effectiveness. Benzotriazole ($C_6H_5N_3$) is a heterocyclic molecule which consists of a benzene and a triazole ring. The nitrogen atoms in the azole ring are responsible for the bonding with a metal and are accountable for its good corrosion inhibition property [18, 19]. The extent of the benzotriazole bonding with a metallic surface can be directly related to the solution pH in which the inhibitor is present [18], since the benzotriazole molecule undergoes acid–basic equilibria.

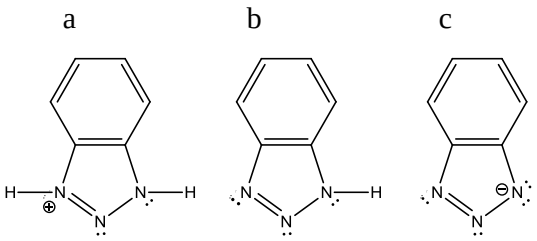

Figure 2.2.1. Benzotriazole chemical structures, (a) protonated ($BTAH_2^+$), (b) neutral (BTAH) and (c) anion (BTA^-) forms.

Indeed, it is well–known that the benzotriazole can exist in three different chemical forms, as shown in Figure 2.2.1 a–c, depending on the pH of the solution. The two equilibrium constants (pK_{a1} and pK_{a2}), Equations 2.2.1 and 2.2.2, establish the pH thresholds which define

the existence–interval between the cationic, the neutral and the anionic forms of benzotriazole, hereafter termed as $BTAH_2^+$, BTAH and BTA^-.

$$BTAH_2^+ \leftrightarrow BTAH + H^+ \qquad pK_{a1} \approx 1 \qquad 2.2.1$$

$$BTAH \leftrightarrow BTA^- + H^+ \qquad pK_{a1} = 8.2 \qquad 2.2.2$$

With respect to the solution pH, one species might predominate over the others: as the pH shifts from either the pK_{a1} or the pK_{a2} towards more alkaline and more acidic pH conditions (Figure 2.2.2), the ratios $[BTAH_2^+]/[BTAH]$ and $[BTA^-]/[BTAH]$ increase until the prevalence of either the cationic or the anion species occurs [18].

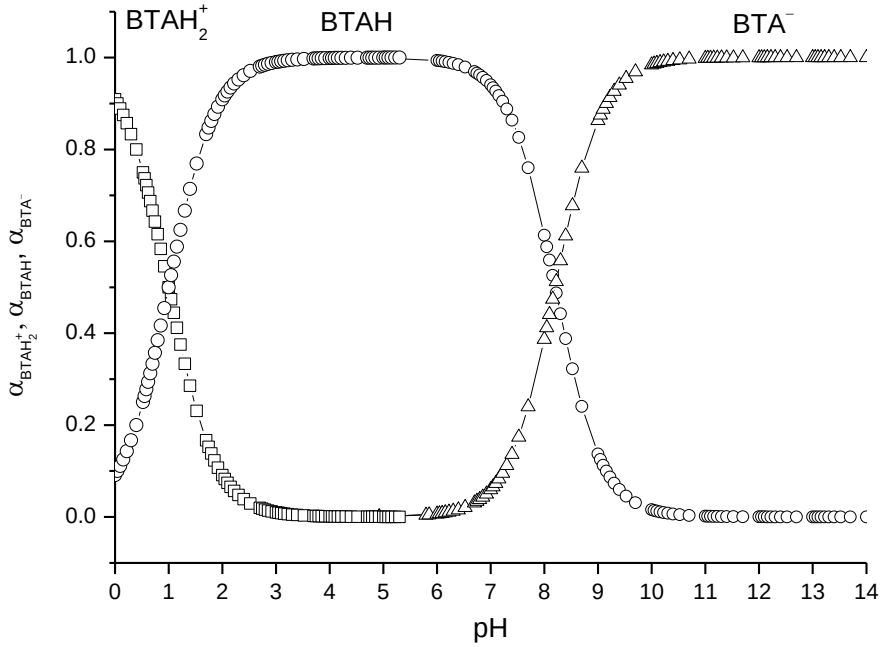

Figure 2.2.2. Speciation of benzotriazole with respect to the pH: (□) $BTAH_2^+$, (○) BTAH and (Δ) BTA^-.

2.2.2 Composition of Adsorbed Benzotriazole Films at Copper Surfaces

Dugdale *et al.* [19, 20] provided one of the early seminal studies into the benzotriazole corrosion–inhibiting effect on copper. They suggested that the corrosion inhibition was not solely correlated to the blocking effect of the heterocyclic compound on the anodic process but it also produced a decrease of the cathodic kinetics, associated with the oxygen reduction reaction (ORR). Since the 1970s numerous studies have been reported in an effort to gain a

deeper understanding of the influence of pH [21], the ionic species present [22, 23], the temperature [24] and the chemical–state of the metallic surface [18, 24-26] on the structure as well as the chemical composition of adsorbed benzotriazole films on copper substrates.

It is generally accepted that benzotriazole decreases the corrosion rate of copper and copper based alloys due to the formation of chemisorbed multilayers of a polymeric structure of benzotriazolium anion (BTA^-) with a cuprous cation, Cu(I) [18, 24, 26]. One of the original studies regarding the composition of the benzotriazole–copper film was reported by Fox *et al.* [27], who indicated that only $Cu(I)BTA^-$ is formed at Cu_2O substrate, and not a mixture of $Cu(I)BTA^-$ and $Cu(II)(BTA^-)_2$ complexes. Subsequently, Hashemi *et al*. [28] using X–ray photoelectron spectroscopy (XPS) studied the chemical composition of copper treated with benzotriazole and identified the presence of the $Cu(I)BTA^-$ complex on copper, where the negative charge of the benzotriazolium anion was delocalised over the three nitrogen atoms.

The surface enhanced Raman scattering (SERS) spectroscopy was first employed by Kester *et al*. [29] as a means to better comprehend the structure of adsorbed benzotriazole on copper in organic solutions. In particular, the authors investigated the benzotriazole interactions that occurred at the copper surface, when subjected to different polarisations. Direct conclusions of the benzotriazole adsorption were drawn from SERS, due to significant changes between the free and the adsorbed benzotriazole spectra. Furthermore, it was also suggested that the initial layer of adsorbed benzotriazole was not present in the polymerised form but rather as a molecular species, $Cu(0)[BTAH]_{ads}$.

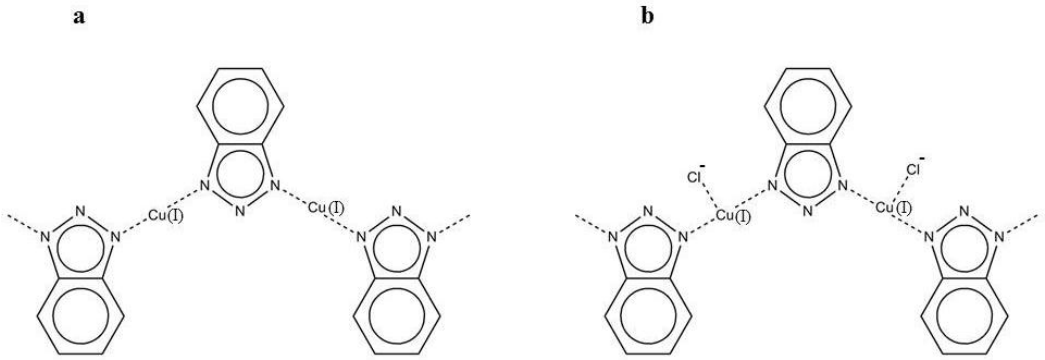

Figure 2.2.3. Polymeric structures of (a) BTA^- and Cu(I) and (b) BTA^-,Cu(I) and Cl^- [30].

Da Costa *et al*. [30] also investigated the benzotriazole adsorption in hydrochloric acid (pH 1.0 to 6.5) on copper substrates under different applied potentials. SERS spectroscopy distinguished two different complexes present at the metal surface, *i.e.*, $[Cu(I)BTA^-]_n$ and

$[Cu(I)Cl^{-}_{ads}[BTAH]_{ads}]_n$ as shown in Figures 2.2.3a and 2.2.3b, whose concentrations were related to the applied potential. Tromans *et al*. [18] proposed a bi–layer structure with an inner film of $Cu(0)[BTAH]_{ads}$ covered by an outer $[Cu(I)BTA^{-}]_n$ matrix. The film structure proposed by Tromans *et al.* was in agreement with that of Da Costa *et al*. [30] in spite of the different electrolyte.

Brusic *et al.* [31] investigated by means of XPS, electrochemical and mass spectrometry techniques the growth of the benzotriazole film on copper substrates in a sulphate environment. They proposed an initial formation of $Cu(0)[BTAH]_{ads}$ at the metal surface, which was subsequently covered by $[Cu(I)BTA^{-}]_n$. Moreover, they indicated that the film–structure reflected the kinetic growth: the slowest is the growing film process and the more polymerised and the more protective the inhibitor film.

In the 1990s, with the development of new surface–sensitive techniques such as atomic force microscopy (AFM) and scanning tunnelling microscopy (STM), new insights were gained regarding the chemical composition of the adsorbed benzotriazole films. Cho *et al*. [32] using STM studied the adsorption of benzotriazole (vapour phase) on oxide–free copper. They showed that BTAH adsorbed on oxide–free copper with a well–oriented structure. It was also reported that the interactions between BTAH and copper occurred via the π–orbital of the triazole ring and that BTAH was horizontally adsorbed at the metal surface.

The film composition of benzotriazole on copper substrate in 0.1 M HCl and 0.01 M H_2SO_4 solutions, using *in situ* STM and *in situ* fourier–transform infrared spectroscopy (FT–IR), was first studied by Vogt *et al*. [33, 34]. For chloride–containing medium [33], three different cases were distinguished by either the presence or the absence of benzotriazole. In particular, a competitive adsorption behaviour of benzotriazole was established with chloride and sensitive to the electrode potential: (*i*) at potentials below –0.6 V *vs*. SCE the metal surface was covered by BTAH, $Cu(0)[BTAH]_{ads}$, which was determined to be chemically adsorbed and organised as superstructure film; (*ii*) at potentials ranging from –0.6 V to –0.3 V *vs*. SCE the copper surface was entirely covered by chloride, due to the replacement of BTAH by Cl^{-}; whereas (*iii*) above –0.3 V *vs*. SCE the formation of an inhibiting $[Cu(I)BTA^{-}]_n$ film occurred at the metal surface. Regarding the sulphate–containing solutions [34], a different adsorption scenario was discussed by Vogt *et al.* due to the absence of the highly competitive adsorption behaviour of Cl^{-} with BTAH. Indeed, at potentials lower than –0.12 V *vs*. SCE, *in situ* STM suggested that benzotriazole was chemisorbed at the copper surface and formed ordered and disordered adsorbed–layer (ad–layer) structures, where the ordered film was associated with

$Cu(0)[BTAH]_{ads}$ whereas the disordered layer was related to $[Cu(I)BTA^-]_n$. At potentials higher than –0.12 V *vs*. SCE, the polymeric film $[Cu(I)BTA^-]_n$ covered the entire copper surface.

Qafsaoui *et al.* [35] investigated the characteristics of adsorbed benzotriazole films in pH 9 borate buffered solutions using coulometry and electrochemical quartz crystal microbalance (EQCM). The benzotriazole concentrations were either 10^{-4} M or 10^{-2} M. Electrochemical tests were based on the anodic polarisation of copper by applying +0.4 V *vs.* SCE, forming principally CuO, and reducing it afterwards by scanning the potential from –0.2 V to –1.2 V *vs.* SCE, either in the presence or in the absence of benzotriazole. In the absence of benzotriazole two layers of copper oxides, CuO and Cu_2O, were reported, whereas in the presence of the inhibitor $[Cu(I)BTA^-]_n$ along with CuO, covered a thick Cu_2O layer. The thicknesses of Cu_2O and CuO were determined to be 303 nm and 167 nm, for the test carried out in the absence of BTAH; and 588 nm and 32 nm for the test performed in the presence of BTAH, as shown schematically in Figure 2.2.4.

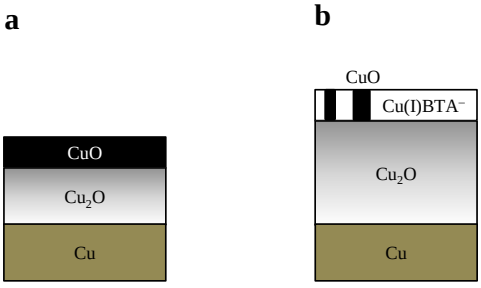

Figure 2.2.4. Proposed structures for films in borate buffered solution (a) without and with (b) inhibitor [35].

Stewart *et al.* [22] studied the anion effect in the growth process of the benzotriazole films on copper using ellipsometry, SERS and mass spectrometry. The electrolytes were 0.1 M KCl, 0.1 M KBr, 0.1 M CH_3COOH, 0.1 M K_2SO_4 and 0.1 M $KClO_4$ solutions at pH of either 8.5 or 2.0, while the benzotriazole concentration was 0.02 M. Thicker $[Cu(I)BTA^-]_n$ films were apparent on copper in the halide–containing electrolytes than those obtained in organic and inorganic solutions. Therefore, an active participation of halides in the benzotriazole–film growth was proposed, where bromide / chloride coordinated with Cu(I) within the film. This insight was further confirmed by mass spectrometry, which indeed demonstrated the presence of Cl^- and Br^- in the protective benzotriazole layers. The protective film structure proposed by Stewart *et al*. was in agreement with that advanced by Da Costa *et al.* [30].

Recently, Kokalj *et al*. [36] investigated the inhibition of benzotriazole on copper in a neutral chloride solution, by using a quantum calculation study. Several phenomena were considered in the theoretical model, such as the interaction of neutral and deprotonated molecules, the role of intermolecular association of inhibitors on the surface, solvation effects, double–layer electric field and the effects on the molecule–surface bonding. High inhibition properties were highlighted for benzotriazole on copper due to its ability of forming strong N–Cu chemical bonds in the deprotonated form. Furthermore, the superior affinity for copper was associated with the ability of forming intermolecular aggregates, such as $[Cu(I)BTA^-]_n$, adsorbed at the metal surface.

2.2.3 Inhibition of Benzotriazole: Mechanism and Adsorption

The inhibition mechanism of benzotriazole, as well as its adsorption on copper surfaces, has been the focus of debate due to the controversial results often reported in different studies throughout literature. Youda *et al*. [37] studied the corrosion behaviour of copper in the presence of benzotriazole in a sulphate medium at different pHs and electrode potentials using SERS. Regarding the inhibition mechanism an adsorption process was proposed dependent on the electrode potential and on the pH. SERS indicated that at potentials below –0.5 V *vs*. SCE the BTAH was predominantly adsorbed at the copper surface, $Cu(0)[BTAH]_{ads}$, whereas at potentials more positive than –0.3 V *vs*. SCE the polymeric structure $Cu(I)[BTA^-]_n$ was the main adsorbed compound. At potentials ranging from –0.5 V and 0.3 V *vs*. SCE the coexistence of both species occurred. Therefore, an adsorption mechanism based on the equilibrium between $Cu(0)[BTAH]_{ads}$ and $Cu(I)[BTA^-]_n$ was suggested, as shown in Equation 2.2.3.

$$Cu(0)\left[BTAH\right]_{ads} \leftrightarrow Cu(I)[BTA^-]_{ads} + H^+ + e^- \qquad 2.2.3$$

The proposed equilibrium also suggested the prevalence of BTAH at low pH and cathodic potentials.

Hope *et al*. [38] investigated the initial interactions of benzotriazole with copper in a 2 M H_2SO_4 solution using SERS and XPS. The adsorption mechanism established by Youda *et al*. [37] was confirmed, where adsorbed BTAH on copper predominated at low pHs and at potentials lower than –0.5 V *vs*. Ag/AgCl. Furthermore, the BTAH adsorption on copper was shown to be a reversible process below pH 3.

Alkire and Cangellari [39] studied the influence of benzotriazole on the anodic behaviour of copper in 1 N H_2SO_4 under high dissolution rates and in the presence of fluid flow. Electrochemical measurements provided information of a dual–layer structure, where the inner

film was shown to be thin and highly resistive, associated with $Cu(0)[BTAH]_{ads}$, whereas the outer was porous and dependent on the flow rate, related to $[Cu(I)BTA^-]_n$. Alkire and Cangellari confirmed the previous studies [29, 31, 34, 38], where BTAH is present at the copper surface as $Cu(0)[BTAH]_{ads}$ and represents the *incipit* of the process, while the formation of $Cu(I)[BTA^-]_n$ is the last step of the adsorption mechanism.

Xue *et al*. [40] proposed a process based on the initial interaction of BTAH with the copper surface, followed by the further formation of $Cu(I)[BTA^-]_n$. Using SERS, XPS and cyclic voltammetry they investigated the adsorption of benzotriazole on freshly etched metallic copper and on oxidised copper substrates in a 1:1 solution of water and ethanol (pH 6) containing 0.1 M of benzotriazole. CV suggested that benzotriazole reacted faster with metallic copper than with the oxidised specimen, thus providing a better inhibition. For the etched copper specimen, a mechanism was proposed which proceeded through the initial adsorption of BTAH at the metal surface (see Equation 2.2.4), followed by the oxidation of copper(0) to copper(I) by co–adsorbed molecular oxygen, forming $Cu(I)BTA^-$ (see Equation 2.2.5). The final step of the adsorption mechanism was considered to be the formation of polymeric benzotriazole–Cu(I) clusters, as reported in Equation 2.2.6.

$$Cu(0) + BTAH \rightarrow Cu(0)[BTAH]_{ads} \qquad 2.2.4$$

$$4Cu(0)[BTAH]_{ads} \xrightarrow{Cu(O_2)_{ads}} 4Cu(I)BTA^- + 2H_2O \qquad 2.2.5$$

$$n\,Cu(I)BTA^- \rightarrow [Cu(I)BTA^-]_n \qquad 2.2.6$$

In accordance with the mechanism discussed by Kester *et al*. [29], Tromans *et al*. [18] suggested a dual–layer structure constituted of an inner thin film of adsorbed BTAH, $Cu(0)[BTAH]_{ads}$, and an outer thick layer of $[Cu(I)BTA^-]_n$. The initial adsorption step was the formation of $Cu(0)[BTAH]_{ads}$, as shown in Equation 2.2.7, however, contrary to Youda *et al*. [37] and Xue *et al*. [40] mechanisms, the formation of the polymeric structure $[Cu(I)BTA^-]_n$ was shown to occur within the diffusion layer between the BTAH and $CuCl_2^-$ (see Equation 2.2.8), rather than at the metal surface between Cu(0) and $BTAH_{ads}$.

$$Cu(0) + BTAH \rightarrow Cu(0)[BTAH]_{ads} \qquad 2.2.7$$

$$nCuCl_2^- + nBTAH \rightarrow [Cu(I)BTA^-]_n + nH^+ + 2nCl^- \qquad 2.2.8$$

$$n\mathrm{Cu(0)[BTAH]_{ads}} + \mathrm{[Cu(I)BTA^-]_n} \rightarrow \mathrm{[Cu(0)[BTAH]_{ads} \cdot Cu(I)BTA^-]_n} \quad 2.2.9$$

The further development of the protective inorganic matrix was indicated to occur through the adsorption of $\mathrm{[Cu(I)BTA^-]_n}$ onto $\mathrm{Cu(0)[BTAH]_{ads}}$, thus obtaining a structure $\mathrm{[Cu(0)[BTAH]_{ads} \cdot Cu(I)BTA^-]_n}$, as highlighted in Equation 2.2.9. Furthermore, electrochemical investigations, performed on copper in chloride media at pHs ranging from 1.0 to 6.5 indicated a poor inhibition by benzotriazole films when the pH decreased below to 3 due to the instability of the $\mathrm{[Cu(I)BTA^-]_n}$ layer.

Xu *et al.* [41] studied the benzotriazole adsorption from aqueous solutions on Cu_2O and CuO surfaces by using XPS, Auger electron spectroscopy and ultraviolet–visible spectroscopy measurements. The Cu_2O surface was achieved by first depositing a metallic copper film over a fused quartz substrate and then exposing the coated samples to the air for 3–5 h, whereas the CuO surface was based on a heat treatment at 150 °C for 2 h of freshly deposited copper. Results indicated the formation of a single chemisorbed layer of BTA^-, at low benzotriazole concentrations ([BTAH] < 5×10^{-3} M), occurring via dissociation of BTAH on BTA^- and H^+ upon the benzotriazole adsorption.

Vogt *et al*. [33, 34] proposed a mechanism where $\mathrm{[Cu(I)BTA^-]_n}$ was formed within the diffusion layer, rather than at the metallic surface, in solutions containing either chloride [33] or sulphate [34]. Regarding the chloride containing solution, as opposed to the mechanism previously reported by Tromans *et al*. [18], it was indicated that BTAH does not undergo interactions with copper surfaces before forming the ad–layer of $\mathrm{[Cu(I)BTA^-]_n}$.

Metikos–Hukovic *et al.* [42] investigated the inhibitor action of benzotriazole on copper in a 1 M CH_3COONa solution varying the pH from 4 to 10 and using CV and EIS measurements. At low inhibitor concentrations, less than 0.5 mM, BTAH interacted with the copper surface forming $\mathrm{Cu(0)[BTAH]_{ads}}$, whereas at benzotriazole concentrations higher than 1.0 mM the process was related to the formation of $\mathrm{[Cu(I)BTA^-]_n}$. The adsorption isotherm employed to fit the data was a modified Flory–Huggins isotherm, see Equation 2.2.10.

$$\frac{\theta}{(1-\theta)^{\chi}} \frac{[\theta + \chi(1-\theta)]^{\chi-1}}{\chi^{\chi}} = K_{\mathrm{ads}}\, \mathrm{c} = \frac{\mathrm{c}}{55.55} \mathrm{e}^{\frac{-\Delta G^{\circ}_{\mathrm{ads}}}{RT}} \quad 2.2.10$$

where θ is the adsorption of benzotriazole on copper, χ is the number of water molecules displaced by a molecule of inhibitor and $\Delta G^{\circ}_{\mathrm{ads}}$ is the standard adsorption free energy. The authors highlighted a decreasing trend of the standard free adsorption energy when changing

from acidic to alkaline conditions, thus suggesting a stronger interaction between the inhibitor and the metallic surface at lower proton concentrations. The determined standard adsorption free energies were –37.8 kJ mol^{-1}, –39.0 kJ mol^{-1}, –31.1 kJ mol^{-1} and –30.0 kJ mol^{-1}, while the χ values were 0.5, 1.5, 0.8 and 1.2, at pHs of 4.0, 6.0, 8.0 and 10.0, respectively.

Cao *et al.* [26] investigated the adsorption of benzotriazole inhibitor, as well as its inhibition efficiency, on different metal substrates (copper, iron and nickel) using SERS and electrochemical techniques. Measurements were made in a 0.1 M KCl solution at the open circuit potential but also cathodically polarised at –1.1 V *vs.* Ag/AgCl. The ability of benzotriazole to coordinate with the metals principally occurred through two of the triazole nitrogen atoms, thus forming strongly adsorbed protective layers insoluble in water. The interactions between benzotriazole and the metallic surfaces were determined to decrease in the order: Cu > Fe > Ni. These results were in good agreement with the corrosion inhibition values determined for the different substrates: 70.4%, 59.9% and 31.9% for copper, iron and nickel, respectively. Moreover, SERS performed on cathodically polarised copper suggested a dissolution of the polymer, $[Cu(I)BTA^{-}]_n$, due to the penetration of H^{+} into the polymeric chain. The manner by which benzotriazole interacts with copper and copper–based alloys has been described by a diverse range of adsorption isotherms. Generally, the standard adsorption free energies reported in the literature for benzotriazole on copper varies between 25 kJ mol^{-1} and 47 kJ mol^{-1}. Subramanian *et al.* [21] electrochemically determined an adsorption behaviour of benzotriazole on copper which followed a Langmuir isotherm, see Equation 2.2.11. The CV and EIS tests were carried out in a 0.1 M NaCl solution in a benzotriazole concentration range from 0.1 × 10^{-3} M to 2.0 × 10^{-3} M. They reported a standard adsorption free energy of –27.9 kJ mol^{-1}, thus indicating a spontaneous adsorption process.

$$\frac{\theta}{(1-\theta)} = K_{\text{ads}}\, \text{c} = \frac{\text{c}}{55.55}\, \text{e}^{\frac{-\Delta G^{\circ}_{\text{ads}}}{RT}} \qquad 2.2.11$$

Antonijevic *at al.* [43] also used the Langmuir isotherm to describe the adsorption behaviour of benzotriazole on copper. The electrolyte considered was a borate–buffered solution at different pHs (8.0, 8.7, 9.3, 10.3 and 12.3), whereas the technique to assess the inhibitor adsorption was the potentiodynamic polarisation. Using Equation 2.2.11 the standard adsorption free energies were determined ranging from –34 kJ mol^{-1} to –47 kJ mol^{-1} (slightly higher than those estimated by Subramanian *et al.* [21]).

Table 2.2.1. Summary of the literature standard adsorption free energies on copper. CV (cyclic voltammetry), CA (chronoamperometry), PP (potentiodynamic polarisation) and WL (weight loss).

Ref.	Substrate	Electrolyte	pH	Method	Isotherm	ΔG_{ads} / kJ mol^{-1}
[21]	copper	0.1 M NaOH	13.0	CV	Langmuir	–27.9
[25]	copper pol.	0.1 M H_2SO_4	0.7	CA	Langmuir	–3.8
[42]	copper	1 M CH_3COONa	4.0	CV	Flory–Huggins	–37.8
[42]	copper	1 M CH_3COONa	6.0	CV	Flory–Huggins	–39.0
[42]	copper	1 M CH_3COONa	8.0	CV	Flory–Huggins	–31.1
[42]	copper	1 M CH_3COONa	10.0	CV	Flory–Huggins	–30.0
[43]	copper	Buff. borate	8.0	PP	Langmuir	–44.0
[43]	copper	Buff. borate	8.7	PP	Langmuir	–
[43]	copper	Buff. borate	9.3	PP	Langmuir	–47.1
[43]	copper	Buff. borate	10.3	PP	Langmuir	–38.7
[43]	copper	Buff. borate	12.3	PP	Langmuir	–
[43]	copper	0.05 M NaCl	8.0	PP	Langmuir	–
[43]	copper	0.05 M NaCl	8.7	PP	Langmuir	–34.1
[43]	copper	0.05 M NaCl	9.3	PP	Langmuir	–43.2
[43]	copper	0.05 M NaCl	10.3	PP	Langmuir	–
[43]	copper	0.05 M NaCl	12.3	PP	Langmuir	–
[44]	copper	0.001 M H_2SO_4	2.7	WL	Frumkin	–27.4
[44]	copper	0.005 M H_2SO_4	2.0	WL	Frumkin	–27.2
[44]	copper	0.01 M H_2SO_4	1.7	WL	Frumkin	–27.8
[45]	copper	0.001 M HCl	3.0	WL	Frumkin	–25.0
[45]	copper	0.005 M HCl	2.3	WL	Frumkin	–22.0
[45]	copper	0.01 M HCl	2.0	WL	Frumkin	–24.0
[45]	copper	0.05 M HCl	1.3	WL	Frumkin	–25.0
[45]	copper	0.1 M HCl	1	WL	Frumkin	–20.0
[45]	copper	0.5 M HCl	0.3	WL	Frumkin	–28.0

Bastidas *et al.* [44, 45], in contrast to the previously reported adsorption mechanisms, *i.e.* [21, 43], determined an adsorption behaviour of benzotriazole on copper following the Frumkin isotherm, as shown in Equation 2.2.12.

$$\frac{\theta}{(1-\theta)} e^{-(g\,\theta)} = K_{ads}\, c = \frac{c}{55.55} e^{\frac{-\Delta G^{\circ}_{ads}}{RT}} \qquad 2.2.12$$

Where g is the interaction parameter term, which denotes the lateral interactions occurring between the different adsorbed molecules at the surface. Two different cases can be distinguished: (*i*) $g < 0$ lateral repulsion between adsorbed BTAH and (*ii*) $g > 0$ lateral attraction between adsorbed BTAH. Two electrolytes were considered, H_2SO_4 and HCl at different concentrations (from 0.001 M to 0.01 M for H_2SO_4 and from 0.001 M to 0.5 M for HCl). The benzotriazole concentrations ranged from 1.0×10^{-5} M to 1.0×10^{-1} M for both studies. Using Equation 2.2.12, the standard adsorption free energies were reported slightly higher for the sulphuric acid electrolyte (from –27.2 kJ mol^{-1} to –27.8 kJ mol^{-1}) than those estimated for hydrochloric acid (from –20.2 kJ mol^{-1} to –20.8 kJ mol^{-1}). This behaviour contradicts those results reported by Stewart *et al*. [22] where halides favoured the formation of thicker and more protective films.

Considering the influence of the applied potential on the benzotriazole adsorption on copper, Allam *et al.* [25] investigated the benzotriazole adsorption on cathodically polarised copper in a 0.5 M Na_2SO_4 + 0.1 M H_2SO_4 solution. The electrodes were polarised at –1.0 V *vs.* Ag/AgCl for 15 minutes, in order to remove the oxide film which covered the metal surface, and then at –0.394 V *vs.* Ag/AgCl. The current was measured (a chronoamperometry process) in the absence and in the presence of 1×10^{-4} M, 1×10^{-3} M and 1×10^{-2} M of benzotriazole. The adsorption isotherm used was the Langmuir isotherm, see Equation 2.2.11. The standard adsorption free energy was estimated to be –3.8 kJ mol^{-1}, considerably lower than those reported at the open circuit potential [21, 43], thus suggesting a benzotriazole adsorption behaviour extremely sensitive to the applied potential.

To date, the standard adsorption free energies of benzotriazole were all determined on copper at different experimental conditions, *i.e.*, electrolyte, pH, ionic strength and applied electrode potential [21, 25, 43-45]. Regarding the adsorption mechanism of benzotriazole on copper–based alloys to the best of our knowledge only a limited number of studies have been undertaken and reported in the literature.

Babic *et al.* [46] investigated the corrosion behaviour of 90/10 CuNi in a 1 M CH_3COOH solution at pH 5.8, in the presence of benzotriazole. The inhibitor concentration ranged from 5.0×10^{-3} M to 10.0×10^{-3} M, while the technique employed to testing the corrosion behaviour was the CV. The best description of the benzotriazole adsorption was provided by the Langmuir isotherm, see Equation 2.2.11, which resulted in a standard adsorption free energy of

–36.7 kJ mol^{-1}. Similar standard adsorption free energies were also determined by Metikoš-Huković [42] for benzotriazole on copper in the same electrolyte conditions (1 M CH_3COOH). The Langmuir isotherm was also employed by Kadhom *et al.* [47] for describing the corrosion behaviour of 90/10 CuNi in a 5% HCl solution in the presence of benzotriazole. The inhibitor concentrations were 8.4×10^{-3} M and 12.6×10^{-2} M while the technique used for the testing was the weight loss (WL). Using Equation 2.2.11 the authors determined a value of standard adsorption free energy of –22.1 kJ mol^{-1}. The value determined by Kadhom *et al.* was comparable with those assessed by Bastidas [45] on copper in acidic chloride environments. Tables 2.2.1 and 2.2.2 list the standard adsorption free energies and the system characteristics at which the tests have been performed, *i.e.*, type and concentration of the electrolyte, pH of the solution, method by which the adsorption evaluations have been carried out and isotherm used for the experimental fitting of benzotriazole on copper and on copper–based alloys.

Table 2.2.2. Summary of the literature benzotriazole adsorption free enthalpy values determined on copper–based alloys.

Ref.	Substrate	Solution	pH	Method	Isotherm	ΔG_{ads} / kJ mol^{-1}
[46]	90/10 CuNi	1M CH_3COONa	5.8	CV	Langmuir	–36.7
[47]	90/10 CuNi	5% HCl	–	WL	Langmuir	–22.1

2.2.4 Summary

Benzotriazole is a well–established and an effective corrosion inhibitor for copper and copper–based alloys. Even though its corrosion inhibition has been attributed to the formation of a polymeric ad–layer of $[Cu(I)BTA^-]_n$, the actual adsorption mechanism, as well as the adsorbed films structures, are still being discussed. Indeed, the initial adsorption step has been shown to take place via either the formation of adsorbed molecular BTAH, $Cu(0)[BTAH]_{ads}$ [18, 37, 39, 40] or the direct adsorption of $[Cu(I)BTA^-]_n$ [33], whereas the issue related to whether the formation of $[Cu(I)BTA^-]_n$ occurs at the metal surface [29, 37-40, 48] or within the diffusion layer [18, 33] remains open [20]. Furthermore, the inconclusive results in the literature regarding the ad–layer structure do not provide insightful indications for establishing the most likely adsorption process of benzotriazole on copper.

Parameters such as pH and applied potential have been reported to significantly influence the presence of adsorbed benzotriazole films. Generally, in low pH solutions (below 3) and at

cathodically polarised copper surfaces the formation of $[Cu(I)BTA^-]_n$ has been shown to be unfavoured.

As far as the adsorption isotherms are concerned, different models have been utilised in the literature to describe the benzotriazole behaviour on copper and copper–based alloys. Benzotriazole spontaneously adsorbs on copper and on copper–based alloys with a standard adsorption free energy ranging from –22.1 kJ mol^{-1} to –47.0 kJ mol^{-1} depending on the experimental conditions.

2.3 Boron–Doped Diamond Electrodes

This literature survey is focused on (*i*) the electrochemical properties of boron–doped diamond (BDD) electrodes in aqueous media (see Section 2.3.2) and (*ii*) the chemical analysis of BDD surfaces using X–ray photoelectron spectroscopy (XPS) (see Section 2.3.3). Regarding (*i*), a detailed review of the most relevant electrochemical properties reported in the literature will allow a comparison with the experimental results determined at the used BDD electrodes (see Section 5.1). Furthermore, since a strict dependence has been established between the chemical surface–state and the electrochemical properties of doped diamond films [49], the (*ii*) will be surveyed to assess the functional groups likely to be present at BDD surfaces, thus allowing to better understand the correlation present between the electrochemical properties and the surface chemical composition. Moreover, a brief description of the BDD synthesis procedures are highlighted in Section 2.3.1 in order to background on the main manufacturing methods employed to date.

2.3.1 Synthesis of Boron–Doped Electrodes

Due to its complete C–sp^3 hybridisation, diamond has outstanding properties such as chemical inertness, extreme hardness and low friction coefficient. The high inherent electrical resistivity makes natural diamond an insulating material not suitable for electrochemical purposes. However, addition of boron atoms in the diamond lattice, *p–doping*, will transform it into a conductive material, thus making BDD substrates useful for a broad range of diverse electrochemical applications [50]. As highlighted in Table 2.3.1, the BDD electrode conductivity has been observed to increase from approximately 10^{-4} S cm^{-1} to ca. 10 S cm^{-1}, when the boron concentration (expressed either as ppm of B in the precursor gas phase or as B atoms within the tetrahedral lattice), varied from 200 ppm to 10000 ppm and from 10^{17} atom cm^{-3} to 10^{21} atom cm^{-3}, respectively.

Table 2.3.1. Conductivity of boron–doped diamond [51].

B / C (gas phase) / ppm	[B] (solid phase) / atom cm^{-3}	Conductivity / S cm^{-1}
200	8×10^{17}	2×10^{-4}
800	2×10^{19}	5×10^{-4}
1200	5×10^{19}	4×10^{-3}
1600	9×10^{19}	0.02
2000	1×10^{20}	0.09
2800	4×10^{20}	–
6000	2×10^{21}	17
6500	3×10^{21}	–
8000	5×10^{21}	17
10000	7×10^{21}	17

The outstanding chemical and physical properties of doped diamond films, originally discovered in the early sixties by Union Carbide Corporation [50], led to extensive investigations of these substrates in order to find better synthesis methods as well as enhancement of their performance. To date, chemical vapour deposition (CVD) is the main synthesis process exploited to produce doped diamond. This technique creates thin layers of diamond, with desirable amounts of doping agent, deposited onto an inert substrate [52]. In addition to CVD, vacuum annealing and the high pressure and high temperature process (HPHTP) have been studied as alternative routes to produce doped diamond materials [50]. Herein are reported a brief description of the principal synthesis procedures of boron–doped diamond and conductive diamond substrates.

- Chemical Vapour deposition: The CVD process was investigated after Union Carbide Corporation discovered the potential to deposit diamond from hydrocarbon or CO/CO_2 gas sources at low pressures and temperatures, where diamond is the metastable carbon phase with respect to the graphite [50]. Consequently, when the diamond deposition is performed it is essential to enhance the sp^3–carbon content and simultaneously suppress the sp^2–structure. To date, CVD has been the technique most employed to manufacture doped–diamond electrode due to its high reproducibility and controllability [50]. This particular procedure is based on a gas–phase non–equilibrium process which uses a high super saturation of atomic hydrogen with various hydrocarbon radicals [50]. Activation of the gas phase can be accomplished using hot filaments [53] or microwave radiation [54], increasing the temperature of the gas phase to 2200–2800 °C. Generally, when the

gas phase is activated by the hot filament it is possible to manufacture a large diamond surface (for industrial purposes), up to 0.3 m^2, whereas using a microwave system a smaller surface area, but with higher diamond purity, is usually produced. In both cases, the gas phase is held at 10–50 mbar and is generally comprised of a carbon source in hydrogen (H_2) with boron or other dopant elements [50]. Specifically, the carbon source methane (0.5–3.0% of CH_4 in hydrogen) has been the most frequently employed compound, although others, such as an acetone / methane mixture (9:1 volume ratio), have been also reported in the literature [55]. As far as the dopant element is concerned, the use of diborane (B_2H_6) can be used in the CVD process as a B source since its concentration can be varied by controlling the flow rate. However, its explosive nature, when in the presence of oxygen, requires special attention. Therefore, B_2O_6 (dissolved in methanol) rather than B_2H_6 [55] is generally preferred. The role of hydrogen in the CVD process is not only confined to be the carrier phase. Indeed, it has been reported that hydrogen promotes the termination of the carbon dangling bonds on the diamond surface and reduces the graphitic carbon (C–sp^2) in the diamond lattice structure. Concerning the substrate material onto which the diamond is deposited, so far the best material is silicon due to its ability to minimise the phenomenon of crossing contamination [55]. Usually, regardless of the type of the substrate, the deposition process is performed onto a substrate maintained a temperature of 750–825 °C [50].

- High pressure and high temperature process (HPHTP): Doped diamond electrodes prepared by the CVD process exhibit excellent electrochemical performances. However, limitations principally due to the complexity of the preparation and the cost of the equipment (high temperature in the presence of hydrogen atmosphere) have limited wider usage [56]. Therefore, alternative diamond preparation methodologies are still required in order to simplify the formation process. For instance, diamond powder, with low specific surface area and a particle size ranging from 0.1 μm to 100 μm, can be produced by high pressure and high temperature synthesis. Problems related to the size–controllability and the low conductivity of the produced diamond powder have been reported to reduce a wider use of HPHTP.
- Vacuum annealing: Doping is not a unique way to obtain conductive diamonds. An alternative approach to impart conductance to polycrystalline CVD diamond is high temperature annealing within a vacuum [57] which has been shown to be mainly related to the graphitised of grain boundaries. Changes in the electrochemical properties of the heat treated films are apparent at temperatures above 1552 °C (with an increase of the conductivity from an initial value of 10^{-11} S cm^{-1} up to 10 S cm^{-1}). The

practical use of this method to form conductive diamond from undoped diamond is still limited and remains questionable [50].

2.3.2 Electrochemical Characterisation of Boron–Doped Diamond Electrodes

BDD properties are influenced by a large range of factors, such as dopant concentration, type of dopant, structural defects in the diamond film, impurities (sp^2–C), crystallographic orientation and surface termination [50, 58]. Chemical and physical properties have been reported to be significantly altered by the surface chemical state of the diamond electrodes. For instance, conductivity has been observed to slightly decrease passing from the hydrogen–diamond surface to the oxygen–diamond surface [50, 59], whereas wettability, which has been associated with the presence of highly oriented surface dipole moments (C—O groups) capable of interacting with polar solvents, has been shown to increase passing from hydrogen– to oxygen–terminated surfaces [50, 58]. It is well–known that doped diamond (produced via a CVD process) has a hydrogen–termination surface, which can be easily transformed to oxygen–termination by oxidation (electrochemical, thermal or by means of oxygen plasma) [50, 58, 60]. Due to the influence of different surface C–species on the chemical and physical properties of BDD electrodes, Ferro *et al.* [49] chemically characterised the surface of an "as–formed", an electrochemically oxidised and a thermally oxidised boron–doped diamond electrode. X–ray photoelectron spectroscopy (XPS) revealed that the "as–formed" doped diamond resulted in a relatively low oxygen–bonded carbon content (mainly alcohols and ethers), while the oxidised electrodes displayed greater carbon–oxygen surface speciation (alcohols, ethers, carbonyls, carboxyls and esters). Regarding the stability of the oxygenated groups at the diamond surface, Goeting *et al*., Ferro *et al*. and Kondo *et al.* [49, 61, 62] determined that these species display an intrinsic stability that the recovery of the pristine surface is achievable only by using a hydrogen plasma treatment.

Electrochemical BDD properties are also expected to change when the electrode surface is transformed from hydrogen– to oxygen–termination [58, 59, 63]. Considering the investigation of the redox couple ferri / ferrocyanide, $[Fe(CN)_6]^{3-/4-}$, on a diamond electrode, a reversible process is usually reported for hydrogen–terminated BDD electrodes, while a quasireversible process is observed for oxygen–termination [59, 64, 65]. This indicates that the "as–formed" diamond electrodes display faster electron transfer kinetics with respect to the oxidised diamond substrates [63, 66].

The $[Fe(CN)_6]^{3-/4-}$ redox system is often used to probe the electrode performance [67]. It is frequently assumed that the mechanism by which the $[Fe(CN)_6]^{3-/4-}$ reacts at the diamond surface is a simple outer–sphere process [68], *i.e.*, an electron transfer where the reactant and the product do not interact strongly with the electrode surface [69, 70]. However, Granger *et al.*

[71] indicated that the redox reaction of ferri / ferrocyanide on BDD electrodes is via an inner–sphere process, through which there are specific interactions at the BDD surface. Subsequently, more recent studies [72] have confirmed the sensitivity of the $[Fe(CN)_6]^{3-/4-}$ system to the condition of the diamond surface, suggesting the establishment of interactions between the surface and the cyanide complex.

Concerning the reactivity of the $[Fe(CN)_6]^{3-/4-}$ redox system on different doped diamond surfaces, Ferro *et al.* [66] investigated the ferri / ferrocyanide kinetics in a 0.5 M H_2SO_4 solution for an "as–formed" and an electrochemically oxidised diamond electrode, by using electrochemical impedance spectroscopy (EIS). The apparent electron–transfer rate constants[1] (k^0_{app}) for $[Fe(CN)_6]^{3-/4-}$ were determined to be 0.04 cm s^{-1} and 0.004 cm s^{-1} for the "as–formed" and the oxidised electrodes, respectively, thus indicating a faster process promoted by the hydrogen–terminated BDD.

Actis *et al.* [65] also compared the electrochemical behaviour of boron–doped diamond electrodes with different surface termination: hydrogen, oxygen (obtained by UV irradiation in air for 2 h) and amine surfaces (plasma treatment at 13.56 MHz in He/NH_3 system). Electrochemical investigations were achieved using cyclic voltammetry (CV) and employing the $[Fe(CN)_6]^{3-/4-}$ redox system in a 0.1 M KCl solution. A quasireversible electron transfer was reported for all the diamond electrodes investigated, even though the faster process was associated with the hydrogen–terminated surface, having an apparent rate constant of 0.012 cm s^{-1}. The slowest electron transfer process was determined to occur at the oxygen–terminated diamond electrode, having an apparent rate constant of 0.0003 cm s^{-1}. The authors claimed that the dipole surface $C^{\delta+}—O^{\delta-}$, present at the oxygen–terminated BDD, was responsible for the reduced kinetic since it unfavourably interacted with the $[Fe(CN)_6]^{3-/4-}$ anions (electrostatic repulsion).

A slow electron transfer process of the $[Fe(CN)_6]^{3-/4-}$ redox system was also highlighted by Zhang and co–workers [73] when an "as–formed" BDD electrode was subjected to anodic treatments, *i.e.*, +1.039 V, +1.539 V, +2.039 V, +2.539 V *vs.* Ag/AgCl in a 0.1 M H_2SO_4 solution for 20, 40 and 60 minutes. In particular, an increase of both the electrode potential and time of the anodic treatments produced a decrease of the apparent electron–transfer kinetic constants associated with the $[Fe(CN)_6]^{3-/4-}$ redox couple, 1.01×10^{-4} cm s^{-1} to 2.49×10^{-4} cm s^{-1}, respectively for the "as–formed" and the oxidised electrodes (+2.5 V for 60 minutes).

Similarly, considering the influence of the diamond surface termination on the kinetics of the $[Fe(CN)_6]^{3-/4-}$ reduction / oxidation process, Boukherroub *et al.* [74] studied the photochemical

[1] The electron–transfer rate constants reported in the literature are generally termed as "apparent electron–transfer rate constants" since they are not usually corrected with the double layer capacitance [24].

oxidation of an "as–formed" BDD. The background solution employed was a 0.1 M KCl solution while the boron doping level of the electrode was 2000 ppm. The photochemical treatment applied to the BDD substrate consisted of vacuum irradiation process with ultraviolet light at a wavelength of 172 nm for 3 h. The apparent electron transfer rate constants promoted by the BDD electrodes for the ferri / ferrocyanide couple were determined to be 0.012 cm s^{-1} and 0.0005 cm s^{-1} for the hydrogen– and oxygen–terminated diamond electrodes, respectively.

The surface termination effect on the electrochemical properties of doped diamond electrodes was also studied by Vanhove *et al.* [75] where a strong influence of the surface chemical state was reported. The BDD electrode employed in the tests had a boron doping level of 2000 ppm while the $[Fe(CN)_6]^{3-/4-}$ redox system in a 0.1 M KCl solution was used to probe its electrochemical reactivity. It was reported that after an "extensive" use of the diamond electrode, the electron transfer rate constant decreased from 6×10^{-2} cm s^{-1} (value determined at the "as–formed" BDD) to 4×10^{-3} cm s^{-1}, indicating a rapid decline of the electrochemical properties. However, the recovery and stabilisation of the electrode reactivity was reported by applying a post–electrochemical treatment cycling the electrode potential from -4×10^{-2} A cm^{-2} and 4×10^{-2} A cm^{-2}. Data indicated that the post–electrochemical treatment conferred more stability and enhanced the electron transfer kinetics, having an apparent rate constant of 2×10^{-2} cm s^{-1} [75].

In contrast to the literature reported to date, McEvoy and Foord [76] suggested that the oxidation treatment achieved on "as–formed" diamond electrode enhances the ferri / ferrocyanide electron transfer kinetics. The background electrolyte employed for the testing was a 0.1 M KCl solution whereas the redox system was $[Fe(CN)_6]^{3-/4-}$. The anodic treatment was performed in a 1 M HNO_3 solution by applying an electrode potential of +1.035 V *vs.* Ag/AgCl for 60 s. Cyclic voltammetry suggested an increase of the electron transfer kinetics after the polarisation treatment (with a reduction of the peak–to–peak response from 0.200 V to 0.090 V). The electron–transfer rate constant, estimated using the Nicholson method, was reported to be 5×10^{-3} cm s^{-1} for the oxidised electrode.

Another important surface feature that has been suggested to markedly influence the electro–catalytic properties of diamond substrates is the superficial graphitic carbon content. Duo *et al.* [77] studied the electrochemical behaviour of diamond electrodes subjected to different anodic polarisation treatments. The electrodes investigated were the "as–formed" diamond electrode and two differently polarised diamond electrodes, *i.e.*, "mild–polarised" (+0.01 A cm^{-2} for 30 minutes in a 1 M H_2SO_4 solution) and "severe–polarised" diamond electrodes (+1 A cm^{-2} for 576 h in a 1 M $HClO_4$ solution).

Table 2.3.2. Summary of the literature kinetic values determined for the $[Fe(CN)_6]^{3-/4-}$ redox system on diamond electrodes.

Reference	k^0_{app} / cm s^{-1} (H–terminated)	k^0_{app} / cm s^{-1} (O–terminated)	Electrolyte	Method	Boron level / ppm
[65]	1.2×10^{-2}	3×10^{-4}	0.1 M KCl	CV	–
[66]	4×10^{-2}	4.0×10^{-3}	0.5 M H_2SO_4	EIS, CV	3500
[73]	1.01×10^{-4}	2.49×10^{-4}	0.1 M H_2SO_4	CV	–
[74]	1.2×10^{-2}	5.0×10^{-4}	0.1 M KCl	CV	≈ 2000
[75]	6×10^{-2}	4×10^{-3}	0.1 M KCl	CV	2000
[77]	4×10^{-4}	8×10^{-5}	0.5 M H_2SO_4	CV	≈ 3000
[78]	–	4.0×10^{-4} to 1.2×10^{-5}	0.5 M KNO_3	CV	≈ 4000
[76]	–	5×10^{-3}	0.1 M KCl	CV	–
[79]	9×10^{-4}	–	0.1 M KCl	CV	≈ 1600

The diamond electrodes had a boron doping level of 3000 ppm. The ferri / ferrocyanide redox system was employed for the electrochemical testing of all the diamond electrodes while the supporting electrolyte was a 0.5 M H_2SO_4 solution. Published data indicated that the $[Fe(CN)_6]^{3-/4-}$ electron transfer kinetic constant decreased significantly going from the "as–formed" to the "mild–anodised" diamond electrodes. The evaluated values were 4×10^{-4} cm s^{-1} and 8×10^{-5} cm s^{-1}, respectively for the "as–formed" and for the "mild–oxidised" diamond substrates. Concerning the "severe–polarised" electrode, a similar electron–transfer rate constant was reported to that of the "mild–anodised", 9×10^{-5} cm s^{-1}. The decrease of the BDD reactivity was explained in terms of "elimination of the graphitic carbon species" from the electrode surface, which were considered as promoters of the charge transfer reaction, $k^0_{graphitic–C} \gg k^0_{diamond–C}$.

Alehashem *et al.* [79] also investigated the influences of the graphitic carbon content on the electron transfer kinetics of ferri / ferrocyanide redox system in a 0.1 M KCl solution. The substrates were an "as–formed" and a chemically etched (for 30 s in a 3:1 vol. / vol. HNO_3 / HF solution) BDD. The reported k^0_{app} for the "as–formed" electrode was 0.01 cm s^{-1} while the value determined for the chemically etched was 9×10^{-4} cm s^{-1}. Hence, in line with observations drawn by Duo *et al.*, it was concluded that the presence of graphitic carbon impurities, likely to be located at the edges of the diamond crystals, affects the catalytic activity of doped diamond substrates.

Table 2.3.2 summarises the rate constants for the electron transfer process related to the $[Fe(CN)_6]^{3-/4-}$ redox system on BDD electrodes, the support electrolytes employed for the testing, the electrochemical technique used and the boron–doping level of the electrodes. The reported kinetic parameters indicate a general faster electron transfer kinetic associated with the hydrogen–terminated doped diamond electrode with respect to the oxygen–terminated.

Another parameter which significantly alters the electrochemical properties of the BDD electrodes is the type of dopant and its concentration. It is widely reported that the *i–E* curves of the diamond electrodes show a ferri / ferrocyanide current peak–to–peak separation which decreases as the doping level increases [68].

The characteristic surface–chemistry displayed by diamond substrates confers to these electrodes a low background current, or capacitive current, due to the absence of redox couples generally present in conventional electrode materials (noble metals and glassy carbon electrodes) [50]. This remarkable feature is attractive especially for those electrochemical measurements (electro–analysis) which require low background currents, since a high capacitive response negatively reduce the faradaic efficiency of the electrochemical signal [79]. It is generally believed that for high quality diamond electrodes, since there are no particular redox–active functional groups and there is no known specific adsorption of electrolyte ions, the capacitance is mainly related to the electrolyte concentration, or more precisely to the ionic strength of the solution [72, 80]. The charging of the double layer is significantly affected by the chemical state of the electrode surface, as well as the content of non–diamond carbon [81]. Martin *et al.* [81] reported a significant influence on the double layer charging caused by the graphitic carbon content in the substrate. They investigated two different types of hydrogen–terminated surface electrodes: a high quality BDD electrode and a low quality BDD electrode. They determined, by using cyclic voltammetry and a 0.5 M H_2SO_4 solution as the supporting electrolyte, a higher capacitance for the low quality diamond electrode (5 μF cm^{-2}) than the high quality diamond electrode (0.05 μF cm^{-2}). The electrode potential interval selected for the capacitance determinations ranged from –0.105 V to +1.495 V *vs.* Ag/AgCl. The enhanced capacitive current for the low quality diamond electrode was explained in terms of the presence of graphitic sp^2 carbon, which was responsible for the strong interactions with the solution species.

Duo *et al.* [77] indicated a reduction of the capacitance passing from the "as–formed" to the "severe–oxidised" diamond electrodes of approximately two orders of magnitude, from 749 μF cm^{-2} to 7 μF cm^{-2} and from 180 μ F cm^{-2} to 11 μF cm^{-2} for potentials of +0.64 V and +0.895 V *vs.* Ag/AgCl, respectively. The method employed to estimate the capacitance was cyclic voltammetry, performed in a 0.5 M H_2SO_4 solution. It was suggested that a change of the capacitance occurs for the different diamond substrates due to the presence / absence of redox

systems. Indeed, the "as–formed" diamond electrode was shown to display a high capacitance, attributed to a (*i*) true double layer capacitance and a (*ii*) pseudo–capacitance, associated with surface redox system (sp^2 graphitic C). Conversely, the lower capacitance value determined for the "severe–oxidised" diamond electrode was an indication of the removal of the surface redox system from the diamond surface, obtaining a capacitance–estimation entirely attributable to a true double layer effect.

In accordance with Duo and co–workers, Granger *et al.* [71] determined a reduced capacitance for an oxidised diamond electrode with respect to an "as–formed" diamond. The oxidation procedure was performed by cycling the electrode potential between the anodic limit of +2 V and the cathodic limit of –0.961 V *vs.* Ag/AgCl in a 1 M H_2SO_4 solution. The capacitance determined, by using cyclic voltammetry in a 1 M KCl solution, ranged from 6 μF cm^{-2} to 11 μF cm^{-2} and from 4 μF cm^{-2} to 6 μF cm^{-2} within an electrode potential interval from –0.461 V to +1.039 V *vs.* Ag/AgCl, for the "as–formed" and the anodically treated diamond substrates, respectively.

Figure 2.3.1 shows a comparison between cyclic voltammograms performed on platinum and on BDD electrodes in a 0.5 M H_2SO_4 solution.

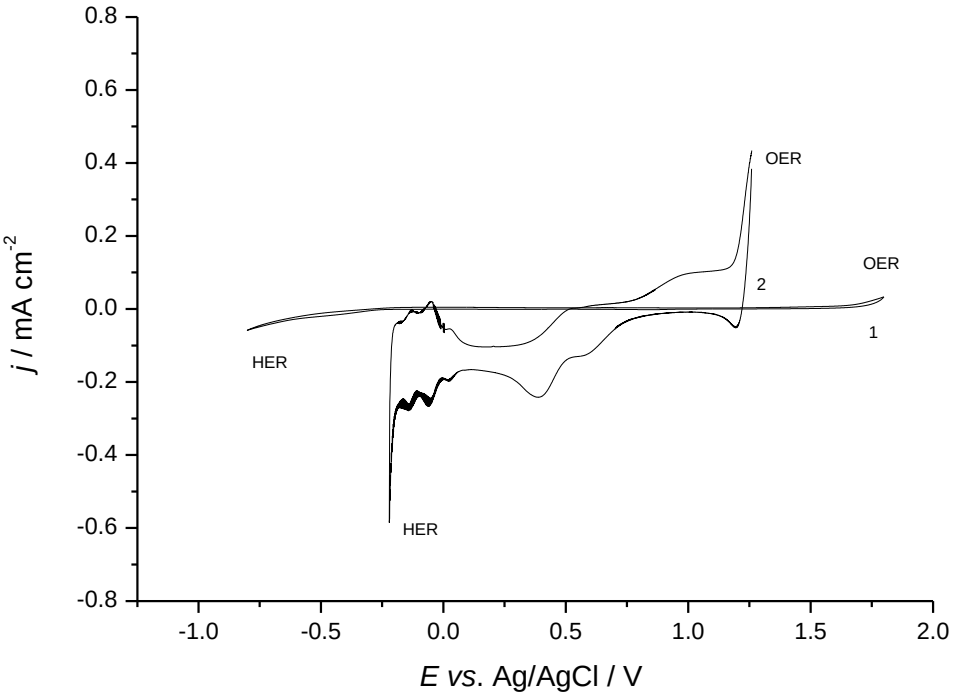

Figure 2.3.1. Cyclic voltammograms carried out on (1) oxygen–terminated surface BDD and (2) on platinum electrodes in a 0.5 M H_2SO_4 solution at 10 mV s^{-1}. OER and HER indicate oxygen and hydrogen evolution reactions.

Noticeable differences are evident between (*i*) the background currents and (*ii*) the potential windows (or window of polarisabilities) of the reported electrode responses. As far as (*i*) is concerned, it should be noted that within the potential extremes determined by the oxygen and hydrogen evolution reactions, hereafter denoted as OER and HER, the platinum displays a higher background current than that of the BDD. Indeed, whereas the Pt response is constituted of a double layer capacitance current and a pseudo–capacitive current (active redox–couples), the small background current recorded for the BDD electrode has been often attributed to a true double layer capacitance [77]. Results and experimental features will be highlighted and better discussed in the Experimental Chapter 5.

Regarding (*ii*), it is generally known that it represents the potential range in which an electrode can be used in a certain medium [82]. The potential window is usually delimited by the HER and the OER and it is an important characteristic especially for the electrochemical analyses, where a wide potential range is required to detect redox couples with high anodic or cathodic potentials. Generally, larger values of potential window are determined at BDD electrodes than at Pt electrodes. Indeed, as can be seen in Figure 2.3.1, the window of polarisability of the BDD electrode is delimited between –0.8 V and +1.8 V *vs.* Ag/AgCl whereas that of the Pt electrode between –0.25 V and +1.25 V *vs.* Ag/AgCl.

The wide potential window exhibited by BDD electrodes in aqueous media is related to the large overpotentials (η) displayed towards both the OER and HER [83] (η_{OER} and η_{HER}). The high values of η_{OER} and η_{HER} are in turn associated with the low stabilising interactions of the intermediates (OH_{ads} / O_{ads} and H_{ads}) at the BDD surface during the OER and HER. As far as the HER is concerned, it has been reported that at a metallic electrode it can take place following either the Volmer–Heyrovsky (see Equations 2.3.1 and 2.3.2) or the Volmer–Tafel (see Equations 2.3.1 and 2.3.3) reaction paths [84-86].

$$\text{Volmer:} \quad M + H^+ + e^- \rightarrow M - H_{ads} \qquad 2.3.1$$

$$\text{Heyrovsky:} \quad M - H_{ads} + H^+ + e^- \rightarrow H_2 + M \qquad 2.3.2$$

$$\text{Tafel:} \quad 2M - H_{ads} \rightarrow H_2 + 2M \qquad 2.3.3$$

Initially, atomic hydrogen is formed at the metal surface (M) as an adsorbed intermediate (H_{ads}), see Equation 2.3.1 referred to as Volmer reaction, and then, hydrogen gas can be generated either via Equations 2.3.2 (the Heyrovsky reaction) or 2.3.3 (the Tafel reaction). Generally, on metal electrodes the adsorbed hydrogen plays an important role in mediating the HER [84] and determinates the overall kinetics [86, 87].

Regarding the HER at hydrogen–terminated BDD electrodes, the high overpotentials generally determined at these substrates suggest that the diamond surfaces undergo little interaction with dissolved species, or in other terms, the adsorption of protons or atomic hydrogen is negligible [81]. The potentials determined at hydrogen– or oxygen–terminated BDD electrodes for HER are usually significantly more positive (approx. –1.45 V *vs*. Ag/AgCl) [81, 82] than the standard electrode potential for the direct liberation of atomic hydrogen [82], see Equation 2.3.4, with a standard electrode potential as described in Equation 2.3.5.

$$H^+ + e^- \rightarrow H\cdot \qquad 2.3.4$$

$$E° = -2.505\ \text{V}\ \textit{vs.}\ \text{Ag/AgCl} \qquad 2.3.5$$

Therefore, the considerable increase in potential from –2.505 V to –1.455 V *vs*. Ag/AgCl can be attributed to the interactions between the diamond surface and the atomic hydrogen. Regarding the HER mechanism at BDD electrodes, it has been proposed the involvement of the dangling hydrogens present at the surface. Yagi *et al.* [88] investigated the contribution of dangling hydrogens to the HER mechanism by using mass spectrometry which indicated that hydrogen evolution occurs at the diamond substrates via radical carbon formation, as shown in Equations 2.3.6 and 2.3.7.

$$H^+_{(aq)} + \equiv C - H + e^- \rightarrow H_{2\,(gas)} + \equiv C\cdot \qquad 2.3.6$$

$$H^+_{(aq)} + \equiv C\cdot + e^- \rightarrow \equiv C - H \qquad 2.3.7$$

The model took into account a number of interactions between the diamond substrate and the hydrogen, since in the complete absence of stabilising interactions the potential at which HER should occur should be –2.505 V *vs.* Ag/AgCl, as suggested by Martin et *al.* [81].

Concerning the OER, the values of the Tafel slope (*b*), which typically range from +30 mV dec^{-1} to +120 mV dec^{-1} at metals and oxide–based electrodes [86], provide insights regarding the rate determining step of the OER mechanism [89]. Considering the BDD electrode, atypical *b* for the OER have often been reported. Indeed, Santana *et al.* [90] reported a *b* between +220 mV dec^{-1} and +415 mV dec^{-1} using a hydrogen–terminated diamond substrate with a doping level of ca. 3500 ppm, Janssen and Blijlevens [91] indicated a *b* of +430 mV dec^{-1} employing a diamond electrode with a hydrogen–termination surface, while Beck *et al.* [92] determined a *b* between +200 mV dec^{-1} and +500 mV dec^{-1} performing the test with a hydrogen–terminated surface BDD with boron doping level ranging from 50 ppm to 230 ppm. Kapalka *et al.* [89] reported a Tafel slope between +340 mV dec^{-1} and +680 mV dec^{-1} at low HER overpotentials, η, (η < 0.995 V *vs*. Ag/AgCl) and a value of +123 mV dec^{-1} at higher η, (η > 0.995 V *vs*.

Ag/AgCl), using a hydrogen–terminated diamond electrode with 1000 ppm of boron doping level. These findings were associated with the presence of surface redox couples / functional groups which acted as a barrier for the OER, thus resulting in unusual *b* [89].

Enache *et al.* [93] also investigated the electrochemical evolution of oxygen on a BDD electrode for different electrolytes and different pHs, from pH 1.0 to pH 11.5, by using differential pulse voltammetry. The data indicated the existence of a shoulder–signal, present immediately before the incipient OER at +2.15 V *vs.* Ag/AgCl (pH 1), which showed a linear dependence with the proton concentration. The assessed potential peak–pH relationship was 0.059 V per pH decade, as shown in Equation 2.3.8, thus suggesting the involvement of the same number of protons and electrons.

$$E_{eq} = +2.15 - 0.059\ \text{pH} / \text{V}\ vs.\ \text{Ag/AgCl} \qquad 2.3.8$$

$$H_2O \rightarrow OH\cdot + H^+ + e^- \qquad 2.3.9$$

In light of the results, the authors attributed the oxidation signal to the formation of the hydroxyl radicals, as shown in Equation 2.3.9.

Concerning the mechanism by which OER occurs at diamond electrodes, Santana *et al.* [90] proposed that the most probable path of reaction was associated with the initial production of the hydroxyl radical at the electrode surface (see Equation 2.3.10), followed by the oxidation of the hydroxyl radical to atomic oxygen (see Equation 2.3.11) and the final recombination of atomic oxygen radicals to form an oxygen molecule (see Equation 2.3.12).

$$H_2O \rightarrow OH\cdot + H^+ + e^- \qquad 2.3.10$$

$$OH\cdot \leftrightarrow O\cdot + H^+ + e^- \qquad 2.3.11$$

$$2O\cdot \leftrightarrow O_2 \qquad 2.3.12$$

$$2OH\cdot \leftrightarrow H_2O_2 \qquad 2.3.13$$

$$H_2O_2 \leftrightarrow O_2 + 2H^+ + 2e^- \qquad 2.3.14$$

Equations 2.3.10, 2.3.13 and 2.3.14 have also been proposed as an alternative path of reaction for the OER, where for high OH· superficial concentrations the recombination process can take place forming hydrogen peroxide (see Equation 2.3.13), which is then electrochemically oxidised to O_2 (see Equation 2.3.14).

Table 2.3.3. Summary of the literature capacitances (*C*) and Tafel slopes (*b*) on diamond electrodes.

Reference	Electrolyte	C / μF cm^{-2} H–terminated	C / μF cm^{-2} O–terminated	b / mV dec^{-1} OER
[71]	1 M KCl	6 and 11	4 and 6	–
[77]	0.5 M H_2SO_4	749 and 7	180 and 11	–
[81]	0.5 M H_2SO_4	5 (low quality) and 0.05 (high quality)	–	–
[89]	1M $HClO_4$	–	–	+340 to +680
[90]	0.5 M H_2SO_4	–	–	+220 to +415
[91]	2.0 M HIO_3	–	–	+430
[92]	1.0 M H_2SO_4	–	–	+340 to +680

However, due to the low concentration of H_2O_2, determined by Marselli *et al.* [94] during $HClO_4$ electrolysis tests, it is more likely that the OER at BDD electrodes takes place via Equations 2.3.10, 2.3.11 and 2.3.12, rather than Equations 2.3.10, 2.3.13 and 2.3.14. An additional indication, that supports an OER pathway occurring through Equations 2.3.10, 2.3.11 and 2.3.12 instead of Equations 2.3.10, 2.3.13 and 2.3.14, has been reported to be the weak adsorption energy displayed by hydroxyl radicals at diamond surfaces [90]. Indeed, the formation of H_2O_2 is generally promoted by those electrode surfaces which provide enough stabilisation of OH·, thus making the steps associated with Equations 2.3.13 and 2.3.14 favourable. Table 2.3.3 summarises the capacitances and the Tafel slopes values reported in the literature for BDD electrodes.

2.3.3 Chemical Characterisation of Boron–Doped Diamond Electrodes

Since the chemical state of the diamond surface fundamentally affects its electrochemical performance [66, 77], investigations of the electrode surface state are essential to correlate the electrochemical properties with the surface chemical composition. Ferro *et al*. [49] investigated the chemical nature of different conductive diamond surfaces using XPS. The electrodes studied were an "as–formed", a "mild–oxidised" (electrode submitted to cyclic voltammetry in a 1 M $HClO_4$ solution within the window potential ranging from –0.561 V to +1.639 V *vs.* Ag/AgCl), a "strong–oxidised" (electrode electrochemically treated under extreme oxygen evolution at +3.0 V *vs.* SCE for 20 minutes) and a "thermally–oxidised" at 400 °C for 30 minutes at room atmosphere. The diamond films used had a boron doping level between 3500

and 5000 ppm. Considering the C 1s spectrum, the "as–formed" diamond surface displayed a band signal associated with four peaks: C(i) at 283.6 eV, related to the graphitic carbon, C(ii) at 284.1 eV, which presented the most intense signal and was attributed to the bulk diamond component, C(iii) at 284.7 eV, associated with the alcoholic and etheric groups and C(iv) at 288.6 eV, related to the carboxylic and esteric carbon species. Regarding the electrochemically treated samples, XPS spectra again revealed signals which were fitted with four different peaks, as done for the "as–formed" electrode. However, the analysis of the relative peak–areas indicated a decrease of the ratio $C_{sp^3}/C_{oxygen\text{-}bonded}$ of about 23 % with respect to the "as–formed", thus suggesting a high $C_{oxygen\text{-}bonded}$ content. Furthermore, an increase of the ratio $C_{sp^3}/C_{graphitic\,C}$, C(i) / C(ii), of 10.5 % and 13.5% was observed for the "mild–oxidised" and for the "strongly–oxidised" substrates with respect to the pristine electrode, respectively. Thus, it was deduced that the electrochemical process contributed to the formation of oxidised forms of carbon, mainly from the graphitic components. Analogous considerations were also drawn for the thermally treated substrate, where the formation of oxidised species was reported to occur at expense of the graphitic carbon. Concerning the O 1s spectra, the responses for the "as–formed", the "mildly–oxidised", the "strongly–oxidised", and the "thermally" treated substrates have shown significant differences [49]. In fact, while the "as–formed" and the "mildly–oxidised" signals were fitted with two different peaks O(v) and O(vi) (centred at 532.7 eV and at 533.9 eV for the "as–formed" electrode and at 532.4 eV and at 533.8 eV for the "mildly–oxidised" substrate, respectively), the XPS analysis of the "strongly–oxidised" electrode was fitted with only one peak, centred at 533.1 eV and identified as O(vi). Conversely, the thermally treated electrode displayed a response fitted with three peaks O(v), O(vi) and O(vii), centred at 532.8, 533.9 and 531.1 eV. Therefore, it was proposed that the signal O(v) was related to the etheric / alcoholic aliphatic compounds, the signal O(vi) to the aromatic oxygenated species and the signal O(vii), only present at "thermally–treated" diamond, to the aromatic carbonyls. In summary, the O 1s study corroborated the findings observed for C 1s: electrochemical and thermal treatments lead to the formation of new oxygenated species depleting the non–diamond carbon species.

Simon *et al.* [95] investigated the effect of the annealing treatment, carried out at 1100 °C for 12 h in a high vacuum chamber, on the electrochemical diamond properties of a boron doped diamond substrate (boron doping level of 800 ppm). It was reported that the "as–formed" diamond presented three components in the XPS spectrum, centred at 283.8 eV, at 284.5 eV and at 286.0 eV, assigned to the C 1s signal of the hydrogenated carbon (C–H), the non–hydrogenated bulk carbon (C–sp^3) and the alcoholic / etheric carbon. Moreover, the annealed sample showed an additional peak related to carbonyl C, centred at 287.5 eV.

Girard *et al.* [96] studied the effect of anodic and the cathodic pre–treatments on the electrochemical properties as well as the evolution of the surface termination of a diamond substrate with a boron doping level of 2000 ppm. Two different anodic pre–treatments were taken into account in their study, a "mild" one, consisting of 10 s of polarisation at a current density of +0.1 mA cm^{-2} and a "severe" one, performed for 10 s at a current density of 100 mA cm^{-2}. After each galvanostatic step applied to an "as–formed" specimen, they investigated the reversibility of the electrode transformations by imposing a cathodic treatment which involved the same coulometric charge, that is, a mild cathodic treatment of –0.1 mA cm^{-2} after the mild anodic process and a severe cathodic treatment –100 mA cm^{-2} after the severe anodic process. The XPS C 1s spectrum for the "as–formed" substrate was fitted with three peaks, *i.e.*, 284.0 eV (attributed to the bulk diamond component), 284.7 eV (related to the polyhydride carbon species), and 285.6 eV (associated with the alcoholic / ether carbon components). After the "mild" oxidation process, the XPS C 1s spectrum was fitted with two further peaks centred at 287.2 eV and 288.3 eV, associated with the carboxylic and the ester groups. A similar XPS response occurred for the "severe" oxidised electrode, even though the abundance of the oxygenated species was reported to be slightly greater. Finally, XPS spectra for cathodically treated substrates, performed after the "mild" and the "severe" anodic procedures, did not show any significant differences with respect to the anodically recorded spectra. This finding corroborated the irreversibility of the surface diamond transformation observed with electrochemical measurements [49, 61, 62].

Salazar–Banda *et al.* [85] investigated the electrochemical behaviour of an "as–formed", a cathodically treated, an anodically treated and a thermally treated conductive diamond substrates, with a 800 ppm of boron doping level. They reported for the pristine and for the cathodically specimens a XPS C 1spectra deconvoluted into four different peaks, centred at 283.5, 284.4, 285.5 and 286.4 eV and assigned to graphitic carbon, bulk diamond carbon, alcoholic / etheric carbon and carbonyl carbon groups, respectively.

Boukherroub *et al.* [74] studied the oxidation process effects on the electrochemical behaviour of BDD electrodes achieved by a photochemical treatment. They reported a XPS C 1s spectrum for the "as–formed" diamond substrate featured by a bulk signal centred at 284.0 eV. After the photochemical process the presence of an additional peak at 287.0 eV was attributed to the carbonyl groups.

Table 2.3.4. Summary of the literature B.E. (eV) of the C 1s XPS spectra recorded on doped diamond films.

Ref.	Substrate	C–sp^3 (diam.)	C–sp^2 (graph.)	–C–H	–C–H_x (x ≥ 2)	–C–OH (alcohol)	O–C–O (ether)	R_2–C=O (Carbonyl)	R–C(O)–H R–C(O)–C (Carboxyl) –Ester)
[49]	H–BDD	284.1	283.6	–	–	284.7	284.7	288.6	288.6
[49]	O–BDD_{mild}	284.1	283.4	–	–	286.0	286.0	288.1	288.1
[49]	O–BDD_{strong}	284.1	283.4	–	–	285.6	285.6	288.3	288.3
[49]	O–$BDD_{therm.}$	284.1	283.8	–	–	285.6	285.6	288.6	288.6
[74]	H–BDD	284.0	–	–	–	–	–	–	–
[74]	O–$BDD_{photo.}$	284.0	–	–	–	–	–	287.0	–
[75]	H–BDD	283.7	–	–	284.2	286.1	–	–	–
[75]	H–$BDD_{treat.}$	283.7	–	–	284.2		285.8	287.1	–
[95]	H–BDD	284.5	–	238.8		286.0	286.0	–	–
[95]	H–$BDD_{anneal.}$	284.5	–	238.8		286.0	286.0	287.5	–
[96]	H–BDD	284.0	–	–	284.7	285.6	285.6	–	–
[96]	O–BDD_{mild}	284.0	–	–	284.7	285.6	–	–	287.2 288.3
[96]	O–BDD_{severe}	284.0	–	–	284.7	285.6	–	–	287.2 288.3
[85]	H–BDD	284.5	283.5	–	–	285.5	285.5	286.4	–
[97]	H–BDD	284.5	284.0	–	–	285.3	285.3	287.5	287.5
[62]	H–BDD	284.0	282.7	–	284.5	285.2	285.2	–	–
[62]	O–BDD_{plasma}	284.0	282.7	–	284.5	285.2	285.2	287.6	287.6
[62]	O–$BDD_{electro.}$	284.0	282.7	–	284.5	285.2	285.2	287.6	287.6
[62]	H–BDD_{plasma}	284.0	282.7	–	284.5	285.2	285.2	–	–
[62]	H–$BDD_{electro.}$	284.0	282.7	–	284.5	285.2	285.2	–	–

Wang *et al.* [97] also monitored using XPS the diamond electrode surface modifications of a BDD electrode (1000 ppm) induced by an electrochemical anodic treatment performed at +0.1 mA cm^{-2} for 17 minutes in a 0.5 M H_2SO_4 solution. They reported that the "as–formed" XPS C 1s spectrum was fitted with four peaks, at 284.0, 284.5, 285.3 and 287.5 eV, and attributed to the graphitic C, the bulk diamond C, the alcoholic / ether C and the carbonyl / carboxylic C, respectively. The anodically treated sample again displayed a response featured with four fitted XPS peaks, centred at similar binding energies of those of the "as–formed" electrode signals. Moreover, it was underlined a diminution of the –C–H bonds at the surface and a simultaneous enhancement of both the alcoholic / ether C and the carbonyl / carboxylic C, due to the formation of oxidised species during oxidation.

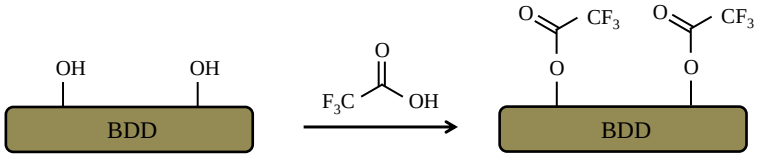

2.3.15

Furthermore, Wang *et al*. attempted to quantify the hydroxyl carbon groups (–C–OH) present at the BDD surface by coupling it with trifluoroacetic acid and detecting the –C–F carbon signal (C 1s), as shown in Equation 2.3.15. The hydroxyl group content in the "as–formed" diamond sample was determined to be 0.2–0.3 %, while a higher value, ca. 6%, was obtained for the oxidised surface. It was also concluded that at least 18% of the C bonded with oxygen was in the form of an alcohol.

Vanhove *et al.* [75] studied the effect of the surface termination on the electrochemical properties of a hydrogen–terminated diamond electrode and reported for the "as–formed" electrode a XPS C 1s response fitted with three peaks, centred at 283.7, 284.2 and 286.1 eV which were attributed to the bulk diamond C, to the polyhydride C and to the alcoholic C groups, respectively. After an "activation" treatment, cycling the electrode potential in a 0.5 M $LiClO_4$ solution from –0.4 A cm^2 to +0.4 mA cm^{-2}, they reported a XPS C 1s spectrum fitted with four signals, centred at 283.7, 284.2, 285.8 and 287.1 eV, and assigned to the bulk diamond C, to the polyhydride C, to the etheric C and to the carbonyl C.

Goeting *et al.* [62] also investigated how the electrochemical and plasma treatments can influence the chemical state of diamond surfaces. The electrochemical modifications were performed by means of both cathodic and anodic treatments, carried out cycling the electrode potential from 0 V to –1.661 V *vs.* Ag/AgCl and from 0.039 V to +2.539 V *vs.* Ag/AgCl in a 0.2 M phosphate buffer solution at pH 2, whereas the plasma treatments were achieved in hydrogen and an oxygen plasma chambers for 3 h and for 1 h at 320 W. The XPS C 1s spectra showed that the bulk diamond carbon was the main species for all the considered substrates, having a peak centred at 284.0 eV. For the "as–formed" substrate, it was also reported a small

content of oxygen, ratio O 1s / C 1s of 3.2 %, either in the form of an alcohol or ether, both at 285.2 eV. Moreover, signals at 284.5 eV and at 282.7 eV were related to the polyhydride and to the graphitic carbon species. Regarding the oxygen–plasma treated electrode and the anodised surface, the authors highlighted in addition to the C 1s signals presented in the "as–formed" substrate spectra, a further peak at 287.6 eV associated with the carbonyl and the carboxyl chemical functionalities. Concerning the cathodically treated and the hydrogen "plasma–treated" substrates, the similarities observed with the "as–grown" BDD C 1s spectra corroborated the irreversibility of the diamond surface transformation.

Table 2.3.5. Summary of the literature binding energies (eV) of the O 1s XPS spectra on doped diamond films.

Ref.	Substrate	–C–OH (Alcohol)	O–C–O (ether)	Ar–OH (Aromatic alcohol)	R_2–C=O (Carbonyl)	R–C(O)–OH R–C(O)–OC (Carboxylic–Ester)	Ar_2–C=O (Aromatic Carbonyl)
[49]	H–BDD	532.7	532.7	533.9	–	–	–
[49]	O–$BDD_{mild\ ox.}$	532.4	532.4	533.8	–	–	–
[49]	O–$BDD_{strong\ ox.}$	–	–	533.1	–	–	–
[49]	O–$BDD_{therm.}$	532.8	532.8	533.9	–	–	531.1

Tables 2.3.4 and 2.3.5 summarise the binding energies reported in this literature chapter for the C 1s and O 1s spectra of BDD electrodes.

2.3.4 Summary

This survey has assimilated the literature regarding the (*i*) principal synthesis, the (*ii*) electrochemical performance and the (*iii*) chemical characterisation of BDD electrodes. Regarding (*i*), it has been highlighted that with respect to the manufacturing method, the produced diamond electrodes have different physical and chemical characteristics, such as electrical conductivity, dimension and chemical composition. To date the most employed BDD synthesis has been shown to be the CVD, since it provides doped diamond films with the desired conductivity in a high reproducibility and controllable way.

Concerning (*ii*), the literature data indicated that the BDD electrochemical performance is significantly controlled by the chemical–termination of the electrode. The "as–formed" BDD electrode, which has a hydrogen–terminated surface, generally promotes a faster electron

transfer for the $[Fe(CN)_6]^{3-/4-}$ redox system with respect to the oxidised BDD, which has an oxygen–terminated surface [66]. This behaviour has been associated with the establishment of interactions between the electrode surface and the chemical species undergoing the electrode reaction (inner–sphere process) [70, 71]. Other important characteristics that feature and distinguish the electrochemical BDD response from other traditional electrodes have been highlighted to be the wide potential window [82] and the low background current [77]. The former characteristic has been associated with the poor catalytic activity towards the HER and the OER, due to the low stabilisations of adsorbed intermediates (H· and OH· / O·) at the diamond surface [82, 83]. Regarding the latter characteristic, *i.e.*, the low background current, it has been shown to be significantly lower than those displayed by other traditional electrodes [50], due to the absence or limited content of surface redox couples [77]. The capacitance of a BDD electrode has been also reported to be influenced by the content of graphitic carbon within the diamond matrix, that is, the higher the sp^2 graphitic carbon and the higher is the capacitance [77], thus providing an indication of the electrode quality.

Concerning (*iii*), different chemical functions have been reported on the BDD surface using the XPS technique. The wide range of the identified chemical groups, such as bulk diamond C, polyhydride C, graphitic C, alcoholic C, ether C, carbonyl C, carboxylic and ester C [49], has been mainly associated with the manufacturing process and the electrode usage. To date, XPS has been proven to be an insightful tool to study the chemical composition of the diamond–surface and of the diamond quality, by estimating the content of the graphitic carbon. This information can be considered crucial since the BDD electrochemical performance is influenced by the surface BDD termination and the content of graphitic carbon.

The insights gained in this literature survey will be employed for an evaluation and comparison of the experimental results of Chapters 5, 6, 7, 8 and 9 in order to have a better understanding of the quality and the electrochemical performances of the electrodes employed.

2.4 Electroanalysis on Boron–Doped Diamond Electrodes

In the following sections the most relevant electrochemical studies regarding the detection of copper–ions (Section 2.4.2) and nickel–ions (Section 2.4.3) in chloride solutions using BDD electrodes have been reviewed in order to establish the most suitable electrochemical detection strategy for crevice corrosion solutions.

It has been reported that the chloride concentration represents a crucial factor for the electrochemical behaviour of copper–ions, due to the establishment of different copper(I)– and copper(II)–chloride complexes [98]. Therefore, the formation and quantitative distribution of

these complexes have been initially examined and reviewed in Section 2.4.1, as a function of the chloride concentration, to acquire a better understanding of the copper(I) and copper(II) species likely to be present in crevice corrosion solutions. The information provided in Section 2.4.1 can be also used to better comprehend the speciation of copper(I)– and copper(II)–chloride complexes during NAB corrosion (Chapter 4).

2.4.1 Chemical Behaviours and Speciation of Copper(I)–Chloride and Copper(II)–Chloride Complexes

The chemical behaviour of copper(I) and copper(II) ions within different electrolyte types is a subject which attracts considerable attention mainly due to their direct and fundamental involvement in chemistry, biochemistry and biology [99]. Regarding the electrochemical detection of copper–ion, the chemical composition of the supporting electrolyte is of importance since copper(I) is subject to different stabilities when in the presence of different anions and complexing agents. It is well–known that copper(I) is not stable in solution as an aqueous complex ($Cu^{+}_{(aq)}$) since (*i*) it is readily oxidised to copper(II) by molecular oxygen and (*ii*) undergoes disproportionation reaction forming $Cu^{2+}_{(aq)}$ and $Cu^{(0)}$ [100]. However, it has been shown that when the electrolyte contains chlorides, a number of different copper(I)–chloride complexes, which are rapidly formed in solution, significantly enhance the stability of copper(I) [99]. Focusing on chloride containing electrolytes, it has been reported that copper(I) can form several complexes. Suckova *et al.* [101] calculated the stability constants of nineteen copper(I) complexes, up to and including $Cu_5Cl_9^{4-}$. However, the constants were found to be in disagreement with those reported in the literature [102, 103]. At chloride concentrations lower than 5 M, the main cuprous chloride complexes present are the $CuCl_2^-$ and $CuCl_3^{2-}$ [102, 104]; this was established by Sharma and Millero [104] via a spectrophotometric study.

One of the earliest studies which provided a $CuCl_2^-$ formation constant, henceforth named as $K_{CuCl_2^-}$, was carried out in 1918 by Noyes and Chow [105]. The determination of the thermodynamic value for the complexation reaction, as expressed in Equation 2.4.1, was achieved by determining the total dissolved copper by electrolysis and the total chloride concentration by precipitating it with silver(I) nitrate. The chloride concentrations investigated were 1.1650, 0.3165, 0.2156 and 0.0978 M (hydrochloric acid). The formation constant of $CuCl_2^-$ was reported to be 0.0611 at 25 ºC. McConnell and Davidson [106] also determined the formation constants, for the reactions expressed in Equations 2.4.1 and 2.4.2, using spectrophotometry. The ionic strength (*I*) solution was 1.0 M (perchloric acid) with chloride

concentrations ranging from 0.08 M to 0.3 M. The reported values for $K_{CuCl_2^-}$ and $K_{CuCl_3^{2-}}$ were 0.075 and 0.034 mol^{-1} L, in agreement with the previous study [105].

Fritz [102] reviewed the available formation constants of a number of cuprous chloride complexes, thus extrapolating the thermodynamic values at a zero ionic strength. The copper(I) complexes considered were the $CuCl_2^-$, $CuCl_3^{2-}$, $Cu_2Cl_4^{2-}$ and $Cu_3Cl_6^{3-}$ associated with equilibria of Equations 2.4.1–2.4.4 at 25 °C.

$$K_{CuCl_2^-} = \frac{a_{CuCl_2^-}}{a_{Cl^-}} \qquad CuCl_{(s)} + Cl^- \rightarrow CuCl_2^- \qquad 2.4.1$$

$$K_{CuCl_3^{2-}} = \frac{a_{CuCl_3^{2-}}}{a_{Cl^-}^2} \qquad CuCl_{(s)} + 2Cl^- \rightarrow CuCl_3^{2-} \qquad 2.4.2$$

$$K_{Cu_2Cl_4^{2-}} = \frac{a_{Cu_2Cl_4^{2-}}}{a_{Cl^-}^2} \qquad 2CuCl_{(s)} + 2Cl^- \rightarrow Cu_2Cl_4^{2-} \qquad 2.4.3$$

$$K_{Cu_3Cl_6^{3-}} = \frac{a_{Cu_3Cl_6^{3-}}}{a_{Cl^-}^3} \qquad 3CuCl_{(s)} + 3Cl^- \rightarrow Cu_3Cl_6^{3-} \qquad 2.4.4$$

The thermodynamic values reported were 0.0602 for $CuCl_{2(aq)}^-$, 0.0128 mol^{-1} L for $CuCl_3^{2-}$, 8.2 × 10^{-4} mol^{-1} L for $Cu_2Cl_4^{2-}$ and 3.5 × 10^{-5} mol^{-2} L^2 for $Cu_3Cl_6^{3-}$. Later, Fritz [107] reviewed the data related to the formation constants of $CuCl_2^-$, $CuCl_3^{2-}$, $Cu_2Cl_4^{2-}$ and $Cu_3Cl_6^{3-}$ present in the literature and corrected them using activity coefficients, as can be seen in Table 2.4.1.

The formation constant of $CuCl_3^{2-}$ was also determined by Sharma and Millero [108] in chloride containing solutions at a fixed ionic strength of 1 M and pH 1. The method employed for evaluating the thermodynamic data was based on the spectrophotometric determination of the oxidation kinetics of copper(I) to copper(II) by molecular oxygen. Spectrophotometric measurements in oxygen saturated solutions and chloride concentrations ranging from 0.5 M to 6.0 M provided a $K_{CuCl_3^{2-}}$ value of 0.398 mol^{-1} L.

Fritz [102] also derived the formation constants of $CuCl_2^-$ and $CuCl_3^{2-}$ from the $Cu_{(aq)}^+$ concentration instead of $CuCl_{(s)}$. These thermodynamic values, hereafter termed as $\beta_{CuCl_2^-}$ and $\beta_{CuCl_3^{2-}}$, were calculated using a $CuCl_{(s)}$ solubility constant (K_s) of 2.3 × 10^{-7} mol^2 L^{-2}, as shown in Equation 2.4.5. The assessment of the $\beta_{CuCl_2^-}$ and $\beta_{CuCl_3^{2-}}$ were then achieved using

Equations 2.4.6–2.4.7 [102]. The values determined $\beta_{CuCl_2^-}$ and $\beta_{CuCl_3^{2-}}$ were 3.0×10^5 mol^2 L^{-2} and 0.64×10^5 mol^3 L^{-3}, respectively.

$$K_s = \alpha_{Cu^+}\alpha_{Cl^-} \qquad CuCl_{(s)} \rightarrow Cu^+_{(aq)} + Cl^- \qquad 2.4.5$$

$$\beta_{CuCl_2^-} = \frac{K_{CuCl_2^-}}{K_s} = \frac{\alpha_{CuCl_2^-}}{\alpha_{Cu^+}\alpha^2_{Cl^-}} \qquad Cu^+_{(aq)} + 2Cl^- \rightarrow CuCl_2^- \qquad 2.4.6$$

$$\beta_{CuCl_3^{2-}} = \frac{K_{CuCl_3^{2-}}}{K_s} = \frac{\alpha_{CuCl_3^{2-}}}{\alpha_{Cu^+}\alpha^3_{Cl^-}} \qquad Cu^+_{(aq)} + 3Cl^- \rightarrow CuCl_3^{2-} \qquad 2.4.7$$

Wang *et al*. [103] surveyed the stability constants and enthalpies of cuprous and cupric ions chlorides complexes. By using a weighted linear regression they extrapolated from the available data the formation constants for $CuCl_2^-$ and $CuCl_3^{2-}$ at infinite dilution, as can be seen in Equations 2.4.8 and 2.4.9. The reported $\beta^\circ_{CuCl_2^-}$ and $\beta^\circ_{CuCl_3^{2-}}$ (infinite dilution) values of 4.85×10^5 mol^{-2} L^2 and 1.05×10^5 mol^{-3} L^3, by using a K_s equal to 1.51×10^{-7} mol^2 L^{-2}.

$$\log K_{CuCl_2^-} = \log K^\circ_{CuCl_2^-} - 0.06 \cdot I_m = -1.14 - 0.06 \cdot I_m \qquad 2.4.8$$

$$\log K_{CuCl_3^{2-}} = \log K^\circ_{CuCl_3^{2-}} - 0.27 \cdot I_m = -1.89 - 0.27 \cdot I_m \qquad 2.4.9$$

where $K^\circ_{CuCl^+}$ and $K^\circ_{CuCl_2}$ are the formation constants at infinite dilution and I_m the molality of the solution.

Since the ionic strengths used in the Result and Discussion Chapters are 0.6 M and 3.0 M (see Chapters 4 and 7), the K and β were re–determined taking into account the used I_m and Equations 2.48 and 2.49, see Table 2.4.1. Figure 2.4.1 shows the speciation of dissolved copper(I) complexes considering the thermodynamic constants provided by Wang *et al.* [103] at I_m of 0.6 M, since these are more accurately treated than those previously determined and reviewed [102, 107]. As can be seen by the distribution of the dissolved species $CuCl_2^-$ and $CuCl_3^{2-}$ (denoted as $\alpha_{CuCl_2^-} = \frac{CuCl_2^-}{Cu(I)_{total}}$ and $\alpha_{CuCl_3^{2-}} = \frac{CuCl_3^{2-}}{Cu(I)_{total}}$) an increase of the chloride concentration leads to a decrease of the $CuCl_2^-$ complex and to a simultaneous increase of the $CuCl_3^{2-}$ complex.

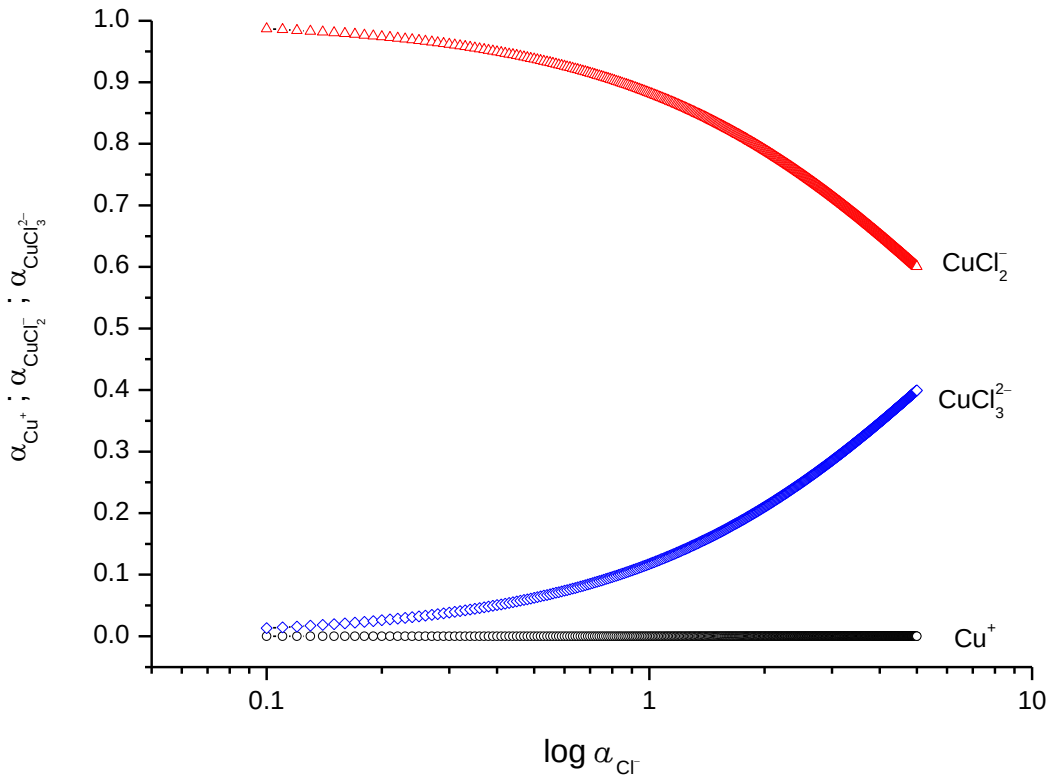

Figure 2.4.1. Speciation of dissolved copper(I) complexes as a function of the chloride concentration at a ionic strength of 0.6 M.

Other polynuclear complexes, such as $Cu_2Cl_4^{2-}$ and $Cu_3Cl_6^{3-}$, were not considered since Sharma and Millero [108] spectrophotometrically proved their absence for chloride concentrations lower than 3 M. Table 2.4.1 lists all the thermodynamic values ($K_{CuCl_2^-}$, $K_{CuCl_3^{2-}}$, $\beta_{CuCl_2^-}$ and $\beta_{CuCl_3^{2-}}$) reported so far in the literature for the copper(I)–chloride complexes and the I_m at which they have been determined.

Regarding the stability of cupric chloride complexes, it has been shown that in chloride containing solutions four copper(II) species such as $Cu^{2+}_{(aq)}$, $CuCl^{+}_{(aq)}$, $CuCl_{2(aq)}$, $CuCl^{-}_{3(aq)}$ and $CuCl^{2-}_{4(aq)}$ can be present [109, 110]. The presence of the chloride complexes becomes significant especially at high chloride contents (higher than 1 M) while at low chloride concentrations it has been shown that the Cu^{2+} aquo–complex is the predominant species. The formation constants for the $CuCl^{+}_{(aq)}$ and $CuCl_{2(aq)}$ complexes (see Equations 2.4.10 and 2.4.11) were determined using spectrophotometry by McConnell and Davidson [106], where the ionic strength was maintained at 1.0 by additions of $HClO_4$. They reported values of β_{CuCl^+} and β_{CuCl_2} of 1.20 mol^{-1} L and 0.21 mol^{-2} L^2, respectively.

Table 2.4.1. Literature values for $CuCl_2^-$ and $CuCl_3^{2-}$. I_m represents the ionic strength, $K_{CuCl_2^-}$ and $K_{CuCl_3^{2-}}$ are the formation constants from CuCl(s) whereas $\beta_{CuCl_2^-}$ and $\beta_{CuCl_3^{2-}}$ are the formation constants determined from $Cu^+_{(aq)}$ (using the solubility constant of $CuCl_{(s)}$ (K_s) = 1.5×10^{-7} mol^2 L^{-2}).

Ref.	I_m / mol Kg^{-1}	$K_{CuCl_2^-}$	$K_{CuCl_3^{2-}}$ / mol^{-1} L	$\beta_{CuCl_2^-}$ / mol^{-2} L^2	$\beta_{CuCl_3^{2-}}$ / mol^{-3} L^3
[105]	–	0.0661	–	–	–
[106]	1.0	0.075	0.034	–	–
[102]	0.0	0.0602	0.0128	3.00×10^5	0.64×10^5
[107]	2.0	0.052	0.040	10.00×10^5	9.70×10^5
[108]	0.5	–	0.398	–	–
[103]	0.0	0.0725	0.0158	4.85×10^5	1.05×10^5
[103]	0.6	0.0667	0.0089	4.44×10^5	0.59×10^5
[103]	3.0	0.0479	0.0020	3.13×10^5	0.14×10^5

Libus [111] spectrophotometrically determined the stability constant of $CuCl^+_{(aq)}$ in a 0.005 M $HClO_4$ solution with a low chloride concentration (0.01 M) to reduce the formation of further copper(I)–chloride complexes, such as $CuCl_{2(aq)}$ and $CuCl^-_{3(aq)}$. The ionic strength was kept constant at 1.2 M, 4.0 M and 7.7 M. The $CuCl^+_{(aq)}$ formation constants ($\beta_{CuCl_2^-}$), associated with Equation 2.4.10, were determined to slightly increase with the ionic strength: 0.30 mol^{-1} L, 0.40 mol^{-1} L and 0.68 mol^{-1} L, for 1.2 M, 4.0 M and 7.2 M of I_m, respectively.

$$\beta_{CuCl^+} = \frac{\alpha_{CuCl^+}}{\alpha_{Cu^{2+}}\alpha_{Cl^-}} \qquad Cu^{2+}_{(aq)} + Cl^- \rightarrow CuCl^+_{(aq)} \qquad 2.4.10$$

$$\beta_{CuCl_2} = \frac{\alpha_{CuCl_2}}{\alpha_{Cu^{2+}}\alpha^2_{Cl^-}} \qquad Cu^{2+}_{(aq)} + 2Cl^- \rightarrow CuCl_{2(aq)} \qquad 2.4.11$$

$$\beta_{CuCl_3^-} = \frac{\alpha_{CuCl_3^-}}{\alpha_{Cu^{2+}}\alpha^3_{Cl^-}} \qquad Cu^{2+}_{(aq)} + 3Cl^- \rightarrow CuCl^-_{3(aq)} \qquad 2.4.12$$

$$\beta_{CuCl_3^-} = \frac{a_{CuCl_3^{2-}}}{a_{Cu^{2+}} a_{Cl^-}^4} \qquad Cu^{2+}_{(aq)} + 4Cl^- \rightarrow CuCl^{2-}_{4(aq)} \qquad 2.4.13$$

Carlsson and Wettermark [112] studied the chemical equilibria of the copper(I)–chloride and copper(II)–chloride systems using UV–spectrophotometry, with a 1.0 M ionic strength solution at pH 1 and chloride concentration ranging from 0.0 M to 0.25 M. From the absorption spectra the authors determined values of β_{CuCl^+} and β_{CuCl_2} of 2.19 mol^{-1} L and 1.51 mol^{-2} L^2, respectively.

Ashurst and Hancock [113] characterised the inner– and the outer–sphere copper(II)–chloride complexes by means of spectrophotometry with chloride concentrations ranging from 0.0 M to 4.8 M, at a fixed ionic strength of 6.58 M and a pH of 1.

Table 2.4.2. Literature values for the formation constants of $CuCl^+$, $CuCl_2$ and $CuCl_3^-$ and $CuCl_4^{2-}$ from $Cu^{2+}_{(aq)}$. I_m is the ionic strength.

Ref.	I_m / mol kg^{-1}	β_{CuCl^+} / mol^{-1} L	β_{CuCl_2} / mol^{-2} L^2	$\beta_{CuCl_3^-}$ / mol^{-3} L^3	$\beta_{CuCl_4^{2-}}$ / mol^{-4} L^4
[106]	1.0	1.20	0.21	–	–
[111]	1.2	0.30	–	–	–
[111]	4.0	0.40	–	–	–
[111]	7.1	0.68	–	–	–
[112]	1.0	2.19	1.51	–	–
[113]	6.58	1.43	0.53	0.011	0.003
[114]	1.0	0.70	–	–	–
[103]	0	4.36	3.98	–	–
[103]	0.6	2.84	2.74	–	–
[103]	3.0	0.51	0.62	–	–

For the evaluation of the formation constant β_{CuCl^+} the chloride level was maintained below 0.03 M in order to reduce the formation of $CuCl_{2(aq)}$, $CuCl^-_{3(aq)}$ and $CuCl^{2-}_{4(aq)}$, whereas for the study of $CuCl_{2(aq)}$, $CuCl^-_{3(aq)}$ and $CuCl^{2-}_{4(aq)}$ the chloride concentration ranges were 1.2 M – 2.2 M, 2.5 – 4.0 M and 5.0 – 6.58 M, respectively. The β_{CuCl^+}, β_{CuCl_2}, $\beta_{CuCl_3^-}$ and $\beta_{CuCl_4^{2-}}$

were assessed to be 1.43 mol^{-1} L, 0.53 mol^{-2} L^2, 0.011 mol^{-3} L^3 and 0.003 mol^{-4} L^4. Byrne *et al*. [114] also evaluated, via spectrophotometry, the formation constant of the complex $CuCl^{+}_{(aq)}$ from aqueous copper(II) ion. The electrolyte considered was a 1.0 M $HClO_4$. The authors indicated a value of 0.70 mol^{-2} L^2.

Wang *et al*. [103] revised the formation constants of copper(II)–chloride. The stability constants extrapolated to infinite dilution for $CuCl^{+}_{(aq)}$ and $CuCl_{2(aq)}$ were reported to be 0.64 mol^{-1} L and 0.60 mol^{-2} L^2. Furthermore, the authors also reported the weighted linear regression of the $CuCl^{+}_{(aq)}$ and $CuCl_{2(aq)}$ formation constants as function of I_m, see Equations 2.4.14 and 2.4.15.

$$\log\beta_{CuCl^{+}} = \log\beta^{\circ}_{CuCl^{+}} - 0.31\cdot I_m = 0.64 - 0.31\cdot I_m \qquad 2.4.14$$

$$\log\beta_{CuCl_2} = \log\beta^{\circ}_{CuCl_2} - 0.27\cdot I_m = 0.60 - 0.27\cdot I_m \qquad 2.4.15$$

where $\beta^{\circ}_{CuCl^{+}}$ and $\beta^{\circ}_{CuCl_2}$ are the formation constants at infinite dilution and. The K and β were then recalculated taking into account the used I_m at 0.6 M and 3.0 M and Equations 2.4.14 and 2.4.15. Table 2.4.2 lists all the thermodynamic values reported in this literature section for the copper(II)–chloride, whereas Figure 2.4.2 shows the speciation of copper(II) as a function of the chloride concentration, obtained using $\beta_{CuCl^{+}}$ and β_{CuCl_2} at I_m of 0.6 M [103] and $CuCl^{-}_{3(aq)}$ and $CuCl^{2-}_{4(aq)}$ from [113] ($\alpha_{Cu^{2+}}$, $\alpha_{CuCl^{+}}$, α_{CuCl_2}, $\alpha_{CuCl_3^{-}}$ and $\alpha_{CuCl_4^{2-}}$ are defined as $\frac{CuCl_n^{-(n+2)}}{Cu(II)_{total}}$).

From Figure 2.4.2, it appears that $Cu^{2+}_{(aq)}$ predominates over the other copper(II)–chloride complexes up to a concentration of 1 M of chloride, whilst at higher chloride concentrations the $CuCl^{+}_{(aq)}$ and $CuCl_{2(aq)}$ species became the most important. The other copper(II)–chloride complexes, $CuCl^{-}_{3(aq)}$ and $CuCl^{2-}_{4(aq)}$, are present in negligible concentrations even at the highest chloride content (3M) explored. In conclusion, from the surveyed literature it appears that chloride significantly affects the formation of both copper(I) and copper(II) species, having speciation of different chloride complexes. This is particularly true for the copper(I) species, where copper(I)–chloride complexes have been proven to greatly enhance its stability.

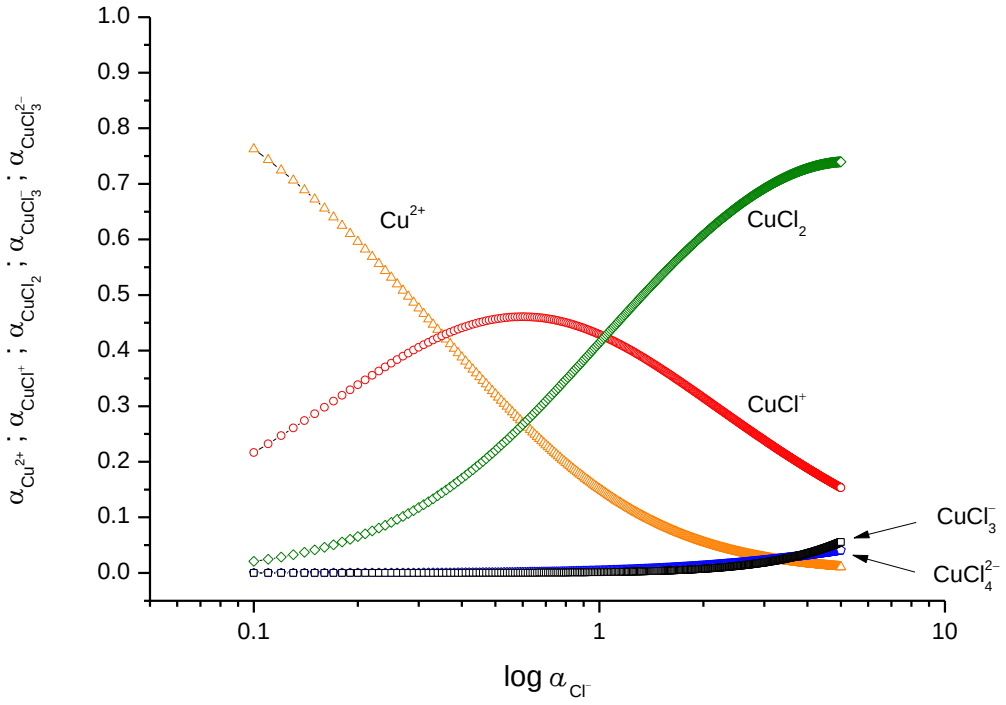

Figure 2.4.2. Speciation of dissolved copper(II) complexes as a function of the chloride concentration at a ionic strength of 0.6 M.

2.4.2 Copper Detection on Boron–Doped Diamond Electrodes

Nakabayashi *et al.* [115] performed the detection of copper(II) in a sulphate solution using a BDD electrode (ca. 5000 ppm of doping level and with a hydrogen–terminated surface) and compared the response with a platinum electrode. Preliminary CV tests, carried out using the $IrCl_6^{3-/2-}$ redox couple in 0.1 M KCl, indicated a metal–like behaviour of the carbon–based substrate since it promoted a reversible electron transfer, similarly to that of platinum. The copper(II) behaviour was then investigated in a 0.1 M Na_2SO_4 electrolyte, on both platinum and doped diamond electrodes at 20 mV s^{-1}. Significant diversities were reported between the two different substrates; indeed, while the platinum displayed a reduction / oxidation of Cu^{2+} / Cu system with an anodic / cathodic charge ratio (Q_A / Q_C) of 1, the BDD electrode response showed an intense reduction peak and a small, broad oxidation signal determined at more anodic values than that recorded on platinum electrode. These differences were explained in terms of metallic–copper cluster formation at the BDD electrode and the Cu^+ disproportionation mechanism. Specifically, the low anodic current at the BDD electrode indicated that only a trace of the reduced copper remained on the electrode surface. This insight was further confirmed by Mie scattering experiments [115], which indicated the formation of weakly

adsorbed metallic–copper clusters at the electrode surface, see Equation 2.4.16, that diffused in the bulk solution undergoing disproportionation, see Equations 2.4.17 – 2.4.19.

$$nCu^{2+}_{(aq)} + 2ne^- \rightarrow n[Cu^{(0)}]_{ads} \xrightarrow{ClusterForm.} [Cu^{(0)}_n]_{ads} \quad 2.4.16$$

$$[Cu^{(0)}_n]_{ads} \xrightarrow{Diffusion} [Cu^{(0)}_n] \quad 2.4.17$$

$$[Cu^{(0)}_n] \rightarrow nCu^{+}_{(aq)} + ne^- \quad 2.4.18$$

$$2nCu^{+}_{(aq)} \rightarrow nCu^{2+}_{(aq)} + nCu^{(0)} \quad 2.4.19$$

Tamilmani *et al.* [116] studied the recovery of copper(II) from waste solutions performing electrolysis on BDD electrode. From the preliminary CV performed in a 0.05 M sulphate solution, see Figure 2.4.3, the Cu^{2+} behaviour significantly differed from that by Nakabayashi *et al.*, where the electrode response of copper(II) was featured by a bi–electronic exchange ($Cu^{2+}_{(aq)}$ / $Cu^{+}_{(aq)}$ / $Cu^{(0)}$), as shown in Equations 2.4.20 and 2.4.21.

$$Cu^{2+}_{(aq)} + e^- \rightarrow Cu^{+}_{(aq)} \quad 2.4.20$$

$$Cu^{+}_{(aq)} + e^- \rightarrow Cu^{(0)}_{(ads)} \quad 2.4.21$$

Furthermore, the two overlapped redox peaks, attributed to $Cu^{2+}_{(aq)}$, $Cu^{+}_{(aq)}$, $Cu^{(0)}$ species, was indicated as direct evidence of the low stability of $Cu^{+}_{(aq)}$.

Zak *et al.* [117] studied the copper deposition / stripping processes on a BDD electrode using CV and different electrolytes, *i.e.*, 0.05 M H_2SO_4, 0.1 M HNO_3 and 0.05 M H_3PO_4. Cyclic voltammograms, performed at 50 mV s^{-1}, indicated a process undergoing an electron transfer via the Cu^{2+} / Cu^0 species, rather than Cu^{2+} / Cu^+ / Cu^0 as reported by Tamilani *et al.*.

The literature cited so far [110, 115, 117] has referred to copper investigations on a BDD electrode in the sulphate medium. Regarding the copper detection in chloride electrolyte on diamond–like electrode, Yoo *et al.* [118] quantitatively investigated the copper deposition and stripping on a tetrahedral amorphous carbon incorporating nitrogen (taC:N) electrodes in a chloride medium. The copper–ion response proceeded via a copper(I) intermediate, due to its stability in the chloride solution.

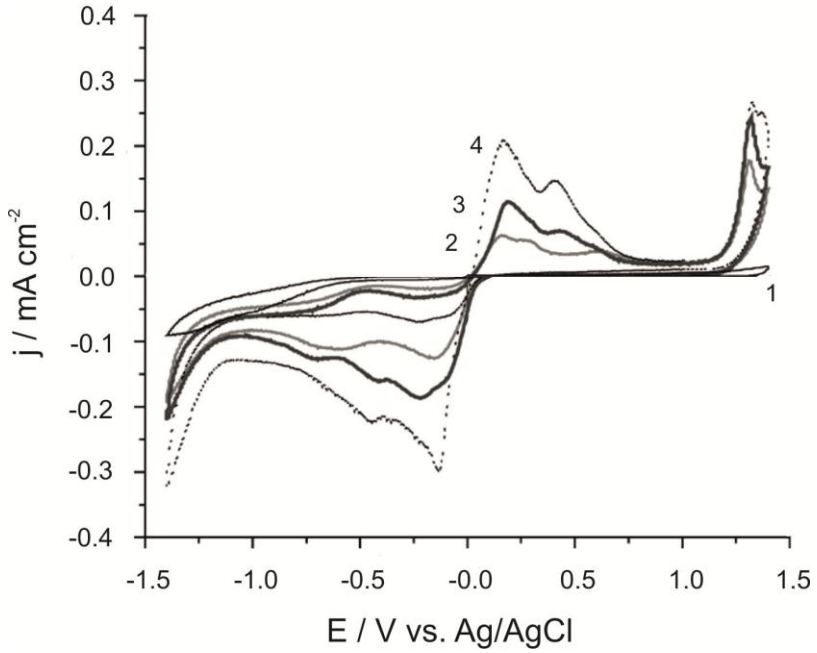

Figure 2.4.3. Cyclic voltammograms on a BDD electrode in: (1) 0.05 M K_2SO_4 pH 4, (2) 0.05 M K_2SO_4 pH 4 + 0.4 M Cu^{2+}, (3) 0.05 M K_2SO_4 pH 6 + 0.8 M Cu^{2+} and (4) 0.05 M K_2SO_4 pH 6 + 0.8 M Cu^{2+} [116].

Concerning the electrochemical behaviour of copper–ion at platinum electrodes, several studies have been addressed the effect of the anion on the electron transfer process [119-121]. In addition to significantly influencing the stability of the species undergoing the electron transfer process (Cu^{2+}, Cu^{+}, Cu^{0}), it has also been claimed that some anions, such as Cl^- and HSO_4^-, have the ability to co–adsorb and interact with copper at the platinum electrode surface, thus enhancing the metal deposition. This particular behaviour, known as underpotential deposition (UPD), gives rise to a bulk deposition at a more anodic potential than that predicted by the Nernst equation [120]. Copper UPD on platinum was studied by White and Abruña *et al.* [121] using CV in the presence of different active anions, such as Cl^-, Br^-, I^- and S^{2-}. They reported an increase of the UPD following the chemical series $Cl^- > Br^- > I^- > S^{2-}$, thus indicating the establishment of more favourable interactions between platinum / copper / chloride than platinum / copper / other anions.

Regarding UPD on doped diamond electrodes, to date, little research has been reported in the literature, most likely due to the poor adsorption phenomena on the inert BDD surface. Only one work has been dedicated to study the UPD of copper on a BDD electrode (boron–doping level ≈ 2600 ppm) [122], where the presence of a "pre–wave" was associated with the bulk copper deposition, attributed to the metal UPD occurring on the crystalline defects present on

diamond electrode surface. It was also highlighted that the observed deposition regarded only 1% of the bulk copper deposited, thus underlining the weakness of the adsorption phenomenon.

2.4.3 Nickel Detection on Boron–Doped Diamond Electrodes

Nickel–ion quantification has been carried out using a wide number of different analytical techniques, such as ion chromatography [123], absorption spectrometry [124], capillary electrophoresis [125] and electrochemical techniques [126-130]. Of these, electrochemical techniques offer sensitive, inexpensive and rapid ways of trace metal determination and the possibility of being used in miniaturised and portable ion detecting devices. The most common protocol for the electrochemical detection of nickel–ions is based on adsorptive stripping voltammetry (AdSV), which relies (*i*) on the initial formation of a Ni(II)–complex using a suitable chelating agent, followed by (*ii*) its adsorption and (*iii*) detection at the electrode surface. The use of a chelating agent in these AdSV methods is indispensable since the redox system Ni/ Ni(II) displays an irreversible electrochemical behaviour [129], therefore not employable for the actual metal ion detection. Due to its high selectivity and ability of forming a stable complex with Ni(II) [131] dimethylglyoxime (DMG) is commonly used as a chelating agent for electrochemical detection of trace nickel–ions [126, 131-140]. The extensive use of DMG in electroanalysis began with Vinogradova *et al.* [141], who reported that DMG enhances the Ni / Ni(II) signal, transforming if from a broad and weak peak into a more intense and sharp signal. Besides DMG, a number of other different chelating agents have also been explored [142-145]; 2–aminocyclopentene–1–dithiocarboxylate [144], 7–iodo–8–hydroxyquinoline–5–sulfonic [144], 8–hydroxyquinoline–5–sulfonic acid [144], methyl–8–hydroxyquinoline [144], morpholine–4–carbodithioates [143], hydroxynaphthol blue [142], and N,N'–bis(salicylaldehydo)–4–carboxyphenylenediamine [145] are all examples of alternative ligands reported to be successfully used in the published research literature.

In addition to AdSV, nickel–ion detection has also been achieved using a cathodic stripping voltammetry (CSV). This procedure involves the redox couple Ni(III) / Ni(II) hydroxide and avoids the introduction of the essential chelating agent into the sample solution. CSV for nickel–ion determination, has been performed on a bare glassy carbon electrode [127] and on a bare boron–doped diamond electrode (BDD) [128], (*i*) initially depositing metallic nickel on the electrode surface in a strongly alkaline solution (pre–concentration step), (*ii*) then oxidising it to Ni(III) hydroxide (transformation step) and (*iii*) finally reducing the electro–formed Ni(III) hydroxide to Ni(II) hydroxide by a sensitive voltammetry technique. Due to the instability of the nickel hydroxides in acidic and neutral pH solutions [100], the procedure strictly required an alkaline environment, a 0.1 M NaOH / 0.1 M NH_4NO_3 solution [127, 128], for the transformation Ni / Ni(III) / Ni(II).

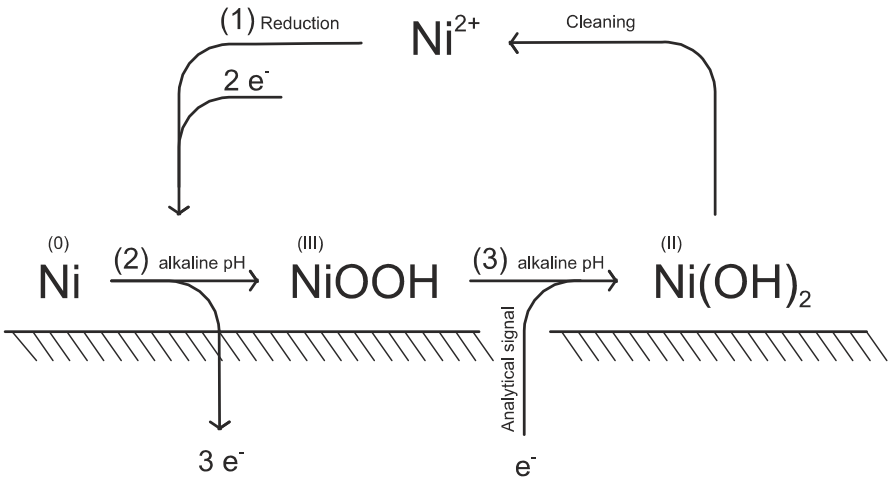

Figure 2.4.4. Schematic of the cathodic stripping voltammetric method for nickel detection: (1) reduction of Ni(II) to Ni(0), (2) oxidation of Ni(0) to Ni(III) in alkaline solution and (3) final reduction of Ni(III) to Ni(II) [128].

Furthermore, the cleaning of the electrode surface immediately after the formation of the nickel hydroxide layer in alkaline environment has been reported to be a problem whenever the recovery of the initial electrode surface condition was required. Mechanical polishing [127], ultrasonic cleaning [127] and electrochemical acidic cleaning (0.1 M H_2SO_4) [128] have been used to re–generate the electrode surface. Figure 2.4.4 shows the chemical pathways for the nickel–ion detection and the electrode surface cleaning reported by Davis *et al*. [127] and Zhang *et al*. [128]. For *in situ* corrosion monitoring, and in particular crevice corrosion, the introduction of a chelating agent in the monitoring environments, as well as the change of the solution pH, are not feasible in most cases since this will significantly modify the operating system environments, possibly adversely affecting performance [146]. Indeed, it has been demonstrated that when crevice corrosion process initiates the pH of the environment rapidly decreases typically achieving ranging between pH 3 and 4 [6]. Therefore, the severe conditions generally employed for nickel-ion detection protocols, *i.e*., alkaline environment [127, 128] and presence of chelating agents [126, 130], often do not adapt well within crevice corrosion solutions.

2.4.4 Summary

The electron transfer occurring for the copper(II) / copper(0) redox has been shown to be significantly influenced by the presence of the electrolyte anion. In the presence of chloride the electron transfer occurring generally proceeds via the formation of copper(I)–chloride complexes, thus having a double–step electron transfer process, related to the copper(II)–

copper(I)–copper(0) species. Conversely, in the presence of other anions, such as sulphate, nitrate, perchlorate, the electron transfer promoted by the electrode has been reported to involve the copper(II) and copper(0) species, due to the low stability displayed by the copper(I) aquo complex. Consequently, the speciation of copper(I)– and copper(II)–complexes has been investigated considering the most significant thermodynamic studies reported in the literature. Due to the high chloride concentration generally reported within crevice corrosion solutions [7], the electrochemical detection of copper–ion can be potentially assessed by studying both the copper(II) / copper(I) and copper(I) / copper(0) redox systems.

Regarding the nickel–ion electrochemical detection, the most common protocol reported relies on the formation and detection of a nickel(II) complex, by using a chelating agent. The use of the complexing agent in the electron transfer process has been reported to be essential, since the redox couple nickel(II) / nickel(0) displays an irreversible electrochemical behaviour not employable for assessing the nickel(II) concentration. In addition to the electrochemical protocol which requires the presence of a complexing agent, another electrochemical method has been developed for evaluating the nickel(II) concentration. This procedure is based on the study of the electron transfer occurring between NiOOH and $Ni(OH)_2$ in alkaline solutions (ca. pH 14). Both the techniques for the evaluation of the nickel–ion concentration can be difficult to employ in crevice corrosion solutions due to significant modifications of the operating environmental conditions required.

3. Materials and Methods

This Chapter reports the material characteristics (for NAB and BDD electrodes) and details the techniques employed in this study, *i.e.*, electrochemical method, atomic force microscopy, scanning electron microscopy, X–ray photoelectron spectroscopy and capillary electrophoresis analysis.

3.1 Materials

3.1.1 Nickel–Aluminium Bronze

The NAB ($CuAl_9Ni_5Fe_4Mn$) ustilised conformed to British naval specification NES 747 Part 2, annealed at 675°C for 2–6 h and cooled in air. Before testing, the specimens were subjected to mechanical surface polishing (to a surface roughness (R_a) of ca. 200 nm, determined with a Taylor Hobson Talysurf 120–L Profilometer) and then cleaned with acetone and rinsed with distilled water. The specimen electrodes were either discs (radius of 0.7 cm and thickness of 0.4 cm) or rectangular–shaped electrodes (3.5 cm × 1.5 cm × 0.5 cm).

3.1.2 Boron–Doped Diamond Electrodes

BDD electrodes were electrochemically and chemically investigated in the as received state, supplied by Diamond Detectors Ltd (Poole, UK). Each BDD electrode had a boron–doping level of 10^{20} atom cm^{-3} (corresponding to 2000 ppm of boron) and an oxygen–terminated surface. The electrode geometry was 0.5 cm in diameter, a thickness of ca. 0.05 cm, and a R_a of less than 10 nm. The BDD electrode was mounted within a polypropylene (internal diameter of 0.6 cm) and sealed using epoxy resin. The electrode was electrically connected via a brass wire attached to the reverse surface. Prior to performing electrochemical testing, the BDD electrode was electrochemically cleaned in a 0.5 M sulphuric acid solution, cycling the potential from –0.60 V to +1.25 V *vs*. Ag/AgCl until a reproducible electrode response was obtained.

3.1.3 Boron–Doped Diamond Microelectrode Array

The BDD microelectrode array, manufactured by Diamond Detectors Ltd (Poole, UK), consisted of five BDD disc electrodes with diameter of 500 μm and thickness of 500 μm embedded into a non–conductive intrinsic diamond–like carbon (DLC) disc with diameter of 1.0 cm and same thickness as BDD disc. Regarding the disposition of the microelectrodes, one was located in the centre of the DLC disc, and other four were arranged with equal separation

between each other around the central one along the circle with a radius of 2.5 mm, see Figure 3.1. The BDD microelectrode array was used for crevice corrosion monitoring.

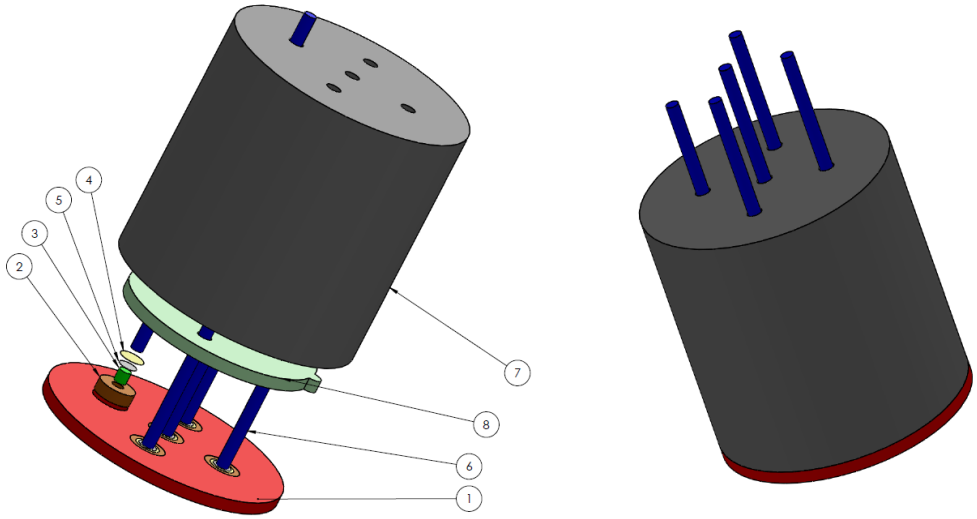

Figure 3.1.1. Fabrication materials and assembly details for the five boron–doped diamond electrode array (scale: BDD disc electrode diameter = 500 μm). (1) Diamond blank front–plate, (2) infill, (3) Boron–doped diamond insert –electrode, (4) metallisation, (5) silver epoxy, (6) connecting pin, (7) encapsulation and (8) silicon support.

3.2 Electrochemical Setup

3.2.1 Electrochemical Setup for Nickel–Aluminium Bronze Corrosion Testing

Investigation of the NAB electrochemical properties were achieved using NAB discs. The discs were inserted into a Teflon holder, where an area of 1.13 cm^2 was exposed to the test solution.

3.2.2 Electrochemical Setup for Nickel–Aluminium Bronze Crevice Corrosion Testing

The NAB crevice corrosion monitoring was achieved using the BDD microelectrode array. The array was positioned within the crevice former and then assembled with the NAB specimen as shown in Figure 3.2.1a–b. The NAB specimens used for the crevice corrosion tests had rectangular shape and were directly placed and tightened at the crevice former, thus forming an artificial crevice. As can be seen in Figure 3.2.1, a thickness of ca. 100 μm was maintained

between the microelectrode and the NAB surfaces. The crevice corrosion setup was then immersed in a 0.6 M NaCl solution, allowing the crevice to be completely filled by the electrolyte.

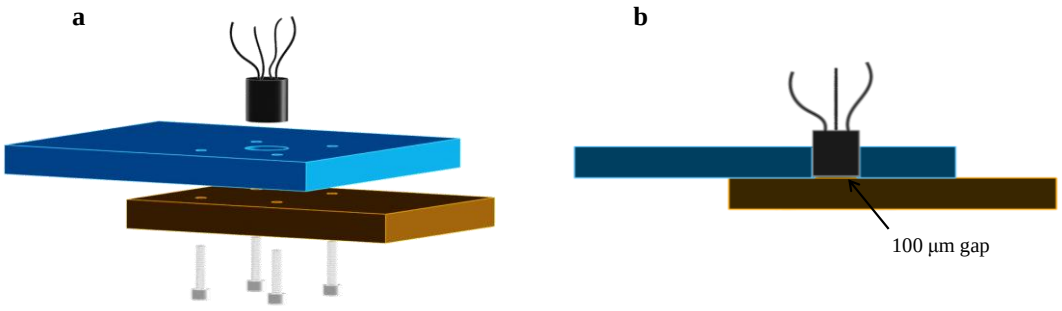

Figure 3.2.1. (a) Schematic of the crevice corrosion setup and of (b) the crevice former with the hosted BDD microelectrode array.

3.3 Methods

3.3.1 Electrochemical Testing

Electrochemical testing was performed at room temperature (ca. 22 °C) using a Gamry Reference 600 potentiostat (Gamry Instruments, USA) and a three–electrode, single–compartment glass cell. The BDD and the NAB electrodes were used as the working electrodes, whereas a large area graphite rod and a 3.5 M KCl Ag/AgCl electrode served as the counter and the reference electrodes, respectively. All potentials reported in this work are with respect to the 3.5 M KCl Ag/AgCl reference electrode. All the solutions were prepared with deionised water (≥ 18 MΩ cm) using analytical grade chemicals. The supporting electrolyte generally used in this study was a 0.6 M NaCl solution. However, when the analysis required a stable pH environment, phosphate buffered solutions were also used (see Chapters 4 and 7). The NaH_2PO_4 and Na_2HPO_4 concentration solutions generally did not exceed 20 mM.

The techniques employed in the current study were:

- Cyclic voltammetry. This is a potentiodynamic reversal technique which yields information on the *i*–*E* dependence. It is generally performed scanning the working electrode potential back and forth, at a certain scan rate and potential step size, and measuring the current response [147]. CVs were carried out at 10 mV s^{-1} with a step size of 1 mV as the default scanning condition, but also at 25, 50, 100, 200 and 300 mV s^{-1} in order to study the effect of the scan rate on the electrochemical response. A number of

CV scans were performed for each investigation until reproducible results were observed and it is the data from the last cyclic scan that is reported here.

- Differential pulse voltammetry. DPV belongs to the pulse voltammetry methods which have been historically developed to suppress the charging current flowing in an electrochemical system [148]. Therefore, DPV provides better sensitivity with respect to the CV technique due to removal of the capacitive current [149]. DPV consists of voltage pulses superimposed on the potential linear sweep or stair steps. The current is measured immediately before each pulse application and at the end of the pulse. The current difference between the recorded values is plotted as a function of potential [150]. DPVs were carried out at 10 mV s^{-1} with a step potential of 2 mV, a potential pulse size of 25 mV, an interval time of 0.2 s and a pulse time of 0.1 s. This technique was particularly useful in Chapters 6 and 9. DPVs reported in Chapter 7 were also carried out to initially pre–concentrating the metal–ion on the electrode surface, –1.5 V *vs*. Ag/AgCl for 30 s, (pre–concentration step) and then scanning the electrode potential from –1.1 V to 1.3 V *vs*. Ag/AgCl.
- Potentiodynamic polarisation. Similar to CV, the PP tests were performed scanning the working potential and measuring the *i*–*E* dependence at a certain scan rate and potential step size. PPs are generally achieved sweeping the potential in one direction, rather than back and forth as conversely carried out for CVs [147]. PPs reported in this work were achieved using the following conditions:
    - (*i*) scan rate of 0.10 mV s^{-1} and a step potential size of 0.15 mV in a potential interval of ±10 mV with respect to the open circuit potential (OCP). These particular conditions were applied for the so–called "quasi–steady potentiodynamic polarisations" (see Chapters 5 and 8);
    - (*ii*) scan rate of 1.00 mV s^{-1} and a step potential of 0.50 mV from the potential intervals ranging from +0.5 V to 2.8 V *vs*. Ag/AgCl and from –0.5 to –1.9 V *vs.* Ag/AgCl (see Chapter 5);
    - (*iii*) scan rate of 0.15 mV s^{-1} with a step potential of 0.50 mV, scanning the potential from –0.200 V up to +0.500 V *vs.* OCP (see Chapter 4).
- Electrochemical impedance spectroscopy. EIS is a powerful electrochemical tool which provides insights into the physical and electrochemical properties of a system by applying a potential perturbation (generally ranging between 5 mV to 10 mV) and recording the impedance response. Since these measurements are achieved at different frequencies, this technique has been named "spectroscopy". Unless otherwise stated, the EIS tests were carried out by applying a potential perturbation of ±5 mV [151] at the OCP over the frequency range of 10^5 Hz to 0.1 Hz with ten frequency points per decade.

- Chronoamperometry (CA). CA is an electrochemical technique which is generally carried applying a stable electrode potential and recording the current [152]. In this study, CAs were employed for the determination of the BDD electrode area (Chapter 4).

3.3.2 Morphological and Chemical Characterisation

The morphological characterisation was carried out using an atomic force microscopy (AFM) MAC III Agilent 5500 in contact mode equipped with a standard silica nitrite tip (Nano World from Windsor Scientific) with a nominal spring constant of 0.32 N m^{-1} and nominal tip radius < 10 nm.

The chemical characterisation of the substrates was assessed using either an X–ray photoelectron spectroscopy (accessing the instrument at Cardiff University) or a Scanning electron microscopy–energy dispersive X–ray spectroscopy (SEM–EDS). The XPS employed was a Kratos Axis Ultra–DLD equipped with a monochromatic dual Al–Mg X–ray source and magnetic lens, which allowed the system to obtain high collection efficiency and high spatial resolution for the test recorded at low angle collections. The spectrometer was equipped with a delay–line detector (DDL). Four different types of spectra were recorded: normal angle (0°), plus 45°, 65° and 75° degrees, in order to follow the chemical average composition of the probed surface layers. The fitting procedures have been achieved after a linear background subtraction and the analytical functions used were linear combinations of Voigt functions, each representing the distinct chemical forms that contribute to the peak shape. The SEM–EDS system used was a scanning electron microscopy JSM 6500F equipped with an energy X–ray dispersive spectrometer Oxford Inca 300.

3.3.3 Capillary Electrophoresis

Within this study, capillary electrophoresis (CE) was used to validate the metal–ion concentrations estimated via electrochemical methods and was particularly employed in Chapters 7 and 9.

CE is a powerful analytical technique that can separate different ionic species within a solution filled capillary under an applied electric field in the range 100–300 V cm^{-1}. It only requires a very small sample volume (several nanolitres), but offers high separation efficiency, high separation selectivity and sensitivity, fast analysis and potentially simple sample preparation methodologies. This technique relies on the different electrophoretic mobilities that generally characterise different metal ions. The separation in capillary electrophoresis is usually performed within a fused silica capillary using a carrier electrolyte (also known as running

buffer solution with a slightly acidic pH), which contains a chelating agent (in the current work 2,6–pyridinecarboxylic, PDCA). The pH of the buffer solution was 4.0 since it represented the best compromise between the ionisability of the PDCA (pK_{a1} = 2.16; pK_{a2} = 6.92) and the metal ion hydrolysis [7]. Indeed, at pH 4 the PDCA is deprotonated (thus, acting as a chelating agent) and the eventual hydrolysis of the metal ions is significantly depressed. In addition to PDCA, the buffer solution also contained a cationic surfactant (cetyltrimethylammonium hydroxide, CTAH) which reversed the direction of the electroosmotic flow, hence allowing the detection of all ions in a single run. The buffer solution was prepared adding 10 mM of PDCA and 2.5 mM of CTAH and adjusting the pH with HCl or NaOH. Before running the CE analysis, all the sampled crevice–corrosion solutions containing the buffer electrolyte were rested for 12 h (overnight), allowing the formation of the metal ion–PDCA complexes.

The system employed was a Prince Technologies PrinCE–560 capillary electrophoresis instrument with a TraceDec contactless conductivity detector with a 100 cm fused silica capillary (93 cm effective length and a 50 μm internal diameter).

The limit of detections (LOD) of the metal ions likely to be present within the crevice corrosion solution (Cu^{2+}, Ni^{2+}, Fe^{3+} and Al^{3+}) were determined in 0.6 M NaCl in either the presence or absence of 0.01 M BTAH. The LODs were estimated by linear regression, determining the confidence interval with Equation 3.1.1 [153].

$$b_0 + b_1 x \pm t_{n-2}\, s \sqrt{\frac{1}{m} + \frac{1}{n} + \frac{(x_0 - \bar{x})}{\sum (x_i - \bar{x})^2}} \qquad 3.1.1$$

where b_0 and b_1 are the intercept and slope of the calibration curve, respectively, t_{n-2} is the student's t parameter associated to n–2 degrees of freedom at 97.5% of the confidence of, m is the number of times that each measure has been replicated, n is the number of x points forming the calibration curve, $\bar{x}$ is the average of the x values and s represents the standard deviation of the calibration curve normalised on the degrees of freedom, determined by Equation 3.3.2 [153].

$$s = \sqrt{\frac{\sum (y_i - \hat{y})^2}{n - 2}} \qquad 3.3.2$$

where $\hat{y}$ is the value predicted by the linear regression whereas y_i represents the i^{th} value of y. Table 3.3.1 lists all the LODS determined for the investigated metal ions. The calibration curves for the studied metal ions, in either the presence or absence of 0.01 M BTAH, are reported in the Appendix of Figure Section, displayed at the end of the thesis.

Table 3.3.1. Capillary electrophoresis Limit of Detections for metal ions in a 0.6 M NaCl solution and 0.6 M NaCl + 0.01 M BTAH solutions.

Metal Ion	LOD in 0.6 M NaCl / μmol L^{-1}	LOD in 0.6 M NaCl + 0.01 M BTAH / μmol L^{-1}
Cu^{2+}	30.3	56.1
Ni^{2+}	80.1	79.9
Fe^{3+}	71.5	295.0
Al^{3+}	108.0	565.1

4. Electrochemical Behaviour of Nickel–Aluminium Bronze in Aqueous Chloride Solutions in either the Presence or Absence of Benzotriazole

In this Chapter the corrosion properties of nickel–aluminium bronze were studied in aqueous chloride media by using potentiodynamic polarisation and scanning electron microscopy. Potentiodynamic polarisation was initially employed to determine the dependence of the NAB oxidation on protons and chloride (therefore establishing their order of reaction), since it has been reported that NAB exhibits an electrochemical behaviour similar to that of copper [9, 14]. The pH interval ranged from 8.2 to 3.0, whereas the chloride concentration was varied from 0.4 M to 1.0 M. Furthermore, a kinetic model for the NAB oxidation was developed on the basis of the determined parameters, *i.e.*, proton and chloride order of reactions. Finally, considering the high affinity of benzotriazole for copper, the corrosion performance of NAB was studied in the presence of the inhibitor in neutral (pH of 6.2) and acidic (pH of 3.5) solutions.

4.1 NAB Microstructure and Phase Chemistry

Figure 4.1.1 shows the SEM of cast NAB with the identification of the different phases present within the microstructure.

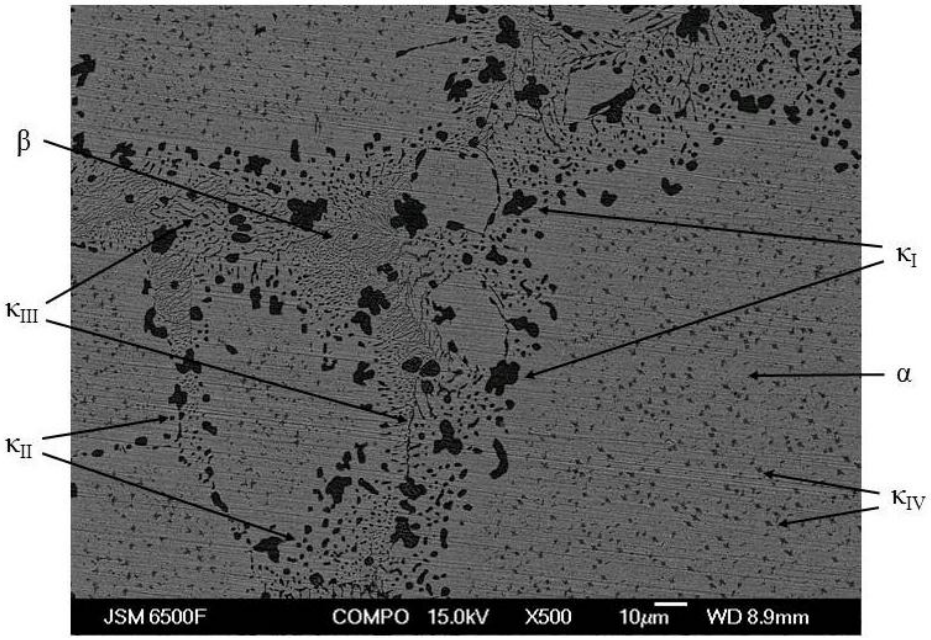

Figure 4.1.1. Backscattered electron microscopy image of cast nickel–aluminium bronze and phase identification.

As reported in the literature, the NAB microstructure is mainly constituted of an α–phase, which is rich in copper, and of a series of κ–phases, which have different shapes, sizes and chemical compositions [10]. Notably, four κ–phases were clearly identified within the NAB microstructure, namely κ_I, κ_{II}, κ_{III} and κ_{IV}, as shown in Table 4.1.1 The elemental analysis of the different phases was consistent with data published by Culpan and Rose (see Table 2.1.1 of Section 2.1.1) [10] since (*i*) the α– and β–phases had a high content of copper, ca. 86 % for both the phases, (*ii*) the κ_I and the κ_{IV} phases were characterised by a high content of iron, 35.69 % and 42.70 % for the κ_I and κ_{IV} phases, respectively, and (*iii*) the κ_{II} and κ_{III} phases displayed a chemical composition relatively rich in aluminium, nickel and iron.

Table 4.1.1. Energy dispersive X–ray spectroscopy analysis of the cast NAB phases.

	Alloy component / wt. %				
Phase	Al	Mn	Fe	Ni	Cu
α	7.90	0.20	2.58	2.91	86.41
β	8.51	0.52	2.20	2.58	86.19
κ_I	17.35	1.25	35.69	18.07	27.64
κ_{II}	19.09	0.93	26.60	26.04	27.34
κ_{III}	18.87	0.45	12.86	26.80	41.03
κ_{IV}	8.12	0.84	42.70	35.32	13.01

4.2 Electrochemical Behaviour of NAB in Neutral and Acidic Chloride Media

Figure 4.2.1 shows the PPs after 30, 300 and 720 minutes in the chloride electrolyte. It is evident that increasing the immersion time slightly resulted in a decreased of the corrosion current density which was probably associated with a thickening of a developing protective layer [4] . The j_{corr} were determined as 4.1 μA cm^{-2}, 3.3 μA cm^{-2} and 1.4 μA cm^{-2} for immersion times of 30, 300 and 720 minutes, as listed in Table 4.2.1. The cathodic branch in Figure 4.2.1 is attributable to the dissolved oxygen reduction reaction (ORR) at the metal surface, which has been indicated to occur on NAB with a limiting step determined by a single–electron exchange [9, 154].

Regarding the anodic Tafel slopes, values of +60 mV dec^{-1} in the initial stage and +210 mV dec^{-1} in the following part, were determined to remain constant for all tests, thus suggesting similar limiting–step processes taking place at the working electrode. Comparable anodic performance has been reported between NAB [9, 14] and copper [155] in chloride environments, where both were observed to have an anodic Tafel slope of +60 mV dec^{-1}, related to a process controlled by a combination of both charge and mass transfer.

The anodic behaviour of copper in chloride media has been the focus of several investigations [155-158]. Lee and Nobe [155] reported that the copper dissolution in chloride media is a pH–independent process which involves: (*i*) a non–activation–controlled anodic mechanism highlighted by an apparent Tafel region (b_a^{app}) of +60 mV dec^{-1} (both charge and mass limited), where $CuCl_2^-$ is the limiting–diffusion species; and (*ii*) a subsequent limiting–current region associated with the formation of a CuCl film on the metal surface. Different mechanisms have been considered to explain the b_a^{app}.

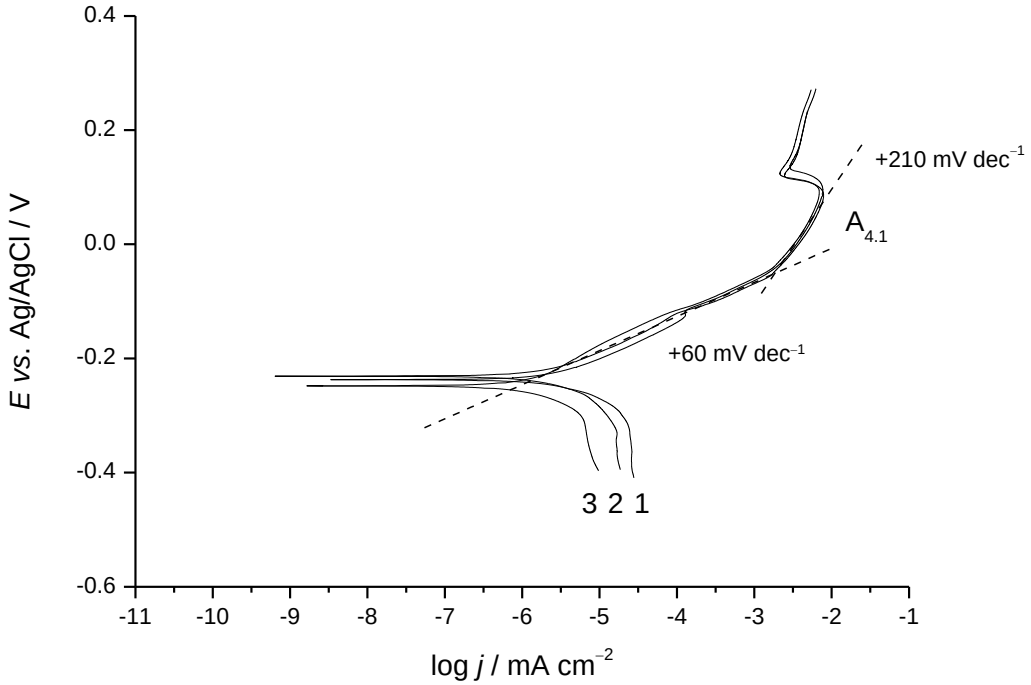

Figure 4.2.1. Potentiodynamic polarisations for NAB in 0.6 M NaCl (ca. pH 6) at 0.15 mV s^{-1} after immersion times of (1) 30, (2) 300 and (3) 720 minutes. Dashed lines represent the extrapolated Tafel slopes.

Bacarella and Griess [159] proposed a model where $CuCl_2^-$ is initially formed at the active interface and then diffused away into the bulk solution, with the latter being the rate determining step (rds). However, this mechanism has been more recently superseded by a two–step reaction, where the first is the reversible electrochemical formation of adsorbed CuCl, see Equation 4.2.1, whereas the second is the CuCl chemical–transformation into $CuCl_2^-$, see Equation 4.2.2 [157].

$$Cu + Cl^- \underset{k_{-1}}{\overset{k_1}{\leftrightarrow}} CuCl_{ads} + e^- \qquad 4.2.1$$

$$CuCl_{ads} + Cl^- \underset{k_{-2}}{\overset{k_2}{\leftrightarrow}} CuCl_2^- \qquad 4.2.2$$

With k_1 and k_{-1} expressed as $k_1(t) = k_a \exp[\alpha_a F E(t)/RT]$ and $k_{-1}(t) = k_c \exp[-\alpha_c FE(t)/RT]$, where k_a and k_c are the anodic and cathodic rate constants, α_a and α_c are the anodic and cathodic transfer coefficients, k_2 and k_{-2} are the desorption and adsorption rate constants [157, 158], *R* is the gas constant, *T* is the temperature, *F* is the Faraday constant and *E* is the electrode potential. The overall process which includes Equations 4.2.1 and 4.2.2 can be summarised by Equation 4.2.3, with an equilibrium electrode potential as expressed in Equation 4.2.4 [18].

$$Cu + 2Cl^- \leftrightarrow CuCl_2^- + e^- \qquad 4.2.3$$

$$E^\circ_{CuCl_2^-/Cu} = +0.019 + 0.059 \log \frac{\alpha_{CuCl_2^-}}{\alpha^2_{Cl^-}} \text{ / V } \textit{vs.} \text{ Ag/AgCl} \qquad 4.2.4$$

To corroborate the involvement of the copper oxidation in the NAB dissolution, the order of reactions with respect to protons and chloride were determined. Figure 4.2.2 shows the potentiodynamic polarisation for NAB in a 0.6 M NaCl deaerated solution (dissolved $O_2 \leq 3$ μM) at a pH ranging from 8.2 to 3.0. Regarding pHs 8.2 to 4.0 (PPs 1–5), the anodic behaviours were similar to those in Figure 4.2.1, that is, the presence of Tafel slopes of +60 and +210 mV dec^{-1} and an OCP of about –0.21 V *vs*. Ag/AgCl. Figure 4.2.2 inset shows the trend of the log *j* determined at –0.110 V *vs*. Ag /AgCl with respect to the log $[H^+]$, whose slope represents the proton order of reaction of NAB, $\Re^E_{H^+}$, as defined by Equation 4.2.5 [160].

$$\left(\frac{\partial \log j}{\partial \log [H^+]}\right)_{\left[Cl^-\right],\, T,\, I_m,\, E} = \Re^E_{H^+} \qquad 4.2.5$$

where $[Cl^-]$ is the chloride concentration (0.6 M) and I_m is the ionic strength of the solution (1.0 M). $[Cl^-]$, T, I_m, and E were all constant. The electrode potential selected was –0.110 V *vs*. Ag/AgCl, since at this value all the PPs exhibited +60 mV dec^{-1} slopes. As can be seen by the Figure 4.2.2 inset, the $\Re_{H^+}^{-110\,mV}$ was evaluated to be zero between the pH interval ranging from 8.2 to 4.0, hence indicating that the NAB oxidation in a chloride environment is governed by the dissolution of copper present within the NAB microstructure. Furthermore, also the anodic currents within the potential range from –0.080 V to 0.050 V *vs*. Ag/AgCl and dominated by a slope of +210 mV dec^{-1} showed a pH–independent behaviour.

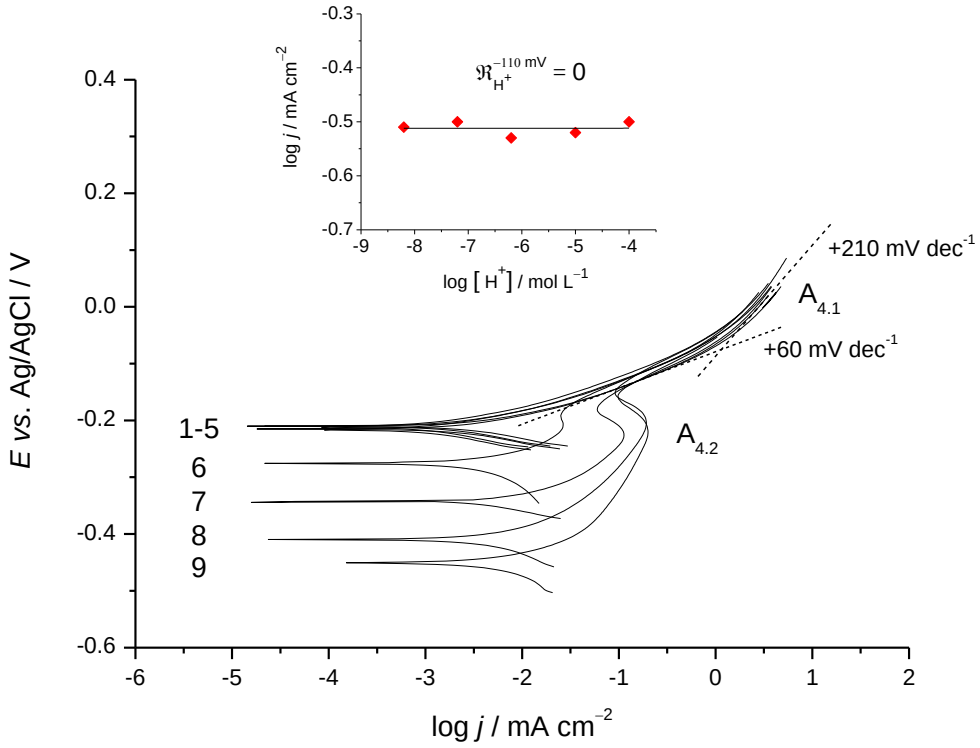

Figure 4.2.2. Potentiodynamic polarisations for NAB at 1.0 mV s^{-1} in deaerated 0.6 M NaCl (dissolved $O_2 \leq 3$ μM) at different pHs: (1) 8.2, (2) 7.2, (3) 6.2, (4) 5.0 (5) 4.0, (6) 3.8, (7) 3.5, (8) 3.3 and (9) 3.0. Tests (1), (2) and (3) were conducted in 0.6 M NaCl + 0.02 M phosphate–buffer solution. Inset shows the NAB order of reaction with respect to the proton concentration at –110 mV *vs*. Ag/AgCl for tests (1) to (5).

Concerning the mechanism behind the copper dissolution, Diard *et al.* [161] theoretically studied it in chloride media on rotating disc electrode. Different models were proposed [161], all of which considered (*i*) an initial apparent Tafel slope of +59 mV dec^{-1}, associated with the

formation of $CuCl_{ads}$, see Equation 4.2.1, whose coverage (Γ) was assumed to be negligible ($\Gamma \rightarrow 0$), followed by (*ii*) a kinetic process which depended on the $CuCl_{ads}$ coverage and the desorption and adsorption rates, see Equation 4.2.2. The model described by Diard et *al*. differed from previously published work [157, 158], since no assumption was made on the low $CuCl_{ads}$ coverage of the electrode surface. Among the models suggested by Diard *et al.* [161], our particular results, *i.e.*, an initial b_a^{app} of +60 mV dec^{-1} with a subsequent slope value of +210 mV dec^{-1}, approach the case combining an initial b_a^{app} of +59 mV dec^{-1} followed by a pseudo–Tafel b_a^{ps} of +236 mV dec^{-1} [161]. These two distinct Tafel behaviours were related to different kinetics, where the former relied on a reversible electron transfer process (Equation 4.2.1 is the fast step), achieved at low current densities (then at $CuCl_{ads}$ $\Gamma \rightarrow 0$) with a semi–logarithm expression as follows:

$$\log j_{app} = \log\left[F\,\Gamma\, k_2 [Cl^-]^2 \left(k_1/k_{-1}\right) / \left(1 + k_{-2}\Gamma/m_{CuCl_2^-}\right)\right] + \left(\frac{FE}{2.3\,RT}\right) \qquad 4.2.6$$

whereas the latter was associated with a complete surface coverage of $CuCl_{ads}$ ($\Gamma \rightarrow 1$), (Equation 4.1.1 represented the slow step whilst Equation 4.2.2 the reversible process), with a kinetic model expressed as in Equation 4.2.7.

$$\log j_{ads} = \log\left[F\,[Cl^-]\left(\left(k_2/k_{-2}\right)k_1\,\Gamma\, m_{CuCl_2^-}\right)^{1/2}\right] + \left(\frac{\alpha_a\, FE}{4.6\,RT}\right) \qquad 4.2.7$$

Where j_{app} and j_{ads} are the currents, Γ is the total surface site concentration, $m_{CuCl_2^-}$ is the ratio between the $CuCl_2^-$ diffusion coefficient and the diffusion thickness layer and α_a is the transfer coefficient (0.5). The order of reaction of chloride considered on Equation 4.2.6 was 2, thus suggesting high dependence of the copper oxidation on the chloride concentration. This value, which can be considered as a characteristic for copper dissolution at a chloride concentration less than 1 M [158], has been determined and reported in different studies [157, 158].

In this work, the NAB order of reaction for the chloride, within the apparent Tafel slope, was assessed with potentiodynamic polarisation at different chloride concentrations, ranging from 0.4 M to 1.0 M at pH 6.2, as shown in Figure 4.2.3. The ionic strength of all the solutions was maintained constant at 1.0 M, by adding aliquots of $NaClO_4$. It is worth noting that as the chloride concentration increased, the OCP shifted towards more negative values, thus indicating a less noble behaviour of the substrate. Figure 4.2.3 inset shows the dependence of the current density (at –0.170 V *vs*. Ag/AgCl) on the chloride concentration, both expressed in logarithmic

form, where the slope of the extrapolated trend represents the chloride order of reaction of NAB, as shown in Equation 4.2.8.

$$\left(\frac{\partial \log j}{\partial \log[\mathrm{Cl}^-]}\right)_{[\mathrm{H}^+],\,T,\,I_\mathrm{m},\,E} = \Re^{E}_{\mathrm{Cl}^-} \qquad 4.2.8$$

The NAB $\Re^{-170\mathrm{mV}}_{\mathrm{Cl}^-}$ was evaluated to be 2, thus indicating that the copper oxidation occurring within the NAB microstructure has the same electrochemical behaviour of unalloyed copper.

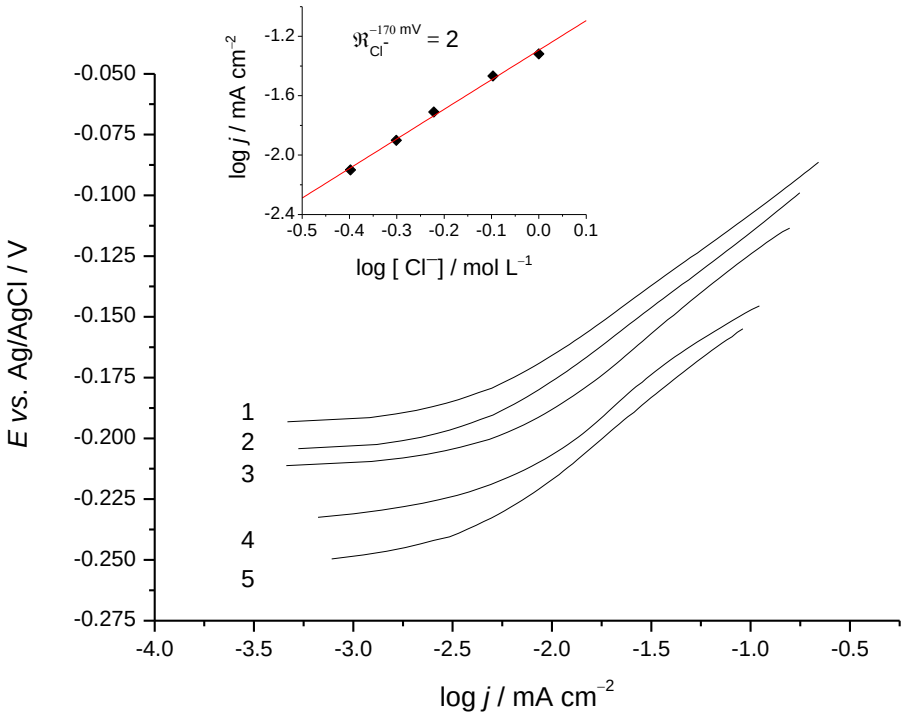

Figure 4.2.3. Potentiodynamic polarisations for NAB at 1.0 mV s^{-1} in (1) 0.4, (2) 0.5, (3) 0.6, (4) 0.8 and (5) 1.0 M NaCl deaerated solutions at pH 6.2. Inset shows the NAB order of reaction with respect to chloride concentration at –170 mV *vs.* Ag/AgCl.

According to Figure 2.4.1 of Section 2.4.1 (which highlights the chemical speciation of copper(I) in chloride solution) and considering the experimental conditions present in Figures 4.2.1 and 4.2.2, it can be inferred that after the electrochemical step has occurred (Equation 4.2.1) the formation of $CuCl_2^-$ dominated the chloride–complexation reaction, since in the explored conditions $CuCl_2^-$ is thermodynamically favoured over $CuCl_3^{2-}$.

Table 4.2.1. Kinetic parameters at different NAB immersion times in a 0.6 M NaCl solution.

	Time / minute		
Parameters	30	300	720
j_{corr} / A cm^{-2}	4.1×10^{-6}	3.3×10^{-6}	1.4×10^{-6}
b_a^{app} / mV dec^{-1}	+60	+60	+60
b_a^{ps} / mV dec^{-1}	+210	+211	+210
$\Re_{H^+}^{-110mV}$ (pH ≥ 4.0)		0	
$\Re_{H^+}^{0mV}$ (pH ≥ 4.0)		0	
$\Re_{Cl^-}^{-170mV}$		2.0	

Table 4.2.1 shows the kinetic parameters, *i.e.*, corrosion current density, Tafel slopes and orders of reaction, determined for the different conditions shown in Figures 4.2.1 and 4.2.2 (tests 1–5).

The formation of cuprite (Cu_2O) during the copper oxidation in a chloride solution at pH 6.2, see Equation 4.2.9, is thermodynamically favoured over CuCl.

$$2Cu + H_2O \leftrightarrow Cu_2O + 2H^+ + 2e^- \quad 4.2.9$$

$$E^\circ_{Cu_2O/Cu} = +0.256 - 0.059pH \text{ / V } vs. \text{ Ag/AgCl} \quad 4.2.10$$

$$E^\circ_{CuCl/Cu} = +0.088 - 0.059\log\alpha_{Cl^-} \text{ / V } vs. \text{ Ag/AgCl} \quad 4.2.11$$

In fact, by considering the equilibrium electrode potential of Equation 4.2.10 [162], the Cu_2O formation should occur at –0.110 V *vs*. Ag/AgCl (at pH of 6.2), whereas that for CuCl should occur at –0.064 V *vs*. Ag/AgCl, estimated using Equation 4.2.11 [18] and a chloride activity (α_{Cl^-}) of 0.0403 mol kg^{-1} (calculated with a NaCl solution density of 1.002 g cm^{-3} and an activity coefficient of 0.673 [162]). However, as can be seen from Figure 4.2.2, the Tafel slopes determined within the pH range from 4.0 to 8.2 all displayed values of +60 mV dec^{-1} and +210 mV dec^{-1}, hence indicating that similar oxidation mechanisms, associated with Equations 4.2.1 and 4.2.2, took place on polarised NAB. This insight is in line with results reported by Tromans *et al*. [18] and Deslouis *et al*. [163], where the formation of the thermodynamically favoured Cu_2O was reported to be negligible whereas that of CuCl dominated the copper oxidation in chloride environments. The establishment of the Cu / CuCl equilibrium can be confirmed by

the good agreement obtained between the thermodynamic potential assessed using Equation 4.2.11, *i.e.*, –0.064 V *vs*. Ag/AgCl at 0.403 m (molality), and that experimentally determined from the intersection of the +60 mV dec^{-1} and +210 mV dec^{-1} Tafel slopes, *i.e.*, –0.068 V *vs*. Ag/AgCl, associated with a NAB active surface covered by $CuCl_{ads}$ ($\Gamma \rightarrow 1$) [161]. The formation of cuprite at the NAB surface cannot be precluded *a priori*, since thermodynamically favoured over CuCl at pH higher than 5.4 and at α_{Cl^-} of 0.403 m. However, its formation seems to be confined to a chemical (hydrolysis) rather than an electrochemical process [161].

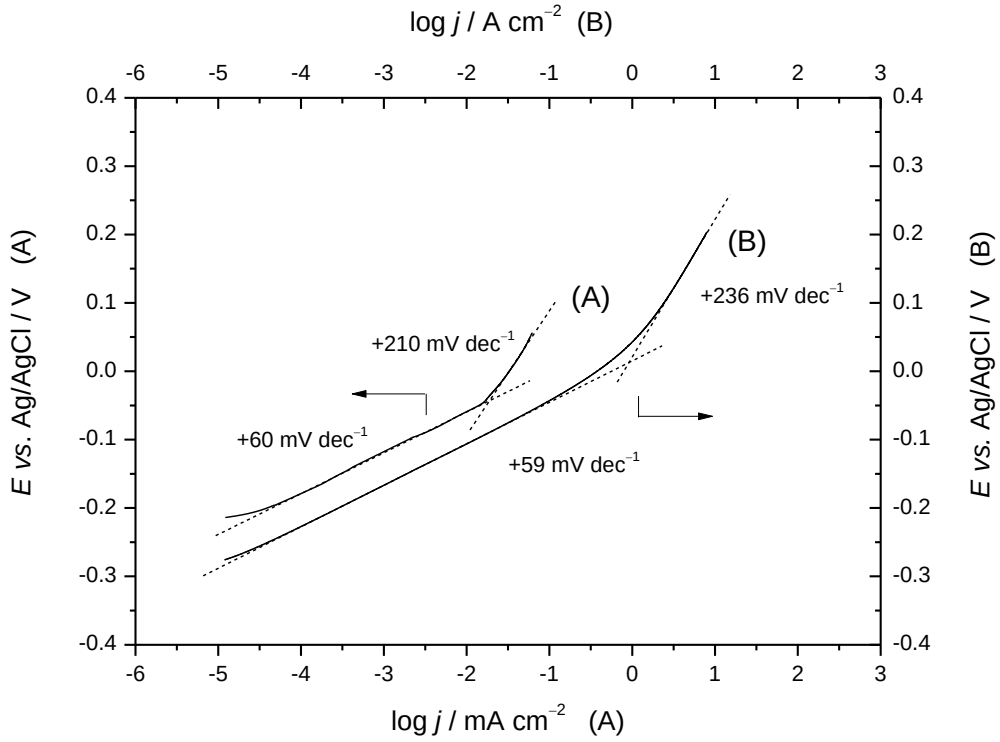

Figure 4.2.4. Experimental (A) and theoretical (B) potentiodynamic polarisations for NAB in deaerated 0.6 M NaCl at pH of 6.2. Test (A) was carried out at 1.0 mV s^{-1}. Test (B) was obtained considering the current expressed by Equations 4.6 and 4.7 with and an equilibrium potential of –0.294 V *vs*. Ag/AgCl.

Figure 4.2.4 shows a comparison between the anodic PP on NAB in 0.6 M NaCl at pH 6.2 (curve A) and the oxidation model proposed by Diard *et al.* [161] for copper using Equations 4.2.6 and 4.2.7 in 0.6 M NaCl (curve B) and an overall current given by $j = (j_{app} \cdot j_{ads}) / (j_{app} + j_{ads})$. According to the model advanced by Diard *et al.*, the following parameters were considered in the determination of curve (B): $\Gamma = 10^6$ mol cm^{-2}, $k_2 = 10^6$ mol^{-1} cm^{-3} s^{-1}, $k_{-2} = 10^6$ mol^{-1} cm^{-3} s^{-1}, $k_1 = 10^5$ mol^{-1} cm^{-3} s^{-1}, $k_{-1} = 10^3$ s^{-1}, T = 298 K, $\alpha_a = 0.5$ and $m_{CuCl_2^-} = 10^{-4}$ cm. The good agreement obtained between curves (A) and (B), notwithstanding the different

conditions of the systems considered (curve (A), NAB oxidation carried out in an quiescent chloride solution; curve (B), theoretical data associated with copper dissolution in chloride media at high mass transfer [161]), can be explained by the charge– and mass–transfer controlled copper dissolution [14] at both $\Gamma \rightarrow 0$ and $\Gamma \rightarrow 1$. The equilibrium electrode potential (E_e) employed for determining curve (B) was assessed using Equation 4.2.4. Equation 4.2.4 was particularly considered since at low overpotentials the electrode surface is negligibly covered by CuCl ($\Gamma \rightarrow 0$) and cuprous chloride is readily transformed into $CuCl_2^-$ [161], hence establishing the existence of an equilibrium between Cu and $CuCl_2^-$. Wharton *et al*. [9] reported an OCP for a NAB rotating–disc electrode of –0.294 V *vs*. Ag/AgCl under high mass transfer conditions (angular velocity of 9500 rpm) [9]. This value is considerably lower than those shown in Figure 4.2.2, due to a high mass transport which de–polarises the anodic equilibrium via the removal of $CuCl_2^-$ from the Nernst diffusion layer [9, 14]. Assuming the establishment of the Cu and $CuCl_2^-$ equilibrium and using Equation 4.2.4, the $CuCl_2^-$ concentration was determined to be 1.8 μM for the specific case of [9]. This concentration value was then used for assessing the E_e (–0.274 V *vs*. Ag/AgCl) of Figure 4.2.4 curve (B), considering $\alpha_{CuCl_2^-}$ of 0.403 m (molal), since the model put forward by Diard *et al*. [161] was based on a high mass transport process.

In Figure 4.2.2, PP tests 6–9 were carried out on NAB in a 0.6 M NaCl solution at pHs lower than 4.0, after an initial electrode immersion of twenty minutes. Marked differences can be appreciated between tests 1–5 and 6–9 in terms of OCP and shape of the recorded responses. Indeed, as soon as the solution pH was reduced below 4.0 the OCP significantly decreased, *i.e.*, –0.280 V *vs*. Ag/AgCl at pH 3.8 and –0.450 V *vs*. Ag/AgCl at pH 3.0, suggesting a pH–dependent behaviour in contrast to that observed at pHs higher than 4.0. Furthermore, the tests 6–9 were clearly characterised by the presence of a pseudo passivation peak ($A_{4.2}$) and, at potentials more positive than –0.135 V *vs*. Ag/AgCl, the current density followed a typical copper oxidation behaviour (*i.e*. initially with a Tafel slope of +60 mV dec^{-1} and then +210 mV dec^{-1}). This behaviour suggests that copper dissolution predominated at an onset potential of –0.135 mV *vs*. Ag/AgCl. To better understand the NAB dissolution in different pHs and possibly identify the phases subject to corrosion, SEM was used to determine the microstructure corrosion features for anodic treatments at –0.100 V *vs*. Ag/AgCl and –0.250 V *vs*. Ag/AgCl in neutral (6.2) and acidic (3.5) pHs, respectively, see Figures 4.2.5 and 4.2.6.

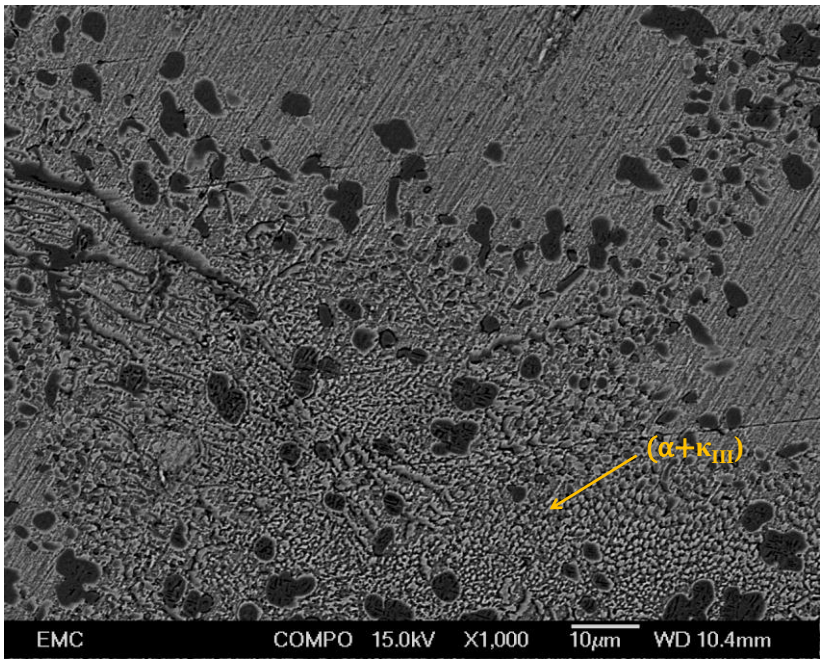

Figure 4.2.5. Backscattered electron microscopy image of cast NAB after an anodic treatment at –0.100 V *vs*. Ag/AgCl for 600 s in 0.6 M NaCl at pH 6.2.

From Figure 4.2.6 it can be observed that the anodic treatment carried out in neutral pH resulted in a darker–colour of the copper rich α–phase of the corroded part with respect to the uncorroded NAB surface.

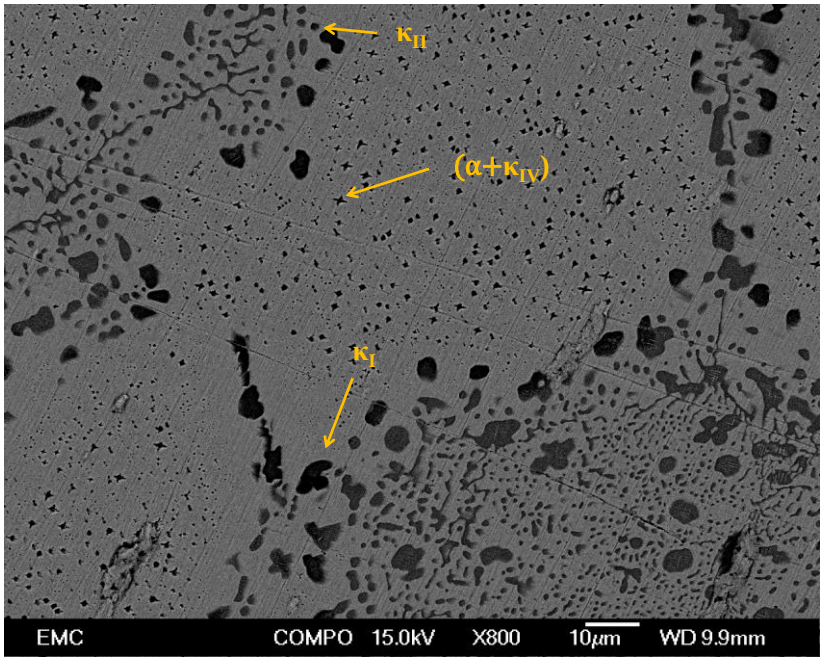

Figure 4.2.6. Backscattered electron microscopy image of cast NAB after an anodic treatment at –0.250 V *vs*. Ag/AgCl for 600 s in 0.6 M NaCl at pH 3.5.

This feature was particularly evident for the copper rich α–phase within the α + κ_{III} eutectoid, where evidence of an electrochemical etching can be seen as related to an active copper dissolution. These results, which corroborate the NAB electrochemical data in Figures 4.2.1 and 4.2.2, are consistent with findings reported in the literature, which indicate an initial corrosion attack of the copper rich α–phase within the α + κ_{III} eutectoid [4]. Conversely, Figure 4.2.6 highlights that after being subjected to an anodic treatment at –0.250 V *vs*. Ag/AgCl in chloride containing solution at pH 3.5, NAB underwent selective phase corrosion at the κ–phases rather than the α–phase. In fact, a number of the κ–phases within the NAB microstructure, particularly the κ_I and κ_{II} at the boundary with the α–phase and the κ_{IV} within the κ_{IV} + α eutectiod, showed darker regions than others κ–phases, thus suggesting that a change in their chemical composition has occurred due to the anodic treatment. The pH–dependent behaviour of NAB shown in Figure 4.2.2 was therefore confirmed by SEM, which supported the existence of selective dissolution processes dependent on pH. In particular at pHs above 4.0, the NAB oxidation was dominated by copper dissolution of the α–phase within the α + κ_{III} eutectoid, whereas the other κ–phases were cathodically protected. Conversely, at pHs below 4.0 the NAB corrosion behaviour was characterised by an inversion of the anodic–cathodic phase behaviour: the copper–rich α–phase (which acted as an anodic phase at pHs greater than 4.0) displayed a cathodic behaviour whereas the other κ–phases, rich in nickel, iron and aluminium, underwent oxidation (anodic sites).

The NAB potentiodynamic polarisations at different pHs in 0.6 M NaCl, shown in Figure 4.2.2, were all carried out after monitoring the OCP for twenty minutes (OCP not shown in Figure 4.2.2). It was noted that, above pH 4.0, the OCP remained stable at –0.21 V *vs*. Ag/AgCl, whereas at pHs below 4.0 the OCP markedly decreased after a few minutes, to a potential dependent on the proton concentration. Figure 4.2.7 shows an overlay of PPs undertaken in 0.6 M NaCl at pH of 6.2 (test 1) and 3.5 (tests 2 and 3), after the OCP was monitored for twenty minutes for tests (1) and (2) and three hundred minutes for test (3). Substantial differences are evident when comparing tests (2) and (3), where in the former case the anodic behaviour is initially attributable to the κ_I–, κ_{II}– and κ_{IV}–phases dissolutions (at approximately –0.3 V *vs*. Ag/AgCl) and then to the α–phase oxidation (above –0.14 V *vs*. Ag/AgCl), whereas in the latter the anodic behaviour is dominated only by copper dissolution of the α–phase. As shown in the Figure 4.2.7 inset, which reports the OCP as a function of the time at pH 3.5, it can be proposed that NAB underwent inversion of the anodic–cathodic phase behaviour within the first two minutes of immersion. However, for an extended immersion the OCP gradually increased, reaching –0.235 V *vs*. Ag/AgCl after three hundred minutes. It can be speculated that under these conditions the α–phase still remains cathodically protected due to its

higher equilibrium potential (at –0.21 V *vs*. Ag/AgCl) than that after three hundred minutes at pH 3.5 (–0.235 V *vs*. Ag/AgCl).

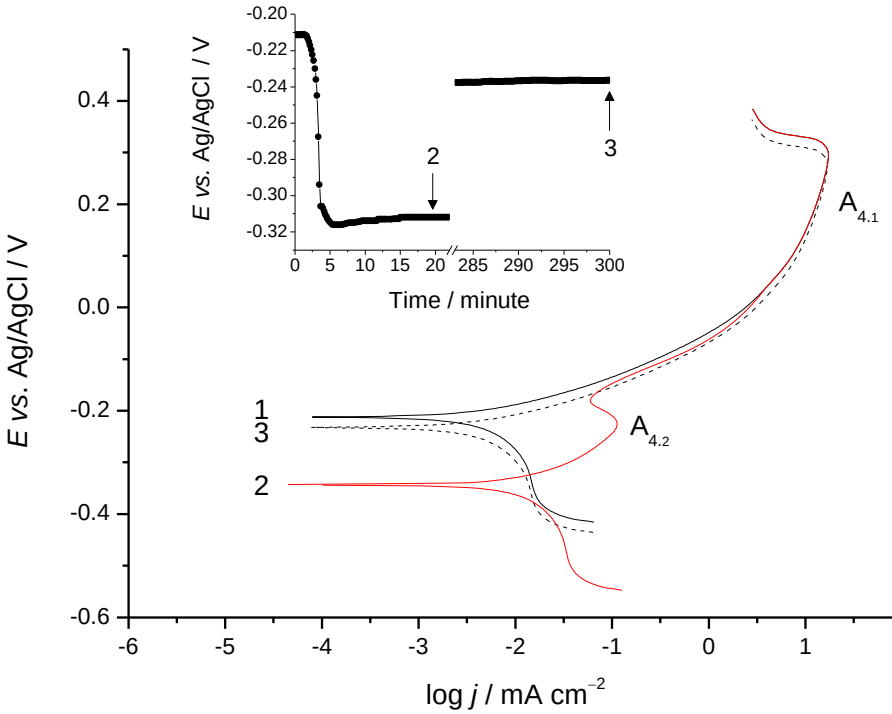

Figure 4.2.7. Potentiodynamic polarisations for NAB at 1.0 mV s^{-1} in 0.6 M NaCl: (1) pH 6.2, both (2) and (3) at pH 3.5. Tests (1) and (2) were conducted after 20 minutes, whereas test (3) after 300 minute from the initial NAB immersion. Inset shows OCP trend and the time interval at which potentiodynamic polarisations (2) and (3) were performed.

4.3 Electrochemical Behaviour of Nickel–Aluminium Bronze on the Presence of BTAH in Chloride Solutions of various pH

The characteristic behaviour of NAB in chloride media (*i.e.*, (*i*) copper dissolution taking place at the copper rich α–phase within the α + κ_{III} eutectoid at pHs above 4.0 and (*ii*) inversion of anodic–cathodic phase behaviour at pHs below 4.0) was investigated in chloride media in the presence of different BTAH concentrations initially in neutral (pH 6.2) and then acidic solutions (pH 3.5), chosen to represent the pH conditions found within crevice environments [4].

Preliminary corrosion inhibition were performed on NAB using a fixed BTAH concentration and PP up to immersion times of 720 minutes, in order to assess the adsorption / desorption

equilibrium. The BTAH adsorption / desorption equilibrium was achieved after about 300 minutes, established by similar j_{corr} values.

Figure 4.3.1 shows the PPs for NAB after a 300 minute immersion in a 0.6 M NaCl solution with and without the BTAH inhibitor at different concentrations, *i.e.*, 0.05 mM, 0.10 mM, 1.00 mM, 5.00 mM and 10.00 mM. A decrease of j_{corr} is clearly evident with increasing inhibitor concentration. Comparing the inhibited responses (lines 2–6) with the uninhibited (line 1), it is evident that an increase of the E_{corr}, equal to +85 mV, occurred with a reduction of the current densities in both the cathodic and anodic branches.

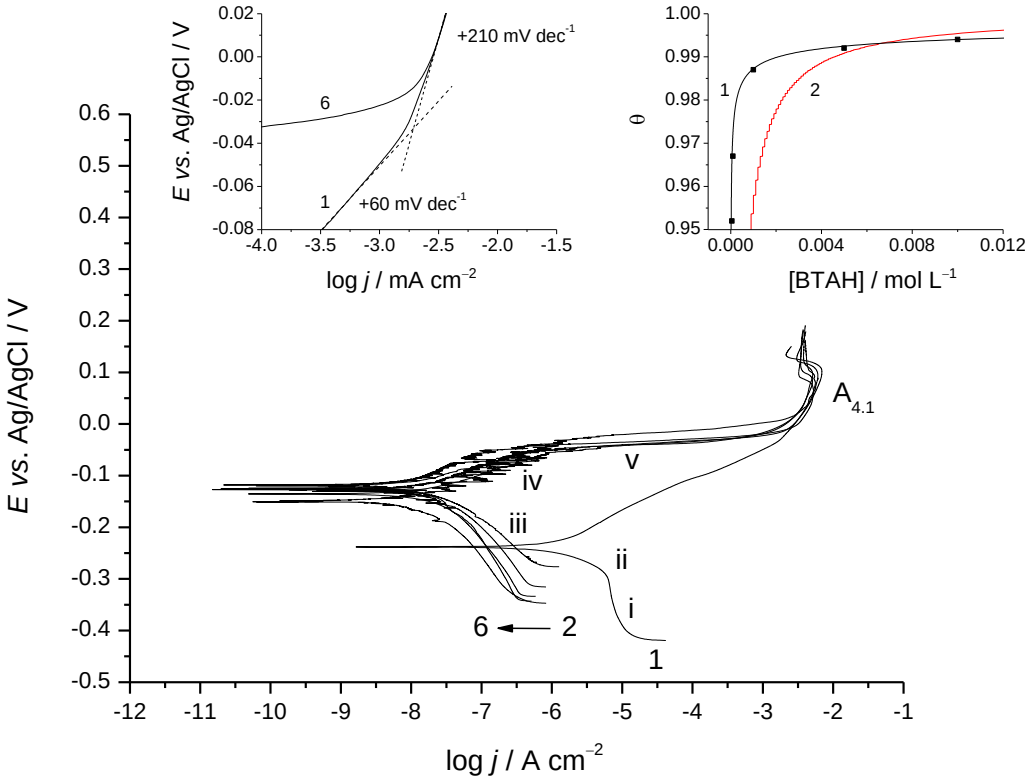

Figure 4.3.1. Potentiodynamic polarisations for NAB at 0.15 mV s^{-1} after a 300 minute immersion in 0.6 M NaCl with BTAH additions: (1) 0 M, (2) 0.05 mM, (3) 0.10 mM, (4) 1.00 mM, (5) 5.00 mM and (6) 10.00 mM. (i), (ii), (iii), (iv) and (v) indicate different potential regions of the potentiodynamic polarisations. Upper–left inset shows an expansion of voltammograms (1) and (6) with extrapolated Tafel slopes, whereas upper–right inset shows a comparison between Kastening–Holleck (1) and Langmuir (2) adsorption isotherm fittings.

Specifically for the cathodic response, the oxygen response on NAB in the presence of BTAH displayed a behaviour mainly governed by both charge and mass transfer processes over the potential range considered (potential interval of Figure 4.3.1, named "iii"), while the cathodic responses on NAB for the not inhibited solution presented two distinct parts, *i.e.*, ("i")

controlled by mass transfer process and ("ii") controlled by both electron transfer and mass transfer. Therefore, the rather linear and sloping trend "iii" can be taken as a proof of the incomplete oxygen mass transport. This behaviour can be ascribed to the adsorption effect of BTAH on the NAB surface which hampers the oxygen diffusion. Regarding the anodic PP responses, it is apparent a marked shift towards more positive electrode potentials, which indicates a less pronounced copper dissolution of NAB. Contrary to the uninhibited PPs, which shows only one characteristic Tafel plot of +60 mV dec^{-1}, the inhibited response has two distinct trends: ("iv") one at slightly more positive potentials than the E_{corr}, of approx. +50 mV dec^{-1}, and another ("v") at a more positive value, at which a small increase of the electrode potential produced a rapid rise of the anodic current density. Therefore, it can be proposed that the different anodic Tafel slopes in the presence and absence of BTAH, *i.e.*, +50 mV dec^{-1} and +60 mV dec^{-1}, are likely to be associated with different anodic mechanisms, where BTAH may play a significant role. The excellent BTAH inhibition properties for copper have been not only related to its affinity towards the metal surface (formation of an adsorbed layer of molecular BTAH), but also, and in particular, to the presence of an inorganic film of Cu(I) and BTA^-, $[Cu(I)BTA^-]_n$, further adsorbed on the metal surface [164, 165]. Therefore, it is proposed that above a pH of 4.0 the NAB oxidation mechanism may involve the formation of both $Cu(I)BTA^-$ and $CuCl_2^-$, the latter through Equations 4.2.1 and 4.2.2, as it has been discussed in the literature [18]. However, as the NAB applied potential is increased, the formation of $CuCl_{2(aq)}^-$ prevails over $Cu(I)BTA^-$, due to the higher solution concentration of Cl^- than BTAH. This insight can be inferred by the upper Figure 4.3.1 inset, which shows the presence of a +210 mV dec^{-1} Tafel slope on both tests (1) and (6), within a potential interval from –20 to 0 mV *vs*. Ag/AgCl, thus indicating a NAB surface significantly covered by CuCl.

Table 4.3.1. NAB potentiodynamic polarisations kinetic parameters obtained after 300 minutes of NAB immersion in a 0.6 M NaCl solution with different BTAH concentrations.

	BTAH Concentration / mM					
Parameters	0	0.05	0.10	1.00	5.00	10.00
I.E. %	0	95.2	96.7	98.7	99.2	99.4
j_{corr} / A cm^{-2}	1.4×10^{-6}	6.6×10^{-8}	4.5×10^{-8}	1.8×10^{-8}	1.0×10^{-8}	0.8×10^{-8}
b_a^{app} / mV dec^{-1}	+60	+52	+50	+48	+50	+51

Regarding the BTAH adsorption mechanism, several models have been proposed describing the structure of the growing BTAH–protective layer, as well as its binding on the metal surface [18, 30, 37, 40, 166]. Musiani *et al*. [166] studied by means of electrochemical and SERS techniques the influence of the pH and the electrode potential on the adsorption of benzotriazole on copper in chloride solutions. The existence of potential–dependent surface acid–basic equilibria was reported to be due to the diverse adsorbed benzotriazole species ($BTAH_{ads}$ and $Cu(I)BTA^{-}$) at the investigated pHs. In particular, SERS suggested the presence of both $BTAH_{ads}$ and $Cu(I)BTA^{-}$ when either the solution was kept at acidic conditions (pH 1) or the electrode was cathodically polarised (–0.561 V *vs*. Ag/AgCl). Conversely, Cu(I)BTA predominated over $BTAH_{ads}$ at neutral pHs and at OCP. Youda *et al.* [37] also considered the existence of a pH–sensitive equilibrium behind the adsorption mechanism of benzotriazole on copper. Indeed, as shown in Equation 2.2.3 of Section 2.2.3, the benzotriazole adsorption relied on the establishment of an equilibrium between adsorbed BTAH and $Cu(I)BTA^{-}$. In agreement with Musiani *et al*., unfavourable formation of $[Cu(I)BTA^{-}]_n$ was observed at low pHs and at more cathodic potentials than the zero charge potential. Also, Tromans *et al*. [18] proposed a pH–dependent process taking place with the initial BTAH adsorption on copper, as shown in Equation 2.2.7 of Section 2.3.3. However, in contrast to Youda *et al.*, they suggested that the formation of a polymeric $[Cu(I)BTA^{-}]_n$ film occurs within the diffusion layer, see Equation 2.2.8 of Section 2.2.3, which was adsorbed on the initial $BTAH_{ads}$ layer, see Equation 2.2.9 of Section 2.2.3.

The ineffectiveness of benzotriazole as an inhibitor in acidic environments (pH 1) has principally been attributed to the inability to form the $[Cu(I)BTA^{-}]_n$ film and to the difficulty of creating the initial $BTAH_{ads}$ layer, due to the protonation of benzotriazole, $BTAH_2^{+}$ [18]. A pH of 3.0 was highlighted as the threshold for the effective and ineffective BTAH inhibition [18].
In addition to pH, the applied potential has also been identified as critical parameter which significantly influences the growth of $[Cu(I)BTA^{-}]_n$ [26, 37, 166] and therefore the benzotriazole inhibition efficiency. Allam *et al.* [25] determined a BTAH adsorption Gibbs energy, on cathodically polarised copper (–0.355 V *vs*. Ag/AgCl), associated with a physisorption process. The estimated value (–3.8 kJ mol^{-1}) was considerably lower than those assessed for unpolarised copper, which generally range from –30 kJ mol^{-1} to –39 kJ mol^{-1} [42, 46, 167]. Metikos–Hukovic *et al.* [42] reported a BTAH adsorption Gibbs energy dependent on the solution pH (pH investigated from 4 to 10). The Flory–Huggins isotherm described the benzotriazole adsorption and provided adsorption Gibbs energies from –30 to –39 kJ mol^{-1}, as the pH changed from 4 to 10. In this work, the assessment of the benzotriazole adsorption on NAB in a neutral chloride media was achieved by using I.E. % listed in Table 4.3.1 and fitting

different adsorption models (Langmuir, Tëmkin, Frumkin, Volmer Hill–De Boer, Helfand–Frisch–Lebowitz, Parsons, Damaskin–Parsons, Kastening–Holleck, Flory–Huggins, Dhar–Flory–Huggins and Bockris–Swinkles [168]). The I.E. % was determined using Equation 4.3.1.

$$\text{I.E.\%} = \frac{j^0_{\text{corr}} - j_{\text{corr}}}{j^0_{\text{corr}}} \cdot 100 \qquad 4.3.1$$

where j^0_{corr} is corrosion current estimated in 0.6 NaCl solution whereas j_{corr} is the corrosion current evaluated in BTAH containing solutions. The determination of the adsorption isotherm was then assessed by considering the inhibition efficiency as the BTAH coverage and assuming an inhibition property associated with the "surface blocking effect" [25] of the organic molecules on the metal surface. The accuracy of the adsorption isotherm fitting with the experimental data was evaluated as follows:

$$S = \Sigma_i \, (x_{i,\ \text{experimental}} - x_{i,\ \text{fitting}})^2 \qquad 4.3.2$$

where $x_{i,\ \text{experimental}}$ is the i^{th} experimental value and $x_{i,\text{fitting}}$ is the i^{th} fitted value. The fitting procedures were attained considering the interaction parameter (g) and solvent molecule displacement (χ) values, ranging from –5 to 5 and 0 to 5 [169], respectively. The best fit occurred for the Kastening–Holleck isotherm. The upper–right Figure 4.3.1 inset shows a comparison between the fittings using the Kastening–Holleck [170] and the Langmuir isotherms [169]. The adsorption Gibbs energy was determined to be –44.0 kJ mol^{-1}, see Equation 4.3.3, and thereby indicated a chemi–type adsorption process.

$$\frac{\theta}{\chi(1-\theta)^{\chi}}\left(1-\theta+\frac{\theta}{\chi}\right)(\chi-1)\exp(-2g\theta) = K_{\text{ads}}\, c = \frac{1}{55.5}\exp\left(\frac{-\Delta G^{\circ}_{\text{ads}}}{RT}\right) \qquad 4.3.3$$

Where θ is the benzotriazole surface coverage on NAB, χ is the solvent molecule displacement per adsorbed BTAH molecule, g is the interaction parameter occurring between adsorbed BTAH molecules, K_{ads} is the adsorption equilibrium constant and c is the concentration. The BTAH adsorption free enthalpy obtained for NAB is similar to those obtained on copper and on copper–based alloys, which are typically in the range between –20 and –45 kJ mol^{-1} [25, 43, 167]. Other indications from the adsorption model suggest that the adsorption mechanism occurs by displacing two adsorbed solvent molecules (χ = 2) and (*ii*) that benzotriazole molecules attract each other when adsorbed at the metal surface (g = 0.8) [169].

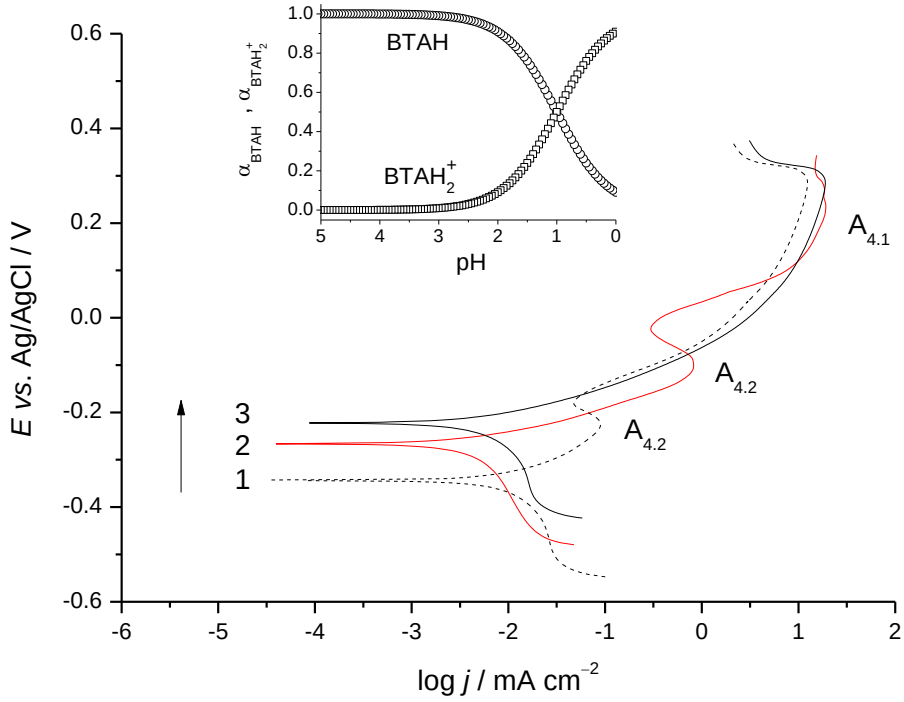

Figure 4.3.2. Potentiodynamic polarisations for NAB at 1.0 mV s^{-1} in 0.6 M NaCl at pH 3.5 with (test 2) and without (tests 1 and 3) 0.01 M BTAH. Test (1) was performed after a 20 minute immersion, whereas tests (2) and (3) after a 300 minute immersion. The inset shows the fractional ionisation of BTAH and $BTAH_2^+$.

The benzotriazole adsorption behaviour was also investigated on NAB in 0.6 M NaCl solution at pH 3.5, at which the copper rich α–phase was cathodically protected and the anodic behaviour of NAB was controlled by the oxidation of the κ–phases, as shown in Figure 4.2.6. Figure 4.3.2 shows an overlay of PPs on NAB in 0.6 M NaCl at pH 3.5 in the presence (tests 2) and in the absence (test 1 and 3) of 0.01 M BTAH after different NAB immersion times: test 1 after 20 minutes, while tests 2 and 3 after 300 minutes. Comparing PPs 2 and 3, it is evident the effects of the BTAH adsorption on the NAB electrochemical behaviour, which significantly reduced the OCP and prevented the passivation of the κ–phases. This latter feature can be particularly appreciated in PP 2 of Figure 4.3.2, which shows the presence of the peak $A_{4.2}$, whereas PP 3 does not. Furthermore, the pseudo passivation peak $A_{4.2}$ of PP 2 was anodically shifted of 0.13 V with respect to that of PP 1, thus indicating that benzotriazole competitively interacted with chloride or water on the κ–phases, preventing their oxidation.

The good inhibition properties exhibited by benzotriazole on NAB in neutral pH, attributable to the formation of an adsorbed $[Cu(I)BTA^-]_n$ [18], were not observed when the pH decreased below 4.0 (j_{corr} = 5.7 mA cm^{-2} for test (2) and 7.0 mA cm^{-2} for test (1)).
It has been reported that the benzotriazole inhibition is significantly reduced in acidic pHs due to the presence of $BTAH_2^+$, which has difficulty to adsorb onto copper surfaces [18]. However, as shown in Figure 4.3.2 inset (which highlights the BTAH and $BTAH_2^+$ fractional distributions), the inhibitor species that predominated at pH 3.5 was BTAH. As such, the low benzotriazole inhibition determined at pH 3.5 results from the weak interactions established between BTAH and the NAB κ–phases, rather than a low adsorbability of benzotriazole when present as a protonated species ($BTAH_2^+$).

4.4 Summary

In this Chapter the corrosion performance of NAB has been investigated using potentiodynamic polarisation and scanning electron microscopy in 0.6 M NaCl over a pH range from 8.2 to 3.0, either in the presence or absence of benzotriazole.

It was observed that the NAB anodic behaviour was controlled by copper oxidation when the solution pH was maintained above 4.0. The mechanism was consistent with the initial and reversible electrochemical formation of adsorbed CuCl followed by the production of $CuCl_2^-$. The NAB order of reaction for protons and chloride were determined to be zero (within the pH interval from 8.2 to 5) and two (within the chloride concentration from 0.4 M to 1.0 M), respectively, as expected for a process driven by copper dissolution. A different form of selective phase corrosion occurred below pH 4.0. Indeed, SEM analysis carried out after an anodic treatment at pH 3.5 in a chloride solution confirmed the selective corrosion attack of the κ_I–, κ_{II}– and κ_{IV}–phases, whereas, SEM results achieved on anodically polarised NAB at neutral pHs highlighted a marked dissolution of the copper–rich α–phase. Therefore, it was concluded that pH variations across the limit value of 4.0 led to an inversion of the anodic–cathodic phase behaviour of NAB.

The Electrochemical tests conducted on NAB in the presence of benzotriazole indicated the high inhibitor affinity towards NAB, provided the solution pH was maintained above pH 4.0. Conversely, as the pH decreased below 4.0, the NAB electrochemical behaviour changed and the inhibition of benzotriazole drastically decreased. This behaviour suggests that the beneficial

use of benzotriazole on NAB is not always exploitable, but is limited to a range of experimental conditions that do not trigger the inversion of the NAB oxidation mechanism.

5. Electrochemical, Morphological and Chemical Characterisations of Boron–Doped Diamond Electrode

In this Chapter chronoamperometry, cyclic voltammetry, potentiodynamic polarisation and electrochemical impedance spectroscopy were employed to investigate the electrochemical performance of the BDD electrode, whereas AFM and XPS were used to gain insights into its surface morphological and chemistry. Regarding the electrochemical characterisation, potentiodynamic polarisation was used to study the oxygen and hydrogen evolution reactions, whereas cyclic voltammetry, electrochemical impedance spectroscopy and quasi–steady potentiodynamic polarisation were used to study the BDD reactivity towards the $[Fe(CN)_6]^{3-/4-}$ redox system. Moreover, since a strong relationship has been observed between the electrochemical properties and the surface chemistry of a BDD electrode, XPS tests were also carried out to characterise the electrode surface chemistry. Full details and protocols of the techniques and equipment used are provided in Chapter 3.

5.1 Electrochemical Characterisation

Figure 5.1.1 shows the chronocoulometry carried out in a 0.6 M NaCl test solution with the addition of 10.0 mM $K_3Fe(CN)_6$. Chronocoulometry measurements were made by first applying an electrode potential of +0.7 V *vs*. Ag/AgCl for 10 s (E_1), at which no reduction of ferricyanide takes place, and then followed by stepping the potential to –0.5 V *vs*. Ag/AgCl (E_2), an electrode potential sufficiently negative to promote the reduction of ferricyanide to ferrocyanide. The inset displayed in Figure 5.1.1 shows the electrode potentials applied in the chronocoulometry test with respect to the electrochemical activity of the $Fe(CN)_6^{3-}$ species. It can be seen that E_1 is above the reduction peak (centred at +0.1 V *vs*. Ag/AgCl) by approximately 0.6 V, while E_2 is below the reduction peak. The actual electrode area was determined using the Cottrell equation [171], see Equation 5.1.1.

$$Q_d = \frac{2\,z\,F\,A\sqrt{D}\,c^*\sqrt{t}}{\sqrt{\pi}} \qquad 5.1.1$$

where Q_d is the faradaic charge associated with the diffusion controlled reduction process, z is number of the electrons involved in the electrochemical reaction (e.g. in this instance 1 electron), D is the diffusion coefficient (7.6 $cm^2\ s^{-1}$) [172], c^* is the surface concentration of

the electro–active species, that in a quiescent solution equals the bulk concentration (10^{-5} mol cm^{-3}) and t is the time (s). The electrode area was evaluation to be 0.184 cm^2 using the slope of the reductive charge trend against the square root of the time, as can be seen in Figure 5.1.1.

Equation 5.1.1 shows that the diffusional component of the faradaic charge is zero at time zero (t_0). However, from the fitted charge trend of Figure 5.1.1, it is clearly evident that at t_0 the charge does not correspond to zero. This behaviour can be explained by additional charge components, such as the double layer capacitance and surface adsorption phenomenon [172].

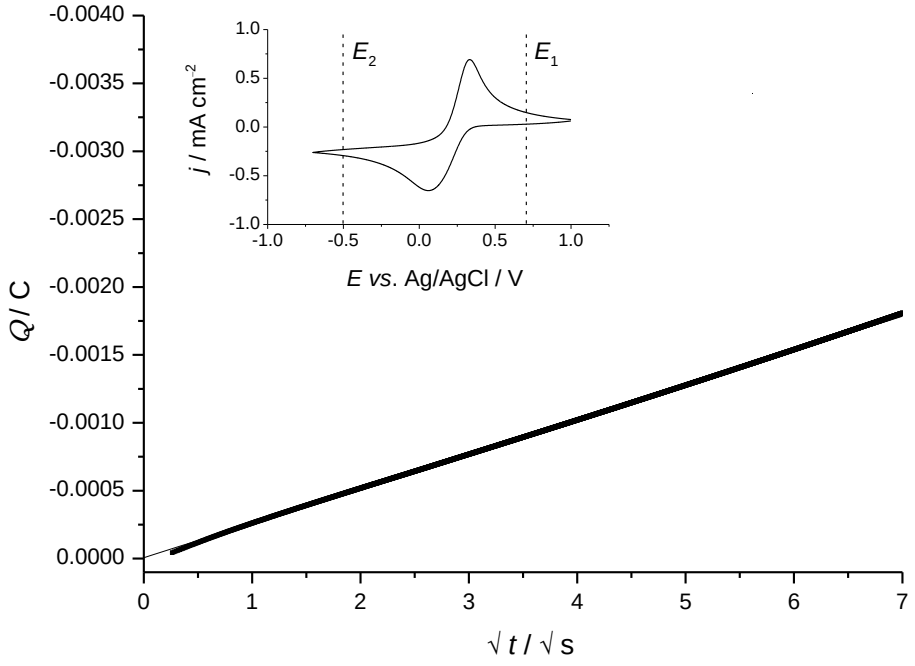

Figure 5.1.1. Chronocoulometry on oxygen–terminated BDD electrode in a 0.6 M NaCl + 10 mM $K_3Fe(CN)_6$ solution at (E_1) +0.7 V *vs.* Ag/AgCl for 10 s and at (E_2) –0.5 V *vs.* Ag/AgCl for 100 s. Inset shows the cyclic voltammogram in 0.6 M NaCl + 10 mM $K_3Fe(CN)_6$ at 25 mV s^{-1}. E_1 and E_2 indicate the potentials at which the chronocoulometry was made with respect to the stability of the $[Fe(CN)_6]^{3-/4-}$ redox system.

In order to test the electrochemical behaviour of the BDD substrate, anodic and cathodic potentiodynamic polarisations were performed in a 0.5 M H_2SO_4 solution within the electrode potential domain of both oxygen and hydrogen evolution reactions. The sulphuric acid solution was chosen instead of a 0.6 M NaCl solution to avoid the possible interference due to the simultaneous chlorine evolution reaction (ChlER) during the anodic polarisation. Figure 5.1.2 shows the anodic PP carried out on the oxygen–terminated BDD electrode in 0.5 M H_2SO_4. The reaction involved in the anodic process of Figure 5.1.2, at a potential greater than 2.1 V *vs.*

Ag/AgCl, is expressed by Equation 5.1.2 with an equilibrium electrode potential (E_{eq}) as assessed using Equation 5.1.3.

$$2H_2O \rightarrow O_2 + 4H^+ + 4e^- \quad 5.1.2$$

$$E_{eq} = +1.025 + \frac{2.303RT}{4F}\log a_{O_2} - 0.059\text{pH} / \text{V } \textit{vs.}\ \text{Ag/AgCl} \quad 5.1.3$$

where a_{O_2} is the oxygen activity. For an oxygen concentration of 0.20 mM (experimentally determined) and a pH of 0.88 (calculated using a molal activity coefficient of 0.1316 and a density of 1.0045 g cm^{-3} [173]) the equilibrium electrode potential was determined to be 0.974 V *vs*. Ag/AgCl. Therefore, at an onset OER potential of 2.10 V *vs*. Ag/AgCl the η_{OER} was estimated to be 1.12 V, using Equation 5.1.4.

$$\eta = E - E_{eq} \quad 5.1.4$$

As can be seen in Figure 5.1.2 inset, the extrapolated Tafel slope was +334 mV dec^{-1}, in line with results reported in the literature [89-92] (see Table 2.3.3). The estimated kinetic values (b_{OER} and η_{OER}) indicate an inhibited OER taking place at the BDD electrode, due to the establishment of weak interactions between the electrode surface and the reaction intermediates, *i.e.*, OH· and O· radicals [82].

It is generally reported that at BDD electrodes the OER undergoes a reaction mechanism which proceeds via the initial formation of OH· [90], as shown in Equation 2.3.9 of Section 2.3.2, with an equilibrium electrode potential as described in Equation 5.1.5 [93, 174].

$$E_{eq} = 2.15 - 0.059\text{pH} / \text{V } \textit{vs.}\ \text{Ag/AgCl} \quad 5.1.5$$

However, from Figure 5.1.2 there is no evidence of the oxidation signal H_2O / OH· at potential of about 2 V *vs*. Ag/AgCl [93], as instead reported in the literature [82, 93], at hydrogen– and fluorine–terminated BDD electrodes. This clearly suggests that in spite of the poor BDD property towards OER, stabilising interactions occurred between the BDD surface and the reaction intermediates due to the absence of the signal H_2O / OH·.

Figure 5.1.3 shows the cathodic PP for an oxygen–terminated BDD electrode in 0.5 M H_2SO_4. The predominant electrochemical reaction involved is the hydrogen evolution (see Equation 5.1.6).

$$2H^+ + 2e^- \rightarrow H_2 \quad 5.1.6$$

$$E_{eq} = -0.205 - 0.059\text{pH} / \text{V } \textit{vs.}\ \text{Ag/AgCl} \quad 5.1.7$$

As can be seen in the Figure 5.1.3 inset, the Tafel slope was estimated to be –600 mV dec^{-1}. Depending on the rate–determining step, which limits and controls the reaction kinetics, the Tafel slopes for HER are reported to range from –30 mV dec^{-1} to –120 mV dec^{-1} on platinum and ruthenium oxide electrodes [84, 86].

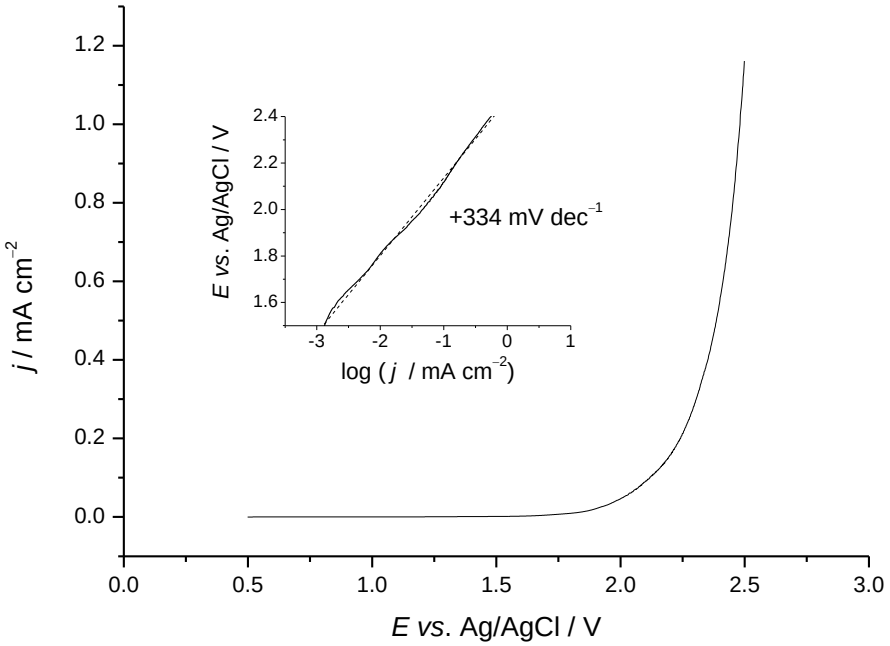

Figure 5.1.2. Anodic potentiodynamic polarisation on oxygen–terminated BDD electrode in 0.5 M H_2SO_4 at 1 mV s^{-1}. Inset displays the Tafel plot within the electrode potential interval from +1.5 V to +2.4 V *vs.* Ag/AgCl.

However, the b_{HER} value evaluated for the BDD electrode was significantly greater than those obtained using the more traditional electrodes and thus indicates an inhibited process.

The formation of atomic hydrogen on BDD has been observed only on substrates with a fluorine–terminated surface [82]. In fact, the HER at potentials close to the thermodynamic value for the H· / H^+ (see Equation 5.1.8 [82]) has been determined by Ferro and De Battisti on fluorine–terminated BDD and explained in terms of "lack of stabilising interactions between the electrode surface and the H· species" ($\eta_{H+/H\cdot} \approx 0$).

$$H^+ + e^- \rightarrow H\cdot \qquad E° = -2.505\,V \textit{ vs. } Ag/AgCl \tag{5.1.8}$$

$$2H\cdot \rightarrow H_2 \tag{5.1.9}$$

The reaction mechanism proposed accounted for the direct production of H· (Equation 5.1.8) followed by a chemical recombination step (Equation 5.1.9). In the current study the HER

clearly started at an onset potential of –1.2 V *vs*. Ag/AgCl, significantly distant from the equilibrium electrode potential of H^+ / H·. Therefore, a reaction mechanism which relies on the formation of hydrogen radicals cannot adequately describe the process occurring at our BDD substrate. A different reaction mechanism has been advanced by Yagi *et al*. [88] for BDD electrodes, see Equations 2.3.6 and 2.3.7 of Section 2.3.2. For this proposed mechanism, the BDD surface actively takes part in the HER via the formation of a carbon radical, see Equation 2.3.6 (see Chapter 2.3), and accordingly justifies the smaller η_{HER} on oxygen–terminated BDD than that at fluorine–terminated BDD. Considering the increase of the surface hydrophilicity observed when the BDD is cathodically and anodically polarised, Equation 2.3.7 can be replaced with Equation 5.1.10 [82].

$$H^+ + H_2O + \equiv C\cdot + e^- \rightarrow \equiv C - OH + H_2 \qquad 5.1.10$$

In our specific case, the η_{HER} was determined to be –0.95 V considering an HER onset potential of –1.2 V *vs*. Ag/AgCl and an equilibrium electrode potential of –0.257 V *vs*. Ag/AgCl (calculated using Equation 5.1.7 and considering a pH of 0.88).

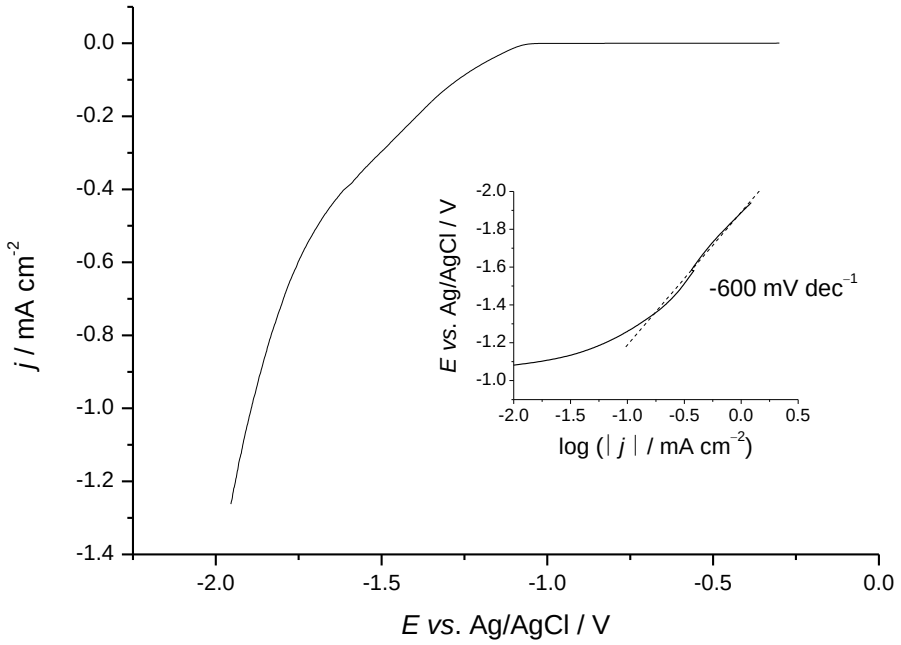

Figure 5.1.3. Cathodic potentiodynamic polarisation on oxygen–terminated BDD electrode in 0.5 M H_2SO_4 at 1 mV s^{-1}. Inset displays the Tafel plot within the electrode potential interval from –0.9 V to –2.0 V *vs*. Ag/AgCl.

The low double layer capacitance exhibited by the doped diamond electrodes is an important electrochemical characteristic that means this type of substrate is attractive especially for electro–analysis purposes. It has been reported that the double layer charging for BDD electrodes is directly linked to the quality of the electrode itself, *i.e.*, content of surface graphitic carbon [77]. High quality BDD electrodes (low levels of graphitic carbon) generally show lower capacitance values than those with high unsaturated carbon content. However, for low quality BDD electrodes, oxidation treatments have generally indicated decreases in the capacitance due to transformation of the graphitic carbon to the less active aliphatic alcohol, ketone or carboxylic–like groups [77]. According to Table 2.3.3 of Section 2.3 (which lists the literature capacitance values) the measured capacitance ranges from 0.05 μF cm^{-2} to 749 μF cm^{-2}, depending on the quality of the electrodes and the solution ionic strength. In our particular case, the double layer capacitance was evaluated by current density approach from CV tests (0.5 M H_2SO_4 solution), and using Equation 5.1.11.

$$I_c = AC\upsilon \qquad 5.1.11$$

Where I_c (A) is the capacitive current, A (cm^2) is the electrode area, C (F cm^{-2}) is the capacitance and υ (V s^{-1}) is scan rate at which the CVs were carried out [149]. The double layer capacitance, estimated at +0.400 V *vs*. Ag/AgCl, was determined to be 20 μF cm^{-2}. Since the electrochemical responses displayed in the current study are made on oxygen–terminated BDD electrodes, the calculated capacitance is in good agreement with those published in the literature for the same substrate (ca. 10 μF cm^2) [71, 77]. Evidently, experimental differences between the compared systems, such as electrolyte concentration and electrolyte type and doping level of the electrode, must be taken into account. Table 5.1.1 summarises the electrochemical characteristics (η, b and C) determined for the oxygen–terminated BDD electrode in 0.5 M H_2SO_4.

Table 5.1.1. Summary of the electrochemical values (overpotential, Tafel slope and capacitance) determined on BDD electrode in a 0.5 M H_2SO_4 solution.

η_{HER} / V	η_{OER} / V	b_{HER} / mV dec^{-1}	b_{OER} / mV dec^{-1}	C / μF cm^{-2}
–0.95	+1.12	–600	+334	20

Figure 5.1.4 shows the CV tests carried out in a 0.6 M NaCl + 10 mM $[Fe(CN)_6]^{3-/4-}$ solution at different scan rates, ranging from 25 mV s^{-1} to 300 mV s^{-1}. From cyclic voltammogram 1, performed in 0.6 M NaCl, the capacitive current was estimated using Equation 5.1.11. The double layer capacitance, determined at +0.4 V *vs*. Ag/AgCl, was

evaluated to be 6 μF cm^{-2}, slightly lower than that obtained in a 0.5 M H_2SO_4 solution. This behaviour was expected since the ionic strength of the sulphuric acid solution (1.5 mol L^{-1}) was more than two–fold greater than that of the 0.6 M NaCl solution (0.6 mol L^{-1}). Before making the CVs, the OCP of the system was determined for the redox system under investigation. The measured value was 0.147 V *vs*. Ag/AgCl, in close agreement with the equilibrium electrode potential associated with an equimolar concentration solution of $[Fe(CN)_6]^{3-/4-}$, (0.153 V *vs*. Ag/AgCl), see Equation 5.1.12.

$$E_{eq} = +0.153 + 0.059 \log \frac{[Fe(CN)_6^{3-}]}{[Fe(CN)_6^{4-}]} \text{ / V } vs. \text{ Ag/AgCl} \qquad 5.1.12$$

Considering the electrochemical features displayed by cyclic voltammograms 2–6 shown in Figure 5.1.4, two current signals ($C_{5.1}$ and $A_{5.1}$) are apparent within the potential range from –0.2 V to 0.5 V *vs*. Ag/AgCl. These responses are associated with the reduction / oxidation processes of the ferro / ferricyanide complexes, as shown in Equation 5.1.13.

$$[Fe(CN)_6]^{3-} + e^- \underset{k_{-e}}{\overset{k_e}{\leftrightarrow}} [Fe(CN)_6]^{4-} \qquad 5.1.13$$

with k_e and k_{-e} (constant rates) expressed as $k_e = k^0_{app} \exp[-\alpha_c F\eta / RT]$ and $k_{-e} = k^0_{app} \exp[\alpha_\alpha F\eta / RT]$ where k^0_{app} is the standard apparent electron transfer rate constant [175]. The electron transfer of the $[Fe(CN)_6]^{3-/4-}$ redox couple can be attributed to a quasireversible process, since the peak–to–peak potential difference (ΔE_p) was dependent on the scan rate and ranged from +0.186 V to +0.270 V, as can be seen in Table 5.1.2.

Table 5.1.2. Peak–to–peak potentials for an oxygen–terminated BDD electrode at different scan rates in a 0.6 M NaCl + 10 mM $[Fe(CN)_6]^{3-/4-}$ solution.

Scan rate / mV s^{-1}	ΔE_p / V
10	0.319
25	0.387
50	0.414
100	0.434
200	0.502
300	0.543

This behaviour was found to be in line with results reported in the literature, where generally oxygen–terminated BDD electrodes promote quasireversible electron transfers for the ferro / ferricyanide system [66].

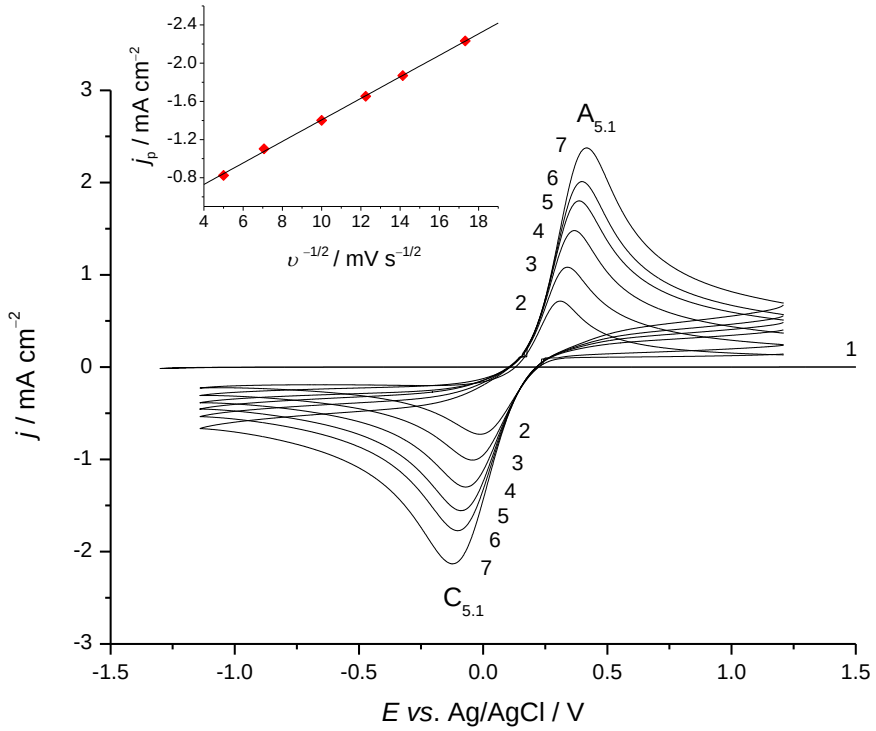

Figure 5.1.4. Cyclic voltammograms on oxygen–terminated BDD electrode in a 0.6 M NaCl + 10 mM $[Fe(CN)_6]^{3-/4-}$ solution at: (1) 25, (2) 50, (3) 100, (4) 150 (5) 200 and (6) 300 mV s^{-1}. Cyclic voltammogram (1) was carried out in 0.6 M NaCl at 50 mV s^{-1}. Inset shows the trend of the cathodic current peak density with respect to the square root of the scan rate.

Figure 5.1.4 inset shows the trend of the current density with respect to the square root of the scan rate: the good linear relationship between the two variables indicates a diffusion controlled process. In order to assess the electrochemical behaviour of the used oxygen–terminated BDD electrode, the standard apparent electron transfer rate constant for the $[Fe(CN)_6]^{3-/4-}$ system was estimated and compared with values reported in the literature [65, 66, 73-79]. Different electrochemical protocols and techniques can be used for assessing a quasireversible standard rate constant of an electron transfer process. For instance, Nicholson [176] correlated the peak–to–peak potential separation of a quasireversible process with a dimensionless parameter (ψ), which in turn was related to the k^0_{app}, see Equation 5.1.14. The simplicity of the procedure (k^0_{app} calculated from CVs) means that this method is often used in the literature.

$$\Psi = \frac{\left(\frac{D_\alpha}{D_c}\right)^{\alpha_e/2} k^0_{app}}{\sqrt{\left(D_\alpha \, \pi \, \upsilon \frac{z\,F}{R\,T}\right)}} \qquad 5.1.14$$

where D_a and D_c are the diffusion coefficients (cm^2 s^{-1}) of the oxidant and the reducer, respectively, and α_e is the symmetry factor [177]. In this case, the ψ parameter cannot be evaluated from the CVs found in Figure 5.1.4, since the ΔE_p provided in [176] are restricted to an interval ranging from 0.061 to 0.212 V. Therefore, the assessment of the k^0_{app} was achieved using quasi–steady PP and EIS.

Figure 5.1.5 shows the quasi–steady PPs at an oxygen–terminated BDD electrode in 0.6 M NaCl with $[Fe(CN)_6]^{3-/4-}$ concentrations ranging from 1.0 mM to 7.5 mM. Tests were conducted at 0.1 mV s^{-1} over the potential interval from (OCP –10 mV) to (OCP +10 mV).

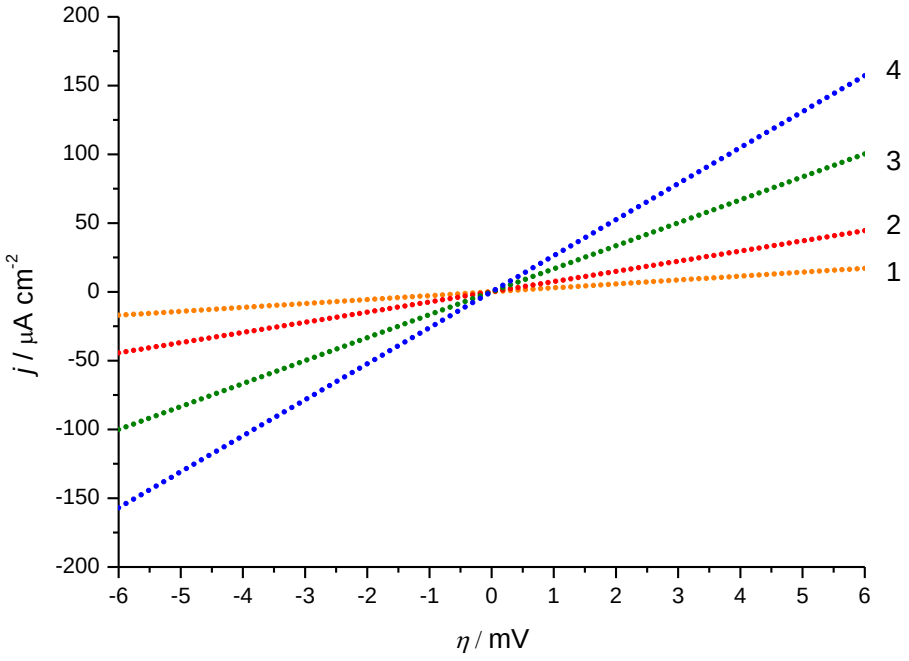

Figure 5.1.5. Quasi–steady potentiodynamic polarisation curves on an oxygen–terminated BDD electrode for: (1) 1.0, (2) 2.5, (3) 5.0 and (4) 7.5 × 10^{-3} M $[Fe(CN)_6]^{3-/4-}$ in a 0.6 M NaCl solution at 0.1 mV s^{-1}.

The experimental conditions allowed the $[Fe(CN)_6]^{3-/4-}$ electrode–surface concentrations to be stable, due to the low currents obtained by the slow scan rate and the restricted potential interval. Inspecting the quasi–steady PPs, an increase of the current density is clearly evident

as the concentration of the electro–active species increased. The model which approximates the electrode response, for these conditions is Equation 5.1.15 [178], which represents the low–field approximation of the Butler–Volmer equation, see Equation 5.1.16 [175].

$$j = j_0 \frac{z F}{R T} \eta \qquad 5.1.15$$

$$j = j_0 \left[c_{\alpha}^{*} \exp\left(\frac{\alpha_{\alpha} F \eta}{RT} \right) - c_{\mathrm{c}}^{*} \exp\left(\frac{-\alpha_{\mathrm{c}} F \eta}{RT} \right) \right] \qquad 5.1.16$$

where j_0 is the exchange current density and c_{α}^{*} and c_{c}^{*} are the surface concentrations of the oxidation / reduction species, respectively. The determination of the k_{app}^{0} was then achieved using Equation 5.1.17.

$$j_0 = F\, k_{\mathrm{app}}^{0}\, c_{\mathrm{a}}^{*(1-\alpha_{\alpha})}\, c_{\mathrm{c}}^{*(\alpha_{\mathrm{c}})} \qquad 5.1.17$$

Assuming $\alpha_{\alpha} = \alpha_{\mathrm{c}} = 0.5$ and approximating the surface concentrations with those of the bulk solution (c) (due to the low current flowing), Equation 5.1.17 can be rewritten as follows [175].

$$j_0 = F\, k_{\mathrm{app}}^{0}\, c \qquad 5.1.18$$

Therefore, considering Equation 5.1.18, the k_{app}^{0} values were estimated for all the concentration experiments, as seen in Table 5.1.3. The average value was assessed to be $(8.3 \pm 0.2) \times 10^{-4}$ cm s^{-1}.

Table 5.1.3. Kinetic parameters determined from quasi–steady potentiodynamic polarisation curves in a 0.6 M NaCl solution with different $[Fe(CN)_6]^{3-/4-}$ concentrations.

Conc. / mM	j_0 / μA cm^{-2}	k_{app}^{0} / cm s^{-1}
1.0	72	7.5×10^{-4}
2.5	188	7.8×10^{-4}
5.0	424	8.8×10^{-4}
7.5	667	9.3×10^{-4}
Average	–	$(8.3 \pm 0.2) \times 10^{-4}$

Figure 5.1.6 shows the (c) Nyquist and (b and d) Bode (phase angle *vs*. frequency and modulus *vs*. frequency) plots for the oxygen–terminated BDD electrode at different $[Fe(CN)_6]^{3-}$

$^{/4-}$ concentrations in a 0.6 M NaCl solution. It can be noted that the impedance behaviour is controlled by the electron transfer reaction occurring between the $[Fe(CN)_6]^{3-/4-}$ redox couple, having one characteristic semicircle associated with the time constant ($R_{ct}C$), as also shown in the Bode plot at ca. 2 kHz. Estimation of the k^0_{app} was achieved from the fitting of the impedance responses, using an equivalent circuit shown in Figure 5.1.6 a, which consisted of a solution resistance, R_s, a charge transfer resistance, R_{ct}, and a double layer capacitor, C. The assessment of the j_0 and k^0_{app} was achieved considering the extrapolated R_{ct} values and by means of Equation 5.1.18 [179] and 5.1.19.

$$j_0 = \frac{R\,T}{z\,F\,R_{ct}} \qquad 5.1.19$$

The charge transfer resistances, C, j_0 and k^0_{app} are listed in Table 5.1.4.

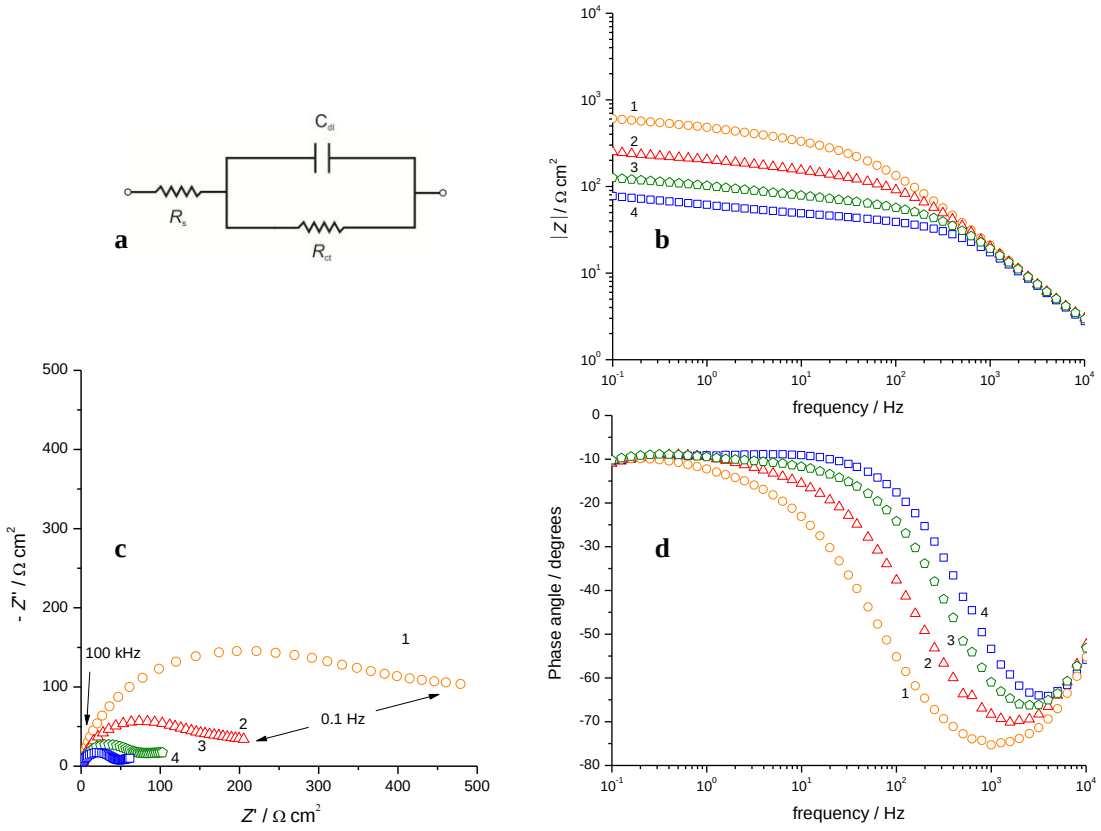

Figure 5.1.6. (b) Bode (Modulus *vs.* frequency), (c) Nyquist and (d) Bode (Phase angle *vs.* frequency) plots on an oxygen–terminated BDD electrode for: (1) 1.0, (2) 2.5, (3) 5.0 and (4) 7.5 mM $[Fe(CN)_6]^{3-/4-}$ in a 0.6 NaCl solution using a potential perturbation of ±5 mV at the open circuit potential over a frequency range of 10^4 Hz to 0.1 Hz.

As can be seen, the average C was estimated to be (4.1 ± 0.1) μF cm^{-2}, slightly lower than that obtained from CV tests, whereas the average of the k^0_{app} was calculated to be (9.0 ± 0.3) × 10^{-4} cm s^{-1}, in agreement with the value obtained with the quasi–steady PP.

Table 5.1.5 summarises the k^0_{app} and the C determined at the oxygen–terminated BDD electrode by means of CV, quasi–steady PP and EIS. Comparing the k^0_{app} available in the literature and reported in Table 2.3.2 of Section 2.3.2 and those experimentally determined in this section (by EIS and quasi–steady PP, see Table 5.1.5), a similar order of magnitude is apparent between 10^{-3} cm s^{-1} and 10^{-4} cm s^{-1} for the k^0_{app} reported in the literature [65, 66, 73-79], and ca. 10^{-4} cm s^{-1} for those experimentally assessed in this thesis.

Table 5.1.4. Fitted parameters determined from the electrochemical impedance spectroscopy of Figure 5.1.6; R_{ct} charge transfer resistance, C double layer capacitance, χ^2 accuracy of the fitting, j_0 exchange current density and the k^0_{app} apparent electron transfer constant rate.

Conc. / mM	R_{ct} / Ω cm^2	C / μF cm^{-2}	χ^2	j_0 / μA cm^{-2}	k^0_{app} / cm s^{-1}
1.0	315	4.2	20 × 10^{-3}	81	8.4 × 10^{-4}
2.5	129	4.3	15 × 10^{-3}	197	8.2 × 10^{-4}
5.0	64	4.0	12 × 10^{-3}	397	8.2 × 10^{-4}
7.5	31	4.1	9 × 10^{-3}	820	11.3 × 10^{-4}
Average	–	(4.1 ± 0.1)	–	–	(9.0 ± 0.3) × 10^{-4}

Evidently, the wide k^0_{app} value range found in the literature probably reflects the diverse experimental conditions, *i.e.*, doping level of the diamond substrate, type and concentration of the supporting electrolyte, temperature, etc. [176]. From the electrochemical characteristics shown in Figure 5.1.4 (peak–to–peak potentials) and the kinetic values (k^0_{app} and j_0) estimated by quasi–steady PP and EIS for the $[Fe(CN)_6]^{3-/4-}$ redox system, it appears that the BDD investigated in this work promoted a quasireversible electron transfer rather than a fully reversible behaviour, as generally determined at metallic electrodes. This indicates that the used oxygen–terminated BDD electrode has a semiconductor behaviour (rather than a metal–like behaviour), which is likely to be due to its relatively low boron–doping concentration (10^{20} atom cm^{-3}). Furthermore, the significantly low C values (estimated using CV and EIS) indicate

the good quality of the used diamond electrode and its promising characteristics for electro–analysis purposes.

Table 5.1.5. Apparent electron transfer rate constants and double layer capacitances determined using quasi–steady potentiodynamic polarisation and electrochemical impedance spectroscopy on the BDD electrode.

	C / μF cm^{-2} (CV)	C / μF cm^{-2} (EIS)	k^0_{app} / cm s^{-1} (PP)	k^0_{app} / cm s^{-1} (EIS)
Average	6	(4.1 ± 0.1)	(8.3 ± 0.2) × 10^{-4}	(9.0 ± 0.3) × 10^{-4}

5.2 Morphological Characterisation

Figures 5.2.1 and 5.2.2 show the AFM images of the BDD electrode surface. The BDD morphology has a flat and uniform surface characterised by the presence of aligned nano–abrasions.

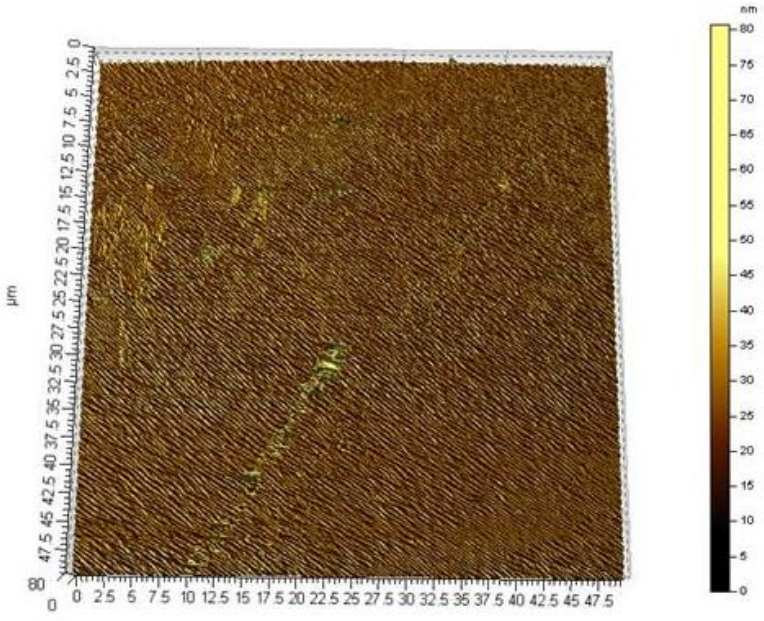

Figure 5.2.1. Atomic force microscopy 3D image of the BDD electrode surface features (50 × 50 μm area scale).

These surface nano–scratches are related to the polishing treatment performed by the original manufacturer. From Figure 5.2.2 and from its 2D roughness profile inset, it was possible to assess the abrasion roughness; the estimated value (ca. 5 nm) was in agreement with that provided by the manufacturer.

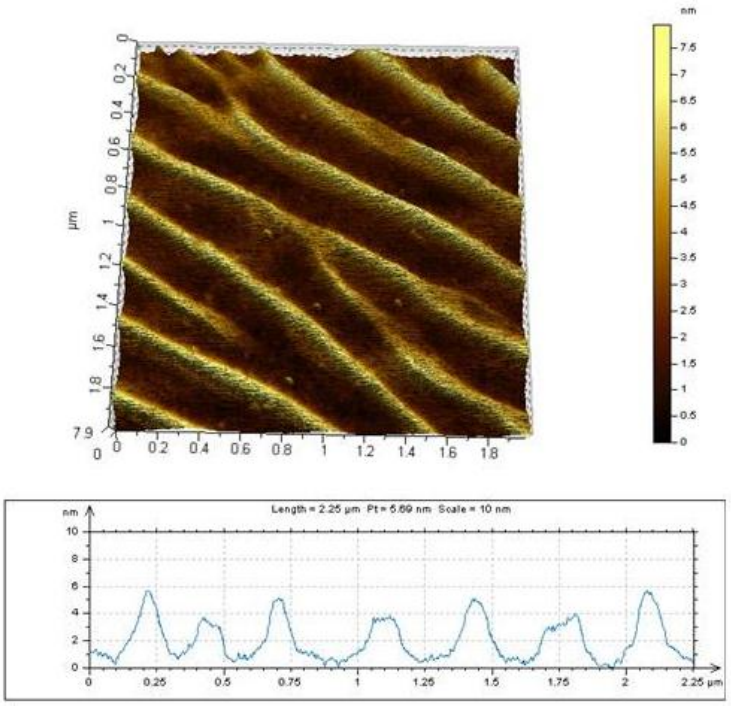

Figure 5.2.2. Atomic force microscopy 3D image of the BDD electrode surface features (2.0 × 2.0 µm area scale). Inset shows the 2D roughness profile of the scanned surface area.

5.3 Chemical Characterisation

As evident from the carbon binding energies (B.E.) often discussed in the literature (see Table 2.3.4 of Section 2.3.3), several chemical species are present at the diamond surfaces as a direct result of the deposition procedure and the electrode usage. The Scienta ESCA300 Database [180] reports a binding energy of 285.0 eV for quaternary carbon in a long aliphatic chain and a B.E. shift within the range –0.3 and 4.2 eV caused by the presence of double bonds and different oxygen–containing chemical functions, see Table 5.3.1. Figure 5.3.1 shows the XPS survey spectrum of the BDD electrode. The characteristic B.E. signal centred at 283.9 eV was attributed to C 1s carbon, while the signals at 530.9 eV and at 189.9 eV were associated with O 1s and the B 1s responses, respectively. The relative chemical abundance determined for each component was estimated to be 89.2 % for carbon, 10.3 % for oxygen and 0.5 % for boron.

Table 5.3.1. Scienta ESCA300 Database energy shifts for the C 1s binding energy (eV) with respect to the C 1sp^3 [180].

Chemical functions	Binding energy shift / eV
C=C	–0.3
C–O–C	+1.4, +1.5
C–OH	+1.5
R–C(O) –R	+2.8, +3.5
R–C(O)O–R	+3.9, 4.2

Considering the C 1s response, see Figure 5.3.2, the fitting of curve 1 produced three peaks, centred at 284.7 eV (peak 2), 286.1 eV (peak 3) and 288.4 eV (peak 4). According to Table 5.3.1 the peaks 2–4 can be assigned to the bulk diamond carbon (peak 2), the alcoholic / etheric group carbon (peak 3) and the carbonyl / estheric carbon (peak 4). Table 5.3.2 summarises the B.Es as well as the atomic abundances, *i.e.*, C, O and B, and the different photo–electron take–off angle tests; as can be seen there is good agreement between the B.E. determined for the oxygen–terminated BDD electrode and those reported in the literature (also see Table 2.3.4 for comparison).

Table 5.3.2. Summary of the experimental binding energy (eV) and atom abundances for the BDD electrode surface.

Angle	C %	O %	B %	O 1s	B 1s	C sp^3 (bulk diam.)	–C–OH (alchol)	O–C–O (ether)	2R–C=O (carbonyl)	R–C(O)–OH R–C(O)–OC (Carboxyl; Esther)
75	89.2	10.3	0.5	530.9	189.9	284.7	286.1	286.1	288.4	288.4
65	89.2	10.2	0.6	530.9	189.9	–	–	–	–	–
45	90.1	9.3	0.6	530.9	189.9	–	–	–	–	–
0	91.7	7.9	0.4	530.9	189.9	–	–	–	–	–

The related carbon abundances of the bulk diamond, alcoholic / etheric and carbonyl / estheric species were determined to be 79.7 %, 15.7 % and 4.5 %, respectively. This finding

revealed a surface abundance of the carbon oxygen–containing species of more than 20 % of the total carbon content, (peak 4 + peak 3) / peak 2.

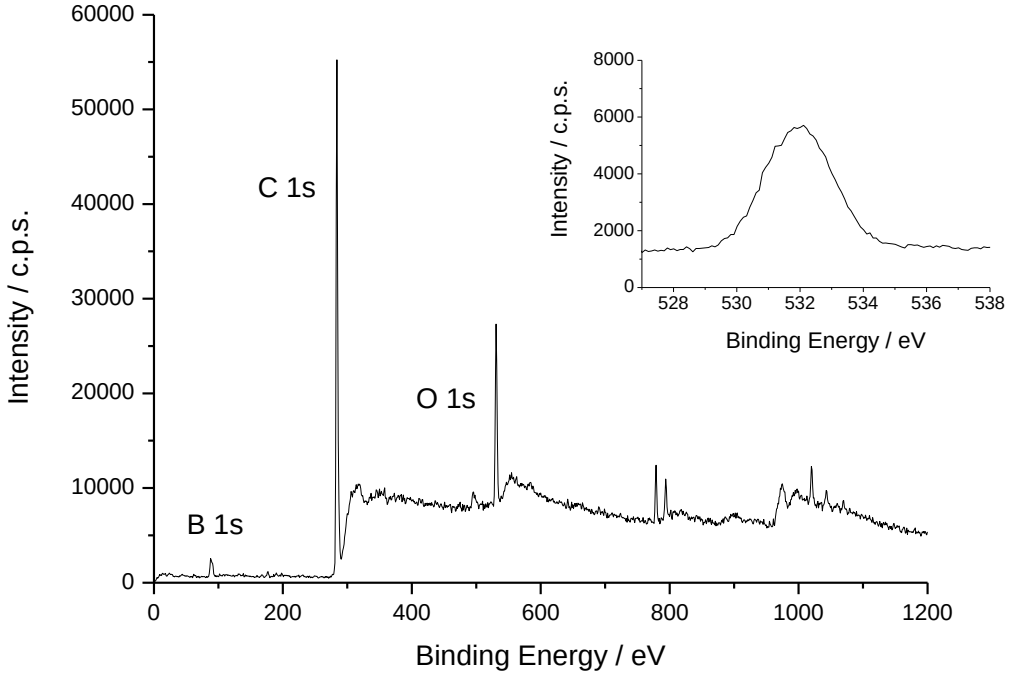

Figure 5.3.1. XPS survey spectrum of BDD electrode at an incident X–ray angle of 75°. Inset shows an enlargement of the O 1s spectrum.

It is well–known that the XPS technique is a characterisation method which provides information of the average chemical composition of the top 3–10 nm of the surface. The size of the investigated superficial thicknesses is directly related to the angle of the incident photoelectron X–ray to the surface: the higher the angle and the smaller the thickness of the investigated surface, meaning a more superficial analysis [49]. Regarding the XPS measurements carried out at different incident X–ray angles, an increase of the photoelectron take–off angle produced a marked weakening of the O 1s signal and a simultaneous increase of the C 1s response, while the boron content was present in the concentration range 0.4 % to 0.6 % for all the XPS tests. In particular, the oxygen abundance was evaluated to be 10.2 %, 9.3 % and 7.9 %, while the carbon abundance was estimated 89.2 %, 90.1 % and 91.7 %, respectively for the 75°, 45° and the 0° XPS measurements (Figures not displayed).

This behaviour was expected since the 75° photoelectron take–off angle test produced an average chemical composition more representative of the sample surface (the thickness

surveyed was generally 3 nm) than the normal photoelectron take–off angle test, which provides a chemical average composition response associated to the first 10 nm layer of the sample [49].

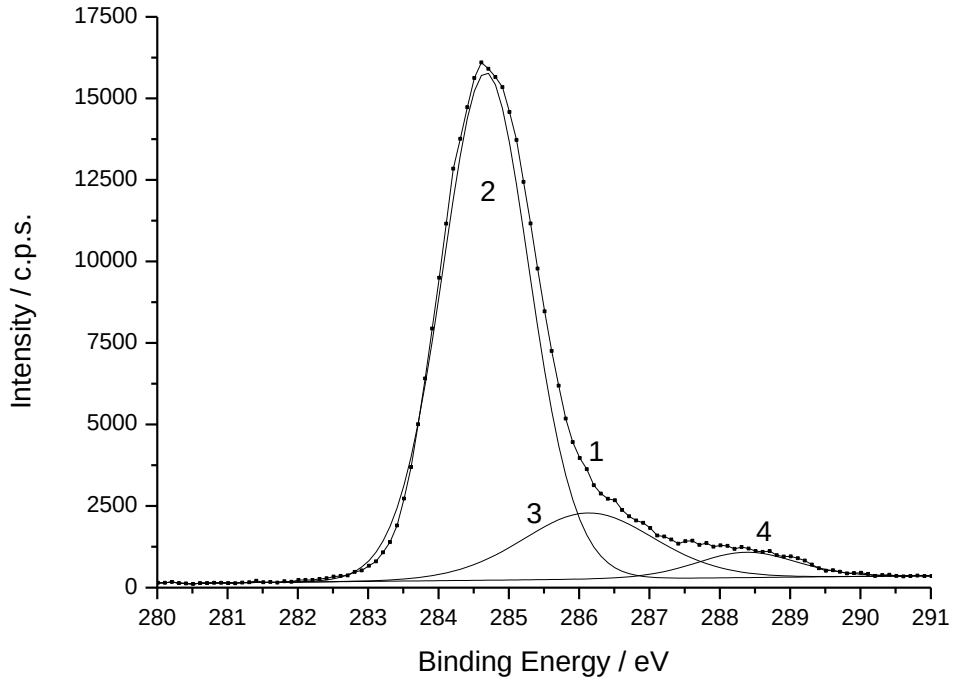

Figure 5.3.2. C 1s spectrum of BDD electrode at an incident X–ray angle of 75° angle (1). Peaks (2), (3) and (4) represent the fitted signals of the recorded XPS response.

In conclusion, from the XPS data it is possible to infer the good quality of the BDD substrate utilised in the current study, since the spectra did not show any significant graphitic sp^2 carbon content of, which is considered as an impurity.

5.4 Summary

A preliminary electrochemical characterisation of the BDD performance was achieved in order to compare its electrochemical behaviour with those generally reported in the literature. Furthermore, since it has been indicated a strict dependence between the BDD electrochemical performance and its chemical surface composition [66], XPS investigations were also carried out to assess the chemical functional groups present at the electrode surface.

The reactivity of the BDD electrode was studied with the $[Fe(CN)_6]^{3-/4-}$ redox couple using CV, PP and EIS. CVs recorded in a 10 mM ferri / ferrocyanide solution at different scan rates,

suggested a quasireversible electron transfer taking place at the BDD electrode, since the peak–to–peak potential exceeded the theoretical value of 0.059 V for a one electron–transfer reaction. Corroborations of the slow kinetic were also provided by the quasi–steady PPs and EIS tests, which in fact revealed k^0_{app} values of (8.3 ± 0.2) × 10^{-4} cm s^{-1} and (9.0 ± 0.3) × 10^{-4} cm s^{-1}, for the PP and for the EIS, respectively, hence confirming a quasireversible process [181]. The k^0_{app} values generally reported in the literature (for $[Fe(CN)_6]^{3-/4-}$ at BDD electrodes) suggest a slow process, often attributed to a quasireversible or an irreversible process. A significant influence of the BDD chemical termination has also been highlighted in the literature for BDD electrodes: "as–formed" doped diamond electrodes, which display a hydrogen–terminated surface, promote a faster electron transfer for $[Fe(CN)_6]^{3-/4-}$ than those with an oxygen–terminated surface [66]. The k^0_{app} reported within this study are in good agreement with those reported for oxygen–terminated electrodes, at 10^{-4} cm s^{-1}.

Further electrochemical investigations carried out in a 0.5 M H_2SO_4 solution highlighted other important BDD characteristics, such as (*i*) the wide potential window available and (*ii*) the low background current. In particular, considering (*i*), CV data showed a wide window of polarisability mainly related to the high overpotentials displayed towards both the oxygen and hydrogen evolution reactions. Corroborations of this finding were provided by the additional Tafel polarisation tests, carried out in sulphuric acid solutions within the oxygen and the hydrogen evolution domains. Anomalously high Tafel slopes for both of the electrochemical reactions, that is, +0.334 and –0.600 V dec^{-1}, were determined at the BDD electrode. Concerning (*ii*), capacitance values within the range from 10^{-6} and 10^{-4} F cm^{-2} [77] have been reported in the literature so far and related to the quality of the electrode, *i.e.*, the higher the quality of the diamond and the lower is the capacitive current. In this report, a value of 20 μF cm^{-2} was determined in 0.5 M H_2SO_4, whereas values of 6 μF cm^{-2} and 4 μF cm^{-2} were assessed in 0.6 M NaCl. These results, provide information of the good BDD electrode quality and also indicated its favourable characteristics for electro–analytical purposes.

The morphology and the chemical composition of the BDD surface were investigated using AFM and XPS. The AFM analysis indicated an electrode surface characterised by its smoothness, whereas the XPS tests supported the electrochemical responses, that is, the high quality of the electrode due to the absence of the sp^2 graphitic carbon, which is considered as an impurity.

6. Copper–Ion Detection on Boron–Doped Diamond Electrode

In the next Section the behaviour of the copper(I)–copper(II) system has been studied on BDD electrode in different supporting electrolytes, *i.e.*, $NaClO_4$, Na_2SO_4 and NaCl, in order to understand the influence of the electrolyte–anion on the copper electrochemical response.

Previously, Section 2.4 highlighted that chloride has an important role on the copper(I)–copper(II) electrochemical behaviour. Indeed, the involvement of chloride in the electron transfer process can be particularly relevant especially when its solution concentration significantly changes, due to the formation of different metal ion–complexes. During NAB crevice corrosion in seawater, the chloride concentration can vary from an initial 0.6 M (level naturally present in the solution) to ca. 3 M [7]. Accordingly, the kinetic and the reaction mechanism of the copper(I) / copper(II) electron transfer have been investigated in Section 6.1 at chloride levels which ranged from 0.2 M to 3.0 M by using cyclic voltammetry and quasi–steady potentiodynamic polarisation. Full details and protocols of the techniques and equipment used have previously been provided in Chapter 3.

6.1 Copper–Ion Detection on Boron–Doped Diamond Electrode

Preliminary investigations of the electrochemical behaviour of the copper(I)–copper(II) system were achieved in different electrolyte compositions to highlight the key–role played by the electrolyte–anion in the electron transfer process. The three electrolyte compositions considered in this study were (*i*) $NaClO_4$, (*ii*) Na_2SO_4 and (*iii*) NaCl solution, at concentrations of 0.6 M, 0.2 M and 0.6 M, respectively, in order to have an equivalent ionic strength of 0.6 M. The background electrolyte choice was determined by their diverse complexing properties, which in turn can significantly affect the metal–ion electrochemical behaviour. Perchlorate–based electrolytes were particularly considered since ClO_4^- generally shows an unreactive behaviour as a complexing agent [182]; conversely, chloride significantly stabilises copper(I) and, depending on the solution concentration, a number of copper(I)–chloride complexes can been formed, see Section 2.4. All the solution pHs were corrected at 4.5 to avoid formation of cuprous and cupric oxides.

Figure 6.1.1 shows an overlay of cyclic voltammograms carried out in 0.6 M $NaClO_4$ containing variable copper(II) concentrations, from 0.15 mM to 3.00 mM. At potentials greater than 1.0 V *vs*. Ag/AgCl the CVs showed negligible anodic currents, due to the high overpotentials exhibited by BDD electrodes for the OER (see Section 5.1). Conversely, the

HER was determined to occur at ca. –0.9 V *vs*. Ag/AgCl, which is a potential more positive than those generally assessed at BDD electrodes in neutral pHs. This behaviour indicated an increase of the BDD catalytic activity towards the HER due to the presence of electro–deposited copper nanoparticles.

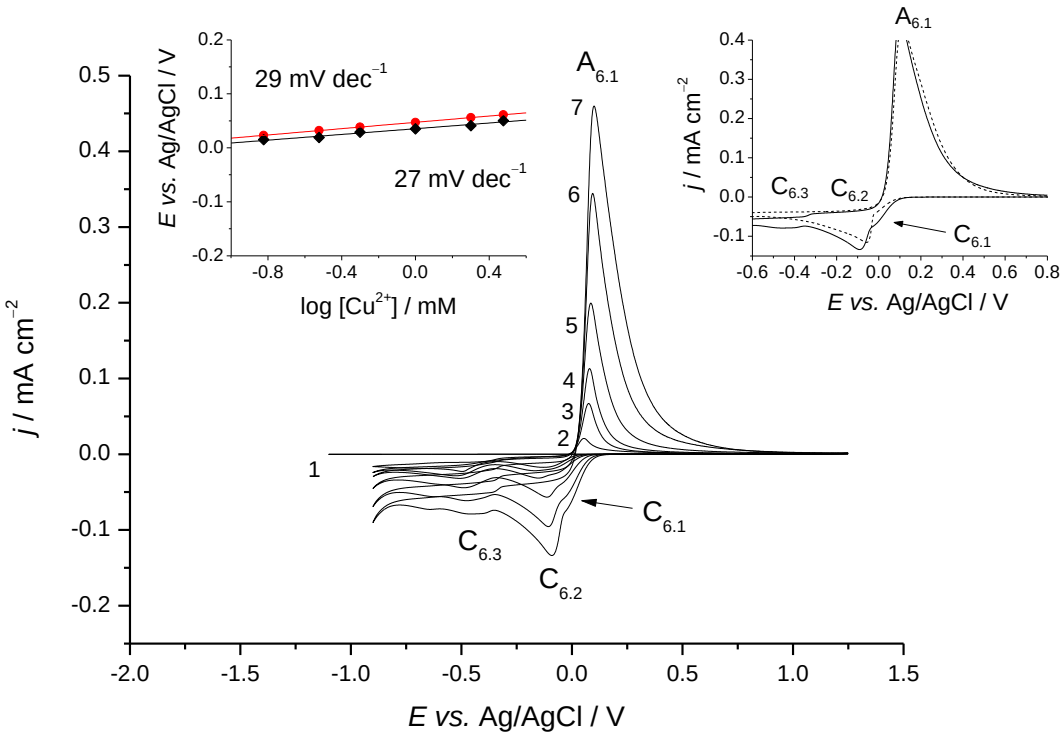

Figure 6.1.1. Cyclic voltammograms carried out on a BDD electrode in (1) 0, (2) 0.15, (3) 0.30, (4) 0.50, (5) 1.00, (6) 2.00 and (7) 3.00 mM $CuClO_4$ in a 0.6 M $NaClO_4$ solution (pH 4.5) at 10 mV s^{-1}. Left hand side inset shows a comparison between the theoretical equilibrium potentials (red circles) and the experimental equilibrium potentials (black diamonds). Right hand side inset highlights the cyclic voltammograms performed at BDD electrode in (dashed line) deaerated ($O_2 \leq 3$ μM) and (solid line) aerated 0.6 M $NaClO_4$ + 3 mM $CuClO_4$ solutions at 10 mV s^{-1}.

By inspecting CVs 2–7, it is worth noting that a number of cathodic signals ($C_{6.1}$–$C_{6.3}$) were recorded whereas only one sharp oxidation peak, $A_{6.1}$ at a potential of ca. 0.070 V *vs*. Ag/AgCl, characterised the anodic responses. The equilibrium electrode potential recorded at the lowest copper(II) concentration (0.15 mM) was 0.005 V *vs*. Ag/AgCl and progressively shifted towards more positive values as the copper(II) concentration increased; at 3 mM the equilibrium potential was determined to be 0.026 V *vs*. Ag/AgCl. The underlying process occurring in Figure 6.1.1 can be described by Equation 6.1.1, with an equilibrium electrode potential expressed by Equation 6.1.2 [162].

$$Cu^{2+}_{(aq)} + 2e^- \leftrightarrow Cu^{(0)}_{(ads)} \quad 6.1.1$$

$$E_{eq} = 0.135 + \frac{2.303RT}{2F} \log \alpha_{Cu^{2+}} \text{ / V } \textit{vs.} \text{ Ag/AgCl} \quad 6.1.2$$

Since the copper–ion test solutions were significantly dilute, the equilibrium potentials were calculated approximating the copper(II) activity to that of the copper(II) molar concentration, giving values which ranged from 0.023 V to 0.061 V *vs*. Ag/AgCl, as the copper(II) concentration increased from 0.15 mM to 3.00 mM, respectively. In Figure 6.1.1 the left hand side inset shows a comparison between the equilibrium potentials calculated using Equation 6.1.2 (red circles) and those experimentally assessed at the BDD electrode (black diamonds). The good agreement between the two data sets, *i.e.*, theoretical (29 mV dec^{-1} = 2.303 RT / 2F) and the experimental (27 mV dec^{-1}), suggests that the background anion does not participate in the direct formation of copper(II) complexes, as expected using a chemically inert species such as perchlorate [182]. Regarding the shape of the electrode responses 2–7, the presence of one sharp and asymmetric anodic peak ($A_{6.1}$) indicated that the copper(0) oxidation occurred via one–step electron transfer process producing copper(II). Further corroboration of the electrode mechanism was also achieved by carrying out CVs in the same solutions but at higher potential scan rates (Figure A_7.shown in the Appendix), where transient copper(I) species generated during the electrochemical process could be detected. However, the similar current responses for scan rates up to 300 mV s^{-1} confirmed an oxidation mechanism involving the copper(0) / copper(II) system.

Grujicic and Pesic [183] studied the reaction and nucleation mechanisms of copper electrodeposition at a glassy carbon electrode in a 1 M $(NH_4)_2SO_4$ solution (I_m of ca. 2.5 m) at pH 4. An electrochemical response characterised by the presence of a sharp anodic peak was attributed to Equation 6.1.1, followed by a shoulder–peak associated with the oxidation of copper(I) to copper(II). The presence of copper(I) was explained in terms of a disproportionation mechanism, which involved the electro–generated copper(II) (present within the Nernst diffusion layer) and the adsorbed metallic copper, as shown in Equations 6.1.3.

$$Cu^{(0)}_{(ads)} + Cu^{2+}_{(aq)} \rightarrow 2Cu^{+}_{(aq)} \quad 6.1.3$$

For Figure 6.1.1, the electrode responses did not show any evidence of copper(I) oxidation, thus indicating negligible disproportionation.

Figure 6.1.2 shows an overlay of cyclic voltammograms performed in 2.0 M $NaClO_4$ + 3 mM $CuClO_4$ solution at scan rates from 10 mV s^{-1} to 300 mV s^{-1}. For scan rates greater than 50 mV s^{-1}, an additional shoulder–peak is clearly apparent ($A_{6.2}$ at ca. 0.3 V *vs*. Ag/AgCl), which is

dependent on the square root of the scan rate (see Figure 6.1.2 inset), hence indicating a diffusion–controlled behaviour. It is worth noting that signal $A_{6.2}$ was only evident at scan rates higher than 50 mV s^{-1}, probably resulting from a higher accumulation of copper(II) within the Nernst diffusion layer. Also, the higher ionic strength significantly improved the copper(I) detectability, due to its influence on the Nernst diffusive layer its effect generally observed on the Nernst diffusion layer. In fact, an increase of the I_m often produces a compression of the Nernst diffusion layer, which in turns results in higher copper(II) and copper(I) concentrations at the near electrode surface [160].

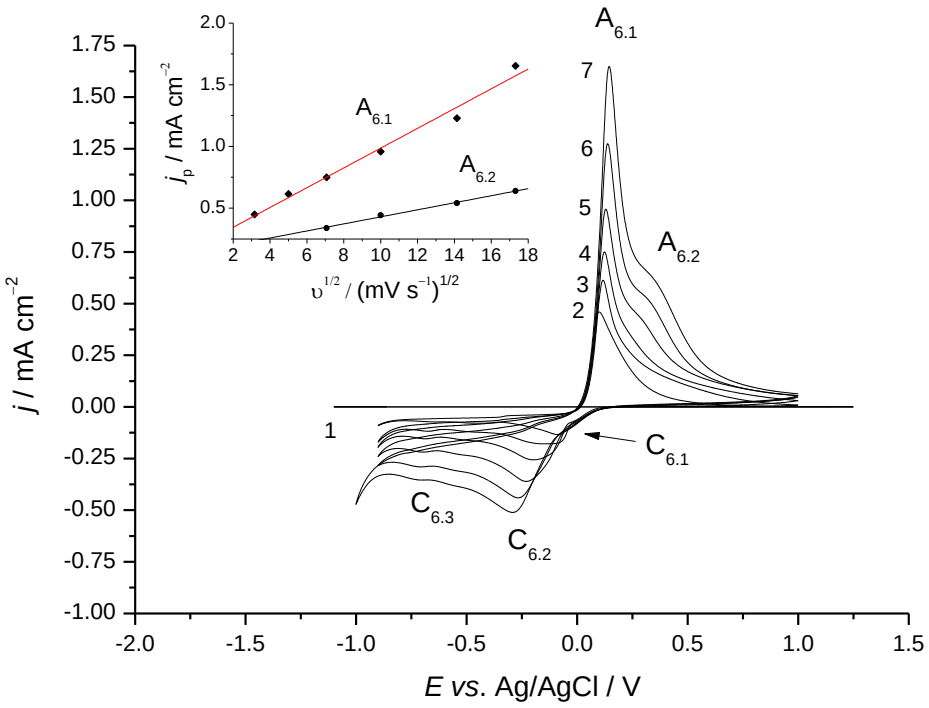

Figure 6.1.2. Cyclic voltammograms carried out on a BDD electrode in a 0.6 M $NaClO_4$ + 3.00 mM $CuClO_4$ solution (pH 4.5) at (2) 10, (3) 25, (4) 50, (5) 100, (6) 200 and (7) 300 mV s^{-1}. The inset shows the linear trends of the current peak density of the $A_{6.1}$ (diamond) and $A_{6.2}$ (circle) signals as a function of the square root of the scan rate. Cyclic voltammogram (1) was performed in a 2.0 M $NaClO_4$ solution at 10 mV s^{-1}.

Regarding the cathodic sweeps, a more complex scenario can be seen in the responses 2–7 of Figures 6.1.1 and 6.1.2, in fact, one shoulder–peak $C_{6.1}$ and two distinct signals ($C_{6.2}$ and $C_{6.3}$) were evident within the potential range from –0.010 V to –0.600 V *vs.* Ag/AgCl. According to results reported in the literature [183], the signal $C_{6.2}$ can be attributed to the reduction of

copper(II) to metallic copper, see Equation 6.1.1, which proceeds via one–step electron transfer process. Concerning the shoulder–peak $C_{6.1}$, Grujicic and Pesic [183] attributed this signal to the electro–generation of copper(I) via Equation 6.1.4, using a glassy carbon electrode–generator (which performing CVs in a 10 mM copper(II) solution electro–formed copper(I)) and a platinum microelectrode–detector (which was located in close proximity to the generator so as to detect the copper(I) formation).

$$Cu^{2+}_{(aq)} + e^- \rightarrow Cu^{+}_{(aq)} \qquad 6.1.4$$

However, as can be seen in the CVs of the right hand side inset in Figure 6.1.1, when the solution was deaerated by sparging with nitrogen gas (resulting in an oxygen level ≤ 3 μM) the signal $C_{6.1}$ nearly disappeared. This behaviour indicates that signal $C_{6.1}$ cannot be simply described by the reduction of copper(II) to copper(I), since, as it appears from Equation 6.1.4, the process occurs independently from oxygen. Furthermore, due to the absence of peak $C_{6.3}$, the cathodic response can be attributed to the oxygen reduction reaction (see Equation 6.1.5).

$$O_2 + 4H^+ + 4e^- \rightarrow 2H_2O \qquad 6.1.5$$

Despite the apparently simple electrochemical behaviour of copper(II), different responses have been reported at BDD electrodes in copper(II) containing sulphate solutions. Generally, either a process undergoing an initial metallic–copper cluster formation followed by its rapid dissolution before being oxidised at the electrode surface [115] or a process characterised by a two–step electron transfer process [116] have been reported in the literature on diamond substrates. Also, Matsushima *et al*. [184] indicated a copper(0) anodic behaviour (deposited at BDD electrodes in sulphate solutions at pH 5) characterised by a one–step electron transfer followed by the oxidation of copper(I), produced by a disproportionation reaction (see Equation 6.1.3).

Figure 6.1.3 shows the electrochemical responses recorded in 0.2 M Na_2SO_4 at copper(II) concentrations ranging from 0.15 M to 3.00 mM. It is worth noting that different responses were determined as the copper(II) concentration was increased. Indeed, as can be seen in the Figure 6.1.3 inset, which reports the CVs at copper(II) concentrations of 0.15 mM (1, dashed line), 0.30 mM (2, solid line) and 0.50 mM (3, red line), the lack of anodic signals at the lowest copper concentration indicates that the deposited metal dissolved into solution before being detected at the electrode. The presence of an anodic–broad peak was recorded only at concentrations of 0.30 mM and 0.50 mM and at potentials considerably more positive (ca. 0.4 V *vs*. Ag/AgCl) than those of $A_{6.1}$: this response was attributed to the oxidation of copper(I) to copper(II), as reported in the literature [115]. Furthermore, looking closely at CV 3, two

additional small peaks ($A_{6.1}$ and $A_{6.2}$) were also recorded and assigned to the oxidation of metallic copper to copper(II) and copper(I) to copper(II), respectively. Peaks $A_{6.1}$ and $A_{6.2}$ can be better appreciated in CVs 5–7, where the copper(II) concentration ranged from 1.00 mM to 3.00 mM.

The different overpotentials observed between peaks $A_{6.2}$ and $A_{6.3}$ (both assigned to the oxidation of copper(I)) suggests that different mechanisms took place. Nakabayashi *et al.* [115] confirmed by means of Mie scattering measurements that the broad and shallow signal at ca. 0.45 V *vs*. Ag/AgCl was related to the oxidation of copper(I), which was produced via a disproportionalisation (see Equations 6.1.5–6.1.9). According to this reaction mechanism, signal $A_{6.3}$ (0.43 V *vs*. Ag/AgCl) can be attributed to the oxidation of copper(I), where the large overpotential may reflect the poor electro–catalytic properties of the BDD electrode.

$$nCu^{2+}_{(aq)} + 2ne^- \rightarrow n[Cu^{(0)}]_{ads} \xrightarrow{\text{ClusterForm.}} [Cu^{(0)}_n]_{ads} \qquad 6.1.5$$

$$[Cu^{(0)}_n]_{ads} \xrightarrow{\text{Diffusion}} [Cu^{(0)}_n] \qquad 6.1.6$$

$$nCu^{(0)} + nCu^{2+}_{(aq)} \rightarrow nCu^{+}_{(aq)} \qquad 6.1.8$$

$$nCu^{+}_{(aq)} \rightarrow nCu^{2+}_{(aq)} + ne^- \qquad 6.1.9$$

Conversely, the reaction mechanism behind signal $A_{6.2}$ must relate to a number of interactions between copper(I) and the electrode surface in order to explain the significantly reduced overpotential. An enhanced BDD electrode–catalytic activity, obtained by the presence of residual copper nanoparticles adsorbed at the diamond surface [185], can possibly explain the improved kinetics. Regarding the cathodic sweeps, only one cathodic peak $C_{6.2}$ was apparent and attributable to the reduction of copper(II) to copper(0). Furthermore, similar to the tests shown in Figure 6.1.1, the $C_{6.3}$ signal was assigned to the oxygen reduction reaction.

The electrochemical tests performed in perchlorate and sulphate media containing different copper(II) concentrations highlighted a similar electrochemical behaviour, which was characterised by a one–electron transfer process (peaks $A_{6.1}$ and $C_{6.2}$). However, CVs made in sulphate solutions showed oxidation signals ($A_{6.2}$ and $A_{6.3}$) not observed in perchlorate media and associated with the oxidation of copper(I) (obtained by a disproportionation reaction). This particular behaviour suggests that the adhesion of the nanoparticles in sulphate solutions was lower than that obtained in perchlorate solution. Corroboration of this insight was attained by estimating the ratios between the anodic and cathodic charge densities for CV 7 of Figure 6.1.3 and CV 7 of Figure 6.1.1. The near doubling of the charge ratio determined for perchlorate solutions (0.89) in comparison with the sulphate media (0.43) indicates that almost all the

deposited copper nanoparticles were stripped off during the anodic sweep in $NaClO_4$ whereas, conversely those electrodeposited in a sulphate solution principally diffused into solution before being oxidised.

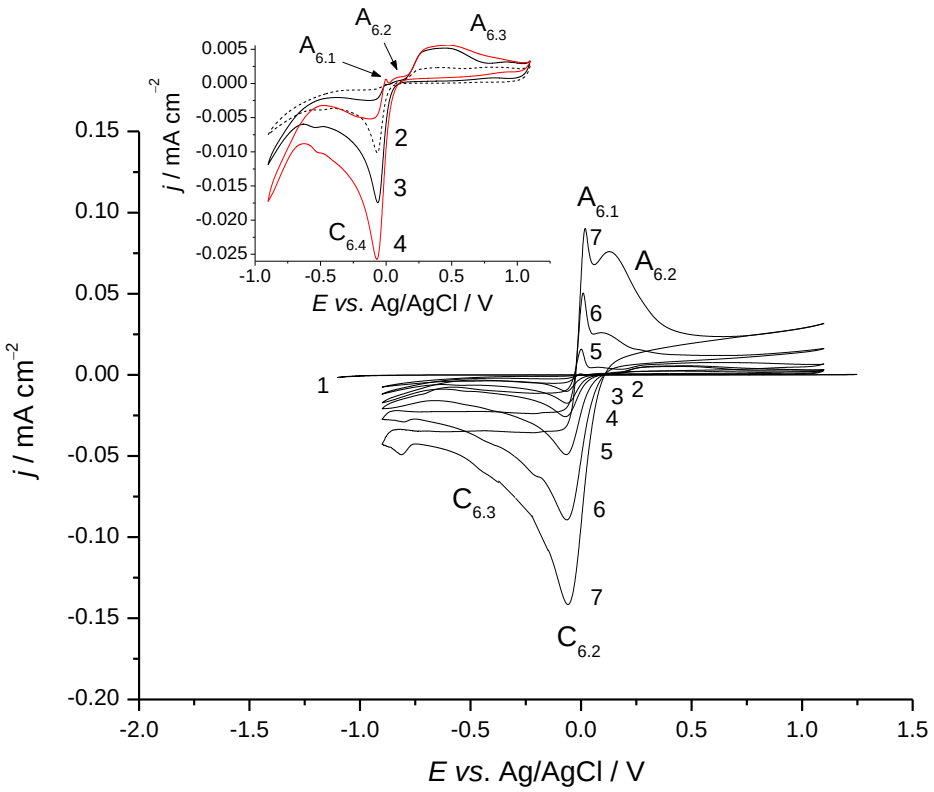

Figure 6.1.3. Cyclic voltammograms carried out on a BDD electrode in (1) 0, (2) 0.15, (3) 0.30, (4) 0.50, (5) 1.00, (6) 2.00 and (7) 3.00 mM $CuSO_4$ in a 0.2 M Na_2SO_4 solution (pH 4.5) at 10 mV s^{-1}. The inset shows cyclic voltammograms carried out in 0.2 M Na_2SO_4 solution with 0.15 mM (dashed line), 0.30 mM (solid line) and (red line) or 0.50 mM $CuSO_4$ additions at 10 mV s^{-1}.

In contrast to the measurements performed in perchlorate and sulphate media, experiments carried out in chloride containing solutions presented two well–separated pairs of peaks $A_{6.4}$ / $C_{6.5}$ and $A_{6.5}$ / $C_{6.4}$, as can be seen in Figure 6.1.4. Considering the copper(I) and the copper(II) speciation shown in Figures 2.4.1 and 2.4.2, at the chloride level of 0.6 M NaCl (which equals an activity of 0.4 M [173]) the $CuCl_2^-$ and $Cu^{2+}_{(aq)}$ complexes result the predominant species ($\alpha_{CuCl_2^-}$ = 0.73 and $\alpha_{Cu^{2+}}$ = 0.71). Accordingly, the electrochemical processes $A_{6.5}$ / $C_{6.4}$ and $A_{6.4}$ / $C_{6.5}$ can be described by Equations 6.1.10 and 6.1.11, respectively.

$$Cu^{2+}_{(aq)} + 2Cl^- + e^- \rightarrow CuCl_2^- \qquad 6.1.10$$

$$CuCl_2^- + e^- \rightarrow Cu + 2Cl^- \qquad 6.1.11$$

Comparing CVs 3 and 2 of Figure 6.1.4, it can be seen that an extension of the electrode potential towards more negative values produced an increase of the $A_{6.5}$ peak current, due to the high $CuCl_2^-$ concentration obtained within the Nernst diffusion layer by the stripping $C_{6.7}$ peak.

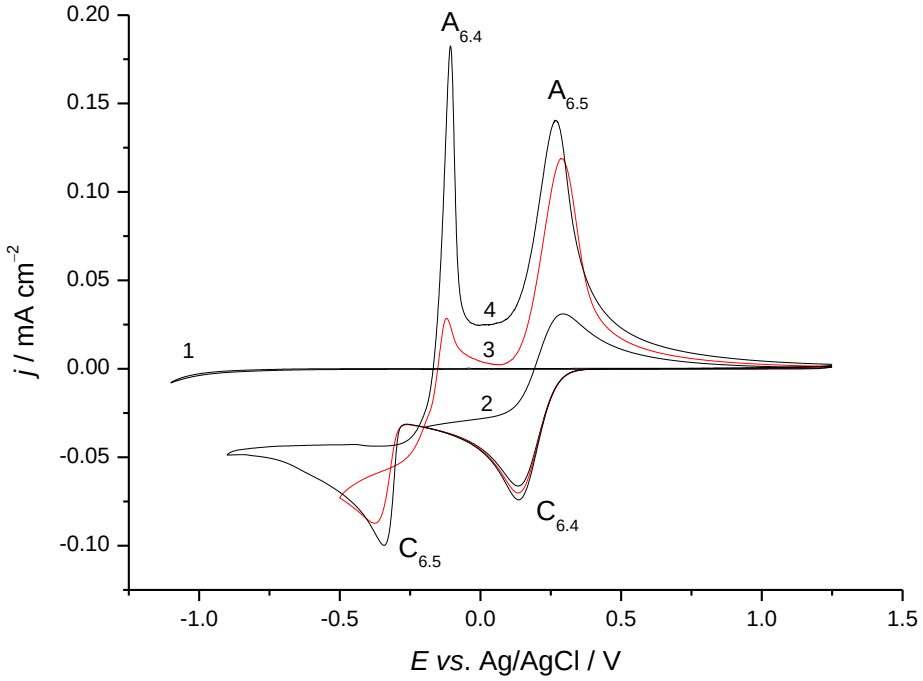

Figure 6.1.4. Cyclic voltammograms carried out on a BDD electrode in a 0.6 M NaCl + 3.00 mM $CuCl_2$ solution (pH 4.5) at 10 mV s^{-1} at different potential windows (2) +1.25 V to –0.25 V *vs.* Ag/AgCl, (2) +1.25 V to –0.5 V *vs.* Ag/AgCl and +1.25 V to –0.9 V *vs.* Ag/AgCl. Cyclic voltammogram (1) was carried out on a BDD electrode in 0.6 M NaCl at 10 mV s^{-1}.

The chloride concentration is a parameter of great importance for the copper(0)–copper(I)–copper(II) system since it significantly affects the equilibria and may also influence the rate of the electron transfer. In order to have a better insight of the chloride influence on the copper(I) / copper(II) system, cyclic voltammetry and quasi–steady potentiodynamic polarisation were carried on BDD electrode in equimolar copper(I) and copper(II) concentrations and different chloride levels. Figure 6.1.5 shows the cyclic voltammograms carried out on a BDD electrode in a 5 mM copper(I) / copper(II) solution containing 0.6 M, 1.6 M and 3.0 M NaCl. All the solutions were deaerated by sparging with nitrogen gas until $O_2 \leq 3$ μM, in order to decrease

the copper(I) oxidation by dissolved molecular oxygen [186]; also, the I_m was maintained constant at 3.0 M for all the CVs by $NaClO_4$ additions. It can be noted that all the CVs underwent a quasireversible electron transfer process, since the peak–to–peak potential separation (ΔE) increased as the scan rate was increased. Furthermore, as can be seen in the Figure 6.1.5 inset, the peak–to–peak potential separations (ΔE) was determined to be constant at all the considered chloride concentrations, thus indicating that the chloride did not influence the electron transfer.

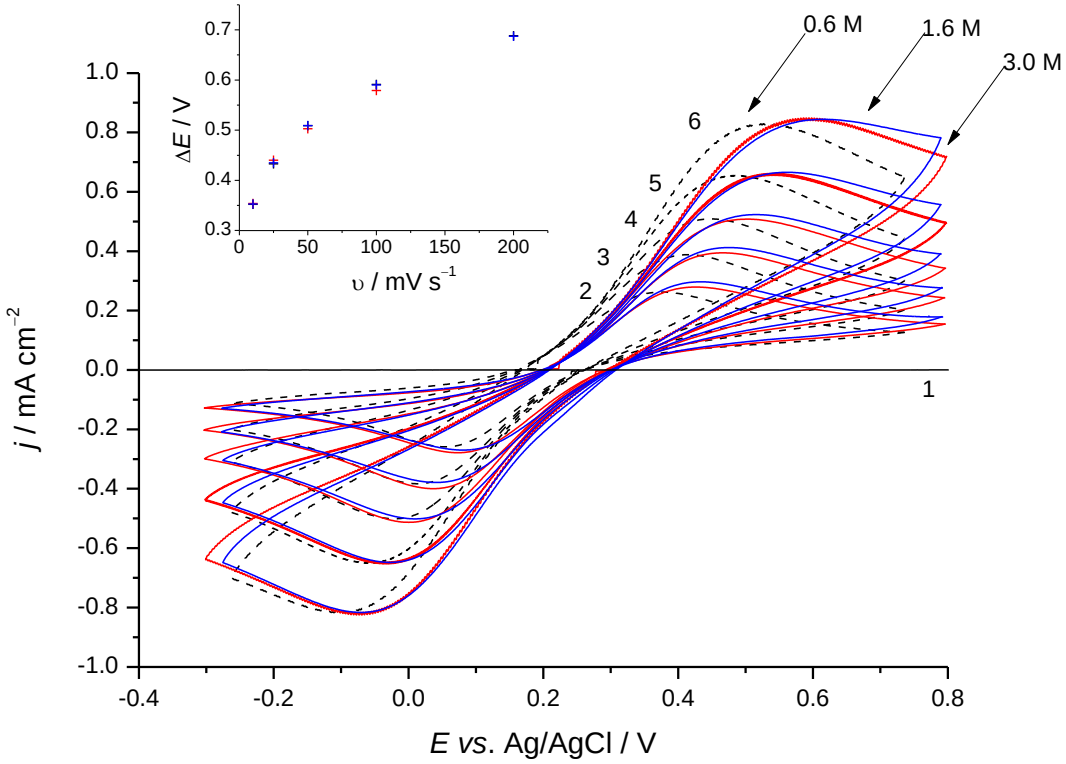

Figure 6.1.5. Cyclic voltammograms carried out on a BDD electrode in a 5 mM copper(I) / copper(II) solutions (pH 4.5) at different scan rates: (1–2) 10, (3) 25, (4) 50, (5) 100 and (6) 200 mV s^{-1}. The chloride concentrations investigated were: (black dashed line) 0.6 M NaCl, (red solid line) 1.6 M and (blue solid line) 3.0 M; the ionic strength was maintained constant at 3.0 M. M by additions of $NaClO_4$. Test (1) was carried out in 3.0 M NaCl. All the solutions were deaerated by sparging with nitrogen gas until $O_2 \leq 3$ μM. Inset shows the peak–to–peak potential difference determined at the different scan rates and chloride concentrations.

Figure 6.1.6 highlights the equilibrium potentials (red circles) determined in 5 mM copper(I) / copper(II) solutions in the presence of different chloride activities and the theoretical values (black squares) estimated using Equation 6.1.12 [187]. In particular, the activities were 0.40 M (0.60 M of concentration), 0.66 M (1.00 M of concentration), 1.00 M (1.60 of concentration),

1.54 M (2.40 of of concentration) and 1.99 M (3.00 M of concentration). These values were determined using the activity coefficients as listed in Table 6.1.1 [173], which also provides the logarithm of the activities used in Figure 6.1.6 and the activity coefficients. As can be seen in Figure 6.1.6, within the a_{Cl^-} range from 0.40 M to 1.00 M the copper(I) / copper(II) system followed the behaviour of Equation 6.1.12, where the dependence of the equilibrium potential on chloride was 118 mV dec^{-1} (2.303 2*RT* / *F*).

$$E_{eq} = +0.252 + \frac{2.303RT}{F}\log\left(\frac{a_{Cu^{2+}}}{a_{CuCl_2^-}}\right) + \frac{2.303\cdot 2RT}{F}\log\left(a_{Cl^-}\right) / \text{V } \textit{vs.}\ \text{Ag/AgCl} \qquad 6.1.12$$

The physical meaning behind a slope of 118 mV dec^{-1} relates to a chloride stoichiometric number of two, which indicates that the electrochemical process can be schematised as in Equation 6.1.10. Conversely, the equilibrium potentials determined within the a_{Cl^-} range from 1.54 M to 1.99 M significantly deviated from the predicted behaviour and the extrapolated trend was found to be nearly independent from chloride. The overall process can be therefore described as in Equation 6.1.13, where the reaction is independent from chloride.

$$CuCl_{2(aq)} + e^- \rightarrow CuCl_2^- \qquad 6.1.13$$

For these particular conditions, Equation 6.1.12 did not adequately predict the equilibrium potential, which was instead better described by Equation 6.1.14.

$$E_{eq} = +0.255 + \frac{2.303RT}{F}\log\left(\frac{a_{CuCl_{2(aq)}}}{a_{CuCl_2^-}}\right) / \text{V } \textit{vs.}\ \text{Ag/AgCl} \qquad 6.1.14$$

These insights can be further corroborated by the copper(I)– and copper(II)–speciation diagrams, see the insets of Figure 6.1.6. The copper(I)– and copper(II)–complex distributions were determined using the formation constants provided by Wang *et al*. [103], which were further corrected at a ionic strength of 3.0 M using Equations 2.4.8–2.4.9 and 2.4.14–2.4.15 of Section 2.4.1.

Table 6.1.1. Correlation between chloride concentrations and activities (and logarithm of activity).

$[Cl^-]$ / M	$\gamma_{\pm}$	α_{Cl^-} / M	log α_{Cl^-} / M
0.60	0.673	0.40	–0.40
1.00	0.657	0.66	–0.18
1.60	0.625	1.00	0.00
2.40	0.642	1.54	0.19
3.00	0.662	2.00	0.30

According to derived speciation diagrams of Figure 6.1.6, at a_{Cl^-} of 0.40 M, 0.6 M and 1.00 M the predominant copper(I) and copper(II) species were $CuCl_2^-$ and $Cu^{2+}_{(aq)}$, whereas at α_{Cl^-} of 1.54 M and 2.00 M the main copper(I) and copper(II) complexes were $CuCl_2^-$ and $CuCl_{2(aq)}$ / $CuCl^+_{(aq)}$, respectively.

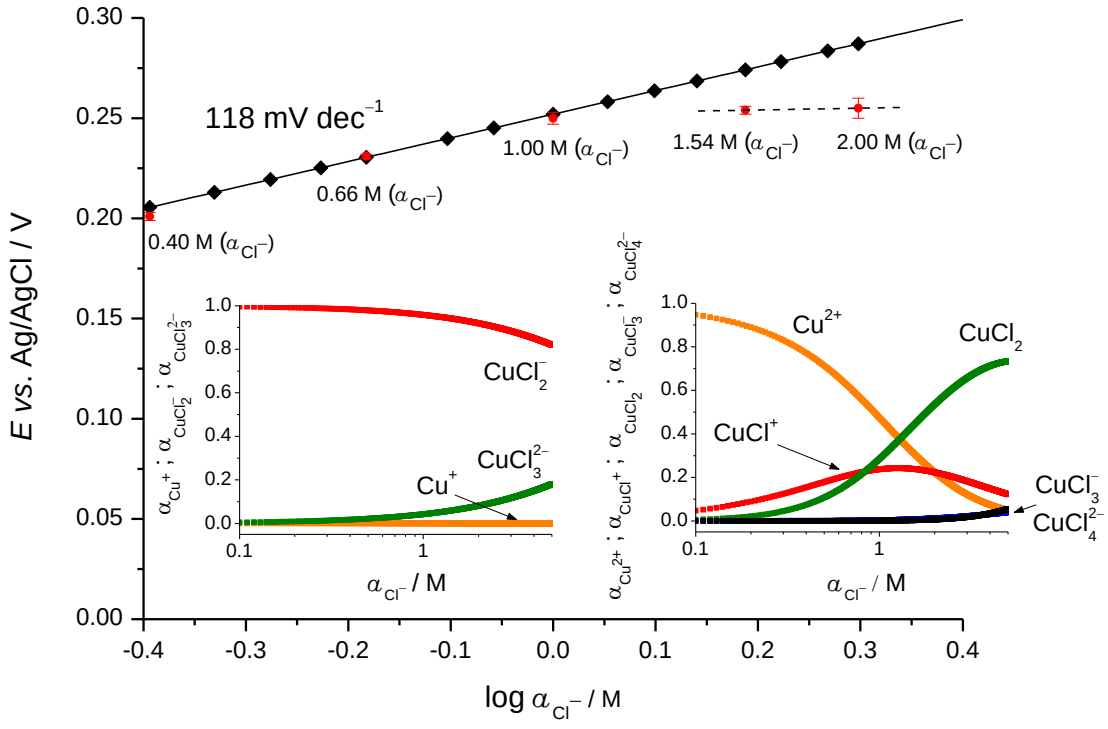

Figure 6.1.6. Equilibrium electrode potentials estimated using Equation 6.1.12 (black diamonds) and experimentally assessed in 5 mM copper(I) / copper(II) solutions (pH of 4.5) at different chloride activities. The left hand side and the right hand side insets show the copper(I) and copper(II) speciation in chloride solution with a ionic strength of 3.0 M. The formation constants were those provided in [103], corrected considering a ionic strength of 3.0 M (see Equations 2.4.8–2.4.9 and 2.4.14–2.4.15).

These findings are in good agreement with the experimental results, where (*i*) within the chloride activity range from 0.40 M to 1.00 M the chloride stoichiometric number was determined to be 2, associated with the $Cu^{2+}_{(aq)}$ / $CuCl^{-}_{2}$ equilibrium system, whereas (*ii*) within the chloride activity range from 1.54 M to 2.00 M the electrode equilibrium appeared to be independent from the chloride concentration, due to the establishment of the $CuCl^{-}_{2}$ / $CuCl_{2(aq)}$ equilibrium. Cyclic voltammograms reported in Figure 6.1.5 highlighted that the copper(I) / copper(II) electron transfer was not affected when the chloride concentration was varied between 0.6 M and 3.0 M. However, it is worth mentioning that cyclic voltammetry is not the most accurate technique to study the kinetic of a redox system [188], especially when the partners of the electro–active couple may have different diffusion coefficients.

Table 6.1.2. Kinetic parameters determined from quasi–steady potentiodynamic polarisation curves in a 5 mM copper(I) / copper(II) solution at different NaCl concentrations. The ionic strength was maintained constant at 3.0 M.

$[Cl^-]$ / M	α_{Cl^-} / M	j_0 / μA cm^{-2}
0.6	0.4	44
1.6	0.9	44
3.0	2.0	45

Therefore, the copper(I) / copper(II) kinetic was studied using quasi–steady potentiodynamic polarisation in the same experimental conditions explored in CVs of Figure 6.1.5 and assessing the related exchange current densities. As can be seen in Figure 6.1.7, the quasi–steady potentiodynamic polarisations for the system copper(I) / copper(II) exhibited similar slopes, thus indicating similar electron transfer kinetics at the BDD electrode. The exchange current densities were determined to be 44 μA cm^{-2}, 44 μA cm^{-2} and 45 μA cm^{-2} for the 0.6 M, 1.6 M and 3.0 M NaCl solutions (see Table 6.1.2), respectively, by using Equation 5.1.15 (see Chapter 5). According to the speciation diagrams and the equilibrium potentials shown in Figure 6.1.6, the most likely electrochemical processes can be related to Equation 6.1.10 for the 0.6 M and 1.6 M NaCl solution tests and to Equation 6.1.13 for the 3.0 M NaCl medium.

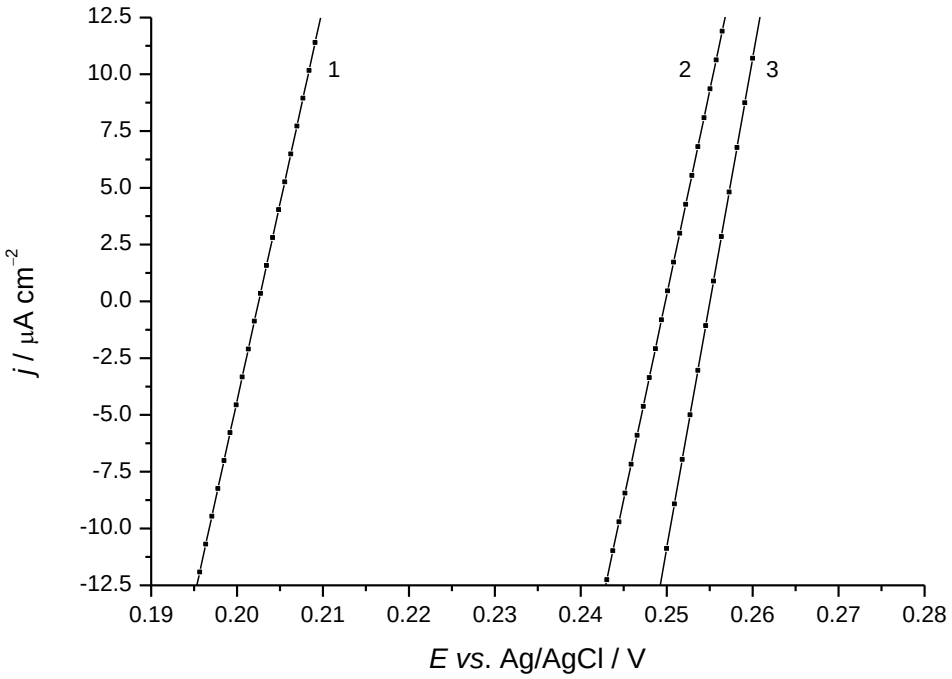

Figure 6.1.7. Quasi–steady potentiodynamic polarisation curves carried out on BDD electrode in 5 mM copper(I) / copper(II) solutions (pH of 4.5) at different chloride concentrations: (1) 0.60 M (0.40 M activity), (2) 1.6 M (1.0 M activity) and 3.00 M (1.99 M activity). The scan rate was 0.10 mV s^{-1}. All the solutions presented an ionic strength of 3.0 M and were deaerated by sparging with nitrogen gas until O_2 ≤ 3 μM.

The independence exhibited by j_0 on the chloride content suggests that the reaction mechanism for Equation 6.1.10 can be represented by the scheme shown Figure 6.1.8, where the electron transfer initially occurs between the thermodynamic species $Cu^{2+}_{(aq)}$ and $CuCl^{-}_{2}$ and is likely to be followed by a fast dissociation / formation chemical equilibrium.

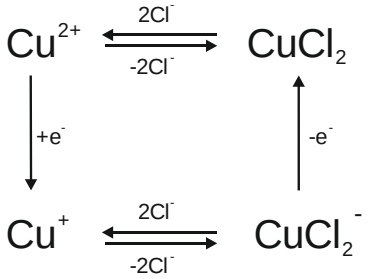

Figure 6.1.8. Schematic of the proposed electrochemical mechanism for the system copper(I) / copper(II).

6.2 Copper Ion Determination in Simulated Marine Corrosion Solutions using Differential Pulse Voltammetry

DPV is known to be a more sensitive technique than CV, due to removal of the non–faradic current (or capacitive current) from the electrode response [189]. Thus, the determination of copper ions has been carried out in a 0.6 M sodium chloride solution using DPV in the presence of different concentrations of fresh aliquots of iron(III), nickel(II) and aluminium(III).

Calibration: Figure 6.2.1 shows the overlay of DPVs carried out on BDD electrode in a 0.6 M NaCl solution at different copper(II) concentrations, from 0.010 mM to 3.00 mM.

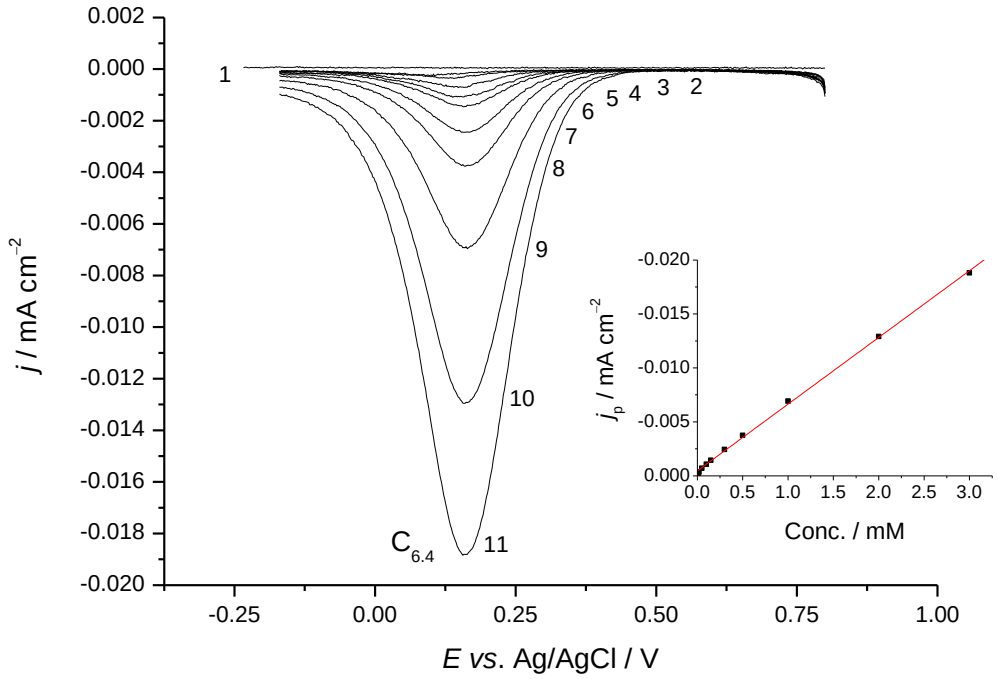

Figure 6.2.1. Differential pulse voltammograms carried out on a BDD electrode in a (1) 0.6 M NaCl solution + (2) 0.01, (3) 0.02, (4) 0.05, (5) 0.1, (6) 0.15, (7) 0.30, (8) 0.50, (9) 1.00, (10) 2.00 and (11) 3.00 mM $CuCl_2$. Inset shows current peak density as a function of the copper(II) concentration.

As can be seen, the copper(II) reduction peaks ($C_{6.4}$) were at electrode potentials significantly more positive than those assessed in copper(I) / copper(II) solutions (approx. 0.17 V *vs.* Ag/AgCl), due to the absence of copper(I) which increased the equilibrium potential. The reduction peak currents for the copper(II) / copper(I) signal clearly increased as the copper–ion concentration increased and was observed to be linear within the investigated concentration

range (R^2 of 0.9932). The limit of detection (LOD) was also estimated to be 0.010 mM, based on a peak current density three–fold the background current density.

Interferences: In Section 2.1 it was highlighted that iron(III), aluminium(III) and nickel(II) can be present in crevice corrosion solutions of NAB [7]. Therefore, the effects of these interferents during the copper(II) detection were investigated on BDD electrode at different concentrations. Figure 6.2.2 shows the overlays of DPVs carried out on a BDD electrode in a 0.6 M NaCl solution containing a fixed concentration of copper(II) (1 mM) and at different iron(III) concentrations, which ranged from 1 mM to 10 mM.

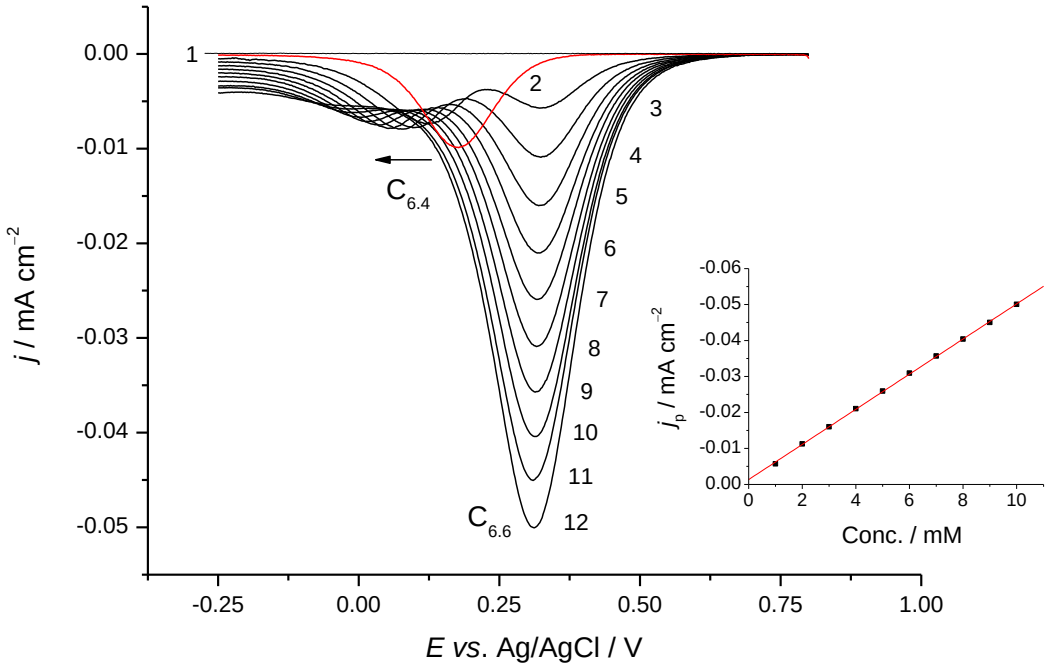

Figure 6.2.2. Differential pulse voltammograms carried out on a BDD electrode in 0.6 M NaCl + 1.0 mM $CuCl_2$ at different $FeCl_3$ concentrations: (2) 0, (3) 1.0, (4) 2.0, (5) 3.0, (6) 4.0, (7) 5.0, (8) 6.0, (9) 7.0, (10) 8.0, (11) 9.0 and (12) 10.0 mM. Differential pulse voltammogram (1) was carried out on 0.6 M NaCl. Inset shows peak current density ($C_{6.6}$) as a function of the iron(III) concentration.

Two cathodic responses were determined at the BDD electrode: $C_{6.6}$ associated with the reduction of iron(III) to iron(II) and $C_{6.4}$ related to the reduction of copper(II) to copper(I), as shown in Equation 6.1.10. The $C_{6.4}$ peak potential of DPV 1 (carried out in the absence of iron(III)) presented a similar value of those of Figure 6.2.1, *i.e.*, ca. 0.17 V *vs*. Ag/AgCl. However, as iron(III) was added into solution, the signal $C_{6.4}$ shifted towards more negative values indicating a higher overpotential for the copper(II) / copper(I) reduction. Furthermore, it was observed that upon additions of equimolar concentrations of iron(III) (1 mM), the $C_{6.4}$ peak

current decreased by approx. 20 %. It was also apparent that further additions of ferric ions did not cause decrease of the $C_{6.4}$ current peak up to a ten–fold molar excess of iron(III). The Figure 6.2.2 inset shows the good linear relationship determined between the ferric ion concentration and the $C_{6.6}$ current peak density, with a correlation of R^2 = 0.9997. Quantification of 1.0 mM copper(II) in a 0.6 M NaCl solution containing different nickel(II) and aluminium(III) concentrations (from 1.0 mM to 10.0 mM) have been also carried out on BDD electrode (figures not shown). Negligible reductions of the $C_{6.4}$ current peak densities were determined when the solutions contained up to ten–fold molar excesses of nickel(II) and aluminium(III). The absence of interferences during the electrochemical detection of copper(II) can be explained by considering their inertness at electrode surfaces.

6.3 Summary

The electrochemical behaviour of the copper(I) / copper(II) system have been investigated on BDD electrode in different electrolyte–anion solutions, *i.e.*, $NaClO_4$, Na_2SO_4 and NaCl. Similar behaviours were observed at the BDD electrode when the solution contained $NaClO_4$ and Na_2SO_4, which was characterised by a one–step electron transfer process associated with the copper(0) / copper(II) system. Conversely, when the solution contained chloride the electron transfer proceeded via double–step electron transfer process. The derived speciation diagrams and the assessed equilibrium potentials indicated that copper(II) and copper(I) underwent different complexation reactions, forming a number of chloride complexes.

7. Nickel–Ion Detection on Boron–Doped Diamond Electrode in Neutral and Acidic Chloride Solutions

As reported in Section 2.1, when NAB crevice corrosion initiates the pH of the crevice solution decreases to values which typically range between 3 and 4 [6] and, as a consequence of the corrosion susceptibility of the κ–phases, nickel(II) can be present in solution [7]. Generally, the operating conditions of the nickel–ion detection require the presence of chelating agents and strong alkaline pHs, which typically range between 13 and 14. These conditions can be difficultly applied for *in situ* corrosion monitoring, since they will adversely affect the NAB corrosion performance.

In the following Sections is reported an electrochemical investigation of the nickel(II) / nickel(III) system in acidic chloride environments, in order to establish a simple protocol for nickel–ion detection in acidic pHs. A preliminary investigation of the nickel(II) / nickel(III) system was carried out on BDD electrode and alkaline solutions using cyclic voltammetry and electrochemical impedance spectroscopy to better understand the electrochemical behaviour of the redox couple. The actual nickel(II) electrochemical detection was then carried out using differential pulse anodic voltammetry (DPAV) in chloride solutions at pHs ranging from 10 to 4.

7.1 Influence of the pH on Ni(II) / Ni(III) Behaviour in Chloride Media

Prior to establishing the procedure for the nickel determination, studies on the Ni(II) / Ni(III) hydroxide behaviour was carried out in 0.6 M NaCl solutions (constant ionic strength of 1.6 M) at different pH values (12.0, 12.5, 13.0, 13.5 and 14.0) using CV, EIS and DPAV, as described in Chapter 3. Figure 7.1.1 shows an overlay of cyclic voltammograms for the Ni(II) / Ni(III) hydroxide couple recorded in 0.6 M NaCl solution at different pH values. It is apparent that as the pH of the solution was increased both peaks of the redox couple shifted towards more negative potentials. The dependence of the peak potentials of the Ni(II) / Ni(III) hydroxide couple on the pH is clearly depicted in the inset of Figure 7.1.1, which shows the good linear relationship obtained between the anodic peak potential and the solution pH, R^2 of 0.995.

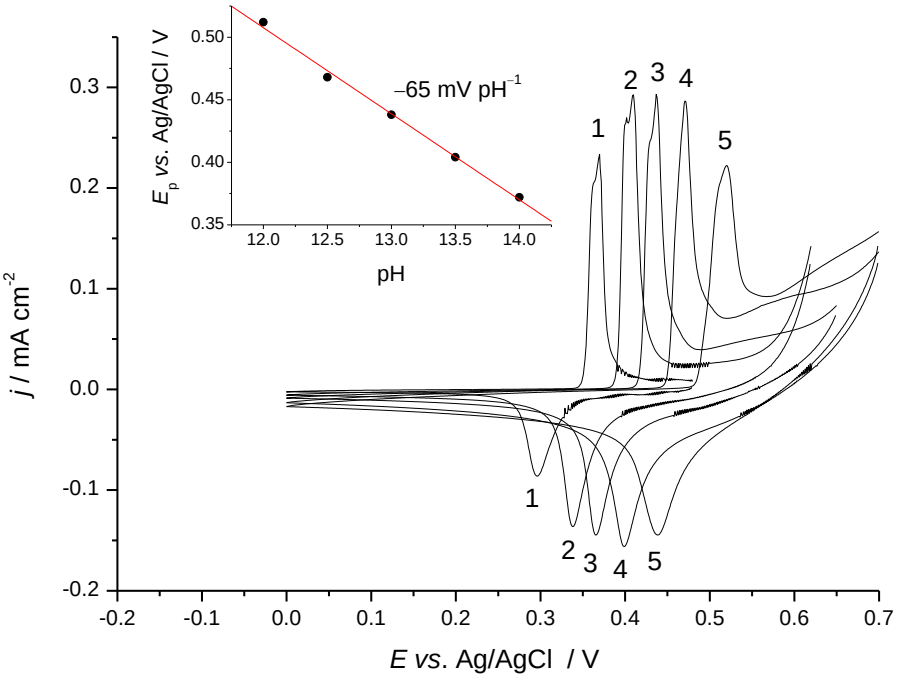

Figure 7.1.1. Cyclic voltammograms recorded on Ni–modified BDD electrode at 10 mV s^{-1} in chloride solution adjusted to pH values of (1) 14.0, (2) 13.5, (3) 13.0, (4) 12.5 and (5) 12.0. The potentiodynamic tests were performed after a nickel pre–deposition process in 0.6 M NaCl + 3 mM Ni^{2+} carried out at –1.5 V *vs.* Ag/AgCl for 300 s and oxidation process of 200 s at +0.7 V *vs*. Ag/AgCl. Inset shows the linear dependence between anodic current peak potential and pH.

A slope of –65 mV per pH unit was estimated from the potential–pH trend shown in Figure 7.1.1 inset, which approaches the thermodynamic value of –59 mV per pH unit for one–proton one–electron exchange reaction. The observed behaviour corroborated the involvement of one–proton one–electron process in the electrochemical response of Ni(II) / Ni(III) hydroxides couple. A greater peak potential shift of –88 mV per pH unit was reported for the Ni(II) / Ni(III) couple in 1.0 M KOH by Toghill *et al.* [190] and attributed to possible potassium intercalation products, such as K_2O, within the hydroxide matrix. However, no sodium intercalated by–products were determined by Von Bode *et al.* [191] in the $Ni(OH)_2$ matrix when prepared in sodium containing solutions. This confirms that the different pH–dependences reported in the literature [190] and within this work are associated with the presence of by–products which changes the hydroxide layer structure.

A peak–to–peak potential separation of 60 mV was determined at the highest pH (14); however, decreasing to pH 12 the peak potential separation slightly increased by 8 mV. This response underlined a transformation of the electrochemical process from fully reversible

behaviour to a quasireversible, most likely to be due to the a change of the hydroxide layer [192-194].

$Ni(OH)_2$ can exist in two different polymorphic states identified as α–$Ni(OH)_2$ and β–$Ni(OH)_2$ [100, 192, 193]. It is reported that in an aqueous alkaline solution the hydroxide layer is originally present in the hydrated form, α–$Ni(OH)_2$, which usually corresponds to $Ni(OH)_2.3H_2O$. However, this undergoes a transformation to β–$Ni(OH)_2$, so–called "ageing effect", with time and increasing electrode potential [192, 195, 196]. The electron transfer occurring between the electro–formed nickel(II) and nickel(III) hydroxides takes place with the involvement of a proton which diffuses through the host active material, as underlined by Equations 7.1.2 and 7.1.3. In the specific instance of Figure 7.1.1, the electrochemical process probably occurred involving the α–polymorphic form since it has been reported that is generally formed via electrochemical process [193].

$$Ni^{2+} + 2OH^- \rightarrow Ni(OH)_2 \qquad 7.1.1$$

$$\alpha - Ni(OH)_2 \rightarrow \gamma - NiOOH + H^+ + e^- \qquad 7.1.2$$

$$\beta - Ni(OH)_2 \rightarrow \beta - NiOOH + H^+ + e^- \qquad 7.1.3$$

Figure 7.1.2 shows the CVs recorded in a 1.0 M NaOH + 0.6 M NaCl solution on BDD Ni–modified electrode at different scan rates. The peak–to–peak electrode potential separation was determined to be 60 mV at both the slowest and highest scan rates, underlying a fully reversible process. However, the anodic and cathodic current peak densities presented different magnitude values, associated with the diverse proton diffusions within the $Ni(OH)_2$ and NiOOH phases [193]; in any case, the ratio between the anodic and cathodic charges were assessed to be 1.0 ± 0.1. Figure 7.1.2 inset shows the trend of the anodic current peak density with respect to the square root of the scan rate. The good linearity, R^2 = 0.994, indicates a process controlled by diffusion in accordance with data present in the literature [197]. Determination of the proton diffusion coefficient through the active material was carried out using Equation 7.1.4.

$$I_p = (2.77\times10^5)\, z^{3/2} A D_H^{1/2} c_H v^{1/2} \qquad 7.1.4$$

where I_p is the current peak, D_H is the diffusion coefficient of the rate determining species (proton) and c_H is the proton concentration. To evaluate the proton concentration in the hydroxide layer, c_H was assumed to be equal to the $Ni(OH)_2$, see Equations 7.1.2 and 7.1.3. The $Ni(OH)_2$ concentration was estimated by dividing its density (2.6 g cm^{-3}) by its molecular mass

[195]. The proton diffusion coefficient was assessed to be (7.1 ± 0.1) × 10^{-11} cm^2 s^{-1}, considering the average of the anodic and cathodic processes.

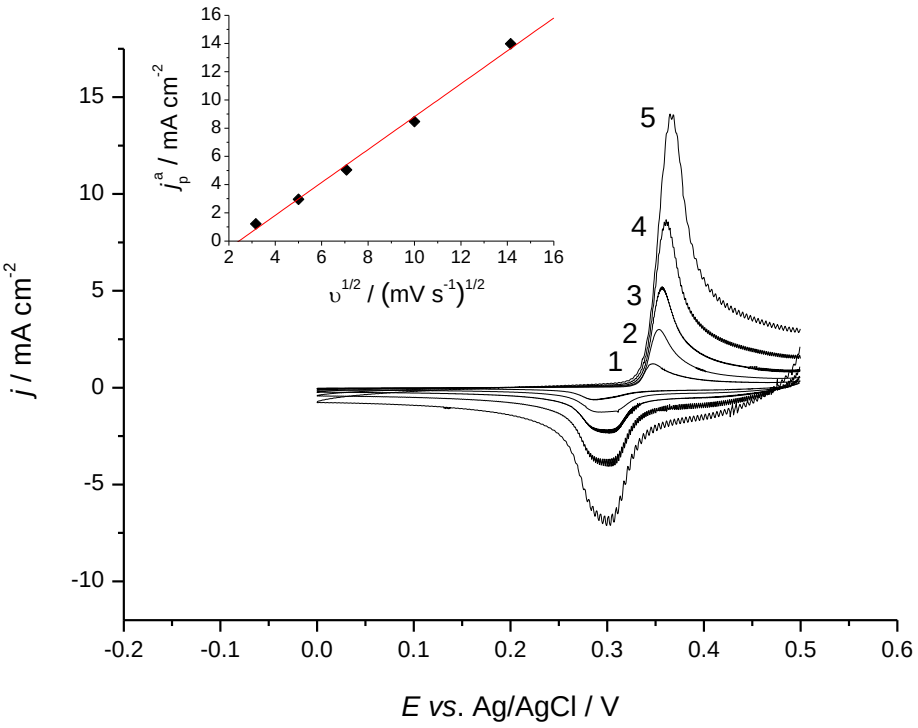

Figure 7.1.2. Cyclic voltammograms recorded on Ni–modified BDD electrode at: (1) 10, (2) 25, (3) 50, (4) 100 and (5) 200 mV s^{-1} in 1.0 M NaOH + 0.6 M NaCl. The potentiodynamic tests were performed after a nickel pre–deposition in 0.6 M NaCl + 3 mM Ni^{2+} at –1.5 V *vs.* Ag/AgCl for 300 s and oxidation process of 200 s at +0.7 V *vs.* Ag/AgCl. Inset shows the linear trend of the anodic current peak density with respect to the square root of the scan rate.

To corroborate the electrochemical behaviour of the BDD Ni–modified electrode in the chloride alkaline solution, EIS was also employed. Figure 7.1.3 shows the EIS measurement in 1.0 M NaOH + 0.6 M NaCl. The electrochemical response displayed a semicircle at high frequency, attributed to the charge transfer process of the redox system Ni(II) / Ni(III), and a diffusion process which consisted of two distinct trends, one at higher diffusion frequencies and another present at lower diffusion frequencies [195]. The high frequency diffusion trend displayed a slope of ca. 42° and was associated with a semi–infinite diffusion (also known as a Warburg impedance). Conversely, the low frequency diffusion impedance showed a nearly vertical impedance response and was related to the capacitive behaviour of the nickel hydroxide layer [195]. The estimation of the proton diffusion within the hydroxide matrix was achieved using Equation 7.1.5.

$$D_H = \frac{2\pi f_c l^2}{\left[2\cos\left(\frac{n\pi}{4}\right)\right]^{2/n}} \qquad 7.1.5$$

where f_c is the characteristic frequency (0.032 Hz), n is the constant phase element (CPE) number (0.74) and l is the thickness of the active layer (5.49×10^{-5} cm). The layer thickness was determined from the anodic potentiostatic experiments, evaluating the charge involved in the oxidation process and assuming a complete presence of the tri–hydrated nickel hydroxide (molecular mass of 146.7 g mol^{-1} and density of 2.6 g cm^{-3} [195]) . The proton diffusion coefficient evaluated from Equation 7.1.5 was 9.4×10^{-11} cm^2 s^{-1}, which is similar to that obtained from cyclic voltammetry.

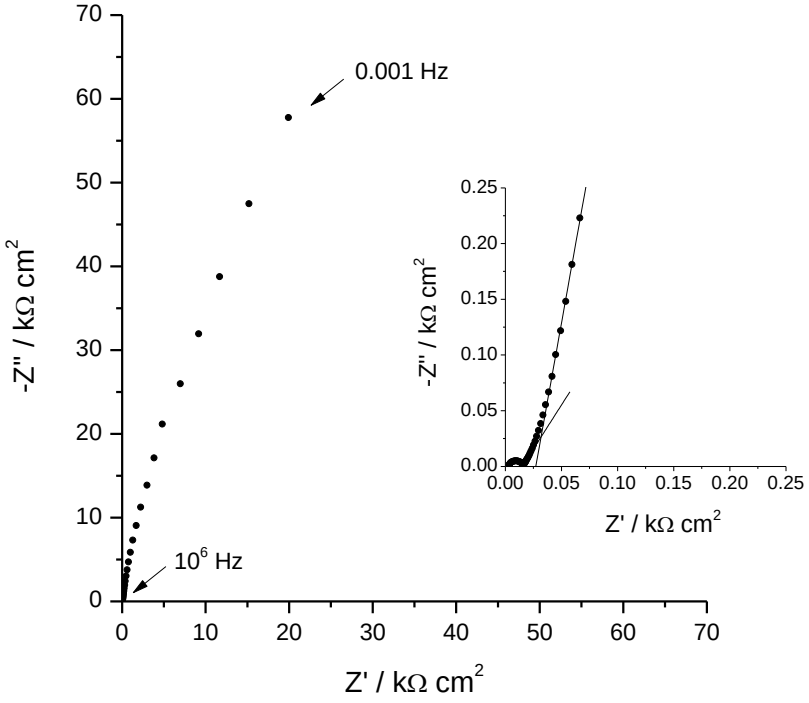

Figure 7.1.3. Electrochemical impedance spectroscopy tests on Ni–modified BDD electrode carried out applying a potential perturbation of ±5 mV in 1.0 M NaOH + 0.6 M NaCl. The nickel hydroxide was prepared by depositing metallic nickel in 0.6 M NaCl + 3 mM Ni^{2+}, applying a potential of –1.5 V for 300 s, and an oxidation process of 200 s at +0.7 V *vs.* Ag/AgCl in 1.0 M NaOH + 0.6 M NaCl.

It has been reported that the electrochemical and physical properties of the $Ni(OH)_2$ / NiOOH (kinetic of the electron transfer, pH–potential relationship and proton diffusion within the layer) strictly reflect the presence of impurities, since they affect the molecular structure of

the electro–formed nickel matrix [190]. From the CV and EIS results, it was observed that the Ni(II) / Ni(III) transaction undergoes a reversible electron transfer process with a pH–potential relationship of –65 mV pH unit^{-1}; this behaviour suggests that, in the experimental conditions investigated, the electro–formation of the nickel hydroxide matrix was achieved with high purity.

Investigated the electrochemical behaviour of the system Ni(II) /Ni(III) in sodium–chloride alkaline solutions, further studies on the Ni(II) /Ni(III) system were carried out at lower pHs by using DPAV. In particular, the DPAVs were performed in 0.6 M NaCl corrected at pH 10.0 and 9.0 using a 1.0 M NaOH solution, and in sodium–phosphate buffered solutions at pH of 8.0 and 6.2, see Figure 7.1.4. From the DPAVs performed at pHs of 10.0 and 9.0, tests 2 and 3, it is apparent the presence of a peak $A_{7.2}$, which can be associated with the $Ni(OH)_2$ / NiOOH species due to their stability in the considered pH interval [100]. The potential peaks were determined at +0.65 V and +0.74 V *vs*. Ag/AgCl for pH 10.0 and 9.0, respectively, in line with the established potential–pH trend of –65 mV pH unit^{-1} shown in the Figure 7.1.1 inset.

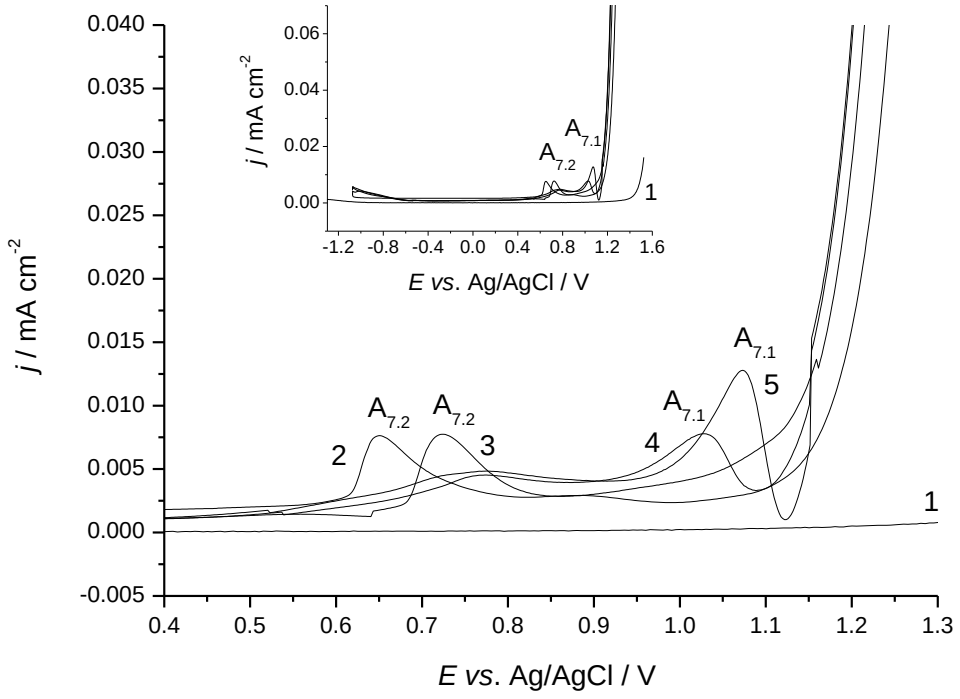

Figure 7.1.4. Differential pulse anodic voltammograms on BDD electrode at 10 mV s^{-1} in phosphate buffered solution + 50 μM Ni^{2+} at (2) pH 6.2 and (3) pH 8.0. Tests (3) and (2) were carried out in 0.6 M NaCl at pH 9.0 and 10.0, respectively. All the differential pulse anodic voltammograms were performed after a nickel pre–deposition process in a 0.6 M NaCl + 3 mM Ni^{2+} solution carried out at –1.5 V for 30 s. Test (1) represents the blank experiment in 0.6 M NaCl. Inset shows an enlargement of the recorded measurements.

Regarding the DPAV measurements carried out in pH solutions of 8.0 and 6.2, tests 4 and 5, the electrochemical responses ($A_{7.1}$) significantly shifted towards more positive values than those at pH 10.0 and 9.0, having potential peaks of +1.02 V and +1.07 V *vs*. Ag/AgCl for pH 8.0 and 6.2, respectively.

The dependence between potential and pH for Ni(II) / Ni(III) system, above and below the critical pH value of 9.0, is shown in Figure 7.1.5. For the assessment, it was considered the trend of the potential peaks with respect to the pH from (*i*) CV experiments within the pH interval from 14.0 to 12.0, reported in Figure 7.1.1 inset, and (*ii*) DPAVs from Figures 7.1.4 and 7.2.2, the latter shown in Section 7.2.

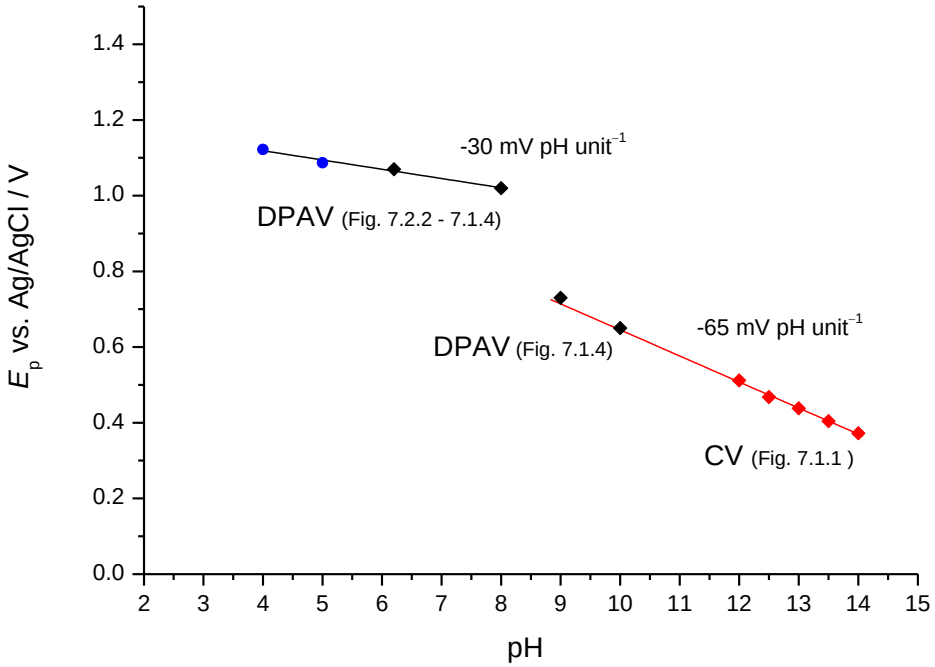

Figure 7.1.5. Potential peaks assessed at different pH values: (red diamond) pH from 14.0 to 12.0 (associated with Figure 7.1.1), (black diamond) pH from 10.0 and 6.2 (associated with Figure 7.1.4), (circles) pHs of 5.0 and 4.0 (associated with Figure 7.2.7). The red line represents the trend extrapolated from cyclic voltammograms whereas the black line is estimated from differential pulse anodic voltammograms.

As can be seen in Figure 7.1.5, above a solution pH of 9 similar potentials were obtained between the predicted value trend obtained by CV, red line which provided +0.735 V at pH 9.0 and +0.645 V *vs*. Ag/AgCl at pH 10.0, and the experimental potentials assessed using DPAV, +0.74 V at pH 9.0 and +0.65 V *vs*. Ag/AgCl at pH 10.0. It is worth mentioning that the good agreement was observed in spite of the different techniques, *i.e.*, CV and DPAV. The peak potentials at pH 10.0 and 9.0, which correlated well on the extrapolated trend characterised by a

slope of –65 mV pH unit^{-1}, indicated the involvement of the redox couple $Ni(OH)_2$ / NiOOH in the peak response $A_{7.2}$. Conversely, the peak potentials determined below pH 9, *i.e.*, 8.0, 6.2, 5.0 and 4.0, were associated with a different trend with a more noble behaviour and a slope of –30 mV pH unit^{-1}, thus indicating that the electrochemical process between Ni(II) and Ni(III) hydroxides is unlikely to have occurred.

It has been reported that the presence of halide and a high proton concentration interfere in the early stage of $Ni(OH)_2$ formation due to a competitive adsorption mechanism between OH^- or H_2O and halide, hence affecting the growth and the structure of the $Ni(OH)_2$ outer layer [198-201]. Specifically, it has been proposed that in solutions containing concentrations of H^+ and Cl^- lower than 1 M (as in the particular case investigated in this study), the dissolution of Ni passes from an adsorbed intermediate of Ni(I) constituted of both Cl^- and OH^-, *i.e.*, $NiClOH^-_{(ads)}$, which undergoes further oxidation to NiClOH, Ni(II), and hydrolysis reaction [200], as shown in Equations 7.1.6–7.1.8.

$$Ni + H_2O + Cl^- \rightarrow NiClOH^-_{(ads)} + H^+ + e^- \quad 7.1.6$$

$$NiClOH^-_{(ads)} \rightarrow NiClOH + e^- \quad 7.1.7$$

$$NiClOH + H^+ \rightarrow Ni^{2+}_{(aq)} + Cl^- + H_2O \quad 7.1.8$$

Therefore, within the pH interval from 14 to 9, the results suggested a process associated with Equation 7.1.2, where the Ni hydroxide structure did not appear to be particularly affected by the presence of chloride, or eventually a chloride adsorption phenomenon. This behaviour can be particularly inferred due to the proton stoichiometric number of one, estimated from a potential–pH dependence of –65 mV pH unit^{-1}. However, as soon as the pH was decreased at 8 or below the electrochemical mechanism changed. Indeed, a value of the potential–pH slope of –30 mV pH unit^{-1} indicates a process characterised by a proton stoichiometric number of 0.5 and therefore not attributable to the Equation 7.1.2. Hence, it can be proposed that the process related to signal $A_{7.1}$ of Figures 7.1.4 and 7.1.5 may be associated with the oxidation reaction of NiClOH [200], initially electrochemically formed at the BDD surface and then further oxidised to Ni(III) involving 0.5 protons per mole of electrons.

7.2 Determination of Nickel–Ion Concentration for Neutral and Acidic Conditions

Figure 7.2.1 shows DPAVs recorded on a BDD electrode in 0.6 M NaCl solutions containing a nickel(II) concentration ranging from 10 μM to 500 μM. The oxidation peak $A_{7.1}$ observed at +1.07 V can be attributed to the oxidation of Ni(II) to Ni(III), which, considering the instability of nickel hydroxides below pH 9 [100], is difficulty attributable to $Ni(OH)_2$ / NiOOH. Figure 7.2.1 inset shows a linear trend of the anodic peak current densities ($A_{7.1}$) with respect to the nickel–ion concentration in the range from 10 μM to 500 μM, based on a deposition time of 30 s at –1.5 V vs. Ag/AgCl. Using the protocol conditions reported above, the limit of detection for nickel–ion was estimated as 26.1 μM, considering a peak current density three–fold the background current density.

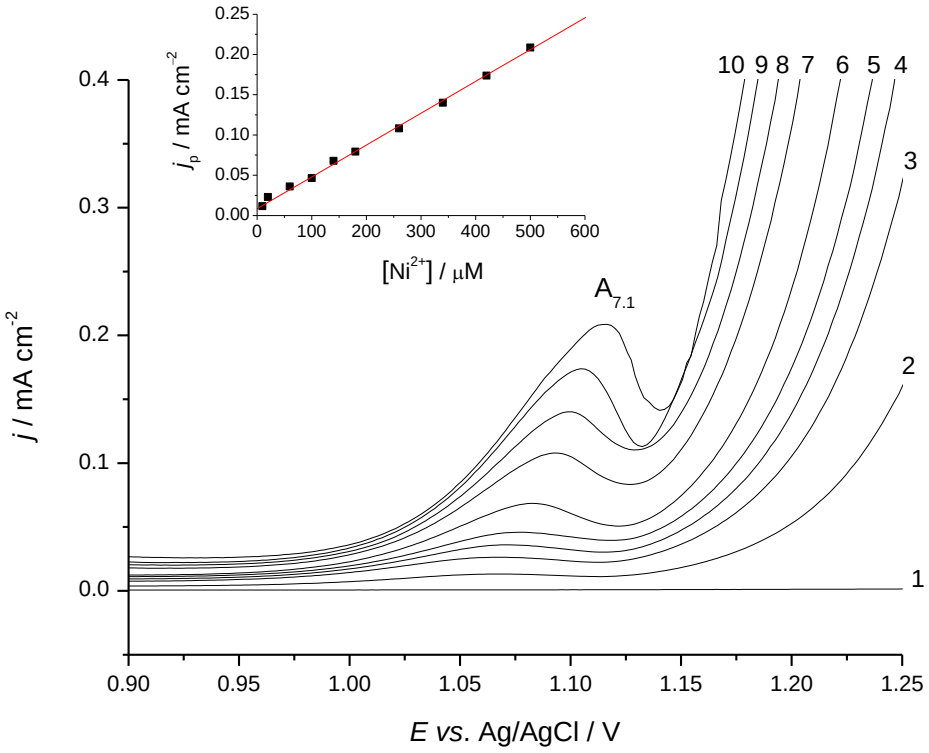

Figure 7.2.1. Differential pulse anodic voltammograms recorded on the BDD electrode at 10 mV s^{-1} in: (1) 0, (2) 10, (3) 20, (4) 60, (5) 100, (6) 140, (7) 260, (8) 340, (9) 420 and (10) 500 μM Ni^{2+} in 0.6 M NaCl. Tests were performed after a nickel pre–deposition process at –1.5 V *vs*. Ag/AgCl for 30 s. Inset shows the trend of the anodic current peak density with respect to concentration.

In terms of crevice corrosion, for certain metal / alloys nickel–ion monitoring may be important especially in those environments which are acidic. It has been reported that crevice corrosion solutions display a markedly acidic pH (from pH 3 to 4 [6]) due to the hydrolysis of corrosion produced metal ions [6]. Therefore, in order to study the feasibility of the metal ion determination in acidic environment, DPAV tests were also carried out in 0.6 M NaCl + nickel(II) solutions at pH down to 3.0. Figure 7.2.2 shows the DPAVs for 50 μM Ni^{2+} at different pH solutions, from 3.0 to 6.2, using a cathodic pre–concentration step (–1.5 V *vs.* Ag/AgCl) followed by DPV from cathodic to anodic potentials. It is evident that as the pH was decreased from 6.2 (test 2) to 3.0 (test 5), the characteristic peak shifted towards more positive values, as expected from a reaction dependent on pH. Nickel(II) detection was achieved at pH of 4.0, while DPAV carried out at a pH of 3.0 produced an oxidation peak overlapped with either chlorine or oxygen evolution reactions [202].

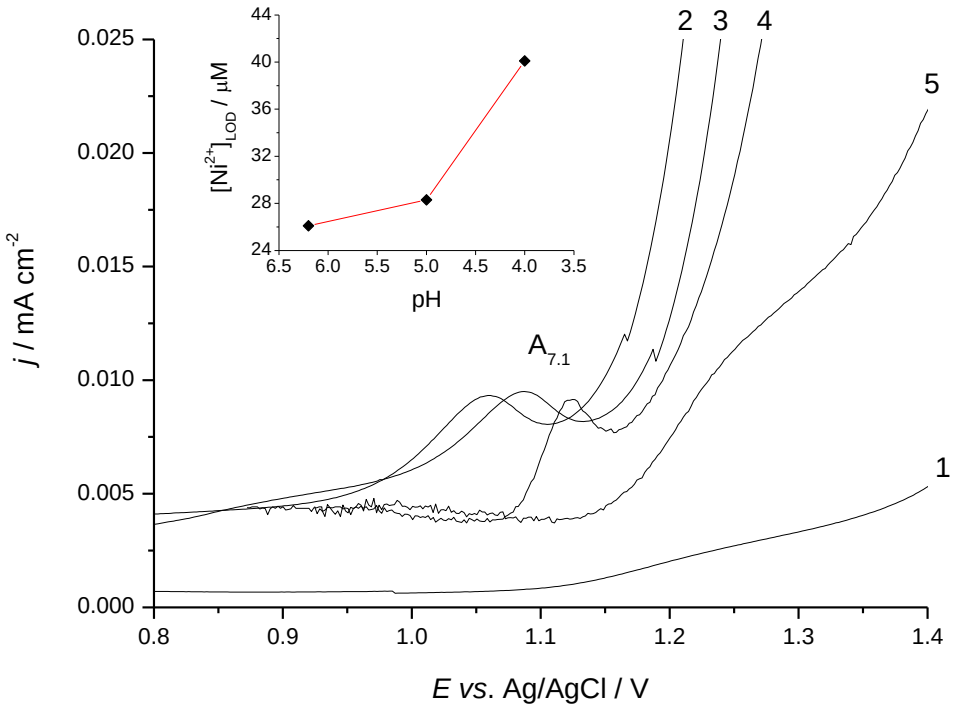

Figure 7.2.2. Differential pulse anodic voltammograms recorded on BDD electrode at 10 mV s^{-1} in 0.6 M NaCl + 50 μM Ni^{2+} at (2) pH 6.2, (3) pH 5.0, (4) pH 4.0 and (5) pH 3.0. The potentiodynamic tests were performed after a nickel pre–deposition process in 0.6 M NaCl + 50 μM Ni^{2+} carried out at –1.5 V *vs.* Ag/AgCl for 30 s. DPAV (1) represent the blank experiment carried out in the absence of Ni^{2+}. Inset show the evaluated limit of detections (LOD) at different pHs.

Concerning the sensitivity at the different pHs, a significant decrease of the estimated LODs was observed by increasing the proton concentration. This behaviour can be interpreted by considering a more favoured hydrogen evolution reaction, which takes place at the electrode surface and simultaneously to the nickel deposition. In any case, it should be underlined that the high overpotentials displayed by BDD electrodes for HER [85] is likely to provide higher efficiencies for Ni deposition with respect to other electrodes employed in electroanalysis, such as platinum and gold [203]. Figure 7.2.2 inset shows the LODs determined at the different investigated pHs, based on a potential deposition of –1.5 V *vs*. Ag/AgCl and 30 s. It can be noted that the LOD increased as the pH decreased, passing from 26.1 μM to 40.1 μM at pHs of 6.2 and 4.0, respectively. As far as the pre–concentration step is concerned, a potential of –1.5 V *vs*. Ag/AgCl produced the best response in terms of LOD.

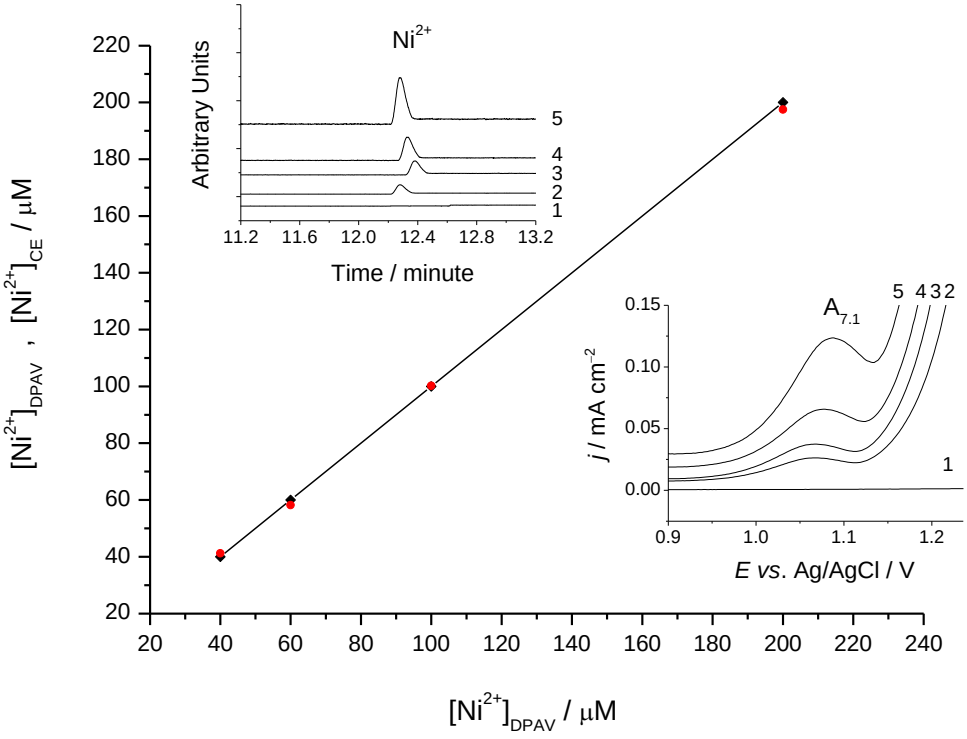

Figure 7.2.3. Correlation between Ni^{2+} concentrations determined using differential pulse anodic voltammetry (inset on the right hand side) and capillary electrophoresis (inset on the left hand side) in 0.6 M NaCl: (1) 0.0, (2) 40.0, (3) 60.0, (4) 100.0 and (5) 200.0 μM.

However, no significant sensitivity losses were observed when the deposition potential ranged from –1.6 V to –1.1 V *vs*. Ag/AgCl. Beyond this potential window the decreased sensitivity was likely to be due to (*i*) a vigorously and concurrently HER occurring with the Ni deposition and (*ii*) a potential not sufficient to efficiently promote the Ni deposition. It was

observed that an extension of the pre–concentration step at –1.5 V *vs*. Ag/AgCl resulted in a significant improvement of the LOD (1.2 μM at –1.5 V *vs*. Ag/AgCl for 360 s at pH of 6.2), even though it might be time consuming. According to Zhang *et al*. [128], a potential increase of the Ni–detection sensitivity can be obtained by acting on the mixing regime during the pre–concentration step. Indeed, Zhang *et al*. reported a substantial enhancement of the LOD when using a rotating disc electrode, rather than a static electrode–system in a stirred solution: the improvement of the nickel(II) sensitivity was related to an enhanced and more controlled mass transfer [128]. The validation of the protocol was carried out comparing the electrochemical measurements with a capillary electrophoresis analysis. The good agreement between the different techniques confirmed the viability of the electrochemical protocol. Figure 7.2.3 shows the correlation between the nickel(II) concentrations determined using DPAV and CE, with an experimental difference of ±1 % evaluated between the two different methods.

7.3 Interferences and Cleaning Process

Interference investigations on the nickel response were carried out for those ions expected to be present in crevice corrosion solutions. Anions such as SO_4^{2-}, F^-, NO_3^- and cations like Ca^{2+}, Mg^{2+}, Al^{3+}, Fe^{3+} and Cu^{2+} were added to the solution in order to observe the variations of the nickel response caused by their presence. Experimental results indicated negligible influence on the electrode response up to three hundred–fold molar excess of SO_4^{2-} and F^-, one hundred–fold molar excess of NO_3^- and fifty–fold molar excess of Ca^{2+} and Mg^{2+}. However, the nickel signal was affected when two–fold concentrations of Al^{3+}, Fe^{3+} and Cu^{2+} were added to the solution.

The regeneration of the electrode surface by the presence of adsorbed nickel has been reported to be a problem, but has been overcome by electromechanical polishing [128] and sonication [127]. The slightly acidic electrolyte in the current experiments, however, allowed simple, fast and effective electrode surface regeneration based on an electrochemical anodic treatment. This approach re–established the pristine electrode surface condition. Figure 7.3.1 shows the DPAV responses on the BDD electrode in a supporting electrolyte (test 1) and in 500 μM Ni solution (test 2) after carrying out a nickel–determination protocol (*i.e*., 30 s at –1.5 V and DPAV followed by 240 s of cleaning treatment at +1.3 V *vs*. Ag/AgCl). As can be seen no peaks were present in the potential range from +0.6 V to +1.3 V *vs*. Ag/AgCl, suggesting complete re–establishment of the pristine electrode surface. The cleaning protocol adopted was based on an anodic treatment of +1.3 V *vs*. Ag/AgCl for 30 s to 240 s, depending on the amount of Ni deposited on the electrode.

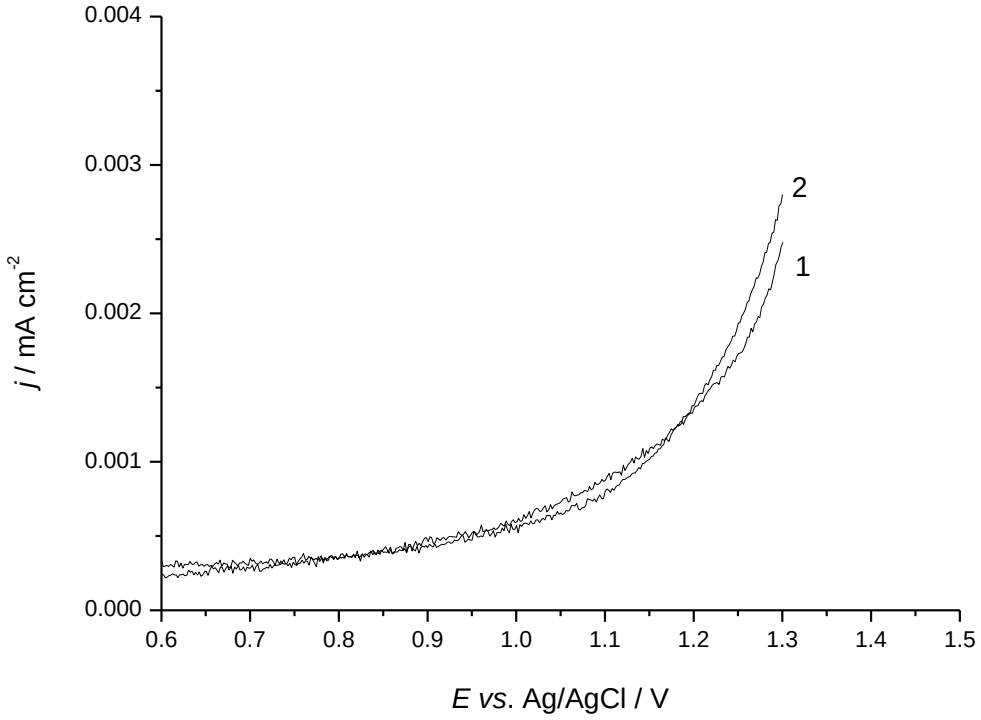

Figure 7.3.1. Differential pulse anodic voltammograms on BDD electrode at 10 mV s^{-1} in (1) a 0.6 M NaCl solution and (2) 0.6 M NaCl + 500 μM Ni^{2+} solution after cleaning process. Both tests were carried out after a pre–concentration step of 30 s at –1.5 V *vs*. Ag/AgCl.

7.4 Summary

In Chapter 4 it was demonstrated that at a pH lower than 4.0 the NAB corrosion performance undergoes an inversion of the anodic–cathodic site behaviour and the anodic behaviour is controlled by the oxidation of the nickel–, iron– and aluminium–rich κ–phases. This particular scenario can be often triggered by the slightly acidic environment present during crevice corrosion.

In this Chapter has been demonstrated the possibility of electrochemically assessing the nickel–ion concentration in neutral and slightly acidic chloride solutions on BDD electrodes. The protocol relied on a simple procedure achievable using relatively inexpensive materials, hence suitable for industrial quality and compliance measures. In particular, the nickel(II) detection was carried out on BDD electrode in acidic environments, without the need to introduce complexing agents into solution or altering the pH to alkaline values. The nickel–ion detection was achieved initially forming a metallic nickel deposit on the BDD electrode, subsequently oxidised using DPAV studying the Ni(II) / Ni(III) redox system. The anodic

response displayed a characteristic peak at markedly anodic potentials, *i.e.*, +1.07 V *vs.* Ag/AgCl, which was linearly dependent with the nickel–ion concentration in the range from 10 μM to 500 μM. Electrochemical investigations revealed a pH–dependence of the characteristic peak potential, which relied on a 0.5 mole of proton per mole of electrons, not attributable to the hydroxide system $Ni(OH)_2$ / NiOOH, but rather to a transient adsorbed nickel(II) form such as NiClOH, as described elsewhere [200]. DPAV tests were also performed in solutions at pHs of 3.0, 4.0 and 5.0 in order to study the feasibility of the electrochemical procedure in slightly acidic environments. Results indicated the possibility of detecting nickel–ions at pH of 4.0.

In contrast to the electrode cleaning–procedures reported in the literature after the nickel(II) detection protocols [127, 128], the pristine electrode surface state was successfully recovered by employing an electropolishing treatment at +1.3 V *vs.* Ag/AgCl, with a treatment time which was dependent upon the amount of nickel deposited on the electrode surface.

8. Boron–Doped Diamond Microelectrode Array Characterisation

The oxygen–terminated BDD microelectrode array performance was electrochemically investigated in its as–received state (supplied by Diamond Detectors Ltd (Poole, UK)). The characterisation was achieved using the same suite of electrochemical techniques utilised in Chapter 5 (Boron–Doped Diamond Electrode Characterisation), namely cyclic voltammetry, quasi–steady potentiodynamic polarisation and electrochemical impedance spectroscopy. This study has provided data on the diamond electrode surface quality, which is considered of significant importance for electro–analytical purposes [204], and also the influence of the microelectrode size on the overall electrochemical performance.

8.1 Electrochemical Characterisation of Boron–Doped Diamond Microelectrode Array

Figure 8.1.1 shows an overlay of the CVs carried out in a 0.5 M H_2SO_4 solution at the oxygen–terminated BDD microelectrode array. By examining the CVs it is evident that all potential windows have similar electrochemical characteristics as those previously presented in Section 5.1. Indeed, as highlighted in the Figure 8.1.1 insets, the HER and OER onset potentials were at around –1.0 V and 1.9 V *vs*. Ag/AgCl, respectively, slightly lower than those assessed for the BDD macroelectrode. The η_{OER} and η_{HER} were estimated for each of the five BDD microelectrodes using the equilibrium potentials of Equations 5.1.3 and 5.1.7 (see Section 5.1) and considering an oxygen activity of 0.20 mM and a pH of 0.88, assessed with a molal activity coefficient of 0.1316 and a density of 1.0045 g cm^{-3} [173]. The determined overpotentials are listed in Table 8.1.1 and suggest that among all the substrates microelectrode 1 showed the lowest catalytic property towards the HER, requiring a potential of –1.1 V *vs.* Ag/AgCl for attaining a j of –0.5 mA cm^{-2}, whereas microelectrode 2 exhibited the lowest activity for OER, needing a potential of 2.3 V *vs.* Ag / AgCl for achieving a current density of 0.5 mA cm^{-2}. Furthermore, before the oxygen gassing evolved at microelectrode 2, the anodic current presented a shoulder–peak ($A_{8.1}$) at 2.08 V *vs.* Ag/AgCl, likely to be related to the H_2O / OH· system, as highlighted in the literature Section 2.3.2. Indeed, Enache *et al*. [93] reported the formation of OH· radical at hydrogen–terminated BDD electrodes at a potential of 2.15 V *vs*. Ag/AgCl, according to Equation 2.3.8. In this specific study, the electrode potential at which the H_2O / OH· signal should occur is 2.09 V *vs.* Ag/AgCl, considering Equation 2.3.8 and a solution pH of 0.88. Therefore, the good agreement between the potential of the $A_{8.1}$ signal

and that predicted using Equation 2.3.8 [93] confirms that the peak–shoulder $A_{8.1}$ is attributable to the H_2O / OH· redox system.

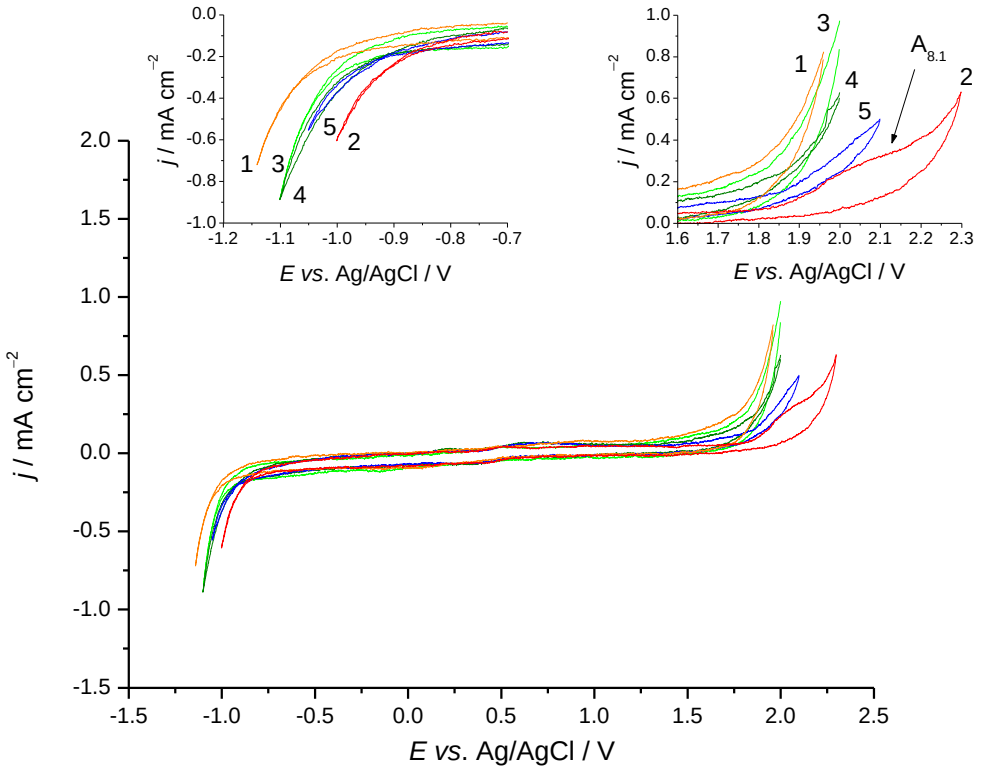

Figure 8.1.1. Cyclic voltammograms on BDD microelectrodes in a 0.5 M H_2SO_4 solution at 50 mV s^{-1}. Insets show the enlargements of the cathodic (left hand inset) and anodic (right hand inset) parts of the cyclic voltammograms. The radius of the BDD microelectrodes were 250 µm.

The slightly different overpotentials determined for HER and OER for the five BDD microelectrodes can be related to the presence of non–diamond carbon [77], which is obtained during the manufacturing process and considered as a charge transfer promoter for HER and OER. In addition to the potential window, the double layer capacitance can also be an useful indicator of the BDD electrode quality. The *C* values were estimated using Equation 5.1.11 reported in Section 5.1 and considering the electrode current at a potential of 0.4 V *vs.* Ag/AgCl. As can be seen in Table 8.1.1, the estimated *C* ranged between 500 µF cm^{-2} and 550 µF cm^{-2}, significantly higher than that determined for the BDD macroelectrode (in this case *C* was equal to 20 µF cm^{-2} for the same experimental conditions). The estimated *C* and overpotentials suggest that the quality of the five microelectrodes is slightly lower than those observed for the macroelectrode (see Table 5.1.1 of Section 5.1).

Table 8.1.1. Summary of the electrochemical characteristics (overpotentials and capacitance) determined at the BDD microelectrodes in a 0.5 M H_2SO_4 solution.

Microelectrode	η_{HER} / V	η_{OER} / V	η_{TOT} / V	C / μF cm^{-2}
1	–0.81	0.92	1.73	550
2	–0.68	1.25	1.93	500
3	–0.77	0.95	1.72	550
4	–0.76	1.04	1.80	500
5	–0.75	1.15	1.90	500

Figure 8.1.2 shows the cyclic voltammograms for the five BDD microelectrodes in a 0.6 M NaCl + 10 mM $[Fe(CN)_6]^{3-/4-}$ solution. The electrochemical processes involved in the anodic and cathodic reactions are the oxidation of $[Fe(CN)_6]^{4-}$ and the reduction of $[Fe(CN)_6]^{3-}$, as highlighted in Equation 5.1.13 of Section 5.1.

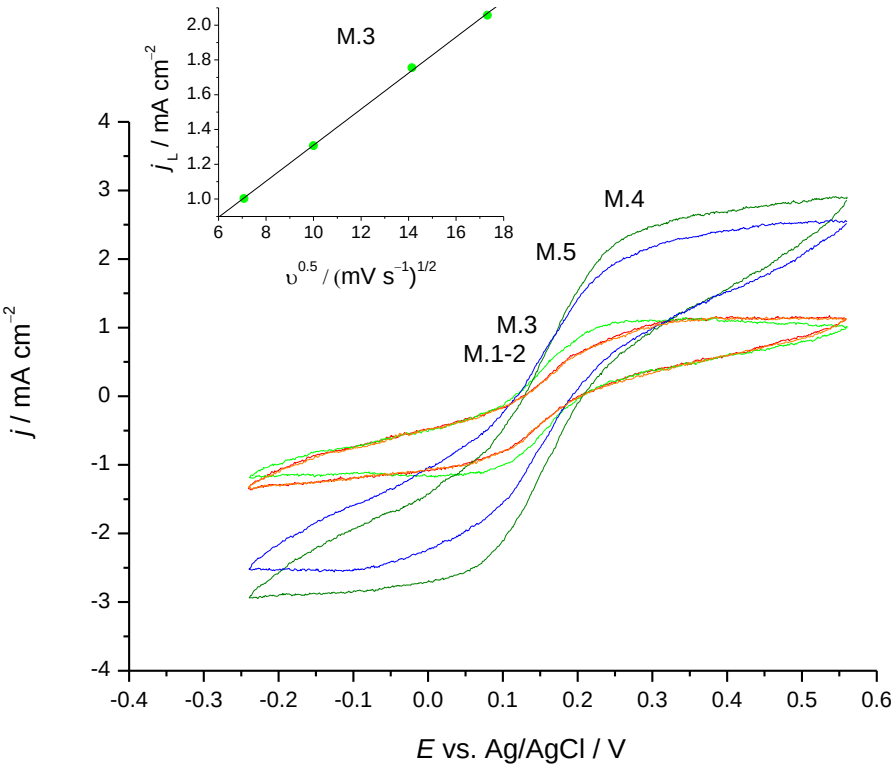

Figure 8.1.2. Cyclic voltammograms carried out on BDD microelectrodes 1 to 5 (M. 1 to M. 5) in a 0.6 M NaCl + 10 mM $[Fe(CN)_6]^{3-/4-}$ solution at 50 mV s^{-1}. Inset shows the relation between the square root of the scan rate and the diffusion current limit for the current response made only on microelectrode 3 (M. 3) in a 0.6 M NaCl + 10 mM $[Fe(CN)_6]^{3-/4-}$ solution at 50, 100, 200 and 300 mV s^{-1}.

It is worth noting that the current responses were not characterised by the typical peak–like trend, as evident for the BDD macroelectrode and thus associated with a semi–infinite linear diffusion (see Section 5.1). In fact, in Figure 8.1.2, the CVs show a plateau–like response which is generally related to a hemispherical diffusion process. Furthermore, the different magnitudes of the anodic and cathodic current plateaux at the BDD array indicate that each microelectrode promotes slightly different electron transfer kinetics of the $[Fe(CN)_6]^{3-/4-}$ redox couple.

It has been reported that for electrode discs with small radii (generally lower than 100 μm), the mass transfer is significantly enhanced due to hemispherical diffusion being more efficient than linear diffusion [205]. The characteristics of the diffusion flux related to (a) hemispherical and (b) linear diffusion are highlighted in Figure 8.1.3. The study of the electrochemical systems undergoing hemispherical and linear diffusions, as well as the transition between these two limit cases, have been achieved by Aoki *et al*. [206] using numerical simulation. They reported that the diffusion of an electro–active species from the bulk solution towards the electrode surface can be described by the *p* parameter, as highlighted in Equation 8.1.1 [206].

$$p = \sqrt{\left(\frac{F}{RT} \cdot \frac{r_d^2}{D} \upsilon \right)} \qquad 8.1.1$$

where r_d is the electrode disc radius. The *p* parameter was described as a dimensionless scan rate which provides insight regarding the type of the mass transfer taking place. Generally, the smaller the *p* parameter and the greater the extent of hemispherical diffusion occurring [206]. In particular, it was shown that the transition from the hemispherical to the linear diffusions took place in the range $0.076 \leq p \leq 150$: where at $p = 0.076$ the diffusion is hemispherical whereas at 150 the mass transfer is completely linear. The linear mathematical relationship between *p* and the electrode radius indicates that small electrodes are generally associated with small *p* values, where the hemispherical diffusion predominates over the linear. Furthermore, as implied by Equation 8.1.3, slow scan rates and high diffusion coefficients also promote hemispherical diffusion [206].

A different approach to understand the transition from the hemispherical to linear diffusion is, to first approximation, comparing the diffusion layer thickness (δ) with the electrode radius. Considering a linear diffusion mass transfer at a planar electrode (see Figure 8.1.3b), it is generally reported that the flux is not entirely perpendicular at the surface, but presents some inclined fluxes at the edge of the electrode area. This behaviour is related to the perturbation of the hemispherical diffusion on the linear diffusion which takes place at only few δ from the electrode surface edges.

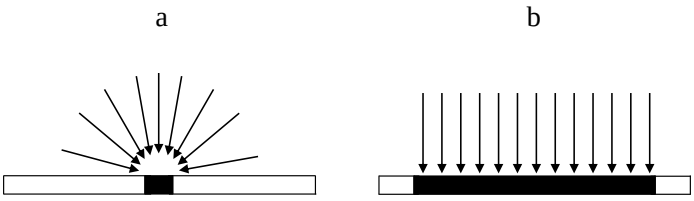

Figure 8.1.3. Schematic of (a) hemispherical and (b) linear diffusion associate with 0.076 and 150 *p* values.

Therefore, for electrodes with radii significantly greater than the diffusion layer thickness ($r_d >> \delta$), only a small fraction of the electrode surface experiences inclined diffusion fluxes and the whole process can be approximated by a linear diffusion. Conversely, when the electrode radius is considerably smaller than the diffusion layer thickness ($r_d << \delta$), the inclination of the fluxes is maximised and the system can be described as in Figure 8.1.3a [205].

For potentiodynamic experiments, the hemispherical diffusion current is generally related to a diffusion–limited process (I_L) which is independent from the scan rate [206]. The general equation which describes the relationship between the hemispherical diffusion current, the potential, the electrode radius and the diffusion coefficient of an electro–active species is highlighted in Equations 8.1.2 and 8.1.3 [206].

$$I_L = \frac{4\,z\,F\,A c\,D}{(1+\mathrm{e}^{-E(t)})} \qquad 8.1.2$$

where $E(t)$ is the time dependent potential, defined as it follows

$$E(t) = \frac{z\,F}{R\,T}(E_i - \upsilon\,t - E^{\circ}) \qquad 8.1.3$$

where E_i represents the initial electrode potential. As can be seen in Equation 8.1.3, the potential is a function of time and when it is sufficiently high to allow the system to be under diffusion mass transfer e^{-E} approaches zero. Therefore, Equation 8.1.3 can be rewritten as Equation 8.1.4 [206].

$$I_L = 4\,z\,F\,A c\,D \qquad 8.1.4$$

Looking closely at the Figure 8.1.2 inset, which shows the I_L *vs.* $\upsilon^{1/2}$ (scan rate ranges from 50 mV s^{-1} to 300 mV s^{-1}), it is apparent that the diffusion–limited current densities and the square root of the scan rate have a linear relationship. This behaviour is unexpected and contradicts Equation 8.1.4, which describes a process which is completely independent from the scan rate. Therefore, it can be inferred that the investigated microelectrode array did not undergo a fully

hemispherical diffusion at scan rates between 50 mV s^{-1} and 300 mV s^{-1}, but rather it underwent a mixed hemispherical–linear diffusion. To better understand the physical behaviour of the microelectrodes the scan rate range was widened from 0.1 mV s^{-1} to 500 mV s^{-1} (see Figure 8.1.4). The variable "scan rate" was purposely considered for this particular investigation, since, from Equation 8.1.1, it appears that *p* proportionally decreases as the υ scan rate is reduced.

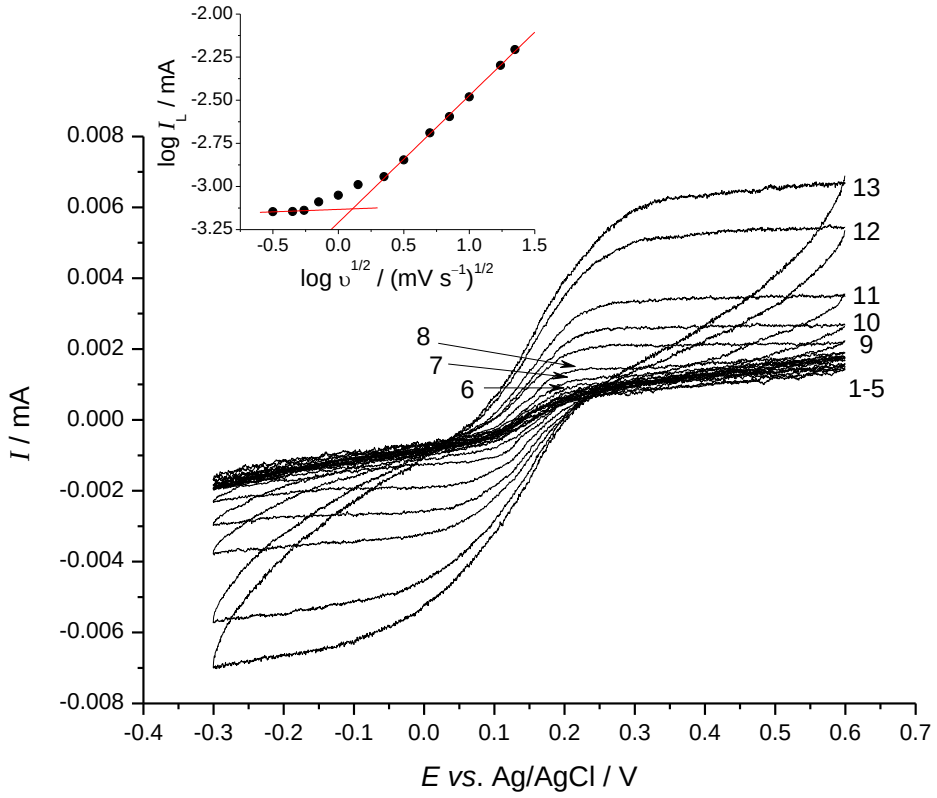

Figure 8.1.4. Cyclic voltammograms carried out on BDD microelectrode 3 in a 0.6 M NaCl + 10 mM $[Fe(CN)_6]^{3-/4-}$ solution at (1) 0.1, (2) 0.2, (3) 0.3, (4) 0.5, (5) 1.0, (6) 2.0, (7) 5.0, (8) 10.0, (9) 25.0, (10) 50.0, (11) 100.0, (12) 300.0 and (13) 500.0 mV s^{-1}. The inset shows the relationship between the diffusion–limiting currents and the square root of the scan rate.

From Figure 8.1.4, a similar current shape characterised by anodic and cathodic plateaux is clearly evident to that shown in Figure 8.1.2. However, as can be seen from the inset (which reports the I_L *vs.* log $υ^{0.5}$) within the log $υ^{0.5}$ range from –0.50 (mV s^{-1})$^{1/2}$ to –0.26 (mV s^{-1})$^{1/2}$, which corresponds to a range from 0.1 mV s^{-1} to 0.3 mV s^{-1}, the I_L magnitude remained stable and independent from υ, thus indicating a fully hemispherical diffusion behaviour. Conversely, when log $υ^{0.5}$ exceeded –0.26 (mV s^{-1})$^{1/2}$ the I_L magnitude increased. This behaviour suggested that the scan rate of 0.3 mV s^{-1} represents the threshold which delineates the BDD microelectrode behaviours from being fully hemispherical to mixed hemispherical–linear.

Table 8.1.2 compares the theoretical p values (determined using Equation 8.1.3 with D = 0.765×10^{-2} cm^2 s^{-1} for $[Fe(CN)_6]^{3-}$ [172] and r_d = 250 μm), I_L and the δ (obtained using Equation 8.1.5 [207]).

$$\delta = \sqrt{\frac{2\,D\,\Delta E}{\upsilon}} \qquad 8.1.5$$

Where ΔE is the potential difference between the oxidation potential and the potential of the limiting current. From Table 8.1.2 it can be seen that within the p range of 0.519 to 0.899, the I_L was determined to be stable at about -0.7×10^{-3} mA, whereas from 1.160 to 36.961 the I_L increased in a dependent manner with the scan rate. Thus, these specific trends indicate that the hemispherical diffusion predominated at low scan rates, as it would be expected from the low p values, whereas the mixed hemispherical–linear diffusion, or eventually a full linear diffusion, occurred at high scan rates due to the higher p values.

Corroboration of this behaviour was also attained by comparing the size of the electrode radius (0.025 cm) with the estimated diffusion layer thicknesses. It was observed that below the scan rate threshold of 0.3 mV s^{-1} the r_d / δ was less than 1 (r_d < δ), whereas above 0.3 mV s^{-1} it exceeded unity, (r_d > δ). This is in line with [205], where generally at r_d / δ ratios less than one the electrode undergoes hemispherical diffusion while greater than one the linear diffusion predominates [207].

The evaluation of the microelectrode surfaces were determined using Equation 8.1.4, since within the scan rate range from 0.1 to 0.3 mV s^{-1} the CV tests were controlled by hemispherical diffusion process. The electrode radius for the microelectrode 3 was determined to be 0.0249 cm, in perfect agreement with the geometrical value provided by the manufacturer, *i.e.*, 0.025 cm.

Knowing the diffusion characteristics of the microelectrode array, the BDD microelectrode electrochemical performance was also assessed using quasi–steady potentiodynamic polarisation and electrochemical impedance spectroscopy in the 0.6 M NaCl + 10.0 mM $[Fe(CN)_6]^{3-/4-}$ solution. Figure 8.1.5 shows the quasi–steady potentiodynamic polarisation curves carried out at the microelectrodes, M.1 to M.5. The expression which best approximates these behaviours is given by Equation 5.1.15, that is, the Butler–Volmer equation for a the low–field approximation [178], as discussed in Chapter 5.

Table 8.1.2. Kinetic and diffusion parameters (experimental and theoretical) determined at BDD microelectrode 3 in a 0.6 M NaCl + 10 mM $[Fe(CN)_6]^{3-/4-}$ solution using cyclic voltammetry at different scan rates.

υ / mV s^{-1}	$\log \upsilon^{1/2}$ / $(mV\ s^{-1})^{1/2}$	I_L / mA	p	δ / cm	r_d / cm	r_d / δ
0.1	0.316	-0.754×10^{-3}	0.519	0.108	0.025	0.231
0.2	0.447	-0.784×10^{-3}	0.734	0.071	0.025	0.352
0.3	**0.548**	$\mathbf{-0.726 \times 10^{-3}}$	**0.899**	**0.049**	**0.025**	**0.510**
0.5	0.707	-0.814×10^{-3}	1.160	0.024	0.025	1.042
1.0	1.000	-0.898×10^{-3}	1.641	0.020	0.025	1.250
2.0	1.414	-1.023×10^{-3}	2.321	0.029	0.025	0.862
5.0	2.236	-1.142×10^{-3}	3.669	0.017	0.025	1.470
10.0	3.162	-1.432×10^{-3}	5.1888	0.012	0.025	2.083
25.0	5.000	-2.048×10^{-3}	8.204	0.009	0.025	2.778
50.0	7.071	-2.546×10^{-3}	11.603	0.007	0.025	3.571
100.0	10.000	-3.315×10^{-3}	16.409	0.005	0.025	5.000
300.0	17.320	-5.042×10^{-3}	28.420	0.003	0.025	8.333
500.0	22.361	-6.213×10^{-3}	36.691	0.002	0.025	12.500

Table 8.1.3 presents the electro–activities of the five microelectrodes. Similar values were estimated for the microelectrodes 1 and 3, whereas slightly higher values were obtained for microelectrodes 2, 4 and 5.

Information of the quality of a doped diamond electrode can often be obtained from electrochemical impedance spectroscopy [78]. In order to confirm the estimated j_0 and k^0_{app} determined using quasi–steady PP for the $[Fe(CN)_6]^{3-/4-}$ system, EIS tests were also carried out in identical experimental conditions at the BDD microelectrodes.

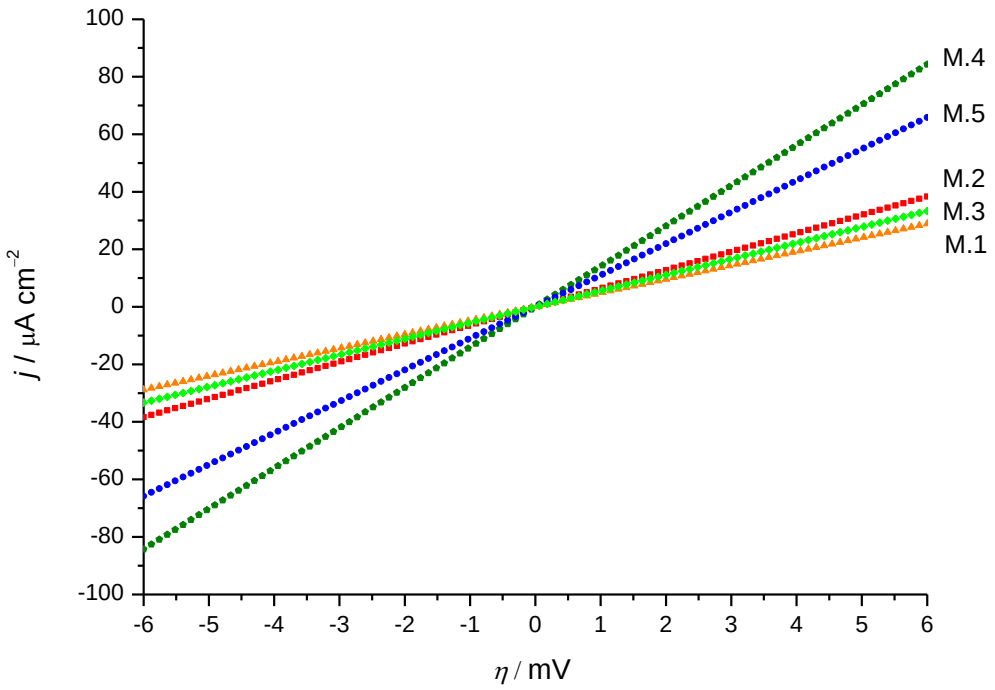

Figure 8.1.5. Quasi–steady potentiodynamic polarisation curves at the different BDD microelectrodes in a 0.6 M NaCl + 10.0 mM $[Fe(CN)_6]^{3-/4-}$ solution at 0.1 mV s^{-1}.

Table 8.1.3. Kinetic parameters determined from quasi–steady potentiodynamic polarisation curves in a 0.6 M NaCl + 10.0 mM $[Fe(CN)_6]^{3-/4-}$ for the five BDD microelectrodes.

Microelectrode	j_0 / μA cm^{-2}	k^0_{app} / cm s^{-1}
1	62	0.65×10^{-4}
2	127	1.31×10^{-4}
3	83	0.86×10^{-4}
4	182	1.88×10^{-4}
5	142	1.47×10^{-4}

Figure 8.1.6 shows the impedance responses, *i.e.*, (b) module impedance–frequency, (c) Nyquist and (d) phase angle–frequency plots, for the BDD microelectrode array in a 0.6 M NaCl + 10.0 mM $[Fe(CN)_6]^{3-/4-}$ solution. The Bode plot reveals that the response of the microelectrodes 1–3 cannot simply be described with one time–constant ($R_{ct}C$), associated with the $[Fe(CN)_6]^{3-/4-}$ electron transfer, as found for the BDD macroelectrode (see Section 5.1). Indeed, only

microelectrodes M.4 and M.5 clearly present evidence of a single time–constant related to the redox process of $[Fe(CN)_6]^{3-/4-}$ (ca. 2 kHz), whereas M.1, M.2 and M.3 responses show an additional time–constant at low frequency, within the frequency range from of 100 Hz to 20 Hz. Polcaro *et al*. [78] characterised the electrochemical behaviour of BDD electrodes subjected to different oxidation treatments in 0.5 M H_2SO_4 using the $[Fe(CN)_6]^{3-/4-}$ redox system. They reported the presence of two time–constants, where the high frequency was attributed to the $[Fe(CN)_6]^{3-/4-}$ electron transfer whereas the low frequency was related to the capacitive response of impurities located at the diamond grain boundaries. Accordingly, the low frequency time–constants for the microelectrodes 1–3 can be related to the presence of impurities [78].

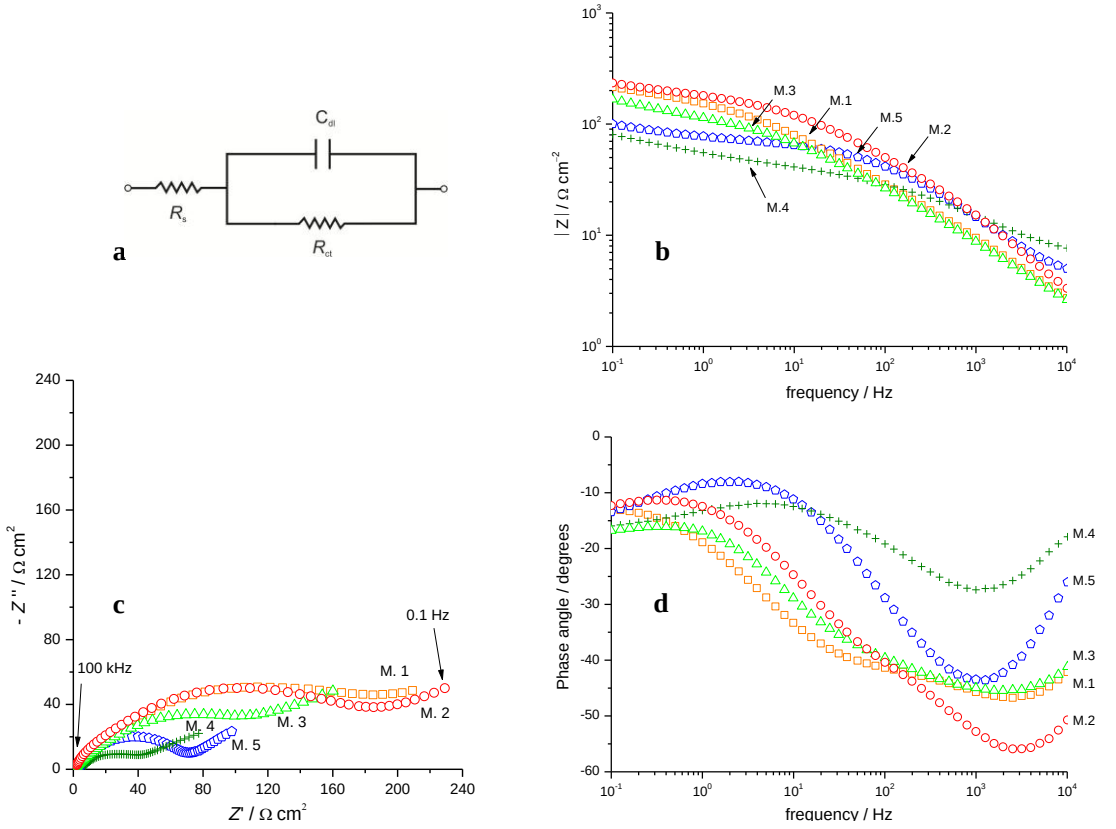

Figure 8.1.6. (b) Bode (Modulus *vs*. frequency), (c) Nyquist and (d) Bode (Phase angle *vs*. frequency) plots on BDD microelectrodes in a 0.6 M NaCl + 10.0 × 10^{-3} M $[Fe(CN)_6]^{3-/4-}$ solution using a potential perturbation of ±5 mV at the open circuit potential over a range of frequency of 10^4 Hz to 0.1 Hz. (a) Equivalent circuit used to fit impedance responses of M.4 and M.5.

This finding appears to be in line with results reported in Figure 8.1.1, where the microelectrodes 1–3 had responses with higher capacitance and lower potential window than those assessed at the macroelectrode reported in Section 5.1. The assessment of the j_0 and k^0_{app}

for BDD microelectrodes 4 and 5 was achieved by fitting the EIS data with the equivalent circuit shown in Figure 8.1.6a.

Table 8.1.4. Kinetic parameters determined using electrochemical impedance spectroscopy for BDD microelectrodes M.4 and M.5 in a 0.6 M NaCl + 10.0 mM $[Fe(CN)_6]^{3-/4-}$ solution.

Microelectrode	R_{ct} / Ω cm^2	j_0 / μA cm^{-2}	k^0_{app} / cm s^{-1}	χ^2
4	43.2	588	6.10×10^{-4}	2×10^{-3}
5	66.7	381	3.94×10^{-4}	8×10^{-3}

Table 8.1.4 lists the kinetic values for the ferro / ferricyanide system, *i.e.*, j_0, k^0_{app}, determined using Equations 5.21 and 5.22 reported in Section 5.1 [179].

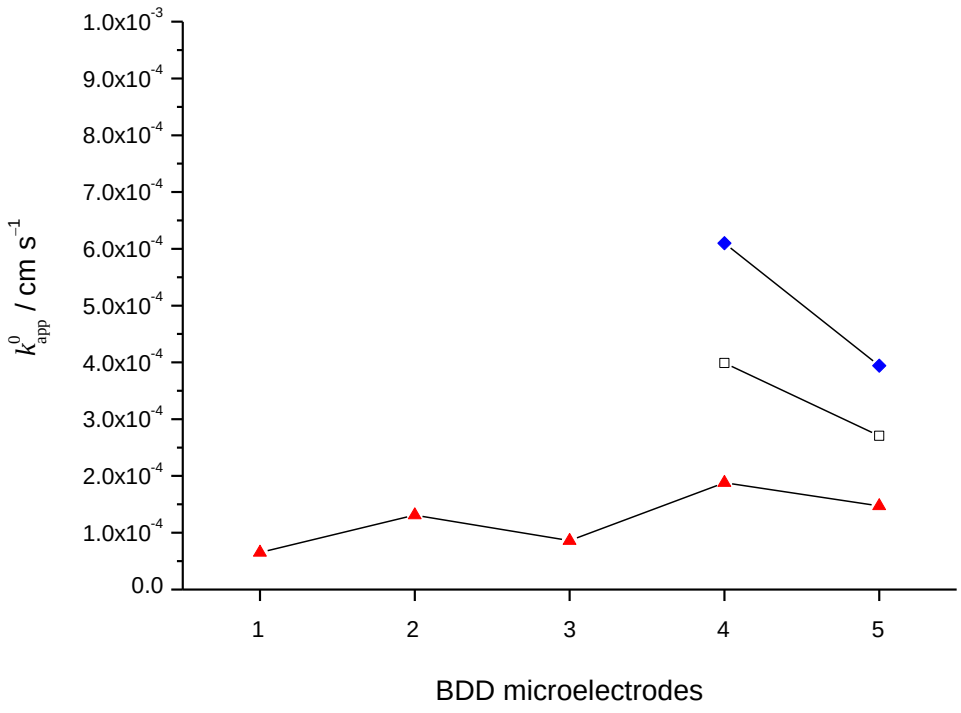

Figure 8.1.7. Evaluated apparent kinetic rate constants for BDD microelectrodes 1 to 5 using quasi–steady polarisation curves (red triangle) and electrochemical impedance spectroscopy (blue diamond). The white squares are the estimated average values.

Figure 8.1.7 shows the estimated k^0_{app} using quasi–steady potentiodynamic polarisation (red triangle) and EIS (blue diamond) for the $[Fe(CN)_6]^{3-/4-}$ system, whereas the white square indicates the average obtained with the two techniques. It is worth noting that the k^0_{app} values obtained via EIS present a similar trend with those estimated via quasi–steady potentiodynamic polarisation, even though slightly bigger. Furthermore, the different magnitude of the anodic and cathodic current plateaux determined at the investigated BDD microelectrodes, see Figure 8.1.2, reflects the catalytic property of the substrates towards $[Fe(CN)_6]^{3-/4-}$ electron transfer. In particular, it was observed that microelectrode 4 promoted a faster electron transfer (ca. two–fold) compared with microelectrodes 1–3.

Table 8.1.8. Evaluated apparent kinetic rate constants for BDD microelectrodes 1 to 5 using quasi–steady polarisation curves (red triangle) and electrochemical impedance spectroscopy (blue rhombus). Withe squares represent the estimated average values.

Microelectrode	k^0_{app} / cm s^{-1} (PP)	k^0_{app} / cm s^{-1} (EIS)	k^0_{app} / cm s^{-1} (Average)
1	0.65×10^{-4}	–	–
2	1.31×10^{-4}	–	–
3	0.86×10^{-4}	–	–
4	1.88×10^{-4}	6.10×10^{-4}	3.99×10^{-4}
5	1.47×10^{-4}	3.94×10^{-4}	2.70×10^{-4}

8.2 Summary

The electrochemical performance of the BDD microelectrode array was studied in either 0.5 M H_2SO_4 or 0.6 M NaCl + 10 mM $[Fe(CN)_6]^{3-/4-}$, using a suite of electrochemical techniques.

Cyclic voltammetry, initially carried out in the sulphuric acid solution, highlighted that the BDD microelectrodes have a wide potential window available for electroanalytical purposes. The overall potential range was generally similar, though slightly narrower, to that determined for the BDD macroelectrode. The double layer capacitance was also determined from CVs in 0.5 M H_2SO_4 and found to be significantly higher than that obtained at the macroelectrode. These findings can be explained in terms of a lower microelectrode diamond quality than that of the macroelectrode.

The cyclic voltammograms responses of the $[Fe(CN)_6]^{3-/4-}$ showed an electrochemical behaviour which changed from fully hemispherical to mixed hemispherical–linear diffusions, as the scan rate was increased from 0.3 mV s^{-1}, which represents the threshold limit between the different diffusion behaviour. This insight was achieved by comparing the electrode radius with the calculated diffusion layer thicknesses of the $[Fe(CN)_6]^{3-/4-}$ responses. Tests carried out using quasi–steady potentiodynamic polarisation and EIS in a 0.6 M NaCl + 10 mM $[Fe(CN)_6]^{3-/4-}$ solution showed similar but not identical electrochemical responses between the five BDD microelectrodes.

9. Nickel–Aluminium Bronze Crevice Corrosion Monitoring using a Boron–Doped Diamond Microelectrode Array in Aqueous Chloride Solutions

This Chapter reports the use of the BDD microelectrode array to assess the *in situ* metal–ion concentrations generated from NAB crevice corrosion. As the last and conclusive part of the Results and Discussion, Chapter 9 brings together the insights obtained from the electrochemical behaviour of NAB in chloride solutions at different pHs and concentrations of benzotriazole (see Chapter 4), the electrochemical performance of BDD electrodes (see Chapters 5 and 8) and the electro–reactivity of metal ions (see Chapters 6 and 7).

The study of NAB crevice corrosion was achieved by artificially generating the crevice environment as described in Chapter 3. The metal–ion monitoring was electrochemically assessed using the BDD microelectrode array during an immersion of three hundred hours (ca. two weeks) in 0.6 M NaCl and in 0.6 M + 10 mM benzotriazole. The validation of the metal–concentration was achieved by simultaneously determining the metal–concentration via capillary electrophoresis.

9.1 Electrochemical Study using a Boron–Diamond Microelectrode Array in Aqueous Chloride Solutions

Section 2.1 highlighted that crevice corrosion monitoring is generally achieved measuring the pH and / or assessing the chloride concentration within the crevice environment [16, 17]. However, even though strictly related to crevice corrosion, these parameters represent the indirect chemical and physical consequences obtained when crevice corrosion is triggered. Indeed, while changes of the pH are related to hydrolysis reactions of crevice corrosion metal–ions (chemical effect) [7], the variation of the chloride concentration is generally associated with a diffusion process which attempts to maintain the crevice electroneutrality (physical effect) [7].

In this current work, the approach used to monitor the time–evolution of crevice corrosion was different from those previously reported in the literature [16, 17] and considered the direct evaluation of the metal–ion concentrations within the crevice solution chemistry. Figure 9.1.1 shows an overlay of DPAVs carried out on BDD microelectrode array, which was embedded in the crevice–corrosion setup as highlighted in Chapter 3 (see Figure 3.2.1). In particular, the

microelectrode used was the 4 (M.4), which according to Section 8.1 exhibited the lowest double layer capacitance. Inspecting Figure 9.1.1, an anodic peak ($A_{9.1}$) at approximately 0.3 V *vs*. Ag/AgCl is clearly evident, which also increased with time. According to tests performed on BDD electrode in chloride solutions containing copper(II) (see Chapter 6), signal $A_{9.1}$ can be reasonably attributed to the oxidation of copper(I) to copper(II); this insight can be further confirmed by comparing the oxidation potential peaks determined for the copper(I) / copper(II) system shown in the calibration curve of Figure 9.1.2. The Figure 9.1.1 inset shows the current peak density (j_p) determined at the different times. As can be seen, the j_p progressively increased from 0.01 mA cm^{-2} to 0.038 mA cm^{-2} within the time range of 62 h to 209 h; however, for NAB exposure times greater than 209 h the signal $A_{9.1}$ remained stable. The j_p values were determined by subtracting to the current peak density the background current density at –0.2 V *vs*. Ag/AgCl, where no faradic processes were observed.

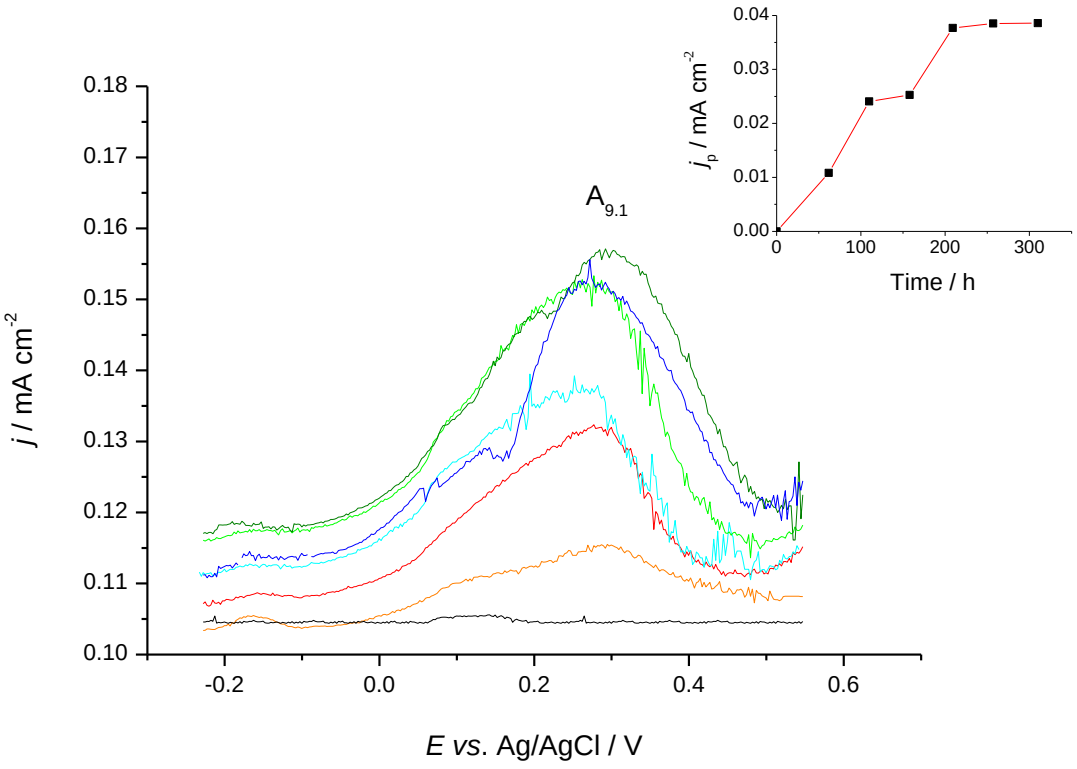

Figure 9.1.1. Differential pulse anodic voltammograms on a BBD microelectrode (M.4) array embedded in NAB crevice–corrosion setup (see Chapter 3), at different exposure times: (black) 0, (orange) 62, (red) 110, (cyan) 158, (green) 209, (olive) 257 and (blue) 310 h. The scan rate was 10 mV s^{-1}. Inset shows the $A_{9.1}$ current peak density as a function of the exposure time.

Chapter 8 determined that the electrochemical performances of the BDD microelectrodes are similar to those reported in the literature [77], which are often characterised by a low double layer current and a wide potential window. Inspecting the DPAVs in Figure 9.1.1, it can be noted that the background current gradually increased with extended immersion times. Therefore, considering the intrinsic "inertness" of the electrode surface (to undergo adsorption phenomena), the increase of the background current density can be entirely associated with a change of the crevice chemical composition, or alternatively, a change of the ionic strength. This insight may represent a plausible explanation for the observed behaviour, since the crevice solution ionic strength can significantly change when metal–ion or the chloride concentrations increase due to the small volume of the crevice.

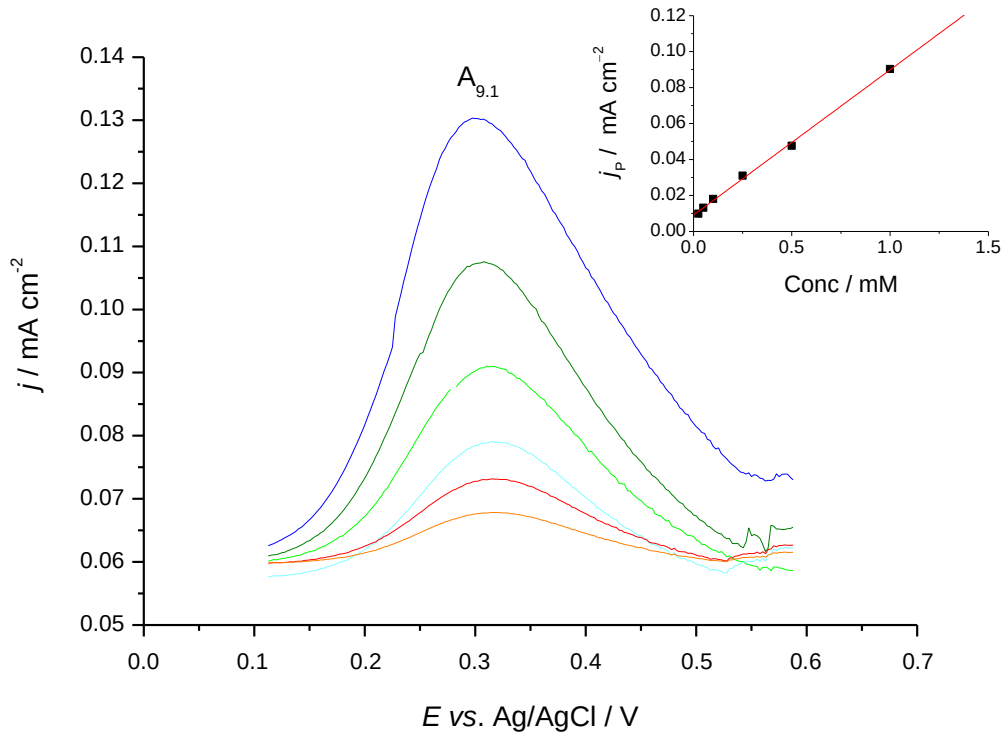

Figure 9.1.2. Differential pulse anodic voltammograms on BBD microelectrode 4 at different copper(I) concentrations: (orange) 0.025, (red) 0.050, (cyan) 0.100, (green) 0.250, (olive) 0.500 and (blue) 1.00 mM. The scan rate was 10 mV s^{-1}. The solutions were deaerated by sparging with nitrogen (oxygen concentration ≤ 3 μM).

Furthermore, as can be seen from the Figure 9.1.1 inset, after 200 h of monitoring the current peak density attained a steady–steady which was characterised by a levelling of the current peak values. This behaviour suggests that an equilibrium occurring between the copper(I) diffusion process and the NAB oxidation was achieved.

Regarding the shape of the DPAVs, the responses exhibited a current peak instead of a clearly defined plateau. However, in Chapter 8 it was established that the mixed hemispherical and linear diffusion conferred to the recorded current of voltammograms a plateau–like shape rather than a peak. This specific behaviour can be explained by considering the differences behind the two measurement techniques. Indeed, while cyclic voltammetry relies on an applied potentiodynamic staircase, the differential pulse voltammetry is based on a potentiodynamic staircase to which has been superimposed a potential pulse (generally between 0.01 V and 0.1 V). Furthermore, as opposed to CV, the current determined in DPV is obtained by subtracting the current at the end of the potential pulse to that measured before the pulse; therefore, at potentials distant from the equilibrium, where the faradic current is under diffusion control, the differential current is approximately zero [169].

Figure 9.1.2 shows the calibration curve carried out on BDD microelectrode (1) array achieving DPAV in 0.6 M NaCl containing different concentrations of copper(I). The presence of a peak at 0.31 V *vs*. Ag/AgCl indicates that the anodic signal recorded in Figure 9.1.1 is related to the oxidation of copper(I) to copper(II).

Table 9.1.1. Copper(I) concentrations determined in crevice solution.

Time / h	Conc. / mM
62	0.125
110	0.289
158	0.304
209	0.458
257	0.468
310	0.468

Considering the good linearity obtained between current peak density and concentration, the copper(I) concentrations of Figure 9.1.1 were estimated to range between 0.12 mM to 0.46 mM, as can be seen in Table 9.1.1.

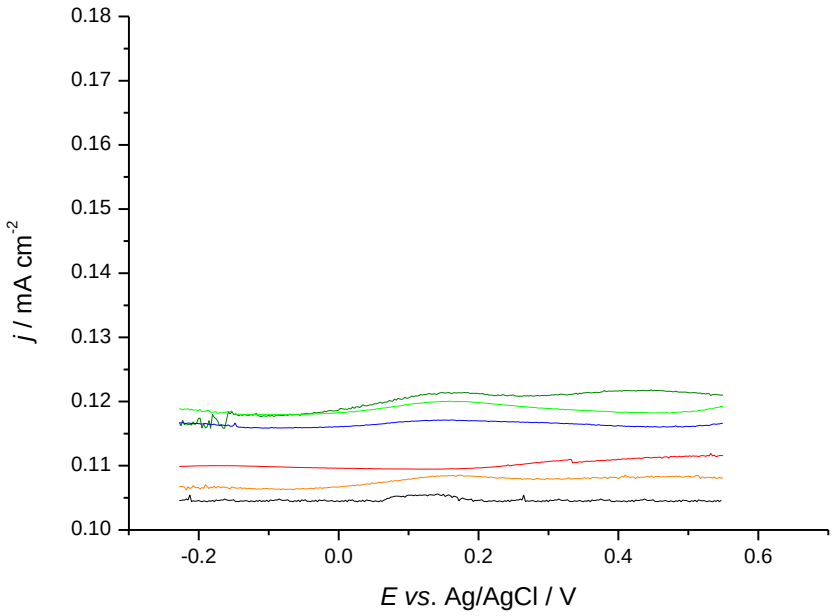

Figure 9.1.3. Differential pulse cathodic voltammograms for 0.6 M NaCl on BBD microelectrode 4, embedded in NAB crevice–corrosion former setup (see Chapter 3), at different exposure times: (black) 0, (orange) 62, (red) 110, (green) 209, (olive) 257 and (blue) 310 h. The scan rate was 10 mV s^{-1}.

Figure 9.1.3 shows the DPAV measurements for the cathodic sweep on BDD microelectrode (M.4) array after different NAB exposure times in 0.6 M NaCl solution. Notably, no cathodic peaks were observed, hence suggesting the low copper(II) concentration within the crevice. This finding agrees with results reported in the literature [7] where, due to the low oxygen concentration often present within crevice solutions, any further oxidation of copper(I) to copper(II) may be limited.

The concentration of copper ions, and possibly those of other metal ions (such as nickel, aluminium and iron), were also assessed using capillary electrophoresis. Details of the metal–ion LODs are reported in Chapter 3 (Material and Methods), whereas calibration curves for copper(II), nickel(II), iron(III) and aluminium(III) are shown in the Appendix (Figure A_1–A_6). The estimation of the metal–ion concentrations was achieved using a crevice corrosion setup similar to that used for the electrochemical monitoring (see Figure 3.2 reported in Chapter 3) and sampling the crevice solution after 62 h, 158 h and 310 h from immersion. Figure 9.1.4 shows the copper ion crevice concentrations determined after 62, 158 and 310 h. The estimated values agree reasonably well with those assessed with DPAV, within the same order of magnitude although at slightly higher concentrations.

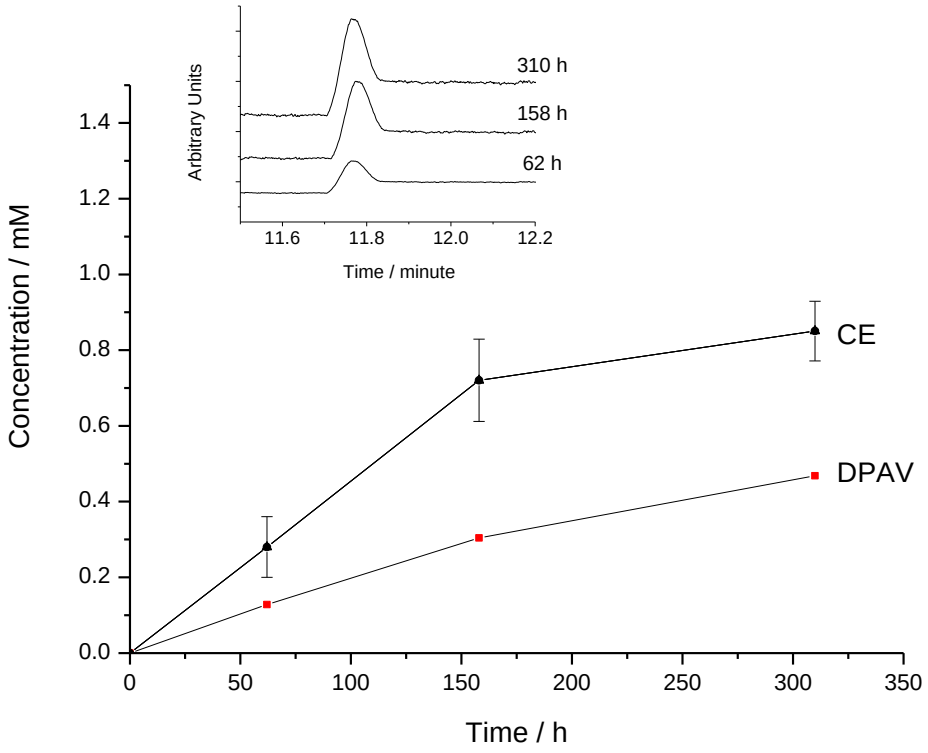

Figure 9.1.4. Comparison between copper ion concentrations assessed using differential pulse anodic voltammetry and capillary electrophoresis at different NAB exposure times in 0.6 M NaCl. Inset shows the electropherograms determined at the different times.

Chapter 4 highlighted that when NAB is exposed to neutral chloride solution its corrosion behaviour is driven by the oxidation of the copper–rich α–phase, whereas the other κ–phases are cathodically protected. However, as the pH decreases below 4, NAB generally undergoes an inversion of the anodic–cathodic site behaviour and the aluminium–, iron– and nickel–rich κ_I–, κ_{II}– and κ_{IV}–phases preferentially corrode. From the CE analysis determined on the sampled crevice corrosion solutions only copper–ion was identified, thus indicating that during the monitored time the NAB corrosion was controlled by the oxidation of the copper–rich α–phase.

9.2 Electrochemical Study using a Boron–Diamond Microelectrode Array in Aqueous Chloride Solutions containing Benzotriazole

Chapter 4 established the good corrosion performance of NAB when exposed to neutral chloride solutions in the presence of benzotriazole. The estimated benzotriazole adsorption free energy (–44.0 kJ mol^{-1}) explained the remarkably reduced anodic and cathodic kinetics and the

improved NAB corrosion performance. Conversely, when NAB was exposed to acidic or slightly acidic chloride solutions (pHs lower than 4), the benzotriazole corrosion inhibition drastically decreased. This particular behaviour, related to the low benzotriazole adsorbability (or affinity) for the corroding nickel–, iron– and aluminium–rich κ–phases, indicated that benzotriazole cannot be always employed as an effective inhibitor.

Figure 9.2.1 shows the metal–ion concentrations assessed within an immersion time of 310 h in a 0.6 M NaCl solution containing 0.01 M of benzotriazole. As can be seen in the inset, which shows the DPAV recorded at the BDD microelectrode (1) array, the recorded current densities were rather scattered and noisy.

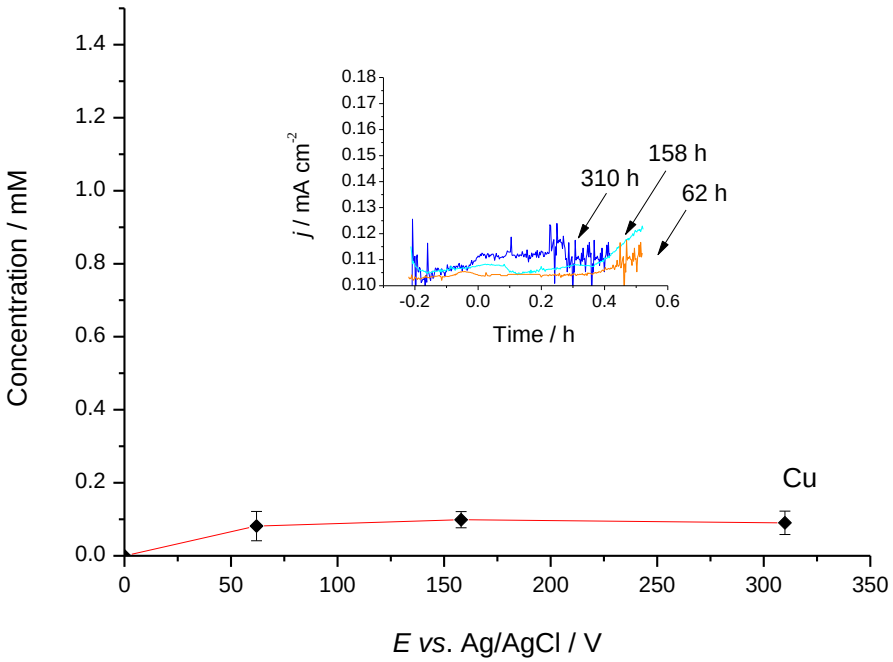

Figure 9.2.1. Copper–ion concentrations assessed using capillary electrophoresis at different NAB exposure times in 0.6 M NaCl + 0.01 M benzotriazole. Inset shows the differential pulse voltammograms recorded at the BDD microelectrode (1) array after: (orange) 62, (cyan) 158 and (blue) 310 h. The DPAV scan rate was 10 mV s^{-1}.

This particular behaviour can be explained considering the formation of the inorganic and non–conductive $[Cu(I)BTA^{-}]_n$ polymer, which, accordingly to the mechanism proposed in the literature [18, 37], is formed via Equations 2.2.4–2.2.9 (see Section 2.2). In the previous Section 9.1, it was shown that, for the considered monitoring time, NAB underwent selective α–

phase corrosion since the copper(I) was the only element found in the crevice solution. Therefore, the formation of the $[Cu(I)BTA^{-}]_n$ film may represent a plausible reason for the measured noisy responses. The determination of the metal–ion concentrations were then achieved using CE. As can be seen in Figure 9.2.1, only copper was detected and its concentration was determined to be about 90 μM throughout the tests. These concentrations were considerably lower than those estimated in the uninhibited solution and can be considered as confirmation of the good corrosion inhibition of benzotriazole.

9.3 Summary

This aspect of the investigation has shown the potential to evaluate the *in situ* crevice metal ion concentration using a BDD microelectrode array, thus allowing the monitoring of the time–evolution of the crevice solution chemistry. The electrochemical investigation was achieved by performing DPV in either anodic or cathodic sweeps. Interestingly, only the DPV performed in the anodic direction showed the presence of an electro–active species, at a potential of 0.3 V *vs.* Ag/AgCl. According to the calibration carried out in 0.6 M NaCl containing a range of copper(I) concentrations, the DPAV response measured within the crevice corrosion solution was attributed to the oxidation of copper(I), whose concentration ranged from 0.125 mM to 0.468 mM. Regarding the NAB crevice corrosion inhibition, benzotriazole was demonstrated to be an effective inhibitor, due to the significantly lower copper ion concentration as estimated within the crevice solution.

10. Conclusions

The current study has investigated the initiation and time–evolution NAB crevice corrosion monitoring using *in situ* BDD electrodes and a microelectrode array. The work programme has comprised a number of different aspects such as: (*i*) the NAB corrosion performance in chloride solutions in either the presence or absence of benzotriazole, (*ii*) the electrochemical and material properties of BDD electrodes, (*iii*) electroanalysis of (simulated) crevice corrosion solutions at BDD electrodes and (*iv*) NAB crevice corrosion monitoring using the BDD microelectrode array. These research topics have been connected together since they critically are part of the same multidisciplinary project. Initially, a literature survey was undertaken to establish the current state–of–the–art / background knowledge of the NAB corrosion mechanisms and BDD electrode performance, thereby providing key insights for the analysis and interpretation of the experimental data. Herein are reported the principal conclusions and major findings for this research programme.

- The NAB corrosion behaviour was controlled by the selective dissolution of the copper–rich α–phase within the $\alpha + \kappa_{III}$ eutectoid when exposed to neutral chloride solution. Its corrosion behaviour was assessed to be similar to that of unalloyed copper due to the same protons and chloride order of reactions. However, when the pH solution was decreased below 4, NAB exhibited a different electrochemical mechanism and the dissolution process was driven by the oxidation of the aluminium–, iron– and nickel–rich κ_I–, κ_{II}– and κ_{IV}–phases at the boundary with the α–phase. These findings support previous studies reported in the literature regarding the NAB crevice corrosion [7], where due to the presence of an acidic crevice environment, metal ions such as iron, nickel and aluminium were determined in the local solution.
- At solution pH higher than 4, benzotriazole significantly reduced the NAB corrosion, decreasing both anodic and cathodic reaction kinetics. The benzotriazole adsorption on NAB followed the Kastening–Holleck isotherm and the determined adsorption free enthalpy was assessed to be –44.0 kJ mol^{-1}. The excellent NAB corrosion performance observed when exposed to neutral chloride solutions in the presence of benzotriazole was explained considering the high affinity of the inhibitor for copper–corroding surfaces. On the contrary, at pHs below 4 the NAB corrosion performance was not specifically affected by the presence of benzotriazole due to the low inhibitor affinity towards aluminium–, iron–, nickel–corroding surfaces. This particular behaviour indicated that once the crevice solution pH attains a value lower

than 4 and the NAB dissolution is controlled by the selective corrosion of the aluminium–, iron– and nickel–rich κ_I–, κ_{II}– and κ_{IV}–phases, benzotriazole does not adequately perform as inhibitor.

- Due to the central–role of copper metal–ion on the NAB corrosion mechanism, and therefore its subsequent detection in terms of crevice corrosion monitoring, the copper(I) and copper(II) electrochemical behaviours were investigated at BDD electrode at different chloride concentration, which ranged from 0.0 M to 3.0 M. It was observed that the electrochemical response of copper–ion is significantly affected by the presence of chloride. Indeed, in the absence of chloride the electrochemical behaviour of copper–ion was characterised by a one–step two–electron transfer process, whereas in its presence the process involved a two–step one–electron transfer mechanism. In the presence of the chloride and up to a concentration 1.6 M, the equilibrium potential for the system copper(I) / copper(II) was observed to be dependent on chloride, whereas at higher concentrations (from 2.4 M to 3.0 M) the equilibrium potential was independent. These observations were found to be consistent with the speciation diagrams for copper(I)– and copper(II)–chloride complexes. The copper–ion electrochemical detection on BDD electrode was then developed further on the basis of these experimental observations.
- When exposed to acidic chloride solutions, NAB undergoes a corrosion mechanism different from only involving copper oxidation. The significant concentration of nickel–ion reported within NAB crevice solutions at acidic pHs [7], required the consideration of an alternative electrochemical protocol for nickel–ion detection, which did not use a chelating agent or was achieved at strongly alkaline solutions. Therefore, a new electrochemical protocol, which relied on the initial metal–ion deposition followed by its actual detection, was studied on BDD electrode. The new protocol clearly demonstrated the assessment of the nickel–ion concentration in a chloride solution at pH of 4. The viability of the procedure was obtained by utilising the excellent electrochemical characteristic exhibited by the BDD electrode, *i.e.*, wide potential window and low capacitive current.
- Investigations (*i*) on the NAB corrosion performance and (*ii*) on the electrochemical behaviour of metal–ions likely to be present within crevice corrosion solutions provided greater understanding of the NAB crevice corrosion to allow an *in situ* monitoring using the BDD microelectrode array. The NAB crevice corrosion monitoring revealed only the presence of copper(I), whose concentration initially increased within the first two hundred hours of immersion and then remained stable

at ca. 0.47 mM. The absence of copper(II) and of other metal–ions suggested (*iii*) the low crevice concentration of dissolved oxygen (which promotes the oxidation of copper(I) to copper(II)) and (*iv*) that the local pH did not decreased below 4, where the NAB corrosion is dominated by the dissolution of the aluminium–, iron– and nickel–rich κ–phases. The use of benzotriazole as an inhibitor for crevice corrosion was successfully demonstrated due to its high affinity for the corroding copper–rich α–phase.

11. Future Work

11.1 Nickel–Aluminium Bronze Corrosion Behaviour

The NAB corrosion performance in acidic chloride solutions can be further investigated. As a matter of fact, the electrochemical mechanism was not completely defined and whether the NAB dissolution was driven by aluminium–, iron– or nickel–oxidations has still to be precisely established.

Different NAB oxidation mechanisms may take place as the solution pH is decreased from 4 to 3. Indeed, the multi–element compositions of the κ_I–, κ_{II}– and κ_{IV}–phases can lead to different and selective oxidations, due to diverse stabilities of the aluminium, iron and nickel oxides. For this particular purpose, the use of a NAB rotating–disc electrode system may provide additional insights regarding the reaction mechanism. In fact, the improved mass transfer of metal ions from the electrode surface to the bulk solution will reduce the possibility of pseudo passivation phenomena (as observed in Figure 4.3 of Chapter 4), hence resulting in better defined Tafel slopes from the absorption and deposition processes.

11.2 Nickel–Ion Detection on Boron–Doped Diamond Electrode in Acidic Solutions

The nickel–ion detection was demonstrated viable in a chloride solution at pH of 4. However, at values lower than 4 (*i.e*, pH 3.0), the oxidation peak was partially overlapped with the ChlER or OER. In fact, in spite of the wide potential window exhibited by the used oxygen–terminated BDD electrode (see Chapter 5), the onset oxidation potential of either chlorine or oxygen evolution reactions did not allow for the clear determination of the characteristic nickel signal.

Ferro and De Battisti [82] showed the possibility of significantly increasing the BDD potential window performing a plasma treatment, which transformed the BDD electrode surface from hydrogen– (or oxygen–) to fluoride–terminations. Indeed, it was shown that fluoride–terminated BDD electrodes do not stabilise the HER and OER reaction intermediates, thus resulting in a 5 V potential window. Hence, the wider window of polarisability exhibited by fluoride–terminated BDD electrode can certainly help the detectability of the characteristic nickel oxidation peak when the solution pHs decrease below 4.

11.3 Electrochemical Monitoring of Nickel–Aluminium Bronze Crevice Corrosion using a Boron–Doped Diamond Microelectrode Array

The NAB crevice corrosion monitoring was investigated during the first 310 hours of the specimen immersion, where the NAB corrosion behaviour was driven by the selective dissolution of the copper–rich α–phase. However, the crevice corrosion test can be prolonged, thus allowing to better understanding when the inversion of the anodic–cathodic site behaviour takes place. From Figure 9.1.1 (see Chapter 9) appeared that at immersion times longer than 200 hours the crevice corrosion concentration of copper(I) attained a steady state (ca. 0.47 mM), hence indicating that an equilibrium between the diffusion processes and the NAB oxidation was achieved. Therefore, it can be reasonably expected that as the NAB oxidation changes from the α–phase to κ–phase dissolutions, the copper(I) concentration within the crevice may decrease. This indication, in addition to other possible electrochemical signals measured at the BDD microelectrode (such as iron–ion or nickel–ion), can provide greater insights regarding the underlying NAB crevice corrosion behaviour at longer immersion times.

Appendix of Figures

Chapter 3

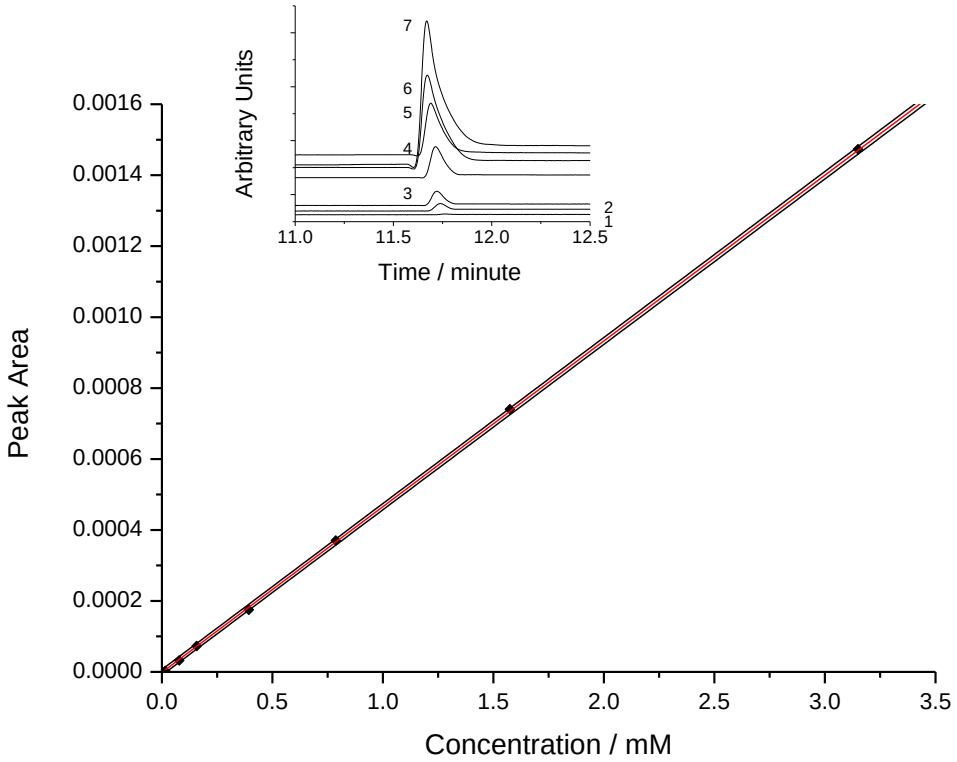

Fig. A_1. Calibration curve with confidence intervals for Cu^{2+} in 0.6 M NaCl determined using capillary electrophoresis. Inset shows the electropherogram at (1) 0.0157, (2) 0.0787, (3) 0.1575, (4) 0.3937, (5) 0.7870, (6) 1.5780 and (7) 3.1496 mM. The evaluated limit of detection is 0.0303 mM.

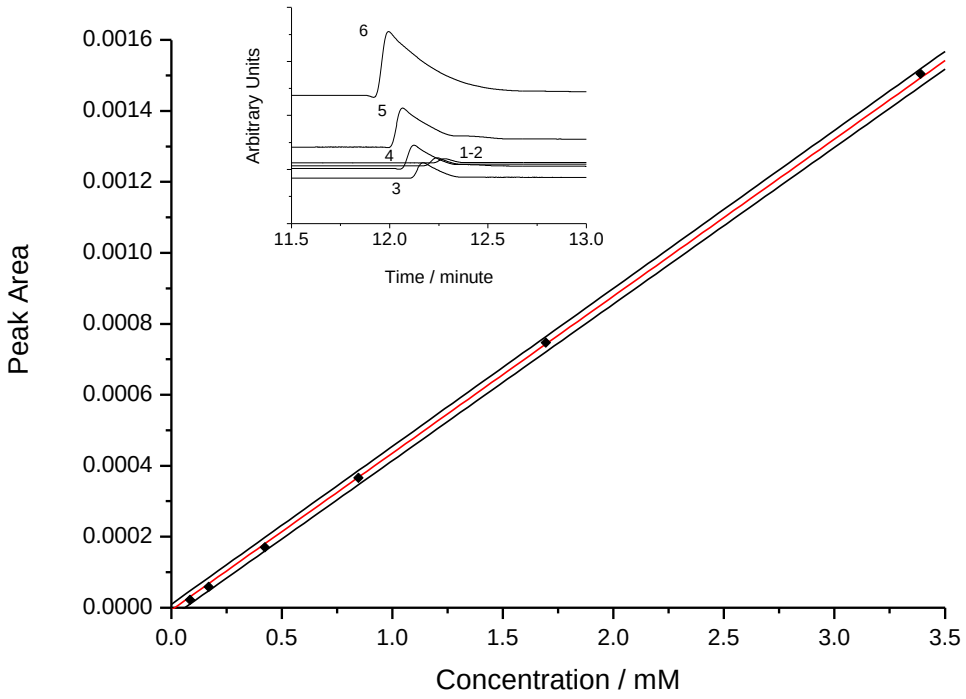

Fig. A_2. Calibration curve with confidence intervals for Ni^{2+} in 0.6 M NaCl determined using capillary electrophoresis. Inset shows the electropherogram at (1) 0.0169, (2) 0.08475, (3) 0.1695, (4) 0.4237, (5) 0.8476, (6) 1.6949 and (7) 3.3898 mM. The evaluated limit of detection is 0.0801 mM.

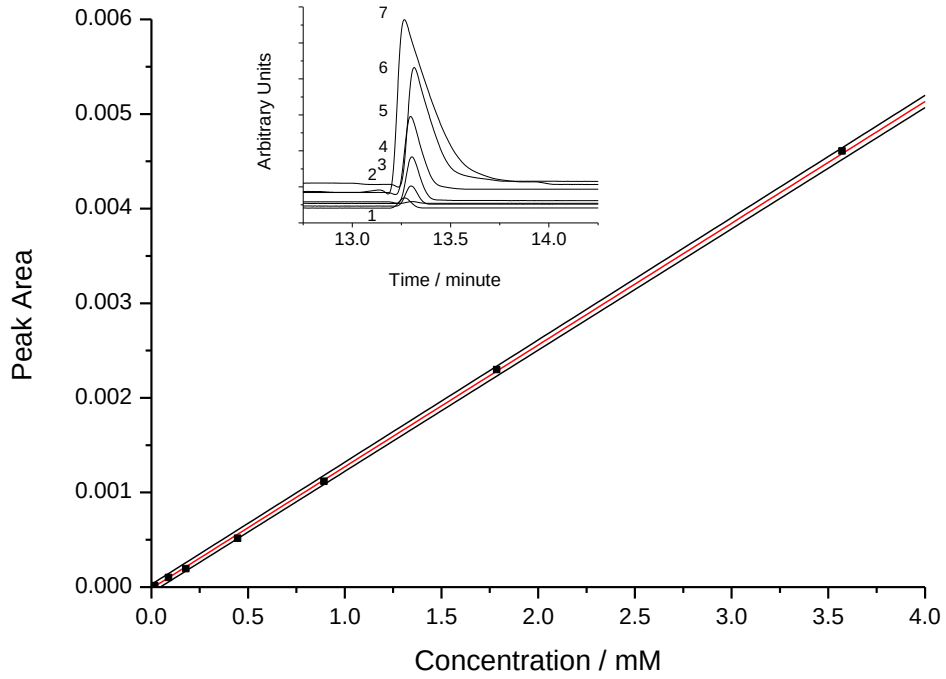

Fig. A$_3$. Calibration curve with confidence intervals for Fe^{3+} in 0.6 M NaCl determined using capillary electrophoresis. Inset shows the electropherogram at (1) 0.0178, (2) 0.0893, (3) 0.1786, (4) 0.4464, (5) 0.8923, (6) 1.7857 and (7) 3.5714 mM. The evaluated limit of detection is 0.0715 mM.

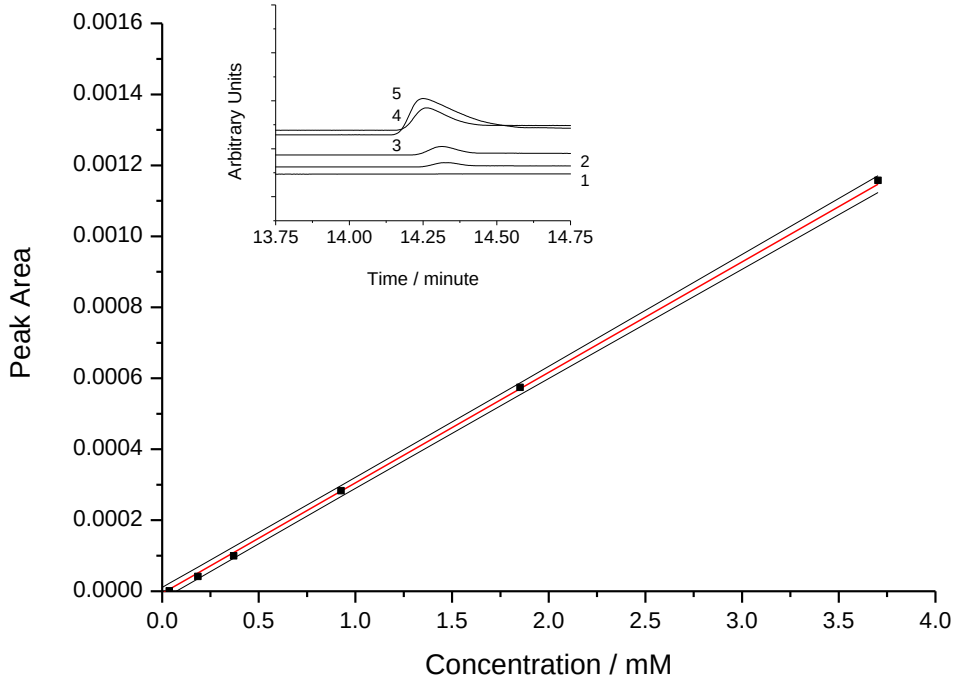

Fig. A$_4$. Calibration curve with confidence intervals for Al^{3+} in 0.6 M NaCl determined using capillary electrophoresis. Inset shows the electropherogram at (1) 0.0370, (2) 0.1852, (3) 0.3703, (4) 0.9259, (5) 1.8518 and (6) 3.7037 mM. The evaluated limit of detection is 0.1080 mM.

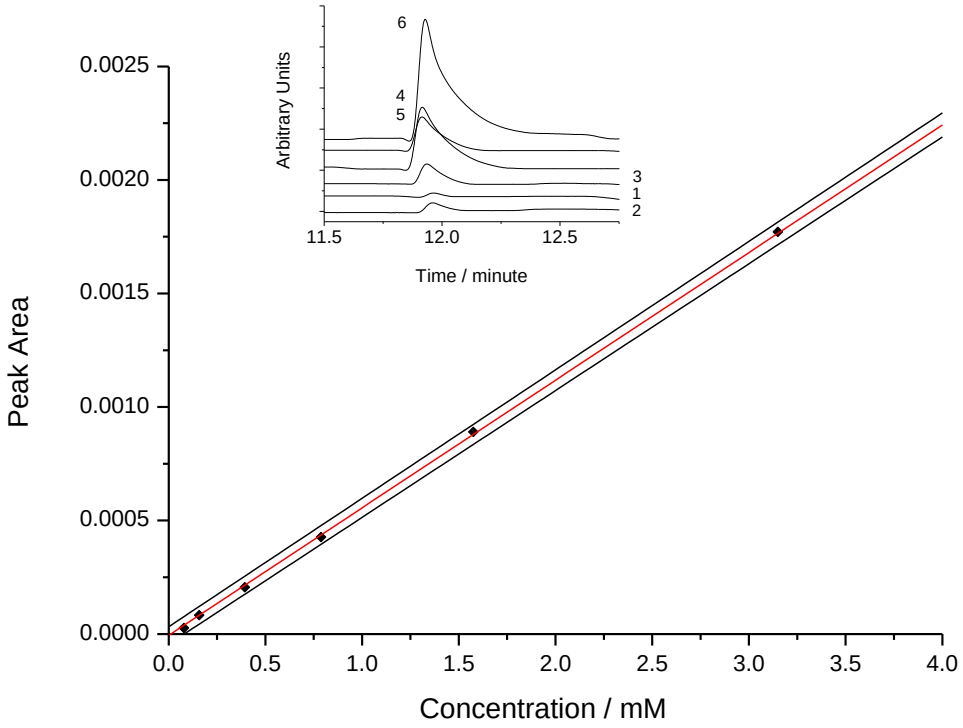

Fig. A$_5$. Calibration curve with confidence intervals for Cu^{2+} in 0.6 M NaCl + 0.01 M bezotriazole determined using capillary electrophoresis. Inset shows the electropherogram at (1) 0.0157, (2) 0.0787, (3) 0.1575, (4) 0.3937, (5) 0.7870, (6) 1.5780 and (7) 3.1496 mM. The evaluated limit of detection is 0.0561 mM.

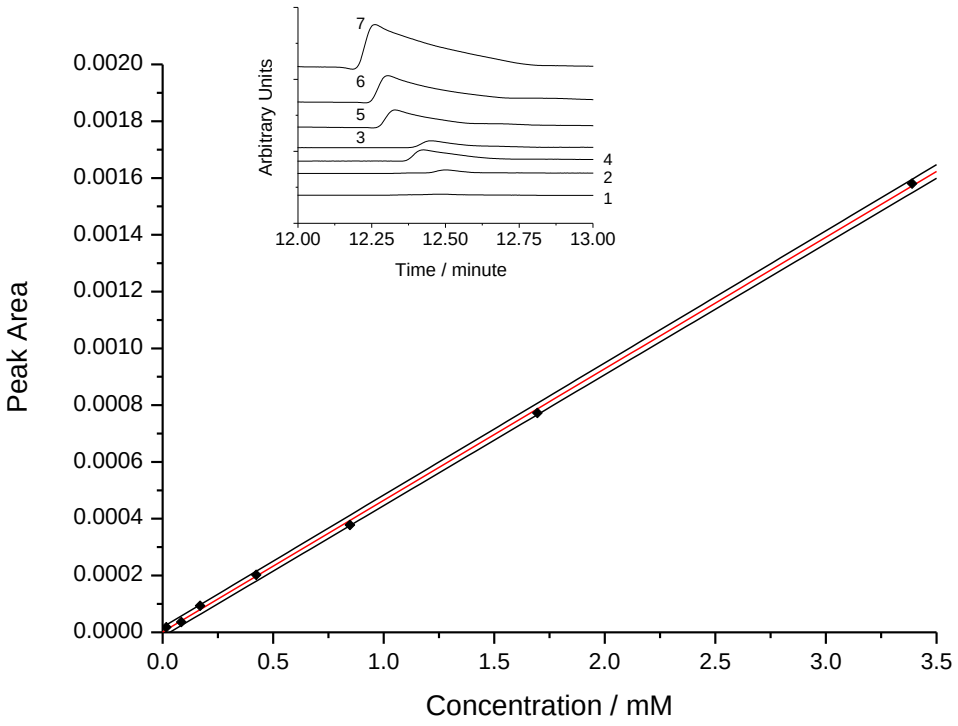

Fig. A_6. Calibration curve with confidence intervals for Ni^{2+} in 0.6 M NaCl + 0.01 M benzotriazole determined using capillary electrophoresis. Inset shows the electropherogram at (1) 0.0169, (2) 0.08475, (3) 0.1695, (4) 0.4237, (5) 0.8476, (6) 1.6949 and (7) 3.3898 mM. The evaluated limit of detection is 0.0797 mM.

Chapter 6

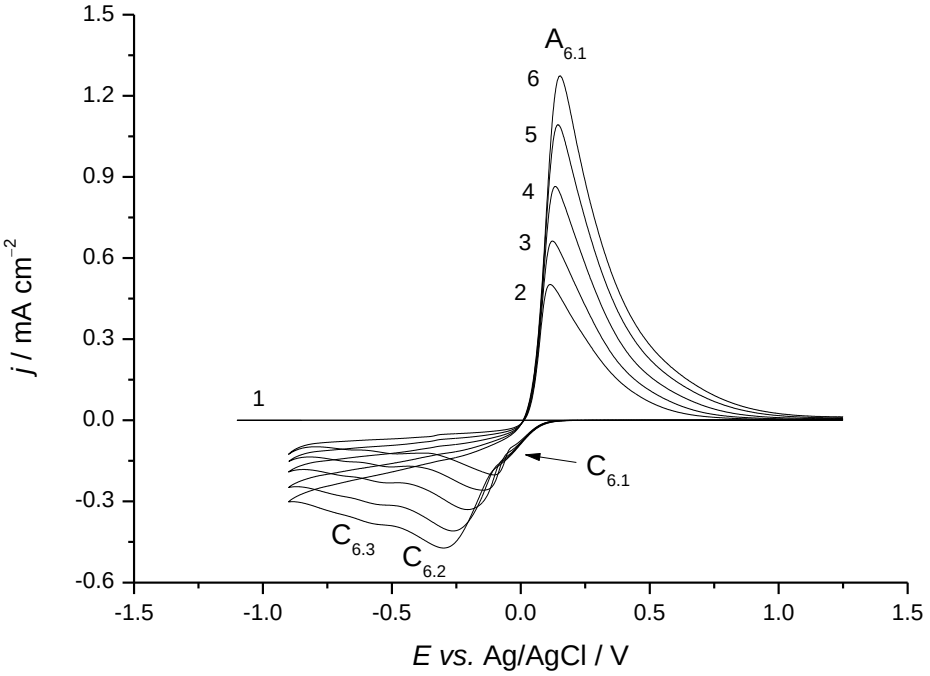

Fig. A_7. Cyclic voltammograms carried out on a BDD electrode in in a 0.6 M $NaClO_4$ + 3.00 mM $CuClO_4$ solution at different scan rates: (2) 25, (3) 50, (4) 100, (5) 200 and (6) 300 mV s^{-1}. Cyclic voltammogram (1) was carried out at in 0.6 M NaCl at 10 mV s^{-1}.

List of References

[1] Corrosion Costs and Preventive Strategies in the United States, www.corrosioncost.com, 2011.

[2] G. Kennell, R. Evitts, K. Heppner, Corros. Sci., 50 (2008) 1716-1725.

[3] G. Engelhard, L. McMillion, D. Macdonald, J. Nucl. Mater., 379 (2008) 48-53.

[4] E. A. Culpan, G. Rose, Br. Corros. J., 14 (1979) 160-166.

[5] J.A. Wharton, K.R. Stokes, Electrochim. Acta, 53 (2008) 2463-2473.

[6] J. C. Rowland, Met. corros. Proc. : Int. Congr. Met. Corr. 8th, 2 1246-1251.

[7] J.A. Wharton, K.R. Stokes, Electrochem. Commun., 9 (2007) 1035-1040.

[8] H. I. Meigh, Cast andWrought Aluminium Bronzes—Properties, processes and structure, Institute of Materials, London, 2000.

[9] J. A. Wharton, R. C. Barik, G. Kear, R. J. K. Wood, K. R. Stokes, F. C. Walsh, Corros. Sci., 47 (2005) 3336-3367.

[10] E. A. Culpan, G. Rose, J. Mater. Sci., 13 (1978) 1647-1657.

[11] R. D. Klassen, C. V. Hyatt, P. R. Roberge, G. A. Botton, J. A. Gianetto, Can. Metall. Q., 41 (2002) 121-131.

[12] F. Hasan, A. Jahanafrooz, G. W. Lorimer, N. Ridley, Met. Trans. A, 13 (1982) 1337-1345.

[13] G. W. Lorimer, F. Hasan, J. Iqbal, N. Ridley, Br. Corros. J., 21 (1986) 244-248.

[14] G. Kear, B. D. Barker, K. Stokes, F. C. Walsh, J. Appl. Electrochem., 34 (2004) 1241-1248.

[15] R.G. Kelly, C.S. Brossia, K.R. Cooper, J. Krol, J. Cromatogr. A, 739 (1996) 191-198.

[16] R. C. Wolfe, K. G. Weil, H. W. Pickering, J. Phys. Chem. B, 108 (2004) 14298-14304.

[17] R.C. Wolfe, H.W. Pickering, B.A. Shaw, J. Electrochem. Soc., 153 (2006) B25.

[18] D. Tromans, R. Sun, J. Electrochem. Soc., 138 (1991) 3235-3244.

[19] I. Dugdale, J. B. Cotton, Corros. Sci., 3 (1963) 69-74.

[20] M. Finšgar, I. Milošev, Corros. Sci., 52 (2010) 2737-2749.

[21] R. Subramanian, V. Lakshminarayanan, Corros. Sci., 44 (2002) 535-554.

[22] K. L. Stewart, J. Zhang, S. Li, P. W. Carter, A. A. Gewirth, J. Electrochem. Soc., 154 (2007) D57-D63.

[23] Y. C. Wu, P. Zhang, H. W. Pickering, D. L. Allara, J. Electrochem. Soc., 140 (1993) 2791-2800.

[24] G. Xue, J. Ding, P. Cheng, Appl. Surf. Sci., 89 (1995) 77-82.

[25] N. K. Allam, H. S. Hegazy, E. A. Ashour, J. Electrochem. Soc., 157 (2010) C174-C177.

[26] P. G. Cao, J. L. Yao, J. W. Zheng, R. A. Gu, Z. Q. Tian, Langmuir, 18 (2002) 100-104.

[27] P.G. Fox, G. Lewis, P.J. Borden, Corros. Sci., 19 (1979) 457-467.

[28] T. Hashemi, C.A. Hogarth, Electrochim. Acta, 33 (1988) 1123-1127.

[29] J. J. Kester, T.E. Furtak, J. Bevolo, J. Electrochem. Soc., 129 (1982) 1716.

[30] S.L.F.A. Da Costa, J.C. Rubim, S.M.L. Agostinho, J. Electroanal. Chem., 220 (1987) 259-268.

[31] V. Brusic, M. A. Frisch, B. N. Eldridge, F. P. Novak, F. B. Kaufman, B. M. Rush, G.S. Frankel, J. Electrochem. Soc., 138 (1991) 2253-2258.

[32] K. Cho, J. Kishimoto, T. Hashizume, H.W. Pickering, T. Sakurai, Appl. Surf. Sci., 87/88 (1995) 380-385.

[33] M. R. Vogt, R. J. Nichols, O. M. Magnussen, R. J. Behm, J. Phys. Chem. B, 102 (1998) 5859-5865.

[34] M. R. Vogt, W. Polewska, O. M. Magnussen, R. J. Behm, J. Electrochem. Soc., 144 (1997) L113-L116.

[35] W. Qafsaoui, C. Blanc, N. Pebere, H. Takenouti, A. Srhiri, G. Mankowski, Electrochim. Acta, 47 (2002) 4339-4346.

[36] A. Kokalj, S. Peljhan, M. Finsgar, I. Milosev, J. Am. Chem. Soc., 132 (2010) 16657-16668.

[37] R. Youda, H Nishihara, K. Aramaki, Electrochim. Acta, 35 (1990) 1011.

[38] G. A. Hope, D. P. Schweinsberg, P. M Fredericks, Spectrochim. Acta, 50 (1994) 2019-2026.

[39] R. Alkire, A. Cangellari, J. Electrochem. Soc., 136 (1989) 913-919.

[40] G. Xue, J. Ding, P. Lu, J. Dong, J. Phys. Chem., 95 (1991) 7380-7384.

[41] Z. Xu, S. Lau, P. W. Bohn, Langmuir, 9 (1993) 993-1000.

[42] M. Metikos-Hukovic, R. Babić, I. Paic, J. Appl. Electrochem., 30 (2000) 617-624.

[43] M. M. Antonijevic, S. M. Milic, M. D. Dimitrijevic, M. B. Petrovic, M. B. Radovanovic, A. T. Stamenkovic, Int. J. Electrochem. Sci., 4 (2009) 962-979.

[44] D. M. Bastidas, P. P. Gómez, E. Cano, Rev. Metal. Madrid, 41 (2005) 98-106.

[45] D. M. Bastidas, Surf. Interface Anal., 38 (2006) 1146-1152.

[46] R. Babic, M. Metikos-Hukovic, M. Loncar, Electrochim. Acta, 44 (1999) 2413-2421.

[47] A. A. Khadom, A. S. Yaro, A. A. H. Kadhum, J. Chil. Chem. Soc., 55 (2010) 150-152.

[48] B. Xu, N. Y. Gao, H. Cheng, C.Y. Hu, S.J. Xia, X.F. Sun, X. Wang, S. Yang, J. Hazard. Mater., 169 (2009) 586-592.

[49] S. Ferro, M. Dalcolle, A. De Battisti, Carbon, 43 (2005) 1191-1203.

[50] J. H. T. Luong, K. B. Male, J. D. Glennon, The Analyst, 134 (2009) 1965-1979.

[51] A. Fujishima, Y. Einaga, T. Narasinga Rao, D. A. Tryk, Diamond Electrochemistry, Elsevier Publisher, (2005) 87.

[52] A. Fujishima, Y. Einaga, T. Narasinga Rao, D. A. Tryk, Diamond Electrochemistry, Elsevier Publisher, (2005) 11-13.

[53] L. Guo, G. Chen, Diamond Relat. Mater., 16 (2007) 1530-1540.

[54] Y. Ando, T. Tachibana, K. Kobashi, Diamond Relat. Mater., 10 (2001) 312-315.

[55] A. Fujishima, Y. Einaga, T. Narasinga Rao, D. A. Tryk, Diamond Electrochemistry, Elsevier Publisher, (2005) 17-19.

[56] A. Cieciwa, R. Wuthrich, C. Comninellis, Electrochem. Commun., 8 (2006) 375-382.

[57] Yu V. Pleskov, M. D. Krotova, V. G. Ralchenko, A. V. Khomichc, R. A. Khmelnitskiy, Electrochim. Acta, 49 (2003) 41-49.

[58] S. C. B. Oliveira, A. M. Oliveira-Brett, Electrochim. Acta, 55 (2010) 4599-4605.

[59] Z. Remes, C. Uzan-Saguy, E. Baskin, R. Kalish, Y. Avigala, M. Nesladek, S. Koizumi, Diamond Relat. Mater., 13 (2004) 713-717.

[60] T. Tachibana, Y. Yokota, K. Hayashi, K. Kobashi, J. Electrochem. Soc., 146 (1999) 1996-1999.

[61] T. Kondo, Y. Einaga, B. V. Sarada, T. N. Rao, D. A. Tryk, A. Fujishima, J. Electrochem. Soc., 149 (2002) E179-E184.

[62] C. H. Goeting, F. Marken, A. Gutierrez-Sosa, R. G. Compton, J. S. Foord, Diamond Relat. Mater., 9 (2000) 390-396.

[63] I. Yagi, H. Notsu, T. Kondo, D. A. Tryk, A. Fujishima, J. Electrochem. Soc., 473 (1999) 173-178.

[64] M. C. Granger, M. Witek, J. Xu, J. Wang, M. Hupert, A. Hanks, M. D. Koppang, J. E. Butler, G. Lucazeau, M. Mermoux, J. W. Strojek, G. M. Swain, Anal. Chem., 72 (2000) 3793-3804.

[65] P. Actis, A. Denoyelle, R. Boukherroub, S. Szunerits, Electrochem. Commun., 10 (2008) 402-406.

[66] S. Ferro, A. De Battisti, Electrochim. Acta, 47 (2002) 1641-1649.

[67] A. Fujishima, T. Y. Einaga, T. N. Rao, D. A. Tryk, Diamond Electrochemistry, Elsevier Publisher, (2005) 103.

[68] A. Fujishima, Y. Einaga, T. Narasinga Rao, D. A. Tryk, Diamond Electrochemistry, Elsevier Publisher, (2005) 39.

[69] S. Szunerits, R. Boukherroub, J. Solid State Electrochem., 12 (2007) 1205-1218.

[70] J. A. Bard, R. L. Faulkner, Electrochemical Methods: Fundamentals and Applications, 2nd ed., John Wiley and Sons, (2001) 116.

[71] M. C. Granger, G. M. Swain, J. Electrochem. Soc., 146 (1999) 4551-4558.

[72] D. Y. Kim, J. Wang, J. Yang, H. W. Kim, G. M. Swain, J. Phys. Chem. C, 115 (2011) 10026-10032.

[73] W. Zhang, S. Xie, H. Chen, M. Li, L. Ma, J. Jia, Collect. Czech. Chem. C., 73 (2008) 73-87.

[74] R. Boukherroub, X. Wallart, S. Szunerits, B. Marcus, P. Bouvier, M. Mermoux, Electrochem. Commun., 7 (2005) 937-940.

[75] E. Vanhove, J. de Sanoit, J. C. Arnault, S. Saada, C. Mer, P. Mailley, P. Bergonzo, M. Nesladek, Phys Stat. Sol. (a), 204 (2007) 2931-2939.

[76] J. McEvoy, J. Foord, Electrochim. Acta, 50 (2005) 2933-2941.

[77] I. Duo, C. Levy-Clement, A. Fujishima, C. Comninellis, J. Appl. Electrochem., 34 (2004) 935-943.

[78] A. Polcaro, P. Ricci, S. Palmas, F. Ferrara, A. Anedda, Thin Solid Films, 515 (2006) 2073-2078.

[79] S. Alehashem, F. Chambers, J. W. Strojek, G. M. Swain, Anal. Chem., 67 (1995) 2812-2821.

[80] D. A. Tryk, K. Tsunozaki, T. N. Rao, A. Fujishima, Diamond Relat. Mater., 10 (2001) 1804-1810.

[81] B. H. Martin, A. Argoitia, U. Landau, A. B. Anderson, J. C. Angus, J. Electrochem. Soc., 143 (1996) L133-L136.

[82] S. Ferro, A. De Battisti, Anal. Chem., 75 (2003) 7040-7042.

[83] A. Kraft, Int.J. Electrochem. Sci., 2 (2007) 355-385.

[84] B. V. Tilak, C. P. Chen, J. Appl. Electrochem., 23 (1993) 631-640.

[85] G. Salazar-Banda, L. Andrade, P. Nascente, P. Pizani, R. Rochafilho, L. Avaca, Electrochim. Acta, 51 (2006) 4612-4619.

[86] N. Krstajic, S. Trasatti, J. Appl. Electrochem., 28 (1998) 1291-1297.

[87] W. Sheng, H.A. Gasteiger, Y. Shao-Horn, J. Electrochem. Soc., 157 (2010) B1529.

[88] I. Yagi, K. Ogai, T. Kondo, A. Fujishima, K. Ueda, K. Uosaki, Chem. Lett., 32 (2003) 1050-1051.

[89] A. Kapalka, G. Foti, C. Comninellis, Electrochem. Commun., 10 (2008) 607-610.

[90] M. Santana, L. Faria, J. Boodts, Electrochim. Acta, 50 (2005) 2017-2027.

[91] L. Janssen, M. H. A. Blijlevens, Electrochim. Acta, 48 (2003) 3959-3964.

[92] F. Beck, H. Krohn, W. Kaiser, M. Fryda, C. P. Klages, L. Schafer, Electrochim. Acta, 44 (1998) 525-532.

[93] T. A. Enache, A. M Chiorcea-Paquim, O. Fatibello-Filho, A. M. Oliveira-Brett, Electrochem. Commun., 11 (2009) 1342-1345.

[94] B. Marselli, J. Garcia-Gomez, P. A. Michaud, M. A. Rodrigo, C. Comninellis, J. Electrochem. Soc., 150 (2003) D79-D83.

[95] N. Simon, H. Girard, M. Manesse, D. Ballutaud, A. Etcheberry, Diamond Relat. Mater., 17 (2008) 1371-1375.

[96] N.S. H. Girard, D. Ballutaud, M. Herlem, A. Etcheberry, Diamond Relat. Mater., 16 (2007) 316-325.

[97] M. Wang, N. Simon, G. Charrier, M. Bouttemy, A. Etcheberry, M. Li, R. Boukherroub, S. Szunerits, Electrochem. Commun., 12 (2010) 351-354.

[98] M. D. Benari, G. T. Hefter, Aust. J. Chem., 43 (1990) 1791-1801.

[99] J. Vazquezarenas, I. Lazaro, R. Cruz, Electrochim. Acta, 52 (2007) 6106-6117.

[100] B. Beverskog, I. Piugdomenech, Corros. Sci., 39 (1997) 969-980.

[101] J.J. Kelly, A.C. West, J. Electrochem. Soc., 14 (1969) 3477-3481.

[102] J. J. Fritz, J. Phys. Chem., 84 (1980) 2241-2246.

[103] M. Wang, Y. Zhang, M. Muhammed, Hydrometallurgy, 45 (1997) 53-72.

[104] V. K. Sharma, F. J. Millero, J. Inorg. Chem., 19 (1990) 375-389.

[105] A. A. Noyes, M. Chow, J. Am. Chem. Soc., 40 (1918) 739-763.

[106] H. McConnell, N. Davidson, J. Am. Chem. Soc., 72 (1950) 3168-3173.

[107] J. J. Fritz, J. Phys. Chem., 88 (1984) 4358-4361.

[108] V. K. Sharma, F. J. Millero, J. Solution Chem., 19 (1990) 375-390.

[109] M. Wang, Y. Zhang, M. Muhammed, Hydrometallurgy, 45 (1997) 37-51.

[110] C. Nila, I. Gonzalez, Hydrometallurgy, 42 (1996) 63-82.

[111] Z. Libus, Inorg. Chem., 12 (1973) 2972-2977.

[112] B. Carlsson, G. Wetterman, J. Inorg. Nucl. Chem., 38 (1976) 1525-1527.

[113] K.G. Ashurst, R.D. Hancock, J. Chem. Soc., Dalton Trans., (1981) 245-250.

[114] R. H. Byrne, C. H. van der Weijden, D. R. Kester, R. W. Zuehlke, J. Solution Chem., 12 (1983) 581-595.

[115] S. Nakabayashi, D. A. Tryk, A. Fujishima, N. Ohta, Chem. Phys. Lett., 300 (1999) 409-413.

[116] S. Tamilmani, W.H. Huang, S. Raghavan, J. Farrell, IEEE T. Seminconduct. M., 17 (2004) 448-454.

[117] J. Zak, M. Kolodziej-Sadlok, Electrochim. Acta, 45 (2000) 2803-2813.

[118] K. Yoo, B. Miller, X. Shi, R. Kalish, J. Electrochem. Soc., 148 (2001) C95-C101.

[119] G. Horanyi, G. Vertes, J. Electroanal. Chem., 45 (1973) 295-299.

[120] N. Markovic, P.N. Ross, Langmuir, 9 (1993) 580-590.

[121] J. H. White, H.D. Abruna, J. Phys. Chem., 94 (1990) 894-900.

[122] F. Bouamrane, A. Tadjeddine, R. Tenne, J. E. Butler, R. Kalish, C. Levy-Clement, J. Phys. Chem. B, 102 (1998) 134-140.

[123] E. C. Demiralay, M. Andac, R. Say, G. Alsancak, A. Denizli, J. Appl. Polym. Sci., 117 (2010) 3704-3714.

[124] M. Gonzalez, M. Gallego, M. Valcarcel, Talanta, 48 (1999) 1051–1060.

[125] K. Sze, W. S. Yeung, Y. Fung, Electrophoresis, 28 (2007) 4156-4163.

[126] Z. Zhang, H. Liu, H. Zhang, Y. Li, Anal. Chim. Acta, 333 (1996) 119-124.

[127] J. Davis, D. H. Vaughan, D. Stirling, L. Nei, R. G. Compton, Talanta, 57 (2002) 1045-1051.

[128] Y. Zhang, S. Yoshihara, J. Electroanal. Chem., 573 (2004) 327-331.

[129] C. J. Flora, E. Nieboer, Anal. Chem., 52 (1980) 1013-1020.

[130] D. R. Crow, Electrochim. Acta, 29 (1984) 1199-1206.

[131] R. P. Baldwin, J. K. Christensen, L. Kryger, Anal. Chem., 58 (1986) 1790-1803.

[132] C. Bing, R. Deen, G. N. Khang, C. Lian Sai, L. Kryger, Talanta, 49 (1999) 651–659.

[133] W. Jin, V. D. Nguyen, P. Valenta, H. W. Nürnberg, Anal. Lett., 30 (1997) 1235-1254.

[134] C. Colombo, C. M. G. van den Berg, Intern. J. Environ. Anal. Chem., 71 (1998) 1-17.

[135] A. T. Paulino, A. M. M. Vargas, L. B. Santos, J. Nozaki, E. C. Muniz, E. B. Tambourgi, Anal. Sci., 24 (2008) 1443-1447.

[136] M. Morfobos, A. Economou, A. Voulgaropoulos, Anal. Chim. Acta, 519 (2004) 57-64.

[137] V. Jovanovski, S. B. Hočevar, B. Ogorevc, Electroanalysis, 21 (2009) 2321-2324.

[138] O. Mikkelsen, S. M. Skogvold, K. M. Schroder, M. I. Gjerde, T. A. Aarhaug, Anal. Bioanal. Chem., 377 (2003) 322-326.

[139] O. A. Farghaly, Microchem. J., 75 (2003) 119-131.

[140] G. Dugo, L. La Pera, V. Lo Turco, G. Di Bella, F. Salvo, J. Agric. Food. Chem., 52 (2004) 1829-1834.

[141] E. N. Vinogradova, G. V. Prokhorova, Zh. Anal. Khim, 23 (1968) 1666.

[142] P. A. M. Farias, A. K. Ohara, I. Takase, S. Ferreira, J. S. Cold, Talanta, 40 (1993) 1167-1171.

[143] S. Puri, R. K. Dubey, B. K. Puri, M. F. Hussain, Anal. Lett., 31 (1998) 283-297.

[144] O. Abollino, M. Aceto, C. Sarzanini, E. Mentasti, Electroanalysis, 11 (1999) 870-878.

[145] M. B. Gholivand, S. Bahrami, S. Abbasi, A. Sohrabi, Electroanalysis, 20 (2008) 1367-1373.

[146] N. S. Zadorozne, C. M. Giordano, M. A. Rodríguez, R. M. Carranza, R. B. Rebak, Electrochim. Acta, 76 (2012) 94-101.

[147] C. M. A. Brett, A. M. O. Brett, Electrochemistry, Principles, Methods and Applications, 2nd ed., Oxford University Press, (1994) 174-175.

[148] J. A. Bard, R. L. Faulkner, Electrochemical Methods: Fundamentals and Applications, 2nd ed., John Wiley and Sons, (2001) 275-290.

[149] J. A. Bard, R. L. Faulkner, Electrochemical Methods: Fundamentals and Applications, 2nd ed., John Wiley and Sons, (2001) 233.

[150] C. M. A. Brett, A. M. O. Brett, Electrochemistry, Principles, Methods and Applications, 2nd ed., Oxford University Press, (1994) 217-218.

[151] A. Lasia, In: B. E. Conway, J. Bockris, R. E. White, editors. Modern aspects of electrochemistry, Vol. 32. New York: Kluwer Academic/Plenum Publishers, (1999) 16.

[152] J. A. Bard, R. L. Faulkner, Electrochemical Methods: Fundamentals and Applications, 2nd ed., John Wiley and Sons, (2001) 158.

[153] D. L. Massart, B. G. M. Vandeginste, S. M. Deming, L. Kaufman, Chemometrics: a textbook, 5th ed., Elsevier, 2003.

[154] G. Kear, B. D. Barker, K. Stokes, F. C. Walsh, J. Appl. Electrochem., 34 (2004) 1235-1240.

[155] H. P. Lee, K. Nobe, J. Electrochem. Soc., 133 (1986) 2035.

[156] C. Deslouis, B. Tribollet, G. Mengoli, M. M. Musiani, J. Appl. Electrochem., 18 (1988) 384-393.

[157] O. E. Barcia, O. R. Mattos, N. Pebere, B. Tribollet, J. Electrochem. Soc., 140 (1993) 2825-2832.

[158] F. K. Crundwell, Electrochim. Acta, 37 (1992) 2707-2714.

[159] A. L. Bacarella, J. C. Griess, J. Electrochem. Soc., 120 (1973) 459.

[160] J. O'M Bockris, A. K. N. Reddy, M. Gamboa-Aldeco, Modern Electrochemsitry 2A: Fundamentals of Electrodics, 2nd ed., Kluwer Academic Publisher (2002).

[161] J.-P. Diard, J.-M. Le Canut, B. Le Gorrec, C. Montella, Electrochim. Acta, 43 (1998) 2469.

[162] W.M. Haynes, CRC Handbook of Chemsistry and Physics, 93th ed. (2012-2013), CRC Press/Taylor and Francis.

[163] C. Deslouis, B. Tribollet, G. Mengoli, M. M. Musiani, J. Appl. Electrochem., 18 (1988) 374-383.

[164] Z.V. Feng, A.A. Gewirth, J. Electroanal. Chem., 601 (2007) 242.

[165] M. Graff, J. Bukowska, K. Zawada, J. Electroanal. Chem., 567 (2004) 297.

[166] M.M. Musiani, G. Mengoli, M. Fleischmann, R.B. Lowry, J. Electroanal. Chem., 217 (1987) 187-202.

[167] T. Simbeck, S. Thomaier, C. Stock, E. Riedl, H. J. Gores, Electrochem. Commun., 13 (2011) 803-805.

[168] B. B. Damaskin, O. A. Petrii, V.V. Batrakov, Adsorption of organic compounds on electrodes, Plenum Press, New York 1971, pp. 86, 87, 94, 95.

[169] J. A. Bard, R. L. Faulkner, Electrochemical Methods: Fundamentals and Applications, 2nd ed., John Wiley and Sons, (2001) 567.

[170] B. B. Damaskin, O. A. Petrii, V.V. Batrakov, Adsorption of organic compounds on electrodes, Plenum Press, New York 1971, pp. 94.

[171] J. A. Bard, R. L. Faulkner, Electrochemical Methods: Fundamentals and Applications, 2nd ed., John Wiley and Sons, (2001) 211-212.

[172] D. R. Lide, CRC Handbook of Chemsistry and Physics, 89th ed., CRC Press/Taylor and Francis. .

[173] W.M. Haynes, CRC Handbook of Chemsistry and Physics, 93th ed. (2012-2013), CRC Press/Taylor and Francis.

[174] U. K. Klaning, K. Sehested, J. Holcman, J. Phys. Chem., 89 (1985) 760-763.

[175] J. A. Bard, R. L. Faulkner, Electrochemical Methods: Fundamentals and Applications, 2nd ed., John Wiley and Sons, (2001) 99.

[176] R. S. Nicholson, Anal. Chem., 37 (1965) 1351-1355.

[177] J. A. Bard, R. L. Faulkner, Electrochemical Methods: Fundamentals and Applications, 2nd ed., John Wiley and Sons, (2001) 242.

[178] J. A. Bard, R. L. Faulkner, Electrochemical Methods: Fundamentals and Applications, 2nd ed., John Wiley and Sons, (2001) 102.

[179] J. A. Bard, R. L. Faulkner, Electrochemical Methods: Fundamentals and Applications, 2nd ed., John Wiley and Sons, (2001) 324.

[180] G. Beamson, D. Briggs, Chichester: John Wiley & Sons Ltd; 1992, ISBN 0-471-93592-1., (1992).

[181] J. A. Bard, R. L. Faulkner, Electrochemical Methods: Fundamentals and Applications, 2nd ed., John Wiley and Sons, (2001) 239.

[182] E.T. Urbansky, Biorem. J., 2 (1998) 81-95.

[183] D. Grujicic, B. Pesic, Electrochim. Acta, 50 (2005) 4426-4443.

[184] J.T. Matsushima, L.C.D. Santos, A.B. Couto, M.R. Baldan, N.G. Ferreira, J. Electrochem. Soc., 159 (2012) D246-D252.

[185] S. Ferro, A. De Battisti, J. Phys. Chem. B, 106 (2002) 2249-2254.

[186] T. Tran, D. A. J. Swinkels, Hydrometallurgy, 15 (1986) 281-295.

[187] D. Pilone, G.H. Kelsall, Electrochim. Acta, 51 (2006) 3802-3808.

[188] J. A. Bard, R. L. Faulkner, Electrochemical Methods: Fundamentals and Applications, 2nd ed., John Wiley and Sons, (2001).

[189] A. Manivannan, M. S. Seehra, D. A. Tryk, A. Fujishima, Anal. Lett., 35 (2002) 355-368.

[190] K. E. Toghill, L. Xiao, N. R. Stradiotto, R. G. Compton, Electroanalysis, 22 (2010) 491-500.

[191] H. Bode, K. Dehmelt, J. Witte, Z. Anorg. Allg. Chem. , 366 (1969) 1-21.

[192] G. Barral, S. Maximovitch, F. Njanjo-Eyoke, Electrochim. Acta, 41 (1996) 1305-1311.

[193] S. Motupally, C. C. Streinz, J. W. Weidner, J. Electrochem. Soc., 142 (1995) 1401-1408.

[194] G. Barral, F. Njanjo-Eyoke, S. Maximovitch, Electrochim. Acta, 40 (1995) 2815-2828.

[195] S. Maximovitch, Electrochim. Acta, 41 (1996) 2761-2771.

[196] M. C. Bernard, P. Bernard, M. Keddam, S. Senyarich, H. Takenouti, Electrochim. Acta, 41 (1996) 91-93.

[197] C. Zhang, S. M. Park, J. Electrochem. Soc., 134 (1987) 2966-2970.

[198] S. G. Real, M. R. Barbosa, J. R. Vilche, A. J. Arvia, J. Electrochem. Soc., 137 (1990) 1696.

[199] R. C. V. Piatti, A. J. Arvia, J. J. Podesta, Electrochim. Acta, 14 (1969) 541.

[200] A. Bengali, K. Nobe, J. Electrochem. Soc., 126 (1979) 1118.

[201] G. T. Burstein, G. A. Wright, Electrochim. Acta, 21 (1976) 311-314.

[202] S. Neodo, D. Rosestolato, S. Ferro, A. De Battisti, Electrochim. Acta, 80 (2012) 282-291.

[203] B.E. Conway, L. Bai, Electrochim. Acta, 31 (1986) 1013.

[204] A. Kapałka, A. Cally, S. Neodo, C. Comninellis, M. Wächter, K. M. Udert, Electrochem. Commun., 12 (2010) 18-21.

[205] K. Stulik, C. Amatore, K. Holub, V. Marecek, W. Kutner, Pure Appl. Chem., 72 (2000) 1483-1492.

[206] R. Aoki, K. Akimoto, K. Tokuda, H. Matsuda, J. Osteryoung, J. Electroanal. Chem., 171 (1984) 219-230.

[207] S. Fierro, A. Kapałka, O. Frey, M. Koudelka, C. Comninellis, Electrochem. Commun., 12 (2010) 587-591.